

**ADVERTIMENT.** L'accés als continguts d'aquesta tesi doctoral i la seva utilització ha de respectar els drets de la persona autora. Pot ser utilitzada per a consulta o estudi personal, així com en activitats o materials d'investigació i docència en els termes establerts a l'art. 32 del Text Refós de la Llei de Propietat Intel·lectual (RDL 1/1996). Per altres utilitzacions es requereix l'autorització prèvia i expressa de la persona autora. En qualsevol cas, en la utilització dels seus continguts caldrà indicar de forma clara el nom i cognoms de la persona autora i el títol de la tesi doctoral. No s'autoritza la seva reproducció o altres formes d'explotació efectuades amb finalitats de lucre ni la seva comunicació pública des d'un lloc aliè al servei TDX. Tampoc s'autoritza la presentació del seu contingut en una finestra o marc aliè a TDX (framing). Aquesta reserva de drets afecta tant als continguts de la tesi com als seus resums i índexs.

**ADVERTENCIA.** El acceso a los contenidos de esta tesis doctoral y su utilización debe respetar los derechos de la persona autora. Puede ser utilizada para consulta o estudio personal, así como en actividades o materiales de investigación y docencia en los términos establecidos en el art. 32 del Texto Refundido de la Ley de Propiedad Intelectual (RDL 1/1996). Para otros usos se requiere la autorización previa y expresa de la persona autora. En cualquier caso, en la utilización de sus contenidos se deberá indicar de forma clara el nombre y apellidos de la persona autora y el título de la tesis doctoral. No se autoriza su reproducción u otras formas de explotación efectuadas con fines lucrativos ni su comunicación pública desde un sitio ajeno al servicio TDR. Tampoco se autoriza la presentación de su contenido en una ventana o marco ajeno a TDR (framing). Esta reserva de derechos afecta tanto al contenido de la tesis como a sus resúmenes e índices.

**WARNING.** The access to the contents of this doctoral thesis and its use must respect the rights of the author. It can be used for reference or private study, as well as research and learning activities or materials in the terms established by the 32nd article of the Spanish Consolidated Copyright Act (RDL 1/1996). Express and previous authorization of the author is required for any other uses. In any case, when using its content, full name of the author and title of the thesis must be clearly indicated. Reproduction or other forms of for profit use or public communication from outside TDX service is not allowed. Presentation of its content in a window or frame external to TDX (framing) is not authorized either. These rights affect both the content of the thesis and its abstracts and indexes.

# **Curcuminoid-based materials toward their use as active components in two and three-terminal devices**

**Teresa Cardona Lamarca**

**Doctoral thesis**

**Ph.D. in Chemistry**

Supervisor: ICREA Prof. Núria Aliaga Alcalde

Supervisor: Dr. Arantzazu González Campo

Tutor: Dr. Ramón Alibés Arqués

**Institut de Ciència de Materials de Barcelona  
(ICMAB-CSIC)**

**2023**



Universitat Autònoma de Barcelona

Departament de Química-Facultat de Ciències

Doctorat en Química

# **Curcuminoid-based materials toward their use as active components in two and three-terminal devices**

**Thesis presented to aspire to the Doctorate in  
Chemistry degree by**

**Teresa Cardona Lamarca**

Supervisor

**ICREA Prof. Núria Aliaga Alcalde**

Supervisor

**Dr. Arantazu Gonzalez Campo**

Tutor

**Dr. Ramón Alibés Arqués**

Bellaterra, 2023





*"What you do makes a difference, and you have to decide what  
kind of difference you want to make."*

*Jane Goodall*



# Agradecimientos/Acknowledgements

*Aquí, ahora y así.* Además de ser el título de la canción que está sonando ahora mismo, son los tres adverbios que describen dónde, cuándo y cómo quiero estar después de estos años de aprendizaje y superación. Por supuesto, todo este tiempo no he estado sola, he estado rodeada de mucha gente que me ha ayudado a llegar hasta aquí, me han acompañado en el viaje, y a los que quiero agradecer su apoyo.

En primer lugar, quiero dar las gracias a mis supervisoras, Núria y Arancha, por la oportunidad que me ofrecisteis de poder trabajar con vosotras, y por prestarme vuestra ayuda cuando la he necesitado. También os quiero agradecer la elección del resto de integrantes del grupo FNS con los que he coincidido, porque gracias a ellos el día a día ha sido más divertido. A Sara, gracias por tu alegría y el tiempo, aunque breve, juntas en el lab. Quiero darte las gracias Daniel, por dedicarme parte de tu tiempo de laboratorio y oficina, compartir tu conocimiento, resolverme todas las dudas de orgánica y facilitarme la síntesis de algunas de las moléculas. También a ti Rossella, quiero agradecerte tu paciencia, todo tu trabajo y especialmente el enorme esfuerzo, sobre todo el de los últimos meses, para poder terminar todas las medidas necesarias lo antes posible y en consecuencia esta tesis. A las dos doctorandas actuales del grupo, Joseline y Raquel, gracias por el apoyo, aguantar mis quejas, la sinceridad, las risas y todas las confesiones y momentos especiales que nos unieron más. ¡Mucho ánimo para las dos, que ya no os queda nada! A los que ya terminaron, Sandra, Dani y Laura, muchas gracias por hacerme sentir acogida cuando llegué y sentir que no solo éramos compañeros de trabajo. Todas las charlas matutinas de despacho, las clases de catalán, todos los trayectos de ferro, con conversaciones íntimas incluidas, los vermouths, las cenas, las fiestas y las risas creo que demuestran muy bien todo lo que os aprecio.

Gracias a todos los colaboradores, dentro y fuera del ICMAB que han hecho posible que este trabajo saliera adelante, en especial a Alejandro y Betty, por invertir muchas de sus tardes midiendo mis muestras.

Gracias a todos los que forman o han formado parte de las familias *Moleculillas*, *Climbing* y *Chachis*, por los momentos dentro del icmab, pero especialmente por los de fuera. Gracias Sole, Jose y Sandra, por los viajes, boda, todas las quedadas y vermouths post cuarentena que eran ya rutina. A Núria, por no perder nunca el interés en seguir teniendo contacto. A Johanna, Jorik, Thomas, Paolo, Marc y Marc el de Marc por todos los buenos momentos. A Cristina, Chiara y Giulia, por vuestra alegría contagiosa. A Alex y Albert, por todo lo aprendido gracias a vosotros, curiosidades, ciencia y música. A los *frenchies*, Nanthilde e Yvan, gracias por hacerme reír siempre y finalmente gracias a vosotras Amanda y Marta por proponer, organizar y decir siempre que sí a los planes, que nos han llevado a fiestas, conciertos, cenas y viajes. Os quiero dar las gracias por animarme en estos últimos meses de escritura, y por la amistad que hemos creado.

Estoy convencida de que mi estancia aquí ha sido mucho mejor gracias a todos vosotros y a todos los planes que hemos ido haciendo durante este tiempo, que se han convertido en recuerdos imborrables.

A veces mudarte a un piso en otra ciudad, con gente desconocida no siempre sale bien. Sin embargo, nosotras no tuvimos este problema, conectamos desde el principio y espero seguir manteniendo esta relación tan especial. Gracias Ainara por las excursiones, cenas, series, fiestas y risas dentro y fuera de casa que te hacen olvidar los problemas del trabajo.

Aunque he estado “lejos” de casa, siempre he tenido a toda mi gente muy presente. Quiero dar las gracias a mis amigas y a Sonia, por su interés en lo que he estado investigando, aunque estuviera muy lejos de sus campos, por escucharme siempre que he estado atascada, por sentir que nada ha cambiado, aunque pasamos algunas temporadas sin vernos y sobre todo por

querer que terminara ya para volver cuanto antes, lo que me ha hecho sentir muy querida.

Uno de los apoyos más incondicionales ha sido el de mi familia, mi abuela Mari, mis padres, mi hermana y Guillermo. Os voy a estar eternamente agradecida por darme todas las oportunidades que estaban en vuestra mano, dejarme siempre elegir con libertad, por respetar y apoyarme en cada decisión que he tomado y guiarme en el camino de la mejor manera que habéis sabido, y gracias a eso y vuestros ejemplos, hoy soy quien soy. Agradecimiento especial a Julia, que, sin saberlo, este último año me ha ayudado a recargar pilas en los momentos más difíciles.

El otro apoyo incondicional has sido tú, David, la otra mitad de este equipo. Has estado acompañándome desde el principio de esta etapa, primero en la distancia y ahora al final desde muy cerquita. Gracias por hacer los viajes en tren, bus o avión y por aguantar la distancia. Gracias por mudarte, escucharme, aguantarme, entenderme y aconsejarme, por darme lo mejor de ti y sacar lo mejor de mí. Eternamente gracias, por todo, lo vivido y lo que queda por vivir. Eres luz y eres casa.

Le estoy agradecida a la vida, por haberos puesto a todos en mi camino y haberos podido conocer y gracias a vosotros por quedaros y acompañarme en este proceso de aprendizaje y crecimiento profesional y personal.



# Abstract

Molecular electronics (MEs), which is based on the use of a single molecule or an assembly of them, as active components in electronic circuits, has emerged as an alternative to the limitations (e.g.: miniaturization) of complementary metal oxide semiconductor (CMOS) technology, currently used in chip processing. Following this motivation, in this doctoral thesis we focus on the design and evaluation of a specific family of molecules, named curcuminoids (CCMoids), as molecular wires to be tested in two- and three- terminal devices.

Specifically, we have examined the electronic performance of a ferrocene-based CCMoid in a vertically configured two-terminal device. The overall system consists of a gold bottom electrode functionalized with a monolayer of cyclodextrin or cucurbituril molecules hosting the CCMoid molecules (guests) to end with an eutectic gallium indium (EGaIn) electrode at the top that completes the device.

Additionally, we have synthesized a variety of CCMoids with different terminal substituents that could promote, in further reactions, extended CCMoid structures. We have explored the conductance in a single molecule regime, of an enlarged CCMoid containing polycyclic aromatic hydrocarbon (PAH) lateral anchoring groups. Such molecules have been deposited in a three-terminal device, which comprises two nanogapped graphene source and drain electrodes separated from the Si gate electrode by a SiO<sub>2</sub> layer. In this way, the terminal PAH moiety can interact by  $\pi$ - $\pi$  stacking with the graphene electrodes, creating a graphene-CCMoid-graphene junction.

Finally, in order to create a more robust device, from a molecule-electrodes contact point of view, we have started the synthetic modifications in the CCMoid backbone for the introduction of a reactive silane group to fix the CCMoid on the SiO<sub>2</sub> layer of three-terminal devices.





# Resumen

La electrónica molecular (MEs) se basa en el uso de una única molécula o un conjunto de ellas, como componentes principales en circuitos electrónicos. Surgió como alternativa a las limitaciones (por ejemplo: miniaturización) de la tecnología de semiconductores complementarios de óxido metálico (CMOS), utilizada actualmente en el procesamiento de chips. Siguiendo esta motivación, en esta tesis doctoral nos centramos en el diseño y evaluación de una familia específica de moléculas, denominadas curcuminoides (CCMoids), como hilos moleculares en dispositivos de dos y tres terminales.

En concreto, hemos examinado el comportamiento electrónico de un CCMoid que contiene ferroceno, en un dispositivo de dos terminales orientado verticalmente. El sistema global consiste en un electrodo inferior de oro funcionalizado con una monocapa de moléculas de ciclodextrina o cucurbituril (anfitriones) que alojan las moléculas de CCMoid (huéspedes) para terminar con un electrodo de galio-indio eutéctico (EGaIn) en la parte superior que completa el dispositivo.

Además, hemos sintetizado una variedad de CCMoids con diferentes sustituyentes terminales que, en reacciones posteriores, han dado lugar a CCMoids extendidos. Hemos explorado la conductancia individual de dos CCMoids extendidos que contienen grupos de anclaje lateral de hidrocarburos aromáticos policíclicos (HAP). Dichas moléculas se han depositado en un dispositivo de tres terminales, que consta de dos electrodos de fuente y drenaje de grafeno, separados del electrodo de puerta de Si por una capa de  $\text{SiO}_2$ . De este modo, los HAP terminales puede interactuar por interacciones  $\pi$ - $\pi$  con los electrodos de grafeno, creando una unión grafeno-CCMoid-grafeno.

Por último, con el fin de crear un dispositivo más robusto, desde el punto de vista del contacto molécula-electrodos, hemos iniciado las modificaciones sintéticas en el esqueleto del CCMoid para la introducción de un grupo

silano reactivo para fijar el CCMoid sobre la capa de  $\text{SiO}_2$  de los dispositivos de tres terminales.

# Abbreviations

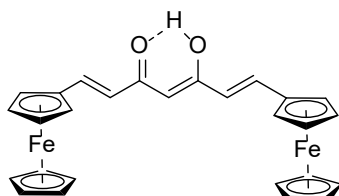
Acetic acid	AcOH
Acetonitrile	ACN
Acetylacetone	ACAC
Anodic peak intensity	I <sub>pa</sub>
Atomic force microscopy	AFM
Attenuated total reflectance	ATR
β-cyclodextrin	βCD
Band gap	E <sub>g</sub>
Bisdemethoxycurcumin	BDMC
Carbon nanotubes	CNTs
Cathodic peak intensity	I <sub>pc</sub>
Chloroform	CHCl <sub>3</sub>
Complementary Metal Oxide Semiconductor	CMOS
Conductive tip Atomic force microscopy	c-AFM
Contact angle	CA
Coordination polymers	CPs
Cucurbit[7]uril	CB[7]
Curcumin	CCM
Curcuminoid/s	CCMoid/s
Cyclic voltammetry	CV

Cyclopentadiene	Cp
Density Functional Theory	DFT
Demethoxycurcumin	DMC
Deuterated chloroform	CDCl <sub>3</sub>
Deuterated dimethyl sulfoxide	DMSO-d <sub>6</sub>
Dichloromethane	DCM
Diethyl ether	Et <sub>2</sub> O
Differential pulse voltammetry	DPV
Diisopropylethylamine	DIPEA
Dimethylformamide	DMF
Dimethyl sulfoxide	DMSO
Ethanol	EtOH
1-ethyl-3-(3-dimethylaminopropyl)carbodiimide	EDC
Ethyl acetate	EtOAc
Eutectic Gallium Indium	EGaIn
Ferrocene	Fc
Fourier transform infrared spectroscopy	FTIR
Gate voltage	V <sub>g</sub>
Hexane	Hex
Highest occupied molecular orbital	HOMO
Infrared reflection absorption spectroscopy	IRRAS

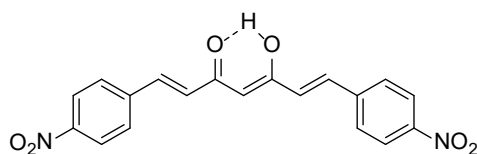
Langmuir-Blodgett	LB
Lowest unoccupied molecular orbital	LUMO
Matrix-Assisted Laser Desorption/Ionization- spectrometry	Time of fly mass MADI-TOF-MS
Mechanically controllable break junction	MCBJ
Metal organic framework	MOF
Methanol	MeOH
Microwave	MW
Molecular Electronics	MEs
Molecular junctions	MJs
N-hydroxysuccinimide	NHS
Nuclear magnetic resonance spectroscopy	NMR
Parts per million	ppm
3-perylenecarboxaldehyde	peCHO
Polycyclic Aromatic Hydrocarbon	PAH
Radial breathing mode	RBM
Room temperature	RT
Scanning electron microscopy	SEM
Scanning probe microscopies	SPM
Scanning tunneling microscopy	STM
Scanning tunnelling microscopy break junction	STM-BJ
Self-assembled monolayers	SAMs

Single walled carbon nanotubes	SWCNTs
Source Drain voltage	$V_{sd}$
Template stripped gold substrates	Au <sup>TS</sup>
Tert-Butyloxycarbonyl	Boc
Tetrabutylammonium hexafluorophosphate	TBAPF <sub>6</sub>
1,1,2,2-Tetrachloroethane	TCE
Tetrahydrofuran	THF
Thermogravimetric analysis	TGA
Thiolated- <i>beta</i> cyclodextrin	SH-βCD
Transmission electron microscopy	TEM
Triethylamine	TEA
Ultraviolet- visible spectroscopy	UV-Vis
X-Ray photoelectron spectroscopy	XPS

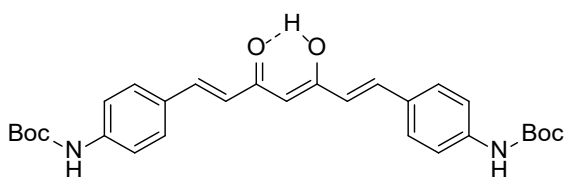
# Synthesized CCMoids



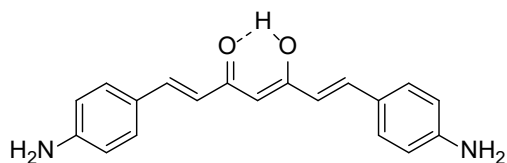
FcCCMoid, **1**



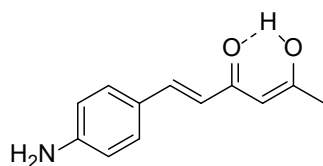
NO<sub>2</sub>CCMoid, **2**



BocNH<sub>2</sub>CCMoid, **3**

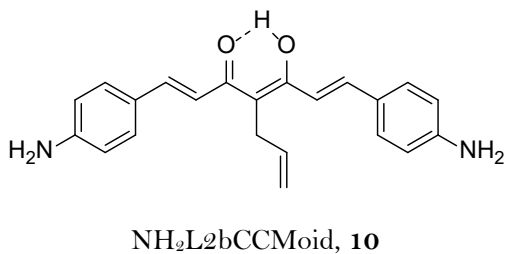
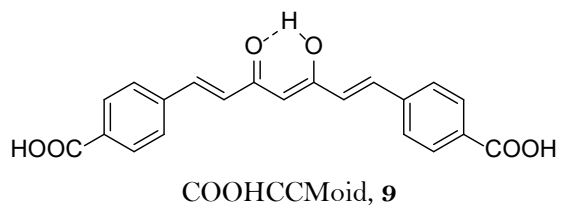
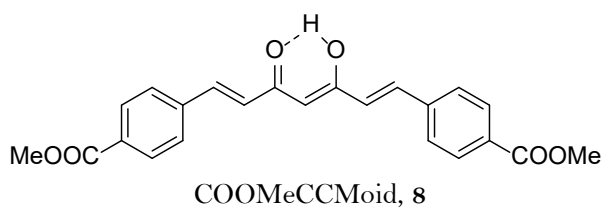
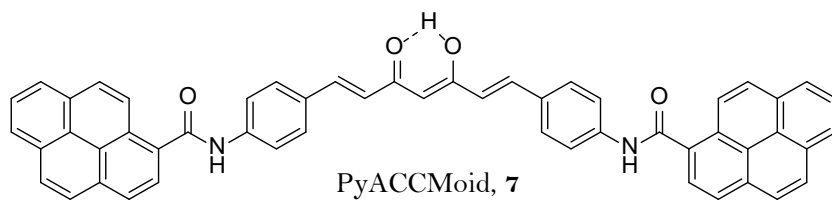
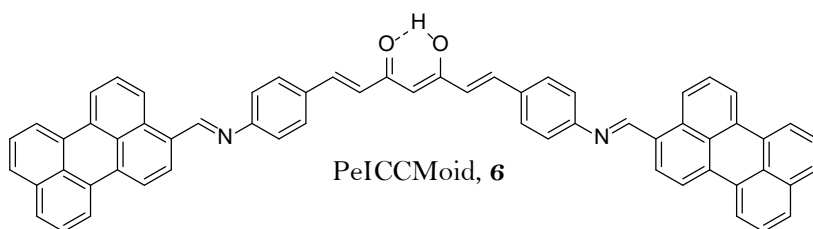


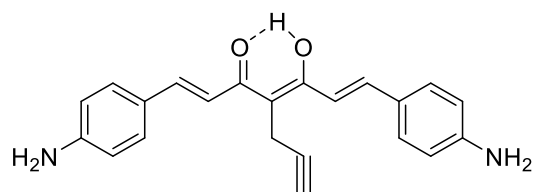
NH<sub>2</sub>CCMoid, **4**



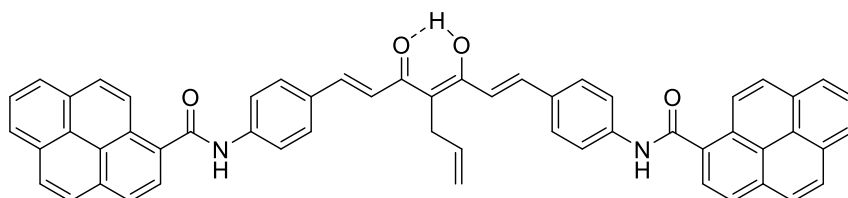
hemiNH<sub>2</sub>CCMoid, **5**



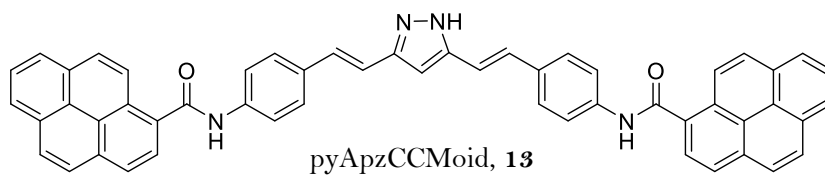




NH<sub>2</sub>L3bCCMoid, **11**



pyAL2bCCMoid, **12**



pyApzCCMoid, **13**



# Table of contents

<b>Agradecimientos/Aknowledgements</b>	I
<b>Abstract</b>	V
<b>Resumen</b>	VII
<b>Abbreviations</b>	IX
<b>Synthesized CCMoids</b>	XIII

## **Chapter 1.** Introduction and objectives

1.1 Curcuminoids (CCMoids)	1
1.2 Molecular Electronics (MEs)	5
1.3 General Objectives	19
References	20

## **Chapter 2.** CCMoid-based host-guest complexes as active components in two terminal devices

2.1 Introduction	29
2.2 Objectives	36
2.3 Results and discussion	37
2.3.1 Synthesis and characterization of FcCCMoid, 1	37
2.3.2 Synthesis and characterization of thiolated- $\beta$ CD	46
2.3.3 Supramolecular systems	48

2.3.3.1 Studies of the encapsulation systems in solution	48
2.3.3.2 Studies of the host-guest complexes on gold surfaces	54
2.4 Conclusions	80
2.5 Experimental section	81
Annex II	87
References	88

## **Chapter 3.** Development of new amino functionalized CCMoid

3.1 Introduction	97
3.2 Objectives	101
3.3 Results and discussion	102
3.3.1 Strategy 1: Reduction of NO <sub>2</sub> CCMoid, 2	103
3.3.1.1. Synthesis and characterization of 2	103
3.3.1.2 Reduction of 2	106
3.3.2 Strategy 2: Protection/Deprotection of -NH <sub>2</sub> groups	107
3.3.2.1. Synthesis and characterization of BocNH <sub>2</sub> CCMoid, 3	107
3.3.2.2. Deprotection of BocNH <sub>2</sub> CCMoid, 3	111
3.3.3 Strategy 3: Direct synthesis of NH <sub>2</sub> CCMoid, 4	112
3.3.3.1 Synthesis and characterization of NH <sub>2</sub> CCMoid, 4	112

3.3.3.2 Synthesis and characterization of hemiNH <sub>2</sub> CCMoid, 5	121
3.4 Conclusions	130
3.5 Experimental section	131
Annex III	135
References	139

**Chapter 4.** Preparation of extended carbon nanotubes and polycyclic aromatic hydrocarbon-based CCMoids as functional units in graphene-based three-terminal devices

4.1 Introduction	147
4.2 Objectives	153
4.3 Results and discussion	154
4.3.1. Covalent functionalization of CNTs with NH <sub>2</sub> CCMoid	154
4.3.2. Synthesis and characterization of perylene-based CCMoid, peICCMoid, 6	162
4.3.3. Electrical characterization of peICCMoid on graphene- based three- terminal devices	169
4.3.3.1. Device fabrication	170
4.3.3.2. Deposition of 6 over three terminal devices	173
4.3.3.3. Strategy 1 for the obtaining of stable perylene-based CCMoids: Reduction of compound 6	177

4.3.3.4. Strategy 2 for the obtaining of stable perylene-based CCMoids: Creation of amide bond	178
4.4 Conclusions	182
4.5 Experimental section	183
Annex IV	186
References	190
<b>Chapter 5.</b> Design of stable pyrene-based CCMoid to be used as nanowire in graphene-based three-terminal devices	
5.1 Introduction	201
5.2 Objectives	203
5.3 Results and discussion	204
5.3.1. Synthesis and characterization of pyACCMoid, 7	204
5.3.2. Deposition of pyACCMoid on the device	214
5.4 Conclusions	217
5.5 Experimental section	218
Annex Va	220
Annex Vb	221
References	227

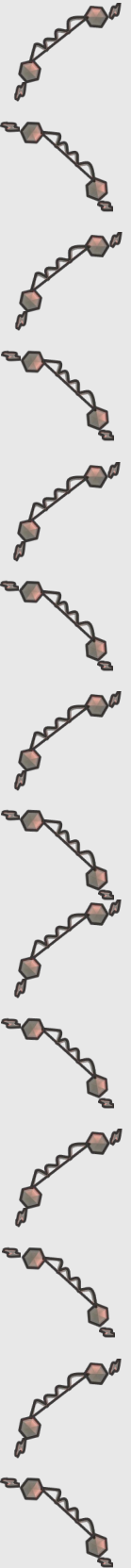
<b>Chapter 6. T-shaped CCMoids</b>	
6.1 Introduction	233
6.2 Objectives	235
6.3 Results and discussion	236
6.3.1. T-shaped CCMoid through the <i>leg</i>	
6.3.1.1. <i>Leg</i> introduction: synthesis and characterization of NH <sub>2</sub> L2bCCMoid, 10	240
6.3.1.2. Extension of the arms: synthesis and characterization of pyAL2bCCMoid, 12	249
6.3.1.3. Hydrosilylation of pyAL2bCCMoid, 12	254
6.3.2. T-shaped CCMoid by customizing the keto-enol moiety	
6.3.2.1. Keto-enol capping: synthesis and characterization of pyrazole-based CCMoid, pyApzCCMoid, 13	256
6.3.2.2. <i>Hat</i> introduction: alkylation of the pyrazole-based CCMoid	261
6.4 Conclusions	263
6.5 Experimental section	265
Annex VI	269
References	276
 <b>General conclusions</b>	 279
<b>Materials and equipment</b>	281





# Chapter 1

## Introduction and objectives





## 1.1. Curcuminoids (CCMoids)

Curcuminoids (CCMoids) are a family of molecules whose chemical structure, shown in Figure 1.1, comprises a conjugated seven carbon chain (*body*) with terminal substituted diaryl groups (*arms*) and a keto-enol moiety in the centre of the chain (*head*). Additionally, diverse functionalities can be attached to the central carbon of the chain, introducing what we call a *leg*.

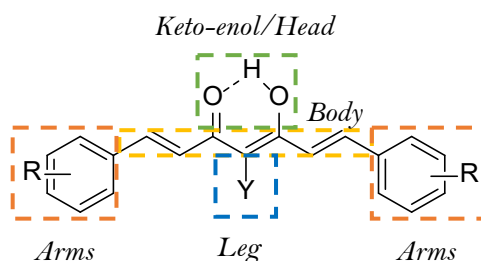


Figure 1.1. General structure of CCMoids.

It is important to highlight that CCMoids exhibit a tautomeric equilibrium between the keto-enol and the diketo forms. However, due to the intramolecular hydrogen bonding and the conjugation of the keto-enol, the former is the most stable tautomer in the solid-state as well as in solution <sup>1</sup>.

Curcumin (CCM), the most well-known CCMoid, is found in nature, together with demethoxycurcumin (DMC) and bisdemethoxycurcumin (BDMC), whose structures are shown in Figure 1.2, all in between 2-8% in the rhizomes of *Curcuma Longa* plants. From the 2-8%, CCM is present in a 70-80%, being the most abundant followed by DMC (15-25%) and BDMC (3-10 %), in that order.

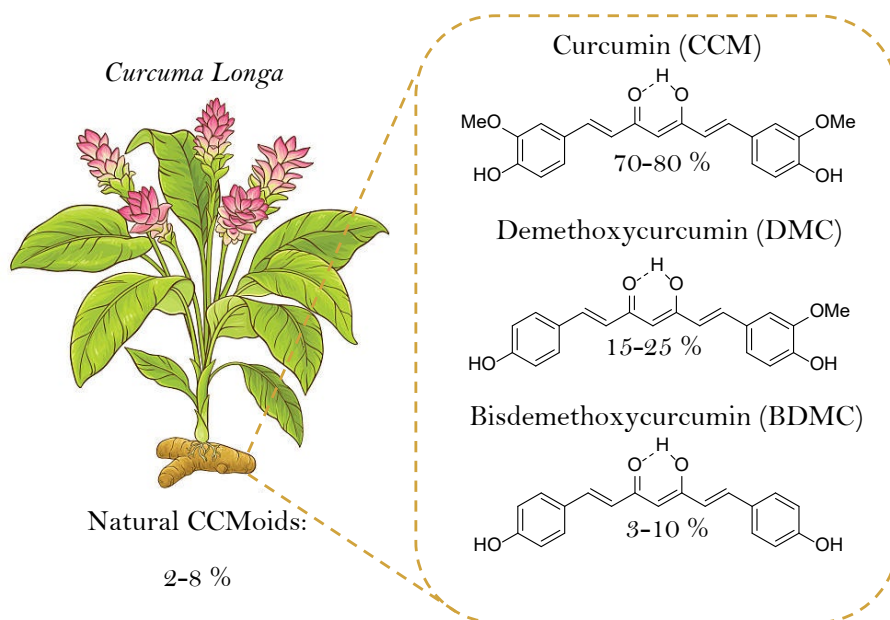


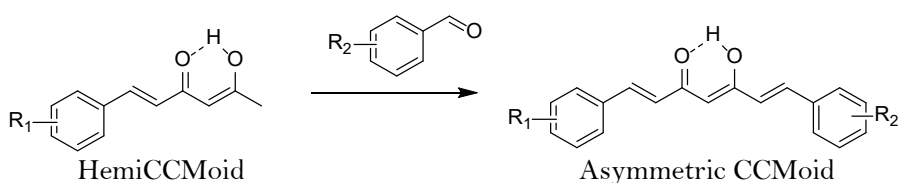
Figure 1.2. Chemical structure of the natural CCMoids: curcumin (CCM), demethoxycurcumin (DMC) and bisdemethoxycurcumin (BDMC).

CCM was first extracted from the turmeric plant in 1824 <sup>2</sup> and despite of some ground-breaking contributions in the subject, such as the description of its chemical formula in 1910 <sup>3</sup>, and the publications of protocols to synthesize it in the laboratory in low yields (around 10 %) <sup>4,5</sup>, it was not until 1964 when Pabon reported the first robust methodology to isolate CCM in a 45 % yield <sup>6</sup>.

Pabon's reaction <sup>6</sup> is based on the condensation between the terminal methyl groups of acetylacetone (ACAC) and the aldehyde vanillin, in a basic catalysed reaction using EtOAc as solvent. As Scheme 1.1. indicates, the first step of the Pabon's reaction is the formation of a boron complex between ACAC and boron oxide in order to avoid the condensation in the central carbon of the ACAC, being the protons more acidic than the terminal methyl ones. Then, the aldehyde involved in the condensation is added, together



piperidine or morpholine <sup>8</sup> or the use of microwave heating <sup>9</sup>, among others. Additional variants, such the decrease in the number of equivalents of the aldehyde used, with respect to the ACAC, could promote the achievement of hemiCCMoids, which contains only one side (*arm*) in the CCMoid, remaining a methyl group intact on the other side of the molecule, as Scheme 1.2 shows <sup>10</sup>. Using hemiCCMoids and by the addition of a different aldehyde from the starting one, asymmetric CCMoids, whose general structure is displayed also in Scheme 1.2, can be obtained <sup>11, 12</sup>.



Scheme 1.2. General scheme for the preparation of asymmetric CCMoids from hemiCCMoids.

Natural CCMoids have been used for decades as dyes, food additives and in traditional medicine, used to reduce pain and swelling, especially in China and India <sup>13</sup>. Currently, the majority of the research investigations involving natural CCMoids is focused on biomedical applications, due to their antioxidant, antiinflammatory and potential anticarcinogenic properties <sup>14,15,16</sup>. However, the versatile chemical modifications in the CCMoids (partially exposed in Figure 1.3), such as the elongation of the body <sup>17</sup> (in yellow, Figure 1.3), the coordination through the keto-enol moiety with metal centres or metalloids <sup>18</sup> (in green, Figure 1.3), the insertion of a *leg* <sup>19</sup> (in blue, Figure 1.3), or the introduction of almost endless variety of *arms* <sup>20,21</sup> (in orange, Figure 1.3) encourage researchers to inspect innovative promising applications, for instance, creation of metal organic frameworks

<sup>22</sup> and coordination polymers <sup>20,23</sup>, or the use of CCMoids as effective molecular platforms in molecular electronics (MEs) <sup>24,25</sup>.

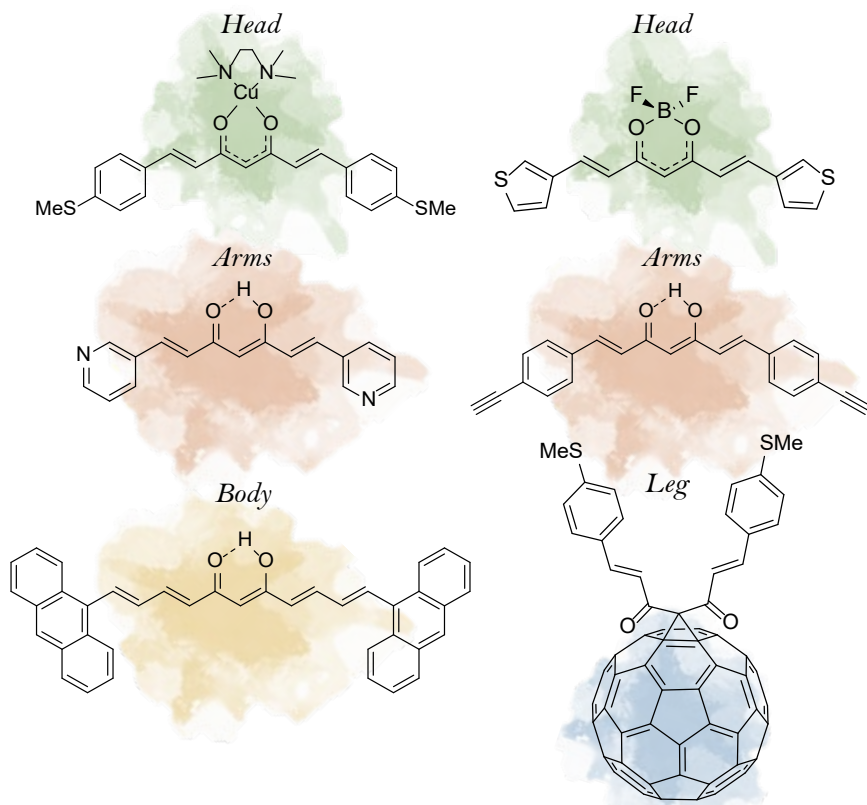


Figure 1.3. Examples of some of the modifications that may be included in the CCMoid structure from references 17-21.

## 1.2. Molecular Electronics (MEs)

Worldwide, 6.37 h is the average time that a person is connected to Internet every day <sup>26</sup>, meaning that during that time, we have an electronic device in our hands or in front of us. Over the years, technology and society have been



requesting for these devices to have a higher capability and capacity; they should be faster, cheaper and smaller, features that can be accomplished by miniaturization processes. The scaling down of transistors, key units in electronic devices, results on the incorporation of higher number of them in processors, which led into higher capacity, speed and lower size <sup>27</sup>. Since one of the first processors fabricated in 1971, Intel 4004, which included 2300 transistors <sup>28</sup>, researchers have been abruptly increasing that number to 134.000 millions of transistors in the M2 Ultra chip presented by Apple at the beginning of 2023 <sup>29</sup>. This miniaturization trend was predicted by Gordon Moore, Intel's co-founder, which suggested that the number of transistors in a circuit is duplicated every 18 months, which is actually known as Moore's Law <sup>30</sup>. However, this miniaturization tendency, due to the actual complementary metal oxide semiconductor (CMOS) technology applied for the chip fabrication is close to the limit, owing to the limitations of present lithographic techniques <sup>27</sup>.

MEs emerged as a suitable alternative to extend the miniaturization process. It is based on the inclusion of a single molecule, or reduced assembly of them, as active component/s in electrical circuits <sup>31</sup>. The use of molecules exhibits several advantages in comparison to the actual CMOS technology <sup>32</sup>, such as the smaller size of the molecules which lead into faster devices because of the integration of more transistors in the device or the ability to chemically modify the variety of available molecules to have specific properties, which could result in novel inaccessible devices.

Although the first studies in the field are dated in the early 70s <sup>33, 34</sup>, in his famous talk "*There's Plenty of Room at the Bottom*" in 1960, Richard Feynman already sowed the idea of making machines smaller by writing: "*I don't know how to do this on a small scale in a practical way, but I do know that computing machines are very large; they fill rooms. Why can't we make them very small, make them of little wires, little elements-and by little, I mean little*" <sup>35</sup>. 11 years later, in 1971, Mann and Kuhn <sup>33</sup> made the first experimental contribution by

reporting the first tunnelling transport measurements through several self-assembled monolayers (SAMs) of fatty acids. In 1974, Aviram and Ratner by running theoretical experiments, proposed the first rectifier system containing a linear molecular system with connected terminal donor and acceptor groups <sup>34</sup>. However, it was not after the development of the scanning probe microscopies (SPM) in 1982, which included scanning tunnelling microscopy (STM) and atomic force microscopy (AFM) when MEs took off <sup>36,37,38</sup>. Since then, research studies have been focused on the fabrication of robust molecular junctions <sup>39</sup>, the exploration of the transport mechanisms through them <sup>40</sup> and the identification of their functional applications such as rectifier, switcher, transistors, or in spintronics, optoelectronics, and thermoelectronics <sup>41</sup>

Molecular junctions (MJs) are composed by a molecule, or an assembly of them, sandwiched between electrodes <sup>42</sup>, as Figure 1.4 exemplifies.

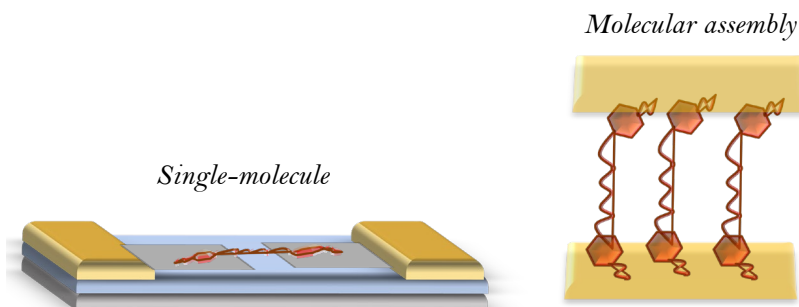


Figure 1.4. Molecular junctions with single or an assembly of molecules.

Most of the molecular systems explored exhibit two common features: a conjugated chain able to assist in the charge transport process and terminal anchoring groups capable of strongly or weakly immobilize the molecule within the electrodes. Depending on the nature of the electrodes, also the nature of the coupling is varied, being mainly covalent if the electrodes are

metallic <sup>43</sup>, or apart from covalent, by  $\pi$ - $\pi$  interactions, if the electrodes are made of graphene <sup>44</sup>.

The charge transport through the molecular junction involves the transmission of electrons between the electrodes that is tuned by the molecular system embedded, acting as a bridge between them <sup>40</sup>. In general, two transport mechanisms can be involved regarding the different couplings between the molecules and the electrodes after deposition, which depend on the location of the molecular HOMO and LUMO levels with respect to the Fermi level of the electrodes. Jia *et al.* <sup>45</sup> labelled the thickness of the HOMO and LUMO level as coupling parameter ( $\Gamma$ ) and the energy difference between them as additional energy ( $U$ ). A weak coupling take place when  $\Gamma \ll U$ , that means, HOMO and LUMO are separated from each other and from the Fermi level. In order to achieve the current flow, the electron must jump from the first electrode to the molecule, and then, jump from the molecule to the second electrode as Figure 1.5 shows. This two-step process is commonly known as “hopping” and as the electron is relaxed inside the junction it needs a thermal activation to trigger the propagation of the charge.

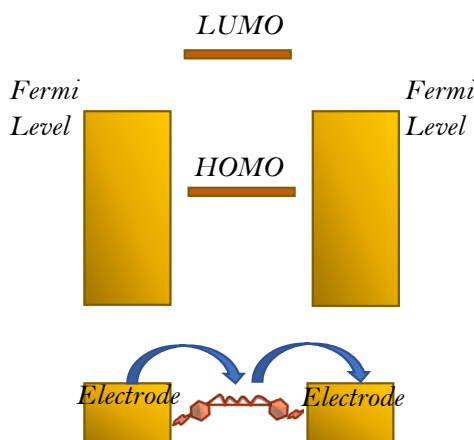


Figure 1.5. Hopping mechanism.

Mathematically “hopping” conductance is described by Equation 1.1, which determines this process is dependent on the temperature.

$$J(V) = J_0(V)e^{-Ea/kT} \quad \text{Eq. 1.1}$$

Where:  $Ea$  is the needed energy for the hopping jump,  $k$  is the Boltzmann constant and  $T$  is temperature <sup>40</sup>.

On the opposite extreme, a strong coupling is observed when the Fermi level and the molecular ones are overlapped,  $\Gamma \gg U$ . In this case, electrons can be transported from the first electrode to the second one without stopping within the molecule, with a maintained energy of the electron implying a “tunnelling” process, as Figure 1.6 displays.

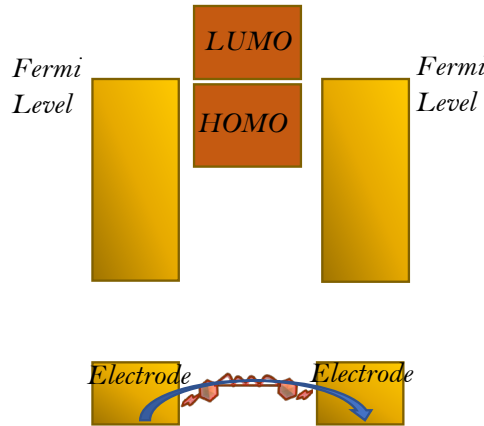


Figure 1.6. Tunnelling mechanism.

Tunnelling mechanism is described by the simplified Simmons model shown in Equation 1.2 <sup>40</sup>

$$J(V) = J_0(V)e^{-\beta d} \quad \text{Eq. 1.2}$$

where:  $J$  is the current density,  $V$  is the applied bias,  $d$  is the separation of the electrodes,  $J_0$  is the theoretical value of  $J$  when  $d=0$  and  $\beta$  is the tunnelling decay coefficient, usually given by the length of the molecule. As Eq 1.2 indicates, the tunnelling conductance is dependent on the molecular length.

Regarding the number of molecules inside the junctions, two different approaches can be found: single molecule junctions, based on the conductance exploration of a single molecule electronic behaviour <sup>41</sup> or molecular ensemble junctions, also called large area junctions, which implies the study of the conductivity of organized molecules, generally in self-assembled monolayers (SAMs) <sup>46</sup>.

To date, the most employed material for electrodes in large area junctions has been gold <sup>47</sup>. Focusing on a vertical configuration of the electrodes, meaning that the current flows perpendicular to the substrate surface, there are different methodologies to anchor organic monolayers onto the bottom substrate <sup>31</sup> for instance, self-assembly <sup>46</sup> or Langmuir-Blodgett <sup>48</sup>, briefly explained below and represented in Figure 1.7.

The self-assembly technique <sup>46</sup> implies the spontaneous chemisorption of a molecule on a surface by means of an anchoring group within the molecular skeleton, followed by an organization of the molecular conformation owing to lateral intermolecular forces between neighbour molecules, which results in an ordered self-assembled monolayer (SAM).

An alternative technique for the monolayer deposition over the surface is the Langmuir-Blodgett (LB) technique <sup>48, 49</sup>, which is based on the creation of a film of amphiphilic molecules at the air-water interface followed by the transference on a substrate located perpendicular Langmuir-Blodgett to the interface. In contrast to the self-assembly methodology, LB allows control of the orientation and packing density of the molecules by the optimization of different parameters (as the compression speed of the film, at the air water

interface, the surface pressure of the transference, from the air water interface to the substrate, or the speed of the emersion of the substrate, among others) that can be adjusted in the process.

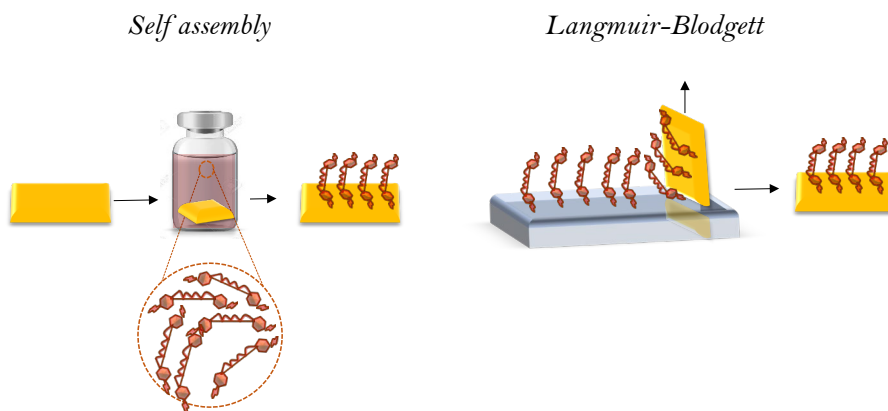


Figure 1.7. Self-assembly and Langmuir Blodgett methodologies.

Equally than the bottom electrode functionalization, for the creation of the top junction in large area devices, several strategies are applied <sup>49</sup>, being the most common, the fabrication of metallic electrodes by thermal evaporation <sup>32</sup> or the use of alternative liquid electrodes such as Hg, or eutectic Gallium Indium oxide (EGaIn) <sup>42</sup>, the later exhibiting some advantages with respect to the formers: (i) it can make contacts without damaging the SAM due to the lack of hot metallic vapours and avoiding alloy with the bottom electrode and (ii) it is not toxic. Briefly, EGaIn is an eutectic alloy of Ga (75.5 %) and In (24.5 %) that can be easily shaped into tips acting as top electrodes for large area devices owing to the non-Newtonian properties provided by the formation of a  $\text{Ga}_2\text{O}_3$  layer over the surface of the EGaIn in presence of atmospheric oxygen <sup>50</sup>.

George M. Whitesides, pioneer in the use of EGaIn as top electrodes, investigated the rectification of undecanethiols SAMs in presence and absence of ferrocene (Fc) terminal moieties. He demonstrated that rectification processes only occurred in the systems containing Fc and

explained that this was due to the asymmetrically position of the Fc inside the junction, which was closer to the EGaIn, separated from the bottom electrode by the alkyl chain, making the HOMO of the molecule close to the EGaIn fermi level <sup>51</sup>. One year later, Wimbush and co-workers, created supramolecular host-guest junctions with Au and EGaIn, as bottom and top electrodes, respectively, using Fc functionalised dendrimers as guest units and undecanethioether functionalized  $\beta$ -cyclodextrin SAM as host entities <sup>52</sup>. The interesting results obtained, together with the ambitious unexplored study of the non-covalent interactions of the supramolecular complex inside the EGaIn junctions, have triggered investigations in this topic, and although recent experiments have been conducted to explore the conductivity of additional host guest complexes <sup>53</sup>, to our knowledge, there is not research including large area (molecular or supramolecular junctions) based on CCMoids.

On the other hand, for the study of charge transport in single molecule regime a variety of experimental platforms are available <sup>32</sup>. Making use of SPM microscopes, the conductance of single molecules has been mainly investigated in a vertical configuration by scanning tunnelling break junctions (STM-BJ) and conductive tip atomic force microscopy (c-AFM) <sup>42</sup>. STM-BJ is based on the repeated contact and controlled withdraw of the STM tip with the functionalized bottom electrode, as Figure 1.8 shows. Usually, the molecule has two extreme anchor points, one interacting with the bottom electrode, and the other free to interact with the STM tip, acting as top electrode, when it is close enough to the molecule, allowing it bridging both electrodes <sup>32</sup>.

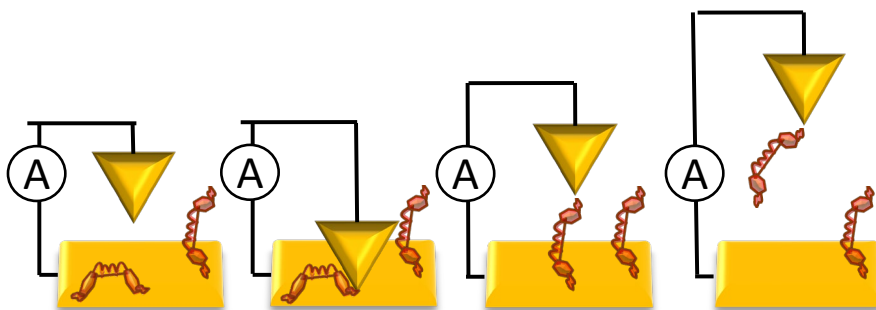


Figure 1.8. Working principle of STM-BJ.

Closely related to STM-BJ is conductive AFM (c-AFM), where the AFM tip is covered with a metallic layer. However, one of the differences between both techniques is the control of the tip position, made by force in AFM in contrast to current in STM<sup>32</sup>.

Apart from the SPM techniques described above, additional conductance measurements are applied for the investigation of the electrical transport using devices with a lateral architecture, meaning that the current goes parallel to the substrate surface. In the following cases, taking into account the average dimension of molecules, it is needed the formation of nanogaps between the electrodes by different techniques. This way, mechanically controllable break junction (MCBJ) has been widely used for the creation of nanogaps, using metallic<sup>24</sup> as well as carbon-based electrodes<sup>54</sup>. It is based, as schemed in Figure 1.9, on the bending of a nanopatterned metallic wire, or graphene layer, on top of a flexible substrate by pushing down two lateral rods until the breaking of the material on top of the flexible support which result into two separated electrodes<sup>55</sup>.



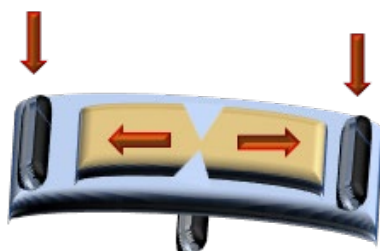


Figure 1.9. Basics of MCBJ technique.

By this technique, and regarding the work performed with CCMoids, the electrical characterization measurements of two identical thiophene terminal CCMoids, displaying the S atoms in two different positions (resulting in 2- and 3-thphCCMoids, respectively) were conducted by Etcheverry-Berríos *et al.* <sup>24</sup>. The chemical structure of the designed ligands, 2-thphCCMoid and 3-thphCCMoid, shown in Figure 1.10, suggest the easier anchoring of the latter on gold substrates because of the outer location of the S atoms, which could result in a higher conductance, however 2-thiophene moieties are well-known in polymers to behave as excellent electron transfer groups <sup>56</sup>. The tests, at the single-molecule level, showed that 3-thphCCMoid presented a conductance value one order of magnitude higher than 2-thphCCMoid ( $3 \times 10^{-4}$  and  $3 \times 10^{-5}$  G<sub>0</sub>), in agreement with DFT calculations.

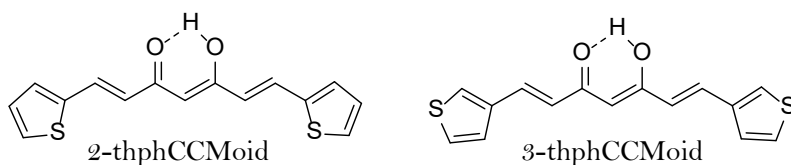


Figure 1.10 Chemical structure of 2-thphCCMoid and 3-thphCCMoid.

Two years later, Olavarria-Contreras *et al.*<sup>18</sup> explored the electron transport of three methyl thio (MeS-) based CCMoids, depicted in Figure 1.11; one of them was the pristine molecule (MeS-CCMoid), and the other two were coordinated compounds by binding the keto-enol moiety of MeS-CCMoid with  $\text{BF}_2$  and  $\text{Cu(II)}$  centres giving rise to MeS-CCMoid- $\text{BF}_2$  and MeS-CCMoid-Cu systems, respectively. The free ligand and the  $\text{Cu(II)}$  coordinated CCMoid presented a single and similar conductance value ( $3.9 \times 10^{-5} G_0$  and  $6.2 \times 10^{-5} G_0$ , in that order). However, they found two well-differentiated conductance values for the  $-\text{BF}_2$  coordinated molecule, at  $5.4 \times 10^{-5}$  and  $1.4 \times 10^{-4} G_0$ , respectively. To understand this behaviour, three more  $-\text{BF}_2$  coordinated molecules with different anchoring groups, (s-thiocarbamate, 3-thiophene, and methyl thio- groups), were studied. They concluded that only CCMoids with  $-\text{BF}_2$  and MeS- ends presented the same bistable behaviour, associating that special characteristic to the combination of the  $-\text{BF}_2$  coordination and the presence of MeS- anchoring groups. Theoretical calculations indicated that this special compound tends to exhibit small conformational changes (by the rotation of the MeS- groups) that affect the dipolar moment of the entire molecule, explaining the existence of two conductance values and to the observed shift between them.

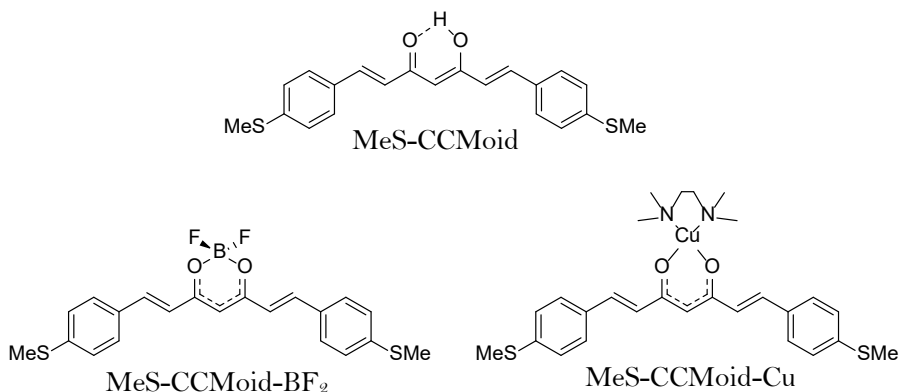


Figure 1.11. Chemical structure of MeS-CCMoid and its  $-\text{BF}_2$  and  $\text{Cu(II)}$  coordinated derivatives.

The most recent CCMoid investigation using MCBJ technique is dated to 2020. Dulic *et al.*<sup>19</sup> studied the conductance of three CCMoids having fullerene groups in, as central legs, and methyl thio terminal arms, as Figure 1.12 shows. The fullerenes bonded to the central position vary: C<sub>60</sub>, C<sub>70</sub> and a functionalized C<sub>60</sub>. In all the cases, the insertion of the fullerene group modified the conformation of the CCMoids, from linear, when not attached to fullerene, to V-shaped, after the attachment. Surprisingly, that dramatic change did not influence in the conductance values obtained by comparing the linear and V-shaped CCMoids, ranging between  $1 - 4 \times 10^{-5}$  G<sub>0</sub>. Additionally, the non-functionalized C<sub>60</sub>-CCMoid displayed an additional lower conductance value, which corresponded to an additional asymmetric junction created by the methyl thio moiety of the CCMoid of one side and the fullerene group on the other side.

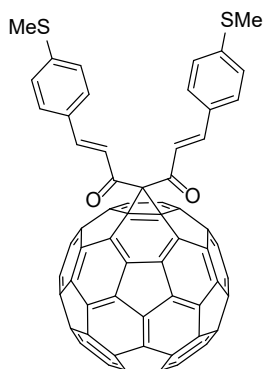


Figure 1.12. Chemical structure of CCM-C<sub>60</sub>.

In the literature, the nanogapped electrodes have been mainly metallic, particularly most of them made of gold. However, due to the high atom mobility, Au nanoelectrodes tend to be unstable at room temperature<sup>57</sup>, driving scientists to examine stable alternatives, finding carbon-base electrodes, especially graphene, as a suitable substitute<sup>25</sup>.

In addition to the above mentioned MCBJ<sup>54</sup>, electroburning<sup>25</sup> is another methodology that allows the nanometric separation between graphene electrodes, providing 1-2 nm gaps. Electroburning, represented in Figure 1.13 is based on the application of consecutive voltage ramps, between the graphene electrodes, while recording the current intensity<sup>25</sup>. When the current intensity drops a certain percentage, which indicates breaking-down of the graphene layer, the voltage applied is automatically backed to zero by the feedback-control. Several cycles of voltage ramps are applied until the absence of current signal within the device, suggesting a complete breaking of the graphene layer, and the opening of a nanogap.

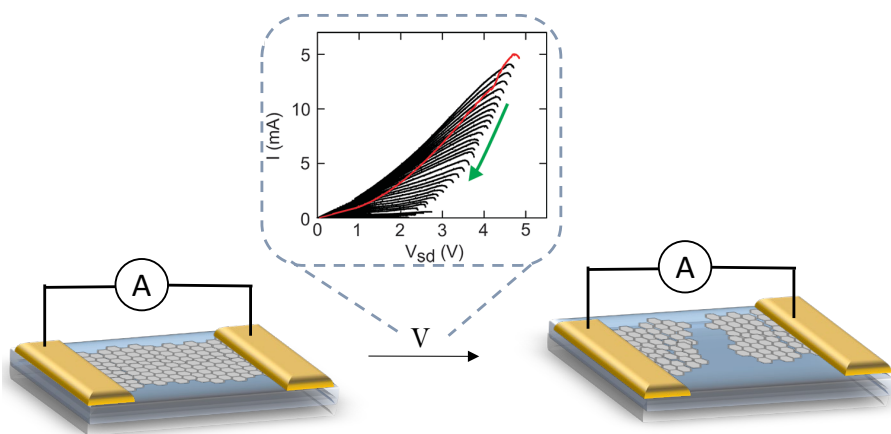


Figure 1.13 Operation principle of electroburning.

In 2011, Prins *et al.*<sup>25</sup> measured the conductance of the first CCMoid in an electroburned graphene based three-terminal device (source, drain and gate electrodes) at room temperature. The so-called 9ACCMoid (Figure 1.14 a), deposited molecule over the device, contained two anthracene moieties functioning as arms, capable to bind by  $\pi$ - $\pi$  stacking with the graphene electrodes. They reported an increase of the current obtained at room and low temperature (10 K) when the CCMoid was present, compared to the

bare nanogap, demonstrating the performance as a nanowire of the CCMoid in the device. The length of 9ACCMoid, 1.68 nm, promoted a  $\pi$ - $\pi$  interaction with the electrodes close to their defected electroburned edges due to the 1-2 nm gap. In order to enhance the anchoring, by locating the anthracene groups further from the edges, few years later, Burzuri *et al.*<sup>17</sup> presented a CCMoid with an enlarged body, called 9ALCCCMoid, shown in Figure 1.14b, which was 2.07 nm long. In a first stage was thought that this increase in length would result in lower conductance values due to the tunnel dependence with the distance. However, it was similar to the one found for 9ACCMoid, which implied a stronger anchoring of the molecule.

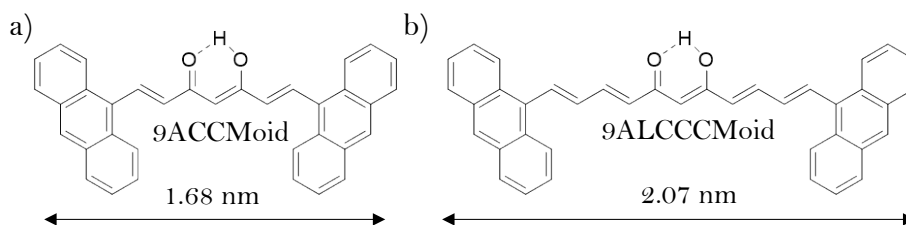


Figure 1.14. Chemical structures and lengths of a) 9ACCM and b) 9ALCCCMoid.

At this point, this doctoral thesis project aims to contribute into the further explorations of CCMoids in molecular electronics, creating large area supramolecular CCMoid junctions as well as single polycyclic aromatic hydrocarbon (PAH) CCMoids junctions.

## 1.3. General objectives

With the main objective of further exploring the use of CCMoids in the field of MEs, the following secondary objectives are proposed:

- Due to the lack of studies of CCMoids framed inside the large area devices category, we proposed to gain insight into the electrical performance of CCMoids. For that, the creation of supramolecular host-guest complexes SAMs on gold bottom electrode with a ferrocene-based CCMoid acting as guest is explored and conductivity studies as molecular ensemble junctions will be studied with EGaIn.
- Focusing on the application of CCMoids as individual nanowires, the preparation and use of extended CCMoids in single molecule graphene junctions, by enlarging the arms with bigger polycyclic aromatic hydrocarbons (PAHs) is investigated. This enlargement would enhance the  $\pi$ - $\pi$  attachments between the molecule and the graphene electrodes due to the further anchoring from the edges as well as due to the increase in the number of aromatic rings in the arms.
- Additionally, in order to obtain more robust devices with single-molecule junctions, the introduction of a reactive functionality in the centre (leg or head) of the extended CCMoids, which can react covalently with the base of the device maintaining the  $\pi$ - $\pi$  attachments between the molecule and the graphene electrodes, will be explored. Therefore, CCMoid with a T-shape will be obtained as well.

## References

- (1) Pettinari, C.; Marchetti, F.; Drozdov, A. Beta-Diketones and Related Ligands. *Comprehensive coordination chemistry II*. **2003**, 97-115.
- (2) Vogel, A Jr. *J. Pharm. Chem.***1842**, 3, 20.
- (3) Milobedzka, J.; Kostanecki, S.; Lampe, V. Zur Kenntnis des Curcumins. *Ber. Dtsch. Chem. Ges.***1910**, 43, 2163– 2170.
- (4) Lampe, V.; Milobedzka, J. Studien uber Curcumin. *Ber. Dtsch. Chem. Ges.***1913**, 46, 2235– 2237.
- (5) Pavolini, T. Nuova sintesi della Curcumina. *Riv. Ital. Essenze, Profumi, Piante Officinali*, **1937**, 19, 167-168.
- (6) Pabon, H. J. J. A Synthesis of Curcumin and Related Compounds. *Recl. Trav. Chim. Pays-Bas* **1964**, 83, 379–386.
- (7) Ferrari, E.; Lazzari, S.; Marverti, G.; Pignedoli, F.; Spagnolo, F.; Saladini, M. Synthesis, Cytotoxic and Combined CDDP Activity of New Stable Curcumin Derivatives. *Bioorg. Med. Chem.* **2009**, 17 (8), 3043–3052.
- (8) Babu, K. V.; Rajasekharan, K. N. Simplified Condition for Synthesis of Curcumin I and Other Curcuminoids. *Org. Prep. Proced. Int.* **1994**, 26 (6), 674–677.
- (9) Pore, D.; Alli, R.; S.C. Prabhakar, A.; R. Alavala, R.; Kulandaivelu, U.; Boyapati, S. Solid-Phase Microwave Assisted Synthesis of Curcumin Analogs. *Lett. Org. Chem.* **2012**, 9 (6), 447–450.
- (10) Kim, E.; Felouat, A.; Zaborova, E.; Ribierre, J. C.; Wu, J. W.; Senatore, S.; Matthews, C.; Lenne, P. F.; Baffert, C.; Karapetyan, A.; Giorgi, M.; Jacquemin, D.; Ponce-Vargas, M.; Guennic, B. Le; Fages, F.; D'Aléo, A. Borondifluoride Complexes of Hemicurcuminoids as Bio-Inspired Push-Pull Dyes for Bioimaging. *Org. Biomol. Chem.* **2016**, 14 (4), 1311–1324.

- (11) Wichitnithad, W.; Nimmannit, U.; Wacharasindhu, S.; Rojsitthisak, P. Synthesis, Characterization and Biological Evaluation of Succinate Prodrugs of Curcuminoids for Colon Cancer Treatment. *Molecules* **2011**, *16* (2), 1888–1900.
- (12) Pedersen, U.; Rasmussen, P. B.; Lawesson, S. O.; Pedersen, U.; Rasmussen, P. B.; Lawesson, S.-O. Synthesis of Naturally Occurring Curcuminoids and Related Compounds. *Liebigs Ann. Chem.* **1985**, 1985 (8), 1557–1569.
- (13) Gopinath, H.; Karthikeyan, K. Turmeric: A condiment, cosmetic and cure. *Indian J Dermatol. Venereol. Leprol.* **2018**, *84* (1), 16–22.
- (14) Madamsetty, V. S.; Vazifehdoust, M.; Alhashemi, S. H.; Davoudi, H.; Zarrabi, A.; Dehshahri, A.; Fekri, H. S.; Mohammadinejad, R.; Thakur, V. K. Next-Generation Hydrogels as Biomaterials for Biomedical Applications: Exploring the Role of Curcumin. *ACS Omega*. **2023**, *8* (10) 8960–8976.
- (15) Hewlings, S. J.; Kalman, D. S. Curcumin: A Review of Its Effects on Human Health. *Foods*. **2017**, *6* (10), 92.
- (16) Maheshwari, R. K.; Singh, A. K.; Gaddipati, J.; Srimal, R. C. Multiple Biological Activities of Curcumin: A Short Review. *Life Sci.* **2006**, *78* (18), 2081–2087.
- (17) Burzurí, E.; Island, J. O.; Díaz-Torres, R.; Fursina, A.; González-Campo, A.; Roubeau, O.; Teat, S. J.; Aliaga-Alcalde, N.; Ruiz, E.; Van Der Zant, H. S. J. Sequential Electron Transport and Vibrational Excitations in an Organic Molecule Coupled to Few-Layer Graphene Electrodes. *ACS Nano* **2016**, *10* (2), 2521–2527.
- (18) Olavarriá-Contreras, I. J.; Etcheverry-Berrios, A.; Qian, W.; Gutiérrez-Cerón, C.; Campos-Olguín, A.; Sañudo, E. C.; Dulić, D.; Ruiz, E.; Aliaga-Alcalde, N.; Soler, M.; Van Der Zant, H. S. J. Electric-Field Induced Bistability in Single-Molecule Conductance Measurements for Boron Coordinated Curcuminoid Compounds. *Chem. Sci.* **2018**, *9* (34), 6988–6996.
- (19) Dulić, D.; Rates, A.; Castro, E.; Labra-Muñoz, J.; Aravena, D.; Etcheverry-Berrios, A.; Riba-López, D.; Ruiz, E.; Aliaga-Alcalde, N.; Soler, M.;



- Echegoyen, L.; Van Der Zant, H. S. J. Single-Molecule Transport of Fullerene-Based Curcuminoids. *J. Phys. Chem. C* **2020**, *124* (4), 2698–2704.
- (20) Rodríguez-Cid, L.; Qian, W.; Iribarra-Araya, J.; Etcheverry-Berríos, Á.; Martínez-Olmos, E.; Choquesillo-Lazarte, D.; Sañudo, E. C.; Roubeau, O.; López-Periago, A. M.; González-Campo, A.; Planas, J. G.; Soler, M.; Domingo, C.; Aliaga-Alcalde, N. Broadening the Scope of High Structural Dimensionality Nanomaterials Using Pyridine-Based Curcuminoids. *Dalton Trans.* **2021**, *50* (20), 7056–7064.
- (21) Riba-López, D.; Zaffino, R.; Herrera, D.; Matheu, R.; Silvestri, F.; Ferreira da Silva, J.; Sañudo, E. C.; Mas-Torrent, M.; Barrena, E.; Pfattner, R.; Ruiz, E.; González-Campo, A.; Aliaga-Alcalde, N. Dielectric Behavior of Curcuminoid Polymorphs on Different Substrates by Direct Soft Vacuum Deposition. *iScience* **2022**, *25* (12), 105686.
- (22) Su, H.; Sun, F.; Jia, J.; He, H.; Wang, A.; Zhu, G. A Highly Porous Medical Metal-Organic Framework Constructed from Bioactive Curcumin. *Chem. Commun.* **2015**, *51* (26), 5774–5777.
- (23) Rodríguez-Cid, L.; Sañudo, E. C.; López-Periago, A. M.; González-Campo, A.; Aliaga-Alcalde, N.; Domingo, C. Novel Zn(II) Coordination Polymers Based on the Natural Molecule Bisdemethoxycurcumin. *Cryst. Growth. Des.* **2020**, *20* (10), 6555–6564.
- (24) Etcheverry-Berríos, A.; Olavarria, I.; Perrin, M. L.; Díaz-Torres, R.; Jullian, D.; Ponce, I.; Zagal, J. H.; Pavez, J.; Vásquez, S. O.; van der Zant, H. S. J.; Dulić, D.; Aliaga-Alcalde, N.; Soler, M. Multiscale Approach to the Study of the Electronic Properties of Two Thiophene Curcuminoid Molecules. *Chem. Eur. J.* **2016**, *22* (36), 12808–12818.
- (25) Prins, F.; Barreiro, A.; Ruitenberg, J. W.; Seldenthuis, J. S.; Aliaga-Alcalde, N.; Vandersypen, L. M. K.; Van Der Zant, H. S. J. Room-Temperature Gating of Molecular Junctions Using Few-Layer Graphene Nanogap Electrodes. *Nano Lett.* **2011**, *11* (11), 4607–4611.
- (26) <https://datareportal.com/reports/digital-2023-global-overview-report>

- (27) Jeong, M.; Doris, B.; Kedzierski, J.; Rim, K.; Yang, M. Silicon Device Scaling to the Sub-10-Nm Regime. *Science*. **2004**, *306* (5704), 2057–2060.
- (28) <https://www.intel.es/content/www/es/es/history/museum-story-of-intel-4004.html?wapkw=4004>.
- (29) <https://www.apple.com/es/newsroom/2023/06/apple-introduces-m2-ultra/>.
- (30) Moore, G. E. Cramming more components onto integrated circuits, Reprinted from *Electronics*, **1965**, *38* (8), 114. J. *IEEE solid-state circuits*. **2006**, *11*(3), 33–35.
- (31) Li, T.; Bandari, V. K.; Schmidt, O. G. Molecular Electronics: Creating and Bridging Molecular Junctions and Promoting Its Commercialization. *Adv. Mater.* **2023**, *35* (22), 2209088.
- (32) Xiang, D.; Wang, X.; Jia, C.; Lee, T.; Guo, X. Molecular-Scale Electronics: From Concept to Function. *Chem. Rev.* **2016**, *116* (7), 4318–4440.
- (33) Mann, B.; Kuhn, H. Tunneling through Fatty Acid Salt Monolayers. *J. Appl. Phys.* **1971**, *42* (11), 4398–4405.
- (34) Aviram, A. Ratner, M. A. Molecular Rectifiers. *Chem. Phys. Lett.* **1974**, *29* (2), 277–283.
- (35) Feynman, R.P. Plenty of room at the bottom. APS Annual meetings. **1960**.
- (36) Joachim, C.; Gimzewski, J. K.; Schlittler, R. R.; Chavy, C. *Electronic Transparency of a Single C60 Molecule*. *Phys. Rev.Lett.* **1995**, *74* (11) 2102–2105.
- (37) Bumm, L. A.; Arnold, J. J.; Cygan, M. T.; Dunbar, T. D.; Burgin, T. P.; Jones, L.; Allara, D. L.; Tour, J. M.; Weiss, P. S. Are single molecular wires conducting? *Science*, **1996**, *271*(5256), 1705–1707.
- (38) Reed, M. A.; Zhou, C.; Muller, C. J.; Burgin, T. P.; Tour, J. M. *Conductance of a Molecular Junction*. *Science*. **1997**, *278* (5336) 252–254.

- (39) El Abbassi, M.; Sangtarash, S.; Liu, X.; Perrin, M. L.; Braun, O.; Lambert, C.; van der Zant, H. S. J.; Yitzchaik, S.; Decurtins, S.; Liu, S. X.; Sadeghi, H.; Calame, M. Robust Graphene-Based Molecular Devices. *Nat. Nanotechnol.* **2019**, *14* (10) 957–961.
- (40) Liu, Y.; Qiu, X.; Soni, S.; Chiechi, R. C. Charge Transport through Molecular Ensembles: Recent Progress in Molecular Electronics. *Chem. Phys. Rev.* **2021**, *2* (2), 021303.
- (41) Sun, L.; Diaz-Fernandez, Y. A.; Gschneidner, T. A.; Westerlund, F.; Lara-Avila, S.; Moth-Poulsen, K. Single-Molecule Electronics: From Chemical Design to Functional Devices. *Chem. Soc. Rev.* **2014**, *43* (21), 7378–7411.
- (42) Gorenskaia, E.; Turner, K. L.; Martín, S.; Cea, P.; Low, P. J. Fabrication of Metallic and Non-Metallic Top Electrodes for Large-Area Molecular Junctions. *Nanoscale.* **2021**, *13* (20), 9055–9074.
- (43) Yuan, L.; Thompson, D.; Cao, L.; Nerngchangnong, N.; Nijhuis, C. A. One Carbon Matters: The Origin and Reversal of Odd-Even Effects in Molecular Diodes with Self-Assembled Monolayers of Ferrocenyl-Alkanethiolates. *J. Phys. Chem. C* **2015**, *119* (31), 17910–17919.
- (44) Zhao, S.; Chen, H.; Qian, Q.; Zhang, H.; Yang, Y.; Hong, W. Non-Covalent Interaction-Based Molecular Electronics with Graphene Electrodes. *Nano Research.* **2023**, *16* (4), 5436–5446.
- (45) Jia, C.; Guo, X. Molecule–Electrode Interfaces in Molecular Electronic Devices. *Chem. Soc. Rev.* **2013**, *42* (13), 5642–5660.
- (46) Vilan, A.; Aswal, D.; Cahen, D. Large-Area, Ensemble Molecular Electronics: Motivation and Challenges. *Chem. Rev.* **2017**, *117* (5), 4248–4286.
- (47) Ratner, M. A Brief History of Molecular Electronics. *Nature Nanotechnol.* **2013**, *8* (6), 378–381
- (48) Zasadzinski, J. A.; Viswanathan, R.; Madsen, L.; Garnæs, J.; Schwartz, D. K. Langmuir-Blodgett Films. *Science* **1994**, *263* (5154), 1726–1733.

- (49) Herrer, L.; Martín, S.; Cea, P. Nanofabrication Techniques in Large-Area Molecular Electronic Devices. *Appl. Sci.* **2020**, *10* (17) 6064.
- (50) Chiechi, R. C.; Weiss, E. A.; Dickey, M. D.; Whitesides, G. M. Eutectic Gallium-Indium (EGaIn): A Moldable Liquid Metal for Electrical Characterization of Self-Assembled Monolayers. *Angew. Chem. Int. Ed.* **2008**, *47* (1), 142–144.
- (51) Nijhuis, C. A.; Reus, W. F.; Whitesides, G. M. Molecular Rectification in Metal-SAM-Metal Oxide-Metal Junctions. *J. Am. Chem. Soc.* **2009**, *131* (49), 17814–17827.
- (52) Wimbush, K. S.; Reus, W. F.; Van Der Wiel, W. G.; Reinhoudt, D. N.; Whitesides, G. M.; Nijhuis, C. A.; Velders, A. H. Control over Rectification in Supramolecular Tunneling Junctions. *Angew. Chem. Int. Ed.* **2010**, *49* (52), 10176–10180.
- (53) Li X.; Zhou, S.; Zhao, Q.; Chen, Y.; Qi, P.; Zhang, Y.; Wang, L.; Guo, C.; Chen, S. Supramolecular Enhancement of Charge Transport through Pillar 5 Arene-Based Self-Assembled Monolayers. *Angew. Chem. Int. Ed.* **2023**, e202216987.
- (54) Caneva, S.; Gehring, P.; García-Suárez, V. M.; García-Fuente, A.; Stefani, D.; Olavarria-Contreras, I. J.; Ferrer, J.; Dekker, C.; van der Zant, H. S. J. Mechanically Controlled Quantum Interference in Graphene Break Junctions. *Nat. Nanotechnol.* **2018**, *13* (12), 1126–1131.
- (55) Martin, C. A.; Ding, D.; Van Der Zant, H. S. J.; Van Ruitenbeek, J. M. Lithographic Mechanical Break Junctions for Single-Molecule Measurements in Vacuum: Possibilities and Limitations. *New J Phys* **2008**, *10* (6), 065008.
- (56) Li, Y.; Yuan, X.; Kim, S.; Zhang, Y.; Xie, D.; Tan, X.; Yang, C.; Huang, X.; Huang, F.; Cao, Y.; Duan, C. Revealing the Molecular Weight Effect on Highly Efficient Polythiophene Solar Cells. *ACS Appl. Mater. Interfaces.* **2023**, *15* (24), 29341–29351.

- (57) O'Neill, K.; Osorio, E. A.; Van Der Zant, H. S. J. Self-Breaking in Planar Few-Atom Au Constrictions for Nanometer-Spaced Electrodes. *Appl. Phys. Lett.* **2007**, *90* (13) 133109.

## Chapter 2

# CCMoid-based host-guest complexes as active components in two-terminal devices

In this section, we examine the behaviour of a curcuminoid containing ferrocene units (Fc) as lateral terminal groups, (FcCCMoid) and its supramolecular host-guest encapsulation in aqueous solutions with CB[7] and  $\beta$ CD macrocycles, respectively, and onto gold substrates as well. Specifically, we investigate the preparation of short thiolated  $\beta$ CD and CB[7] SAMs on Au and their supramolecular complexation with FcCCMoid to measure their conductivity using EGaIn as top electrode.





## 2.1. Introduction

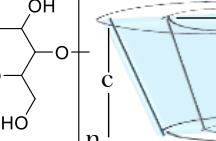
The Nobel prize in Chemistry in 1987, Jean Marie Lehn, defined supramolecular chemistry as the chemistry that includes all the organized systems of higher complexity that arises from the association of different chemical species held by non-covalent interactions <sup>1</sup>. These interactions are mainly intermolecular forces such as Van der Waals interactions, hydrogen bonds or hydrophobic interactions. The smallest class of organization in supramolecular chemistry is the host-guest systems, which are based on molecular recognition interactions between pairs of molecules or ions <sup>2</sup>.

Cyclodextrins (CDs) and cucurbiturils (CBs) are two families of water-soluble macrocycles whose inner hydrophobic cavities allow to form inclusion systems, in aqueous solutions, with different guests such as viologens (V), adamantane (Ad) or ferrocene (Fc) groups, the latter being the subject of study in this chapter. CDs are natural products comprised by glucose repetitive units. Depending on the number of glucose units (6, 7 or 8),  $\alpha$ ,  $\beta$  or  $\gamma$  CDs can be obtained, in that order. On the other hand, CBs are synthetically prepared by the condensation of glycoluril repetitive units with formaldehyde. As in the previous case, depending on the number of repeated units, different CBs can be obtained. The most common are: CB[6], CB[7] and CB[8], with 6, 7 or 8 glycoluril moieties, respectively <sup>3</sup>.

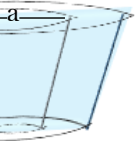
Both families are being compared between them due to their similar cavity size, as Table 2.1 collects. However, they differ in chemical composition and also in the possible binding interactions. CBs exhibit two indistinguishable opening cavities, because of the presence of a symmetric axis, whereas, CDs show two different cavity openings both in size and composition. Additionally, while both families can interact with guests through hydrophobic interactions, CBs can also interact with positively charged guests *via* ion-dipole forces due to the presence of the two carbonyl groups

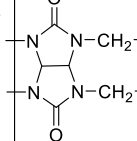


<sup>3</sup>. These variations lead to different complex stabilities depending on the oxidation state of the guest.

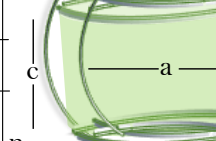


$\alpha\text{CD}, \beta\text{CD}, \gamma\text{CD}$   
 $n = 6, 7, 8$





$\text{CB}[n]$   
 $n = 6, 7, 8$



	$\alpha\text{CD}$	$\beta\text{CD}$	$\gamma\text{CD}$	$\text{CB}[6]$	$\text{CB}[7]$	$\text{CB}[8]$
<b>Cavity (<math>\text{\AA}</math>) (a)</b>	5.3	6.5	8.3	5.8	7.3	8.8
<b>Inner diameter (<math>\text{\AA}</math>) (b)</b>	4.7	5.3	7.5	3.9	5.4	6.9
<b>Height (<math>\text{\AA}</math>) (c)</b>	7.9	7.9	7.9	9.1	9.1	9.1
<b>Outer diameter (<math>\text{\AA}</math>) (d)</b>	14.6	15.4	17.5	14.4	16.0	17.5

Table 2.1. Dimensions of the most common macrocycles in the CDs and CBs families.

Ferrocene is one of the widely explored guest units for both families due to its proper size, reversible redox activity and high binding affinities <sup>4</sup>. A comparative study of the CB and CD families upon ferrocene complexation by Jeon *et al.* <sup>3</sup>, demonstrated that the complex stability between CB and reduced Fc depends on the substituents of the latter, being the positively charged systems the most stable because of the additional ion-dipole forces with the carbonyl groups, followed by the neutral ones, while the negatively charged Fc derivatives showed no binding with the host owing to the repulsion with the carbonyl groups. In contrast, CD forms similar stable complex with all Fc derivatives analysed.

Additionally, focusing on Fc systems, another significant difference between the two macrocycle families must be highlighted; Mastue *et al.*<sup>5</sup> established the electron transfer mechanism for Fc in presence of  $\beta$ CD based on their electrochemical results analysing the ferrocene carboxylate anion. The process involves a first dissociation step of the complex before oxidation, and the incapacity of the host to encapsulate the oxidized specie, as Figure 2.1 a show. In spite of this common behaviour, Ong *et al.*<sup>6</sup>, demonstrated a different path followed by  $\text{Fc}^+$  units to be reduced when CB act as host. These authors show that the electron transference did not occur by a dissociation step and that the  $\{\text{Fc}\}^+$  molecule remained in its encapsulated form as Figure 2.1 b summarised.

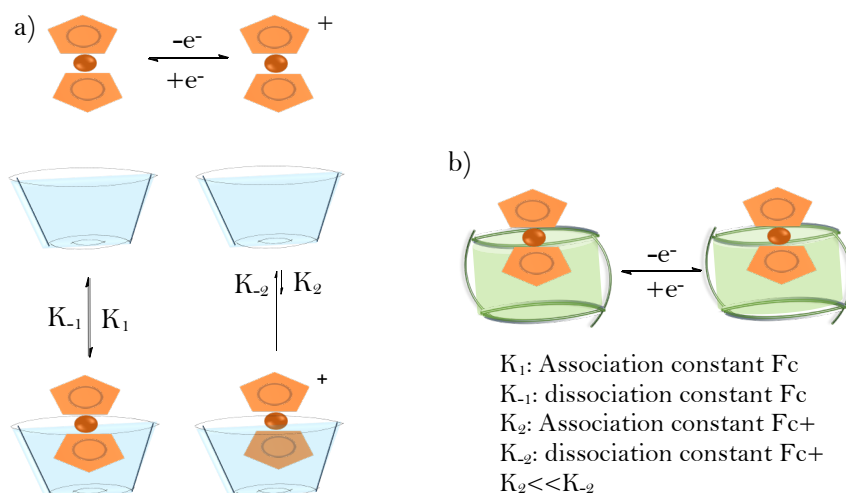


Figure 2.1. Electron transfer mechanism of the inclusion complexes of Fc with a)  $\beta$ CD and b) CB[7].

To fully explore the potential of supramolecular chemistry, scientists have directed their efforts towards investigating the host-guest binding chemistry on surfaces. However, a comparison of the number of publications related to  $\beta$ CD/CB[7]@Fc in solution versus on surfaces indicates that

there is still a plenty of room for research on solid substrates <sup>7</sup>. Furthermore, it is worth noting that CB[7] has not been studied as extensively as  $\beta$ CD in terms of its capabilities as a host molecule.

Investigations related to these encapsulated systems on surfaces are of great interest for bio-applications such as protein immobilization <sup>8,9</sup>, enrichment of labelled proteins <sup>10</sup>, cell adhesion <sup>11</sup> and biosensors <sup>12,13,14</sup>. These hosts have also been analysed as self-healing hydrogels <sup>15</sup>, underwater adhesive <sup>16</sup> as well as basic recognition pairs <sup>17</sup>.

Regarding this matter, only the focus of a small portion of the reported research is in the field of Molecular Electronics. Several top electrodes have been contacted to the different supramolecular systems to measure the changes in current within the molecular junctions and to determine the electrical behaviour of the devices.

Wang *et al.* <sup>18</sup> employed the STM-BJ technique to explore the conductance of CB[5], CB[6], and CB[7] molecules. The STM probe was brought into contact with the modified substrate with a host molecule and then withdrawn to collect the tunnelling current as a function of the probe retraction. The conductance histogram of CB[5], showed a peak at  $10^{-3.9} G_0$  while two times lower conductance values were found for CB[6], and CB[7],  $10^{-4.05}$  and  $10^{-4.15} G_0$ , respectively.

One year earlier, the conductance of CB[7] and CB[7]@Fc modified gold substrate was measured by the STM-BJ technique. The conductance histogram of CB[7] displayed a peak at  $6.8 \times 10^{-5} G_0$ , while for the CB[7]@Fc assembly, two peaks were observed, one around  $4.4 \times 10^{-3} G_0$  and the other overlapped with the empty CB[7] <sup>19</sup>.

Several studies were also focused on investigating the behaviour of devices loaded with Fc systems acting as molecular rectifiers, which the overall systems are two-terminal devices that allow current flow in one direction

while blocking it in the reverse direction <sup>20</sup>. Two crucial requirements must be fulfilled to achieve that performance when these self-assembled monolayers (SAMs) are involved. First, a molecule with a HOMO level close to the Fermi levels of the electrodes must be connected. Second, the active part of the molecule should be asymmetrically located inside the junction, with the HOMO energy level of the molecular system closer to one electrode but far from the other <sup>21</sup>.

These studies were performed using EGaIn as top electrode. Although it was briefly described in Chapter 1, here we provide more detailed information due to its use in this chapter. To summarize, EGaIn is a eutectic mixture of Ga (75.5 %) and In (24.5 %) that presents a Non-newtonian behaviour due to the creation of a  $\text{Ga}_2\text{O}_3$  layer over the EGaIn mixture in presence of oxygen <sup>22</sup>. This particularity provides this material malleability properties, used in this case to prepare conical tips acting as top electrodes. However, it also exhibits some weaknesses, specially related to the  $\text{Ga}_2\text{O}_3$  formed layer, which present a roughness surface and whose thickness can vary with time depending on the measurement conditions, making difficult to know the effective contact area <sup>22</sup>.

Before the contact with the SAM, the EGaIn probe must be created. In the process <sup>22</sup>, a drop of the EGaIn suspended from a filled syringe contacts a bare gold surface, creating a filament of EGaIn between the probe and the gold platform. The filament is becoming thinner until breaking while retracting the syringe, providing a tip attached to it. A sharp drop remains immobilized on the bare gold and is finally discarded, as it is shown in Figure 2.2. The EGaIn probe suspended from the needle remains conically shaped, without turn backwards towards drop shape, due to the  $\text{Ga}_2\text{O}_3$  layer formed in presence of oxygen.



Figure 2.2. EGAIn probe formation process. Image obtained from reference 22.

Once the tip has been formed, the electrode-SAM contact is performed, which is controlled through a camera included in the EGAIn setup. Finally, to explore the conductivity of the SAM, after the proper electrical connections, being the bottom substrate grounded, cycles of positive to negative bias (V) are applied to the EGAIn electrode while the current density (J) is recorded <sup>22</sup>. In order to have reliable results, statistics are needed, due to the difference between every molecular junction formed, owing to possible defects in the SAM or in the bottom electrode.

Wimbush *et al.* <sup>23</sup>, conducted experimental studies of the electron transport through supramolecular platforms using Au and EGAIn as bottom and top electrodes, respectively. They compared the current density of a Fc, biFc or Ad functionalised dendrimer guest molecules that interacted with a well packed undecanethioether functionalized  $\beta$ CD SAM. They claimed the presence of Fc was necessary for the junction to act as a molecular rectifier, because the HOMO of the Fc unit was close to the Fermi levels of the electrodes. Moreover, they asymmetrically placed the Fc moieties close to the EGAIn but separated from the gold by an 11 carbon alkyl chain cyclodextrin.

In a similar way, Yuan *et al.* <sup>24</sup> studied the rectification over a 13 C-alkanethiol SAMs containing a Fc moiety in different positions of the molecular chain. The electron transfer results were grouped into four different categories based on the Fc location in the chain. Rectification was low when Fc was placed in the 1<sup>st</sup> or 2<sup>nd</sup> carbon close to the bottom electrode. It increased substantially when Fc was bonded to the 3<sup>rd</sup> C, but it decreased again if the Fc was further from the bottom electrode by 4 or 5 carbons of the chain. Rectification remained low when Fc occupied the middle position of the chain (from C5 to C9) and it increased abruptly when it was separated from the Ga<sub>2</sub>O<sub>3</sub> EGaIn less than 5 carbons, from C9 to C13. However, even though rectification occurred only in specific positions of the Fc within the molecular unit, they concluded that the devices that did not act as rectifiers, allowed the current to flow at both negative and positive bias.

Recently, EGaIn has been used to explore the conductivity of a host guest complex with a completely different host and guest described above. Specifically, pillar-5-arene (P5A), a macrocycle which possess an electron rich cavity capable of encapsulating cationic guests, acted as the host molecule. In that work <sup>25</sup>, a SAM of a thiolated pillar5arene (P5SA) was grown on a gold substrate and the conductivity was measured before and after the incorporation of various adamantanyl-tailed cationic guests containing different cations. They detected an increase in the current up to 2 orders of magnitude when the guests were present and, in addition, the host-guest system with the highest binding affinity exhibited the most significant enhancement in current density. Thus, it is possible to tune the conductance of the system by playing with the encapsulation of guests with different binding affinities.

However, to date, there has been no EGaIn studies using CCMoids as molecular wires. Moreover, the use of a shorter  $\beta$ CD SAM or CB[7] SAMs, that can act as host of such CCMoids, is also a new approach for supramolecular electronics. Therefore, in this section we propose the

functionalization of Au substrates with short thiolated- $\beta$ CD and CB[7] SAMs to investigate their conductivity through supramolecular complexes with a ferrocene based curcuminoid, FcCCMoid, using the EGaIn as top electrode, as it is represented in Figure 2.3.

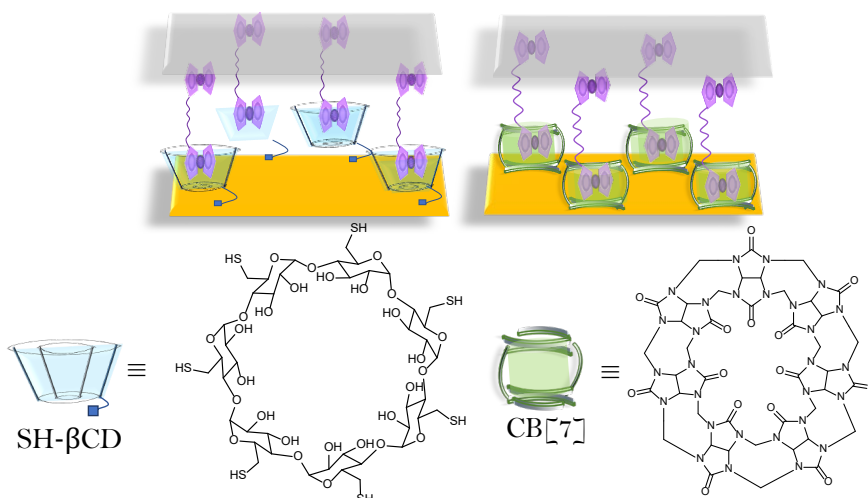


Figure 2.3. Representation of the top EGaIn electrode contacting short thiolated  $\beta$ CD (left) and a CB[7] (right) host-guest complexes with FcCCMoid.

## 2.2. Objectives

As it was previously introduced, the objective of this chapter is to prepare supramolecular host-guest SAMs between ferrocene-based CCMoids and thiolated  $\beta$ CD or CB[7] on gold surfaces and to electrically characterize them by preparing supramolecular junctions.

In order to fulfil this objective, several specific objectives are set:

- Synthesis, modification and characterization of the host and guest molecules.

- Study of the formation of the CCMoid-based complexes with  $\beta$ CD and CB[7] in solution and on Au surfaces.
- Study of the charge transport through the CCMoid supramolecular junctions using the EGain technique.

## 2.3. Results and discussion

### 2.3.1. Synthesis and characterization of FcCCMoid, 1

#### 2.3.1.1 Synthesis of FcCCMoid, 1

FcCCMoid, 1, whose structure is shown in Figure 2.4, was synthesized following the modified Pabon's reaction previously explained in Chapter 1 in 77% yield. The designed CCMoid contains two active terminal Fc moieties, that are capable of interacting with the inner hydrophobic cavities of the host molecules, creating a supramolecular complex.

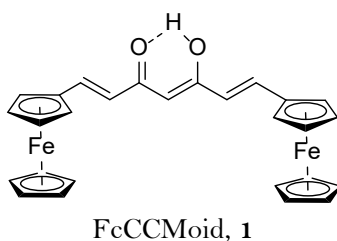


Figure 2.4. Chemical structure of compound 1.

Compound 1 was extensively characterized by several techniques including  $^1\text{H}$  nuclear magnetic resonance ( $^1\text{H}$  NMR), attenuated total reflectance-



Fourier transform infrared spectroscopy (ATR-FTIR), ultraviolet- visible absorption spectroscopy (UV-Vis), cyclic and differential pulse voltammetry (CV and DPV) and MADI-TOF mass spectrometry (spectrum shown in Annex II, Figure A2.1).

### 2.3.1.2. $^1\text{H}$ NMR of compound 1

All CCMoids exhibit common traits in their NMR spectra that allow their identification and comparison. The most recognizable signals of the CCMoid skeleton are: (i) the central proton, which appears as a sharp singlet around 6 ppm, and (ii) the proton related to the enol form, which is the predominant tautomer in solution, appearing as a broad mountain around 16 ppm. In some cases, depending on the deuterated solvent employed, the enol signal may not appear, due to exchange processes with the solvents. In addition, (iii) the signals attributed to the double bonds of the conjugated chain, usually appear in the same region as the aromatic ones, between 6 - 9 ppm, and are differentiated by their relatively large coupling constant. These double bonds, which are in E conformation, present a large coupling constant between 14–16 Hz, whereas the ones for the aromatic protons of the arms vary between 1 and 7 Hz.

The  $^1\text{H}$  NMR spectrum of compound 1 in  $\text{CDCl}_3$  is shown in Figure 2.5. The central proton  $\text{H}_1$ , together with the enol one,  $\text{H}_2$ , are observed in the mentioned regions. In this specific case, the usual six carbon aromatic rings of general CCMoids are substituted by Fc moieties. Thus, the only appreciable signals in the region between 6 and 9 ppm are those of the *trans*  $\text{H}_3$  and  $\text{H}_4$  protons from the CCMoid skeleton, with the  $\text{H}_4$  protons appearing at lower fields due to the higher deshielding effect produced by the keto-enol moiety. The two Fc units of the compound are equivalent, providing only three different signals: one corresponding to the

cyclopentadiene that is not bonded to the CCMoid structure and two assigned to the cyclopentadiene that is directly bonded to the CCMoid backbond.

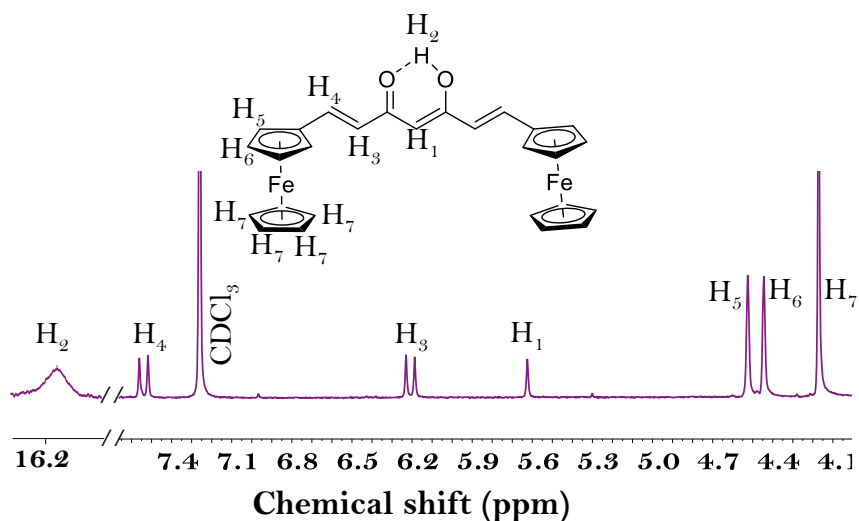


Figure 2.5.  $^1\text{H}$  NMR spectrum of compound **1** in  $\text{CDCl}_3$ .

### 2.3.1.3. ATR-FTIR spectroscopy of compound **1**

ATR-FTIR was done to identify the functional groups contained in compound **1**. In Figure 2.6 the ATR-FTIR spectrum of **1** is presented. The keto-enol component of the CCMoid backbone was evidenced by the characteristic stretching vibration of the carbonyl moiety  $\text{C}=\text{O}$  at  $1614\text{ cm}^{-1}$ . Additionally, the presence of Fc groups in the product was also confirmed by the appearance of the band at  $478\text{ cm}^{-1}$  attributed to the cyclopentadiene (Cp) - Fe stretching vibration, together with the signals at 820, 963 and  $1110\text{ cm}^{-1}$ , corresponding to the out of plane vibrations of the Cp rings <sup>26,27</sup>.

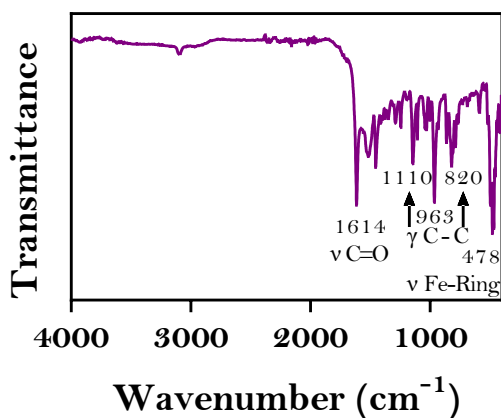


Figure 2.6. ATR-FTIR spectrum of compound 1.

#### 2.3.1.4. UV-Vis absorption spectroscopy of compound 1

UV-Vis experiments of **1** were carried out to extract electronic information of the compound, including the optical band gap. For that purpose, the measurements were performed in both, solution and in the solid-state, owing to the solvochromic behaviour of CCMoids<sup>28</sup>.

The UV-Vis spectrum of compound **1** in THF is shown in Figure 2.7. Oppositely to the general trend of CCMoids which exhibit the  $\pi$ - $\pi^*$  transition related to the backbone around 350 - 450 nm, in this specific case, that band is centred at 521 nm, showing a more intense peak at 392 nm assigned to the ferrocene species.

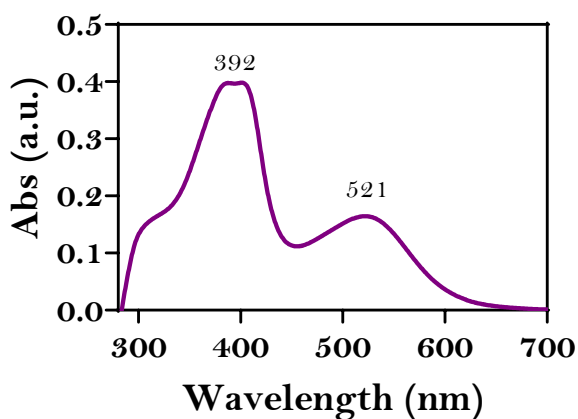


Figure 2.7. UV-Vis absorption spectrum of **1** in THF.

A pellet of our CCMoid was prepared by mixing 0.1 mg of compound **1** and 200 mg of KBr for the solid-state analysis. Figure 2.8 exhibits a spectrum similar to the solution one in terms of number of bands. However, both bands were shifted towards the red region, with a 9 nm shift observed in the case of the Fc and 27 nm in the case of the CCMoid skeleton.

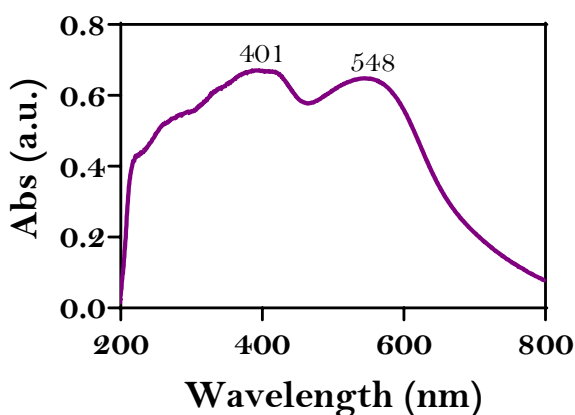


Figure 2.8. Solid UV-Vis absorption spectrum of **1**.

As mentioned above, the solvochromic behaviour of CCMoids, makes unreliable to calculate the band gap ( $E_g$ ) of the product from the solution spectra, therefore the solid-state analysis was employed to extract the bandgap of the molecules, due to the similarities between the electronic transitions involved between two energetic levels, and the HOMO and LUMO levels. Eq. 2.1 could be applied directly for the calculation of the optical bandgap,

$$E_g = \frac{h c}{\lambda} \quad \text{Eq 2.1}$$

Where  $h$  = Plank's constant (eV/s) and  $c$  = speed of light (nm/s).

However, finally the Tauc's equation <sup>29</sup>, Eq. 2.2, was employed due to the better definition of the slope of the curve needed for the estimations.

$$(\alpha h\nu)^{1/n} = A (h\nu - E_g) \quad \text{Eq 2.2}$$

Where:

$$\alpha \text{ (absorption coefficient)} = \frac{2.303 * \text{absorbance}}{l}$$

$l$  = sample thickness (cm)

$h$  = Plank's constant (J/s)

$$\nu = \text{Photon Frequency} = \frac{c}{\text{wavelength (m)}}$$

$c$  = speed of light (m/s)

$n=1/2$  (for direct allowed transitions)

$A$  = proportionality constant

Plotting the  $(\alpha h\nu)^{1/n}$  versus  $(h\nu)$ , the optical bandgap  $E_{g_{op}}$  corresponds with the intersection between the x axis with the tangent of the curve. Applying this methodology,  $E_{g_{op}}$  of **1** extracted from the Tauc's plot represented in Figure 2.9, is 1.72 eV.

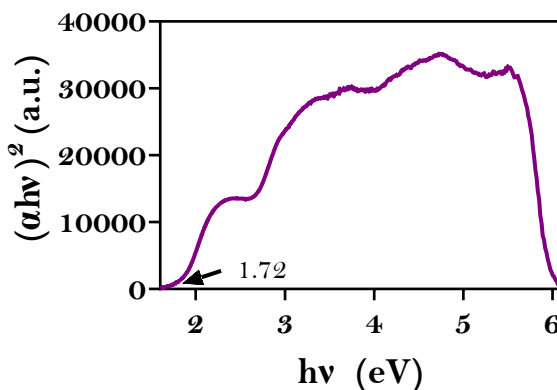


Figure 2.9. UV-Vis spectrum in solid state of **1** using the Tauc's plot of direct transition.

### 2.3.1.5. Electrochemistry of compound **1**: CV and DPV

Fc and CCMoids are electroactive species that have been extensively studied by electrochemical techniques <sup>30</sup>.

To analyse the redox behaviour of compound **1** and gain insight into its bandgap HOMO and LUMO levels, voltametric measurements were performed, specifically, cyclic voltammetry (CV) and differential pulse voltammetry (DPV).

The experiments were measured in dry THF using 0.1 M TBAPF<sub>6</sub> as electrolyte, Pt wires as counter and reference electrodes and glassy carbon as working electrode. Fc was added as internal reference <sup>31</sup>.

Figure 2.10 a displays the CV of compound **1**. Several irreversible reduction processes and two oxidation waves were found in the voltammogram. A reversible oxidative wave was observed at a half wave potential ( $E_{1/2}$ ) of 0.1 V which corresponds to the Fe (II)/Fe (III) transition of the Fc moieties. The appreciation of only one wave for the Fc species implies the independent behaviour of each Fc in the CCMoid, suggesting no-electronic communication between them. The first oxidation wave is followed by other irreversible signal attributed to the CCMoid chain observed at a higher voltage of 0.92 V.

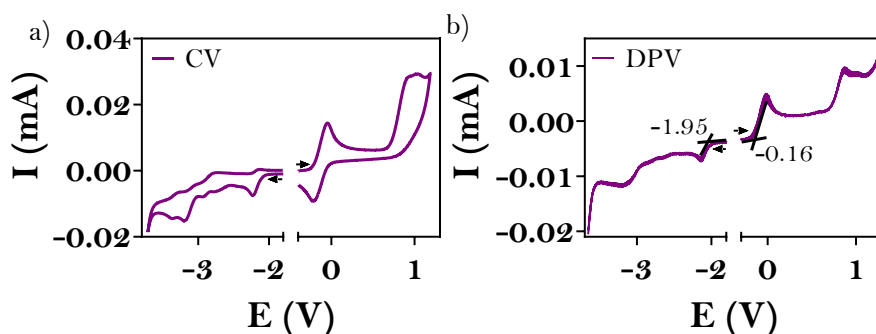


Figure 2.10. Oxidation and reduction a) CVs and b) DPVs spectra of compound **1**.

The DPV graph, exhibited in Fig 2.10 b, was used to calculate the approximated values of the HOMO and LUMO levels, which are related to the needed energy to extract or introduce an electron, therefore they can be correlated to the first electrochemical oxidation and reduction processes as Eq. 2.3 and Eq. 2.4 indicate.

$$E_{HOMO} = -(E_{onset\ oxidation}) + 4.8 \quad Eq\ 2.3$$

$$E_{LUMO} = -(E_{onset\ reduction}) + 4.8 \quad Eq\ 2.4$$

Where 4.8 eV is the value of the Fc/Fc<sup>+</sup> pair in vacuum.

Finally, the bandgap can be calculated following Eq. 2.5.

$$E_g = (E_{HOMO}) - (E_{LUMO}) \quad Eq\ 2.5$$

Table 2.2. summarizes the HOMO, LUMO and the  $E_g$  values obtained by applying the equations described above. The bandgap estimated for **1** was 1.79 eV, exhibiting a semiconductor behaviour. This value is in agreement with the optical bandgap value extracted from the UV-Vis experiment, which was 1.72 eV, both certainly lower than most values reported for CCMoids in the literature <sup>32</sup>, pointing out the relevant role of the coordination of two Fc units in the final energy distribution of the molecule.

<b>E onset ox</b> <b>(V)</b>	<b>Eonset red</b> <b>(V)</b>	<b>E HOMO</b> <b>(eV)</b>	<b>E LUMO</b> <b>(eV)</b>	<b>E<sub>g</sub></b> <b>(eV)</b>
-0.16	-1.95	-4.64	-2.85	1.79

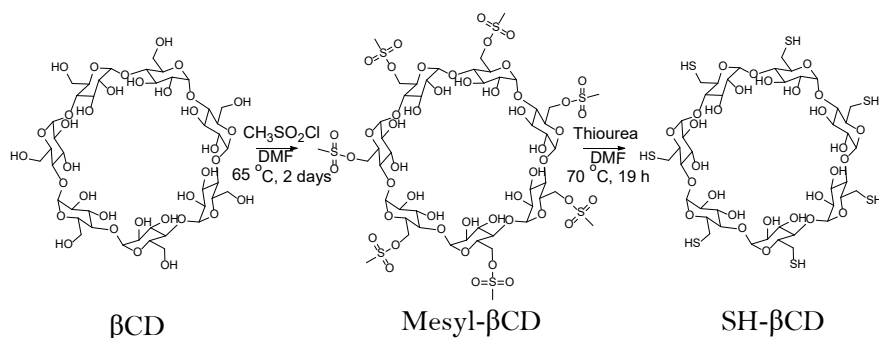
Table 2.2. Potential values for oxidation and reduction, HOMO, LUMO and electrochemical bandgap of compound **1**.



## 2.3.2. Synthesis and characterization of thiolated- $\beta$ CD, (SH- $\beta$ CD)

### 2.3.2.1 Synthesis of SH- $\beta$ CD

To enable the attachment of cyclodextrin onto gold substrates, the seven primary hydroxyl groups of the  $\beta$ CD were chemically modified by converting them into thiol groups, as it is outlined in Scheme 2.1. In a first reaction, the hydroxyl groups were transformed in presence of mesyl chloride and DMF at 65 °C for 2 days, into mesylate groups, which acted as better leaving groups for the subsequent nucleophilic substitution reaction (SN2) with thiourea in DMF at 70 °C for 19 h, to obtain the desired thiolated molecule (SH- $\beta$ CD) <sup>33</sup>.



Scheme 2.1. Schematic representation of the preparation of SH-  $\beta$ CD.

### 2.3.2.2 $^1\text{H}$ NMR of SH- $\beta$ CD

To aid in the interpretation of the result, Figure 2.11 shows the  $^1\text{H}$  NMR spectra of  $\beta$ CD, the intermediate mesityl- $\beta$ CD and the final SH- $\beta$ CD in  $\text{DMSO}-d_6$ , along with the chemical structure of one of the 7 glucose repetitive units of each molecule.

The proton signals of the OH<sub>2</sub> and OH<sub>3</sub> groups appear at lower fields followed by the H<sub>1</sub> proton, as seen in all the three spectra. The rest of the signals of the protons H<sub>3</sub>, H<sub>5</sub> and H<sub>6</sub> appear in the region between 3.2–4.4 ppm along with H<sub>2</sub> and H<sub>4</sub>, overlapped in all the cases with the water signal. Importantly, the signal of OH<sub>6</sub> present in the starting material *beta* cyclodextrin disappears in the spectra of the intermediate and the final compounds, confirming the success of the reactions. However, the peaks of the methyl (CH<sub>3</sub>) and (SH) groups of mesyl- $\beta$ CD and SH- $\beta$ CD, which should appear around 3 ppm and 2 ppm are not detectable by this technique, maybe because of an overlap with the DMSO and water solvents.

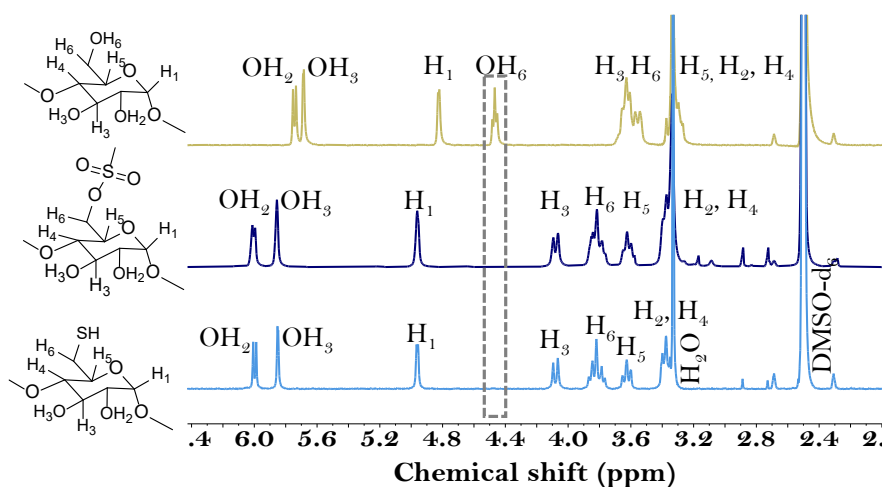


Figure 2.11. <sup>1</sup>H NMR spectra of  $\beta$ CD, the intermediate mesyl- $\beta$ CD and the final SH- $\beta$ CD, in DMSO-*d*<sub>6</sub> along with the chemical structure of one of the 7 glucose repetitive units of each molecule.

The disappearance of the signal from involved hydroxyl groups of the initial cyclodextrin (OH<sub>6</sub>) in the <sup>1</sup>H NMR spectra after the reaction, indicated the modification was favourable. Additional MALDI-TOF experiments to corroborate the synthesis of mesyl- $\beta$ CD and SH- $\beta$ CD were inconclusive, due to the impossibility to ionize the compounds.

### 2.3.3. Supramolecular systems

As it was previously commented, the non-covalent interactions that participate in the formation of the supramolecular complexes, between the Fc and the host systems, are hydrophobic interactions. Therefore, aqueous solutions are the ideal media to prepare these systems. However, it is important to highlight the insolubility of compound **1** in this media in order to understand certain results obtained in this study that will be developed below.

#### 2.3.3.1 Studies of the encapsulation systems in solution

In the following section we describe the formation and characterization of the encapsulation complexes in solution between the host molecules,  $\beta$ CD or CB[7], and the guest, **1**.

##### 2.3.3.1.1 Formation of the inclusion complexes

Depending on the ratio between the precursors, four different  $\beta$ CD@**1** and CB[7]@**1** complexes can be produced in aqueous solution, since two Fc groups are comprised in compound **1**. In  $\beta$ CD@**1** 1:1 and CB[7]@**1** 1:1 mixtures, one equivalent of each reagent was mixed in an aqueous solution while in  $\beta$ CD@**1** 2:1 and CB[7]@**1** 2:1 systems, respectively, the double amount of  $\beta$ CD or CB[7] were added. Theoretically, the 1:1 systems should lead into a one free Fc group whereas, the 2:1 assemblies should result in a full encapsulation of Fc, where both Fc moieties would be covered by host molecules as represented in Figure 2.12.

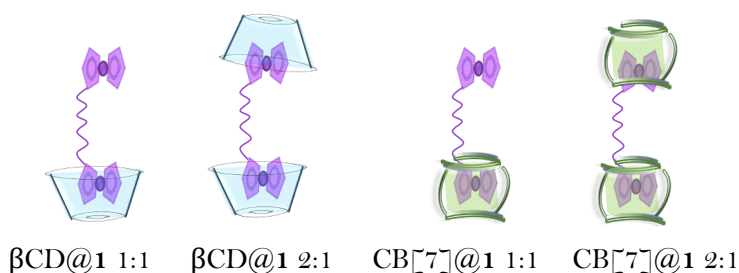


Figure 2.12. Representation of the different host-guest complexes depending on the ratio between the precursors.

#### 2.3.3.1.2 UV-Vis absorption of the supramolecular complexes.

The UV-Vis absorption experiments were conducted by measuring an aliquot of the 2:1 and 1:1 ratio solutions in a 1 cm quartz cuvettes every 24 hours for a period of 18 days.

Preliminary UV-Vis absorption studies shown in Figure 2.13 suggested a slow host-guest formation in all cases. The spectra of  $\beta\text{CD}@1$  inclusion systems (Figure 2.13 a and 2.13 b) indicate that the arrangements were obtained after 17 days independently on the ratio of the precursors, when the absorption bands of the complex reached a maximum intensity.

Regarding  $\text{CB}[7]@1$  1:1 (Figure 2.13 c) the encapsulation system was accomplished in 14 days and after that time the absorbance decayed. Similarly,  $\text{CB}[7]@1$  2:1 (Figure 2.13 d) was achieved after 14 days but in this case the maximum intensity remained constant for 3 more days.

Other than that, the comparison between 1:1 and 2:1 supramolecular complexation experiments did not provide drastic changes to assess the creation of the desired arrangements independently, being difficult in both cases, for  $\text{CB}[7]$  and  $\beta\text{CD}$ , to discriminate and evaluate the creation of the so-called 1:1 and 2:1 supramolecular species. However, in both, the signals

of **1** could be assessed revealing the creation of supramolecular entities that allows the solubility of such CCMoid in water.

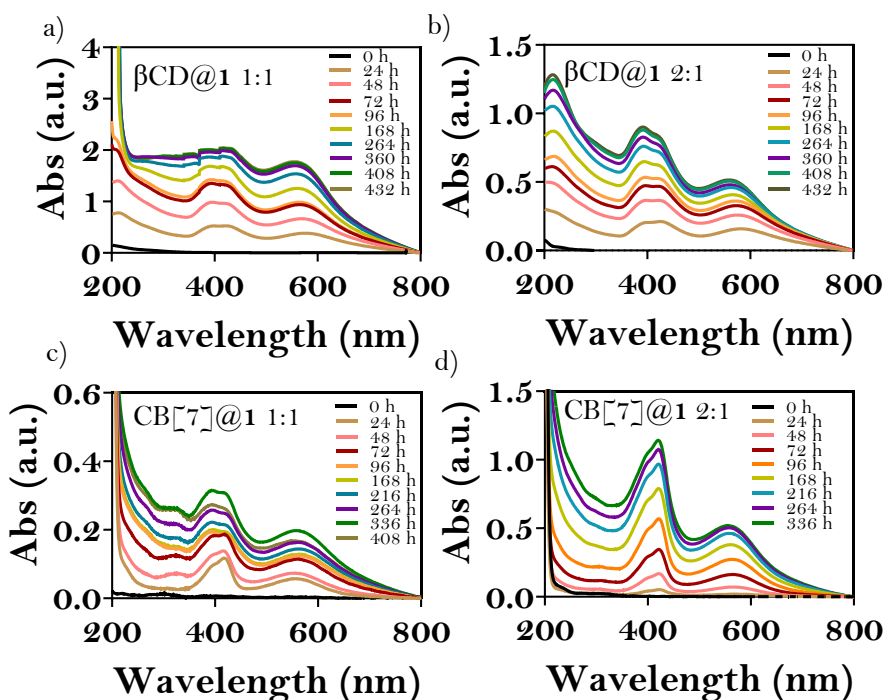


Figure 2.13. Variation of the UV-Vis absorption bands of a)  $\beta\text{CD}@\mathbf{1}$  1:1, b)  $\beta\text{CD}@\mathbf{1}$  2:1, c)  $\text{CB}[\mathbf{7}]\text{@}\mathbf{1}$  1:1 and d)  $\text{CB}[\mathbf{7}]\text{@}\mathbf{1}$  2:1 over 18 days period.

### 2.3.3.1.3 CV of the supramolecular complexes

The reversible electrochemical wave characteristic of Fc offers a great chance to study molecules and complexes containing Fc using voltametric techniques. Prior to performing CV analysis of the complexes, we conducted UV-Vis measurements to determine the time required to form the complex in presence of the electrolyte, as depicted in Figure A2.2 (see Annex II). Using  $\text{Na}_2\text{SO}_4$  as electrolyte, the complex formation time was then reduced to 9 days. Therefore, CV measurements of the inclusion complexes containing 0.1 mM of  $\text{Na}_2\text{SO}_4$  aqueous solution were carried out at 50 mV/s

using a glassy carbon working electrode, Pt counter electrode and Ag/AgCl reference electrode, at the moment of mixing the host and the guest (time zero), as well as 9 days later. The results were plotted in Figure 2.14.

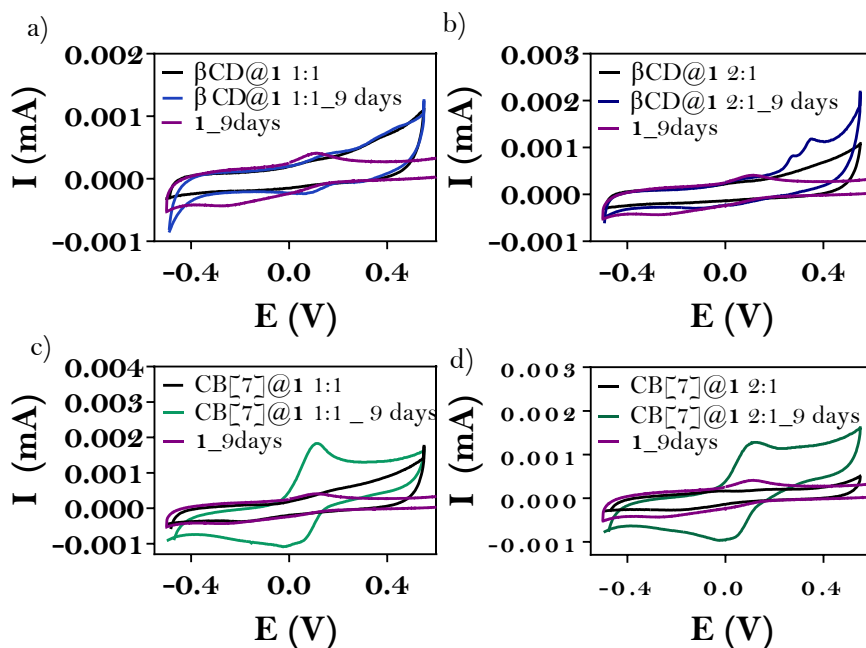


Figure 2.14. Voltammograms of a)  $\beta\text{CD}@1$  1:1 b)  $\beta\text{CD}@1$  2:1, c)  $\text{CB}[\text{7}]\text{@}1$  1:1 and d)  $\text{CB}[\text{7}]\text{@}1$  2:1 supramolecular complexes.

As explained in the introduction section of this chapter, the more complex electron transfer mechanism of  $\beta\text{CD}$  (Figure 2.1) was expected to yield more complex results. 1:1, 2:1 (Figure 2.14 a) and (2.14 b) as well as 10:1 (not shown) embedding provided three irreversible oxidation waves. A possible explanation, schemed in Figure 2.15, suggests a mixture of three different systems in the solution: free compound **1** (a), compound **1** with only one Fc included in the  $\beta\text{CD}$  cavity (b) and the complete encapsulation conformation (c). Since Fc is liberated before its oxidation, the signals observed in the CV are attributed to the pseudo complexes resulted from the disengagement of

the Fc (d,e,f). The wave below 0.2 V would correspond to the free compound **1**, (Figure 2.15, d) with both Fc oxidised. The band located at higher voltage, should be assigned to system f), which arises from the complete coverage of **1**. It provides a distinct signal compared to the free compound **1** due to the influence of the surrounding  $\beta$ CD. Finally, the intermediate signal would be attributed to the option e), where there is mixed valence owing to the presence of one reduced Fc and the other oxidised Fc. Although it is exemplified in Figure 2.15 e) that the Fc close to the  $\beta$ CD is the one oxidised, it cannot be assessed which Fc is indeed oxidised.

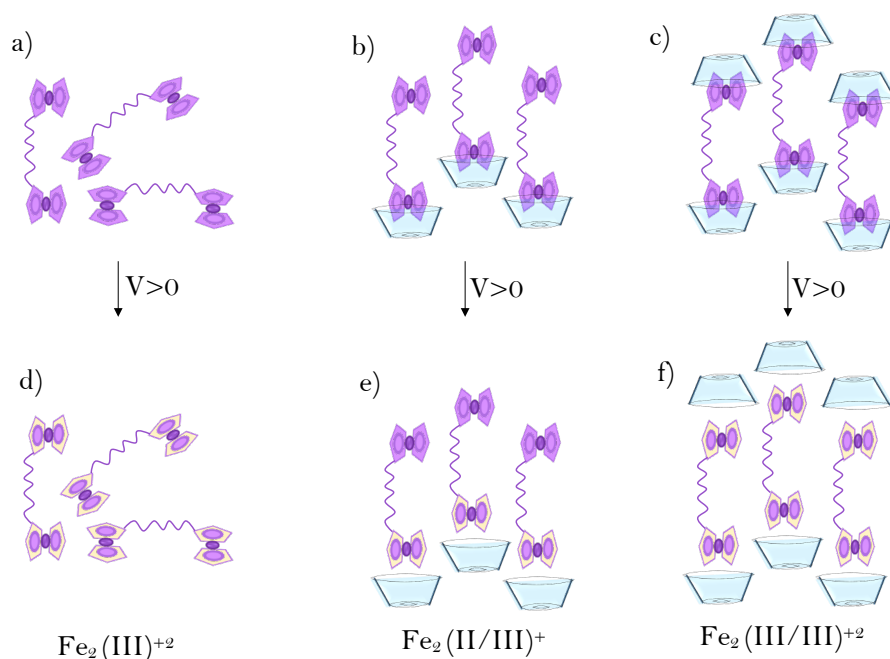


Figure 2.15. Possible explanation of the different redox processes involved in the CVs of  $\beta\text{CD}@\mathbf{1}$  systems.

When  $\text{CB}[7]$  acted as host, a reversible oxidation wave was observed at 0.11 V in both complexes after 9 days. As Figures 2.14 c) and d) illustrate, the

oxidation peak of free compound **1** after 9 days appears at the same voltage than the encapsulated Fc, making it impossible to distinguish between them. This fact does not exactly coincide with the literature, where in general has been reported a shift to more anodic values (ranging from 10 to 100 mV depending on the neutral or positively charged Fc derivatives) when the Fc is inside the CB[7] cavity, suggesting minor or major differences in the stabilities of the complexes formed by reduced or oxidised Fc <sup>3</sup>. However, as the electron transfer mechanism depicted in Figure 2.1 demonstrates, the Fc remains inside the cavity of the CB[7] during oxidation, therefore it is possible to find the oxidation potential for the free and confined Fc so close that they may become indistinguishable. Although the literature highlights a decrease in intensity after the formation of the supramolecular system <sup>3</sup>, our results show a higher intensity signal, although it may be taken into account that the earlier conclusions are based on systems containing only one Fc moiety. Our hypothesis here relates to the increase in solubility of the CCMoid in aqueous solution in presence of the host, which would provide a bigger band.

Unfortunately, due to the limited solubility of **1** and its rather low (and slow) inclusion complexes in water, we were unable to obtain further results from additional characterization techniques, such as <sup>1</sup>H NMR or isothermal titration calorimetry (ITC), that could have been extremely useful for determining the ratio of the host and guest of the system as well as the association constant in solution.



### 2.3.3.2 Studies of the host-guest complexes on gold surfaces

#### 2.3.3.2.1 Gold substrates

The template stripped gold substrates ( $\text{Au}^{\text{TS}}$ ) are employed when working with SAMs and EGaIn top electrode in order to minimize defects in the surface that can affect the SAM and therefore to the conductivity measurements <sup>34</sup>. To achieve this,  $\text{Au}^{\text{TS}}$  were functionalized with the desired systems and characterized afterwards.

Basically, TS methodology <sup>35</sup>, represented in Figure 2.16, consist on evaporating a layer of gold onto a flat surface, a silicon wafer in our case. Then, the deposited gold is glued upside down onto a cleaned glass platform using an epoxy resin, and finally stripped from the silicon wafer obtaining a fresh surface ready to use.

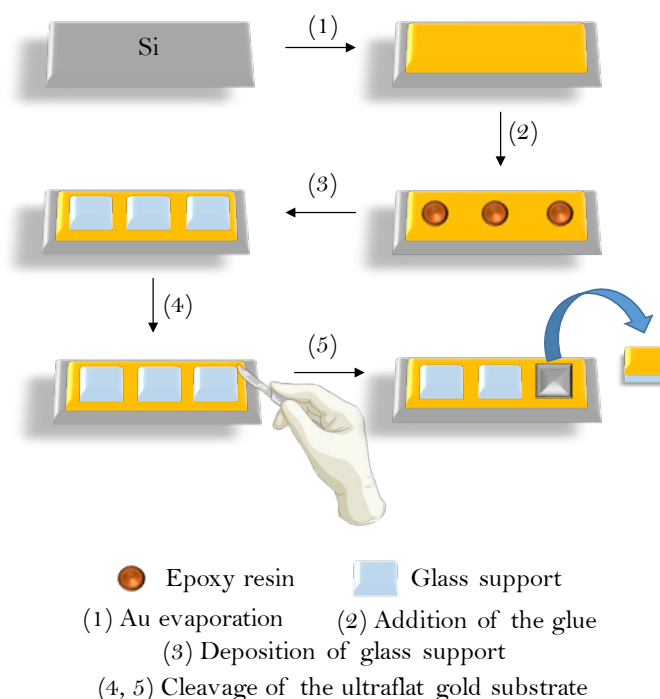


Figure 2.16. Protocol for building template stripped gold surfaces.

### 2.3.3.2.2 Formation of the supramolecular complex on Au

The functionalization of the gold support with the supramolecular complex involved a two-step process, as Figure 2.17 summarizes. The first monolayer which contains the host, was created by the self-assembly methodology. It relies on the spontaneous chemisorption of molecules over the substrates due to the presence of a terminal group capable to be chemisorbed onto the substrate <sup>36</sup>, the thiol –SH group in the SH- $\beta$ CD and the carbonyl –C=O group in the CB[7], respectively <sup>33,37,38</sup>.

The experimental process consisted in a first formation of the host SAM by the substrate immersion in a 1 mM solution of the host for a specific time: 18 h in the SH- $\beta$ CD solution and 24 h in the CB[7] solution. After that time, the substrate was washed with Milli-Q water to remove any physisorbed material. Due to solubility items, the solution of CB[7] was prepared using Milli-Q water as solvent, whereas a mixture of DMSO:H<sub>2</sub>O (3:2) was needed to dissolve the SH- $\beta$ CD.

The second step, which implies the incorporation of the guest, was possible thanks to the hydrophobic interactions between the Fc and the hosts in aqueous media. Ideally, the substrate should have been submerged in a pure aqueous solution of **1**. However, since **1** is totally insoluble in water, a minimum amount of DMSO (20 %) had to be added to facilitate the inclusion of the guest. Besides, the substrate in this case was vertically placed in the solution in order to prevent the deposition of aggregates of **1** on it, as well as to incorporate a magnetic stirrer to help with the stirring of the solution during the 24 h of incubation of the host functionalized substrate.

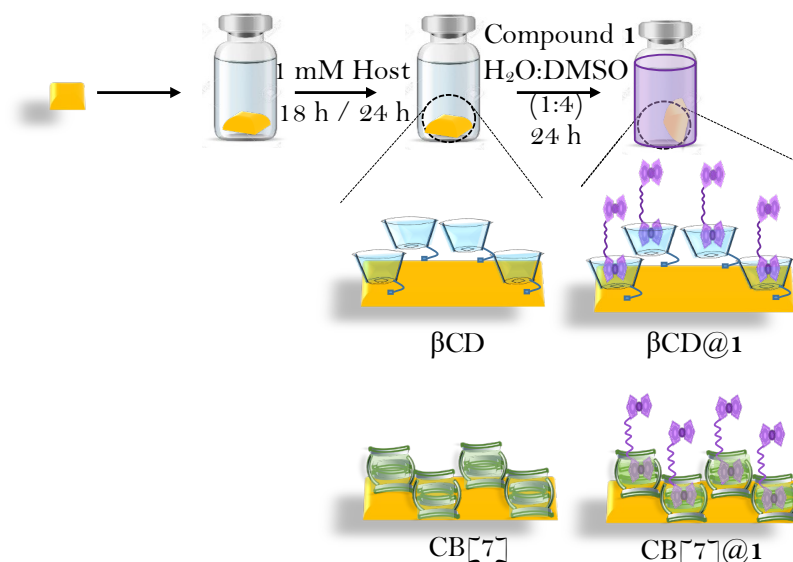


Figure 2.17. Protocol for the formation of the host-guest system on Au surfaces.

Initially, five concentrations of **1** (4.06 mM, 0.40 mM, 0.20 mM, 0.10 mM and 0.04 mM) were used to determine the optimal conditions for the supramolecular complex formation. Figure 2.18 shows the final supports after the entire incubation process in the different concentrated solutions. An excess of **1**, detected as a remaining purple stain, was observed on the substrates immersed in the two highest-concentration solutions of **1**. As compound **1** is not completely soluble in the DMSO:H<sub>2</sub>O (1:4) mixture, some aggregates that cannot be removed by rinsing with Milli-Q water, were deposited on the top of the surfaces, giving rise to dirty substrates. It is not possible to wash these surfaces with organic solvents, where compound **1** is soluble, because the compound included in the cavity of the host would also be dissolved, destroying the supramolecular complex. Hence, the 4 mM and 0.4 mM solutions were discarded, allowing the lowest concentrations to be further studied.

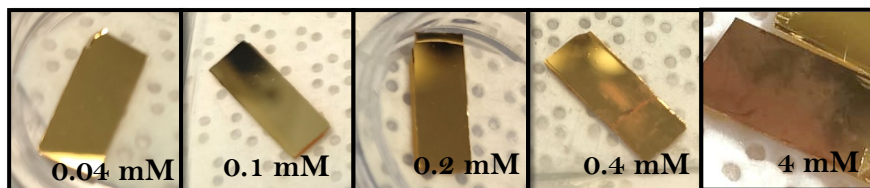


Figure 2.18. Photographic images of the complexes-modified gold substrates immersed in different concentrated solutions of the guest.

### 2.3.3.2.3 Characterization of the supramolecular complex on Au

The obtained SAMs were characterized by contact angle (CA), X-Ray photoelectron spectroscopy (XPS), cyclic voltammetry (CV), Fourier transform infrared reflection absorption spectroscopy (FT-IRRAS) and ellipsometry.

#### Contact Angle measurements (CA)

CA measurements allow to determine the wettability of a surface <sup>39</sup>. Depending on the angle formed by the surface of the substrate and a drop of water deposited on top of it, the surface is considered hydrophobic ( $\theta > 90^\circ$ ) or hydrophilic ( $\theta < 90^\circ$ ) <sup>40</sup>.

The observed contact angle values corresponding to each step of the process are shown in Table 2.3, and the images with the angle variations in Figure 2.19. Au surfaces exhibited a more hydrophobic behavior by showing a CA value of  $74^\circ$ . Upon formation of the host layer, the value decreased to  $40^\circ$  for SH- $\beta$ CD and to  $32^\circ$  for CB[7], which are in agreement with the reported values,  $36^\circ$  for SH- $\beta$ CD and  $32^\circ$  for CB[7] <sup>9,41</sup>, respectively. This diminution of the CA values is attributed to the increase in hydrophilicity of the surface after the immobilization of the host layer, which exposes polar –OH groups in case of  $\beta$ CD and –C=O groups in the case of CB[7], in that

order. After the second step, when compound **1** is present, independently on the concentration used, a significant increment in the CA value to  $63^\circ (\pm 2)$  was identified, which is due to the wettability surface modification from the hydrophilic  $-\text{OH}$  and  $\text{C}=\text{O}$  functional groups to the hydrophobic aromatic nature of the cyclopentadiene moieties of the Fc. The data was reproducible and agree with other systems reported in the literature <sup>11</sup>.

	CA (°)
Au	74
SH- $\beta$ CD	40
CB[7]	32
$\beta$ CD@ <b>1</b>	62
CB[7]@ <b>1</b>	64

Table 2.3. CA values recorded for the different modified gold supports.

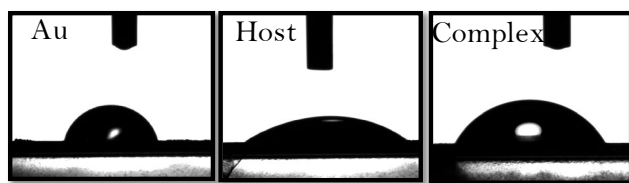


Figure 2.19. Images of the static measurements of CA obtained for the different immobilizations on gold substrates.

## X-Ray Photoelectron spectroscopy (XPS)

The functionalized Au substrates were analysed by XPS, which allowed the identification of the chemical elements present on the surfaces <sup>42,43</sup>. Figure 2.20 displays the C1s, S2p and Fe2p spectra for both the SH- $\beta$ CD SAM and the supramolecular complex.

The thiols bonded to Au (Au-S bond) can be differentiated from the unbonded -SH thiols by a negative 1.5 eV shift for the signal of the anchored S unit <sup>44</sup>. In the S2p spectrum of the SH- $\beta$ CD SAM (Figure 2.20 a), two deconvoluted signals at 161.7 eV and 163.2 eV were identified, which are close to the published values of bonded (161.9 eV) and unbonded (163.4 eV) thiols, respectively <sup>12</sup>. The free/bonded S ratio revealed 4 unbonded SH to 3 A-S bonds, in agreement with the literature values <sup>8</sup>. Upon the inclusion of **1**, (Figure 2.20 b, c and d) the trend is maintained except for the highest concentration, where only bonded thiols were detected.

In the C1s region of the SH- $\beta$ CD sample (Figure 2.20 a), the expected signals at 284.6 eV, 286.5 eV and 287.8 eV were exhibited and assigned to the C-alkyl, C-O and O-C-O bonds <sup>44</sup>, in that order. Most peaks were mostly reproducible with the presence of the guest (Figure 2.20 b, c and d), with the last signal varying by a maximum of 0.4 eV.

To confirm the inclusion of the Fc, the Fe2p region was examined. Due to the low concentration of Fc on the surfaces, diffused Fe peaks were appreciated, in agreement with literature <sup>9</sup>. The typical pattern of Fe (II) is appreciated for the two lowest concentration 0.04 mM (b) and 0.1 mM (c) with two signals at 708.0 eV and 721.1 eV attributed to Fe 2p <sup>3/2</sup> and Fe 2p <sup>1/2</sup>. Additionally, in both cases, it is appreciable a signal centred at 713 eV that could be attributed to the presence of Fe (III) in the sample <sup>45</sup>. However, in the case of the higher concentration (d), only the first signal related to Fe (II) is clearly observed being the one at 721 eV suggested.

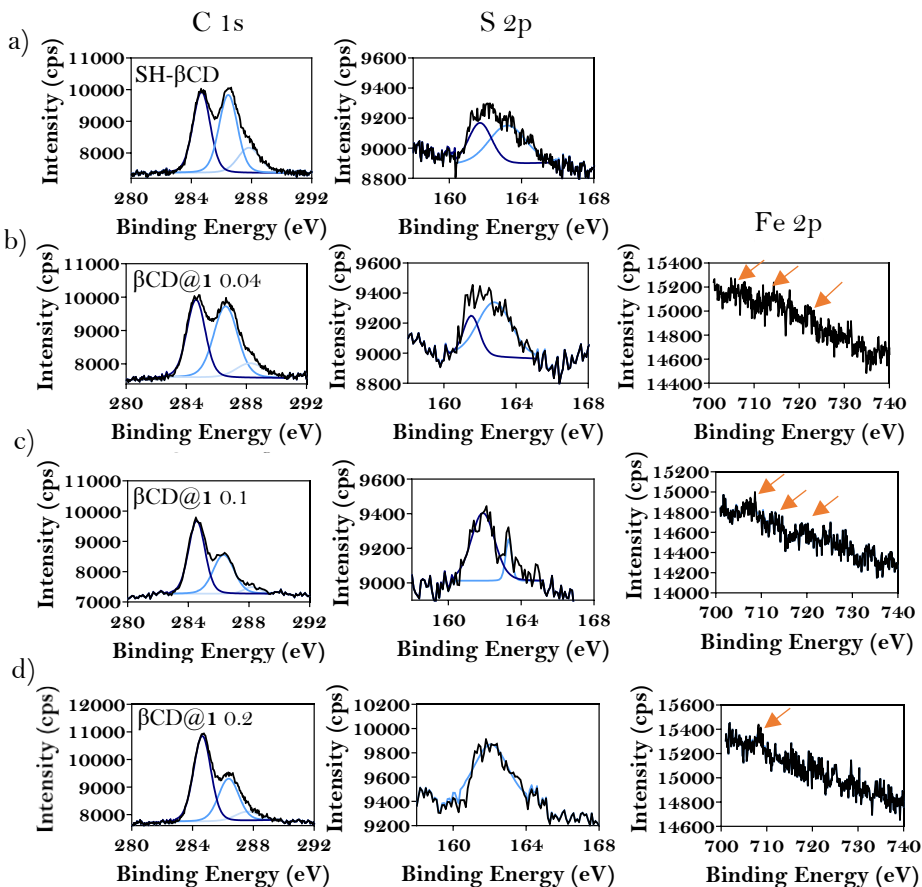


Figure 2.20 Figure 2.19. C1s, S2p and Fe2p region for a)  $\beta$ CD SAM, b)  $\beta$ CD@1 0.04 mM, c)  $\beta$ CD@1 0.1 mM y d)  $\beta$ CD@1 0.2 mM.

Regarding CB[7] SAM, previous studies have compared the spectrum of the O1s area of CB[7] on Si surfaces (where there are not supposed interactions between the host and the surface) with the spectrum in Au substrates where these interactions exist<sup>38</sup>. On the Si surface, a narrow peak appeared around 531.2 eV while in the Au system a broader shifted signal was shown at higher binding energy around 532.5 eV, respectively. This shift was explained by the interaction between the gold surface and the O atoms of the bottom half of the C=O groups of the CB[7], demonstrating

the disposal of the host on the surface. The broadening of the signals was also attributed to the overlapping of the non-interacting upper C=O groups of the CB[7] (531.2 eV) and the bottom interacting C=O group of CB[7] with the gold (532.5 eV).

The results of our analysis of the O1s and C1s region of CB[7] SAM are depicted in Figure 2.21. Here, in the O1s spectrum obtained for the CB[7]-SAMs (Figure 2.21 a), a single signal centred at 532.5 eV was extracted after the deconvolution of the broad band corroborating the proper disposal of the CB[7] molecules. Although the signal of the free C=O groups was not discernible, non-interacting C=O groups are assumed to be present in the sample.

In the C1s region of the sample, the expected signals at 284.9 eV, 286.8 eV and 289.0 eV, were observed and assigned to the C-C, C-N and C=O bonds, respectively, agreeing with others in the literature<sup>38</sup>.

These signals along with C=O signals in the O1s region remained visible after the incorporation of **1** into the system (Figure b, c and d), corroborating the survival of the host monolayers after the incubation with the guest. In order to confirm the presence of compound **1**, the Fe2p region of the sample was analysed. Due to the low concentration of Fe in all the samples, diffuse peaks of this element are detected only for the samples containing 0.1 mM (c) and 0.2 mM (d). For both concentrations, the first signal attributed to Fe (II) at 707-708 eV are observed. However, the second signal corresponding to Fe (II) at 719 eV is only appreciated in the 0.1 mM sample, and the specific of Fe (III) at 712.3 eV was detected in the 0.2 mM concentration.



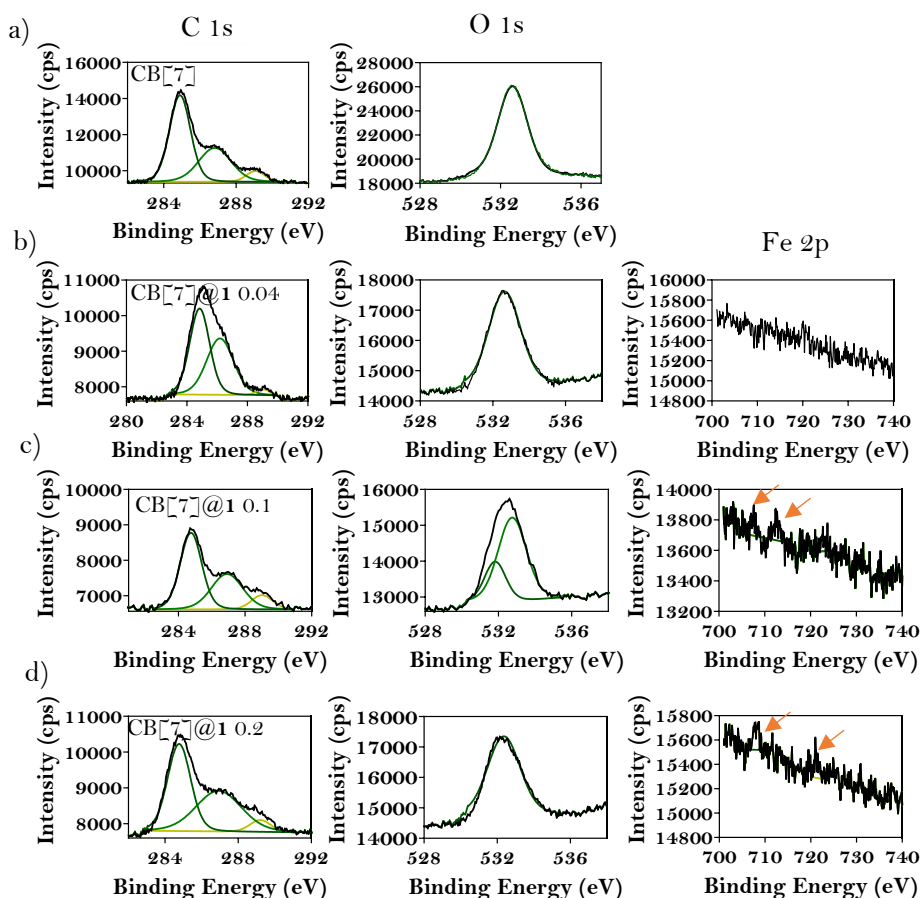


Figure 2.21. C1s, O1s and Fe2p region for a) CB[7] SAM, b) CB[7]@1 0.04 mM, c) CB[7]@1 0.1 mM and d) CB[7]@1 0.2 mM.

In consonance with the results described above, this technique allowed us to clearly identify the elements contained in both macrocycles, C, O and S, indicating the presence of the host SAM in all the samples. However, the low amount of Fe in the sample hinders the proper detection of this element, although it is suggested the appearance of Fe peaks which confirms the formation of the complex and therefore the formation of the guest layer.

Further characterization techniques to reinforce the demonstration of Fc introduction in the sample were applied and discussed below.

### Cyclic voltammetry (CV)

The presence of compound **1** and its interactions with the hosts on Au substrates were explored by CV. CV experiments were performed at 50 mV/s in 0.1 M aqueous solution of Na<sub>2</sub>SO<sub>4</sub> using the modified gold substrate now as working electrode (differing from previous studies, where a glassy carbon electrode was used), Pt wire as counter electrode and Ag/AgCl electrode as reference electrode. The voltammograms of the supramolecular complexes with varying amounts of **1** involved are represented in Figure 2.22.

When SH- $\beta$ CD acted as host, the usual reversibility of the Fc redox pattern was lost in the conditions of the experiments. The oxidation wave centered at 0.30 V and the reduction signal centered at 0.03 V were clearly visible in the case of 0.2 mM and 0.1 mM solutions of **1**. Regarding the lowest concentration, 0.04 mM, a small signal can be appreciated at an exact position, corroborating the presence of the guest in the three experiments.

In contrast, when CB[7] was involved, the unique distinguishable peak was related to the oxidation (semi-wave around 0.38 V, with no appreciation of the corresponding reduction semi-wave).

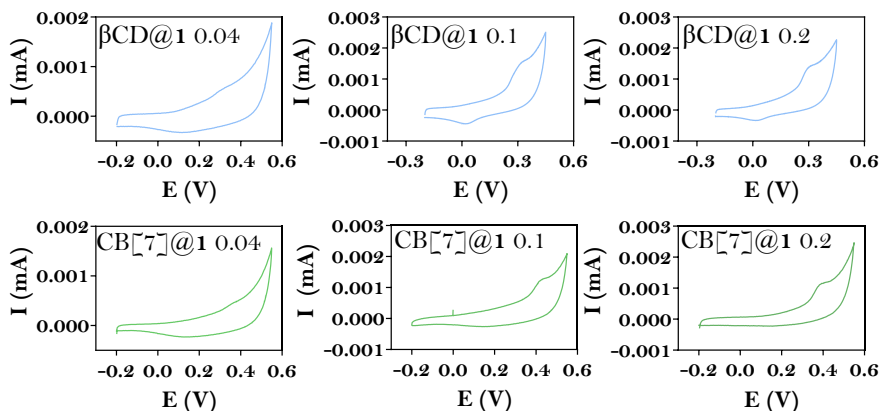


Figure 2.22. CV voltammograms recorded for SH- $\beta$ CD@1 and CB[7]@1 films formed with different concentration solutions of the guest.

On the other hand, the surface coverage of the SAMs can be estimated according to Eq. 2.6, where the number of electrons involved,  $n = 2$  and the area of the electrode,  $A$ , was  $0.15 \text{ cm}^2$ .

$$Q = nFA\Gamma \quad \text{Eq. 2.6}$$

The values of the surface coverage,  $\Gamma$ , obtained by integrating the anodic peak provided at a scan rate of  $50 \text{ mV/s}$  for each experiment, are summarized in Table 2.4. The extracted values were compared with calculated theoretical ones in order to evaluate the percentage of the surface covered with the supramolecular complex.

To estimate the theoretical values, we considered that each host encapsulates one molecule of **1**. Hence, the surface coverage is determined by the number of host molecules that fit into  $0.15 \text{ cm}^2$  (the area exposed to the CV experiments), that is calculated through the area occupied by 1 molecule.

The comparison shows low yields ranging from 1 % to 52 % depending on the host and the amount of **1** used. This estimation indicates a low surface coverage of the final functionalized Au surfaces, which could be caused by the insolubility of compound **1** that hinders the achievement of homogeneous higher coverages.

	Surface coverage (mol/cm <sup>2</sup> )	Surface coverage (%)
SH-βCD@ <b>1</b> 0.04	8.57 x 10 <sup>-13</sup>	4.2
SH-βCD@ <b>1</b> 0.1	8.59 x 10 <sup>-12</sup>	41.7
SH-βCD@ <b>1</b> 0.2	1.07 x 10 <sup>-11</sup>	51.9
CB[7]@ <b>1</b> 0.04	2.32 x 10 <sup>-13</sup>	1.4
CB[7]@ <b>1</b> 0.1	3.34 x 10 <sup>-12</sup>	19.5
CB[7]@ <b>1</b> 0.2	8.45 x 10 <sup>-12</sup>	49.4

Table 2.4. Surface coverage calculated for the two host-guest systems and the three concentrations used on Au substrates.

In addition, to gain insight into the disposition of compound **1** in the cavity of the hosts in order to corroborate the surface coverage estimation (in percentage), theoretical calculations were performed. They revealed that the optimal configuration of compound **1** inside the βCD cavity forces the rest of the molecule to adopt a vertical (or titled) position (0 kcal/mol), being less stable the situation where compound **1** is in a horizontal position in which both Fc of the same CCMoid are included in two neighbouring host units (29.6 kcal/mol), as Figure 2.23 a and b represents. In contrast, in the case of CB[7] acting as host, Figure 2.23 c and d, both conformations are close in energy, 0 kcal/mol for the vertical configuration *vs.* 5.3 kcal/mol for the

horizontal one, suggesting a preferred vertical orientation but being possible to find the horizontal one in the sample.

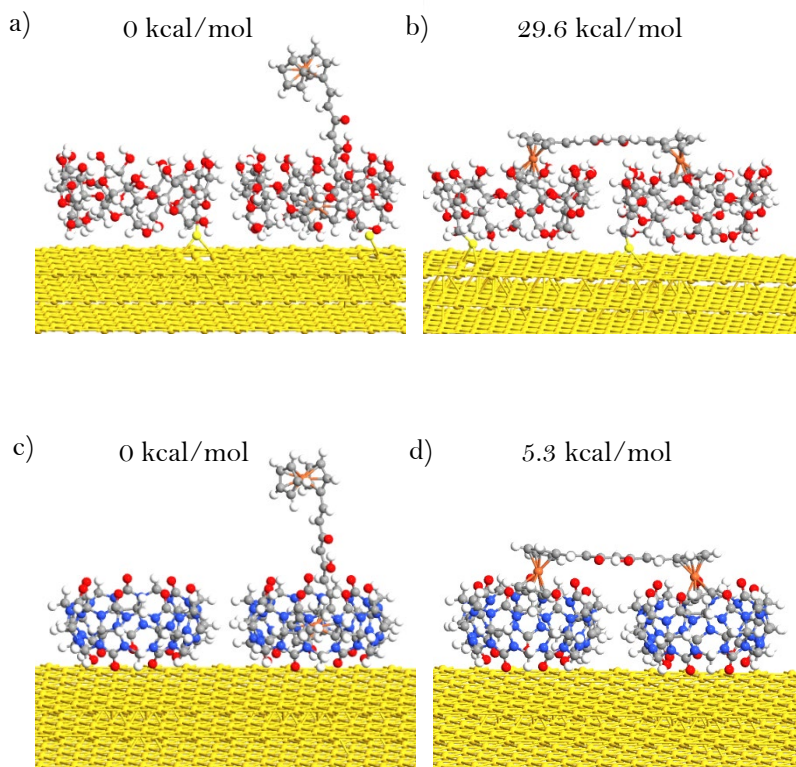


Figure 2.23. Structural optimization calculations of the possible supramolecular complexes between SH-BCD (a, b) or CB[7] (c,d) and compound **1** on gold substrates.

Considering these results, it seems that while in the case of SH-BCD@**1** the estimated surface coverage is calculated with the correct conditions (1 CCMoid for each host), in the case of CB[7]@**1**, if we consider the horizontal disposition, with the 1 CCMoid per 1 host conditions employed, it would lead into a maximum surface coverage of 50 %. Taking into account the information above, we cannot rule out intermediate situations in both

supramolecular systems, where, in different ratios, we could have combinations of tilted and horizontal arrangements of CCMoids.

Therefore, considering the surface coverage values together with the theoretical outcome, further characterization experiments, including the final conductivity measurements, were performed uniquely with the highest concentration of compound **1**, 0.2 mM.

### **Fourier Transform Infrared Reflection Absorption spectroscopy (FT-IRRAS)**

FT-IRRAS enables the determination of vibrations of the molecule anchored to a surface by applying the proper incidence angle of the beam with respect to the surface <sup>46,47</sup>.

For comparative purposes, the spectra obtained at an incident angle of 80 °, for the SH- $\beta$ CD, CB[7], SH- $\beta$ CD@1 0.2 and CB[7]@1 0.2 monolayers along with the FTIR-ATR graph of the host and the guests are shown in Figure 2.24.

Regarding the SH- $\beta$ CD sample, several bands around 1004-1150 cm<sup>-1</sup> related to C-O-C/C-C and C-O stretching vibrations are identified, corroborating the deposition of the SH- $\beta$ CD layer on the Au support <sup>48</sup>. After the inclusion of **1**, the previously defined signals were still detected. Additionally, a small wave around 1610 cm<sup>-1</sup>, that could be attributed to the C=O central group of the CCMoid, can be deduced. Further Fc evidence could not be identified in part due to the working window which limited the analysis.

The deposition of CB[7] layer was clearly evidenced by the recognition of the signals of CB[7] at 1433 and 1733 cm<sup>-1</sup> designated to C-N and C=O bonds <sup>38</sup>. After the formation of the supramolecular complex, the CB[7]

signals were slightly shifted but still visible, and an intense peak around  $1611\text{ cm}^{-1}$ , that could represent the carbonyl group of compound **1** overlapped with other signals, appeared.

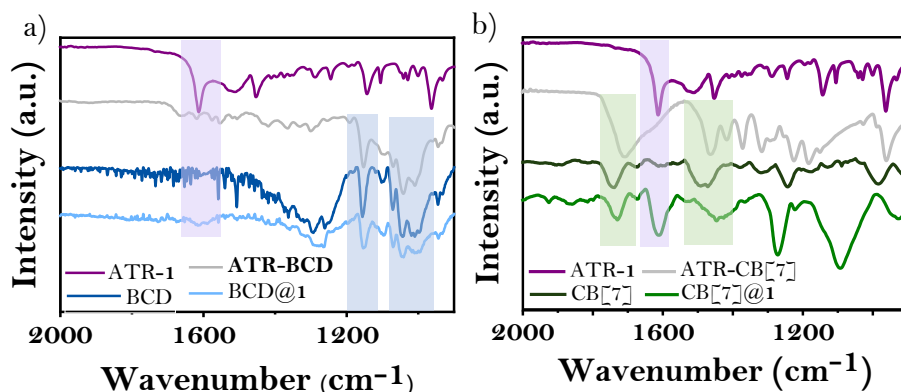


Figure 2.24. Comparison of the ATR-FTIR of the host and guest with the IRRAS of the corresponding SAMs where a)  $\beta$ CD and b) CB[7] act as host, respectively.

As in the XPS experiment, the SAMs of the host were evidently detected, however, evidence of Fc appearance in the complex was difficult to probe using this technique, being CV the best one to do it.

## Ellipsometry

Ellipsometry was employed to determine the thickness of the SAMs <sup>49</sup>. As it was previously explained, the complexes were obtained in a two-step process, where the first step was the formation of the host SAMs. Initially, the Au surfaces were immersed in each host solution for 24 h. However, the ellipsometry value for the thickness of SH- $\beta$ CD was 1.47 nm, which was 0.5 nm higher than a monolayer of thiolated  $\beta$ CD, whose thickness is 1.03 nm, (0.79 nm ( $\beta$ CD) + 0.24 nm (Au-S bond)), being a possible explanation the

presence of bilayers in the sample or even the tilted disposition of the cyclodextrin. However, a reasonable thickness of 0.98 nm was fitted for the SH- $\beta$ CD SAM after finding out the optimized time to form the SH- $\beta$ CD monolayer was 18 h of incubation.

The experimental thickness obtained for the CB[7] SAMs was 1.28 nm, which is 0.14 nm taller than the height of a CB[7] molecule anchored to Au that is 1.14 nm, (0.91 CB[7] + 0.23 (Au-O bond)). This slight difference is within the adjustment error.

An increase in the thickness of the SH- $\beta$ CD@1 0.2 mM and CB[7]@1 0.2 mM layers was detected, revealing values in a range from 1.8 to 2.4 nm, which indicates a predominant vertical configuration of the CCMoid, as suggested by theoretical calculations to be the most stable conformation, without discarding the possible presence of CCMoid molecules interacting with two hosts as well (horizontal disposition). Depending on the degree of insertion of the Fc moiety within the cavity, the height of the complex would vary. Describing the example with CB[7] as host in Figure 2.25, it could vary from approximately 1.83 nm (1.6 nm compound **1** + 0.23 nm Au-O), when Fc is in the deepest position, to approximately 2.74 nm (1.6 nm compound **1** + 0.91 nm CB[7] + 0.23 nm Au-O) when Fc is on the top of the CB[7].

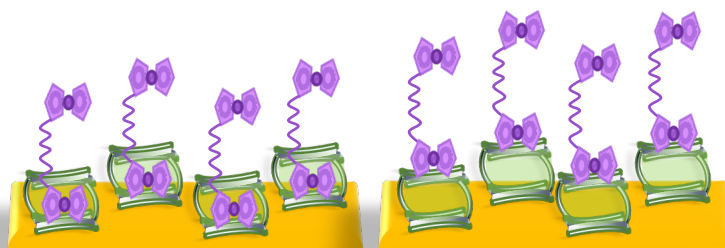


Figure 2.25. Example of the configuration of CB[7]@1 system regarding the depth in the inclusion of **1** inside the cavity.



Considering the majority coverage with a vertical arrangement of the CCMoids and taking into account the small amount of **1** in the sample, suggested by the surface coverage estimated by CV, two different approaches for the formation of the monolayers were tested using SH- $\beta$ CD as host in order to try to increase the amount of **1** on the surfaces.

#### **2.3.3.2.4 Alternative strategies for the formation of the supramolecular complex on Au supports**

The first option consisted on the formation of the host guest complex in solution followed by the immersion of a Au substrate in the mixture for a determined period of time. The second approach was based on the incubation of SH- $\beta$ CD SAMs with a solution of the supramolecular complex  $\beta$ CD@**1**. Both alternatives are depicted in Figure 2.26.

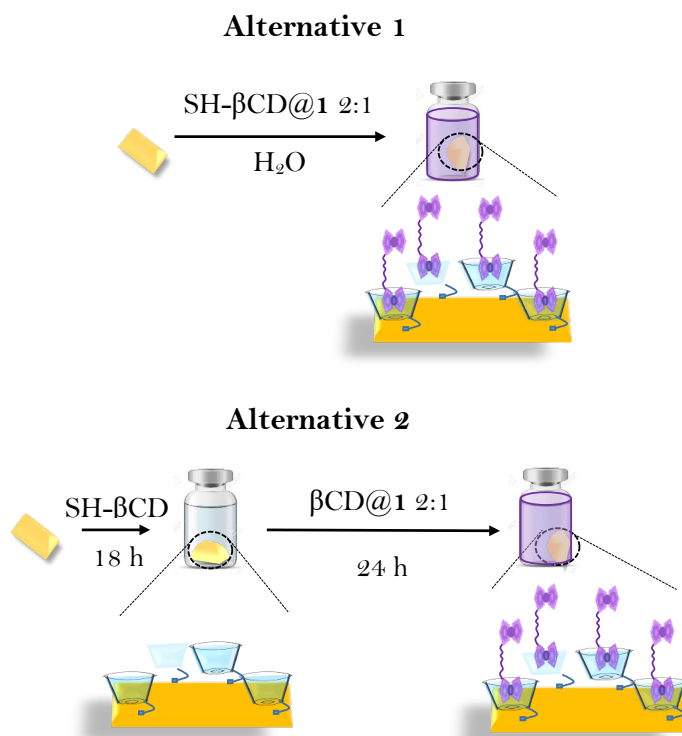


Figure 2.26. Schematic illustration of the approaches used to modify the gold support with the encapsulated systems.

### Option 1: Precomplex

Two aqueous mixtures of SH- $\beta$ CD and compound **1**, in ratio 2:1, were prepared and stirred for 1 or 17 days, correspondingly. After the respective times, a bare gold substrate was immersed in each solution for 24 h. The resulting surfaces were rinsed with Milli-Q water, dried and characterized by CV.

The voltammograms in the same conditions as the previous CV experiments, are represented in Figure 2.27. Both graphs are characterized by the lack of Fc redox signal, indicating no anchoring of the system on the Au layer. The most probable explanation for this fact, is related to the

insolubility of both compounds, thiolated  $\beta$ CD and **1**, in water, preventing the formation of the complex in optimal amounts, and hampering further deposition on the substrate.

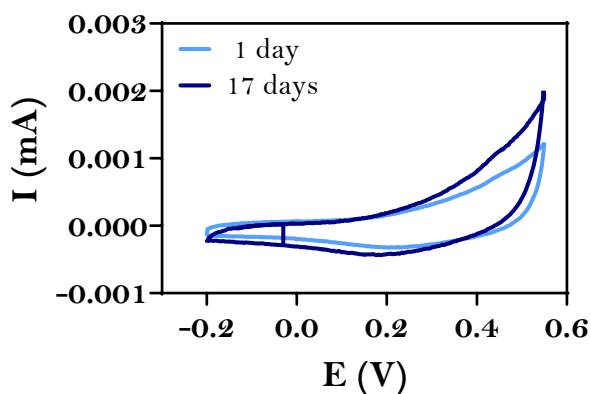


Figure 2.27. CV of the Au substrates after its immersion in a solution of SH- $\beta$ CD@**1** for 1 or 17 days.

## Option 2

The second approach was based on previous works of Wimbush *et al.*<sup>23</sup>. Basically, the process involves the formation of the SAM of the host which is incubated in a solution of the complex in order to increase the solubility of the guest in the aqueous media.

Two Au support were incubated in a 1 mM solution of SH- $\beta$ CD for 18 h to form the  $\beta$ CD SAM. In parallel, an aqueous solution of non-modified  $\beta$ CD, and compound **1**, in a 2:1 ratio, was stirred for 24 h. Next day, the two surfaces were rinsed with Milli-Q and immersed in the pre-formed solution of the complex for 5 h and 24 h, respectively. Finally, both substrates were rinsed, dried and characterized by CV.

The acquired voltammograms are shown in Figure 2.28. Similar results, in terms of recognition of the irreversible Fc redox signal, were obtained in

comparison to the initial methodology explained. In this case, the oxidation of Fc is occurred at 0.35 V and the reduction at 0.12 V, for 5 h immersion, and 0.07 V, for 24 h immersion. However, a small shift about 0.05 V to more positive voltages is detected for these samples.

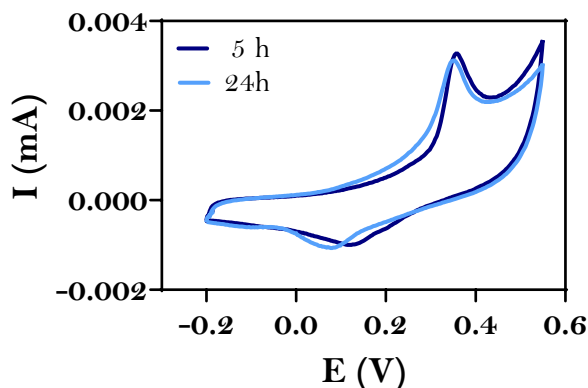


Figure 2.28. Voltamogram obtained after the application of strategy 2 to anchor the SH- $\beta$ CD@1 supramolecular arrangement on Au.

The possible explanation for this positive shift is exposed in Figure 2.29. In the supramolecular solution, both Fc are covered by  $\beta$ CD due to the 2:1 host-guest ratio. When the functionalized Au substrate is immersed in the supramolecular solution, one Fc molecule would still be covered by non-functionalized  $\beta$ CD while the other would be encapsulated by the SH- $\beta$ CD anchored to the substrate, as it can replace some of the non-modified  $\beta$ CD. Based on the behaviour explanation in solution, when both Fc are covered, a higher voltage is needed to oxidise the Fc of the system compared to when only one Fc is encapsulated.

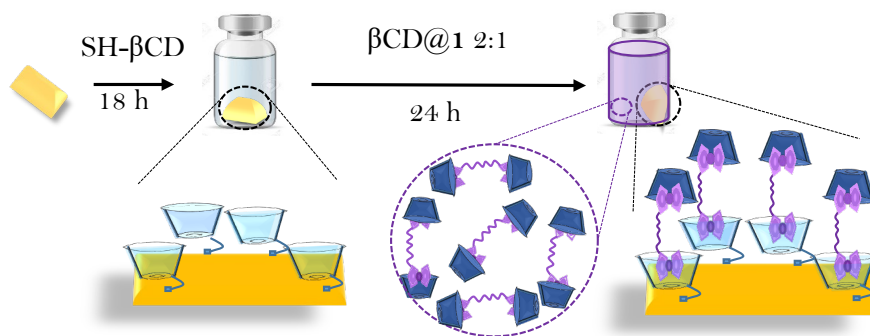


Figure 2.29. Illustrative scheme of the proposed final assembly applying option 2.

Both alternatives were studied but discarded due to the difficulty of assessing the experiments, and therefore the initial and more extensively reported was the chosen one for the conductivity studies by EGaIn technique, after the indication of the presence of compound **1** in the supramolecular complexes.

#### **2.3.3.2.5 Electrical characterization of the supramolecular complex on Au: charge transport measurements by depositing EGaIn top electrode.**

The SAMs of the host-guest systems were prepared with the aim of investigating the current changes in EGaIn junctions when the guest was involved. These measurements allowed previously to study the rectification behaviour of Fc- containing junctions and elucidate the charge transport mechanism within the junctions by performing additional experiments changing the length between the electrodes or varying temperature <sup>22</sup>

When the junction is created, according to the situations reported in previous studies <sup>50,51</sup> the non-encapsulated Fc moiety would interact

through Van der Waals interactions with the Ga<sub>2</sub>O<sub>3</sub> EGaIn top electrode and it would be separated from the Au electrode by the rest of the molecule and the host. This would cause the HOMO of the guest to be asymmetrically located close to, and couple with the Fermi level of the EGaIn.

The energy level diagrams of the system, illustrated in Figure 2.30, helps to outline the charge transport mechanism involved. The estimated HOMO of compound **1** from DPV measurements of the isolated CCMoid, was -4.6 eV which is placed very close to the Fermi levels of the electrodes, - 5.1 eV, for Au, and - 4.3 eV, for EGaIn, which are aligned with an intermediate value of -4.7 eV in the initial state when the  $V = 0$ . However, it is important to note that the HOMO of the compound **1** in the supramolecular systems, and also in the molecular junction, may differ from the isolated molecule, which is used for the estimation, therefore, the energy levels diagram must be taken as an approximation in the absence of further evidence from DFT calculations yet to be done.

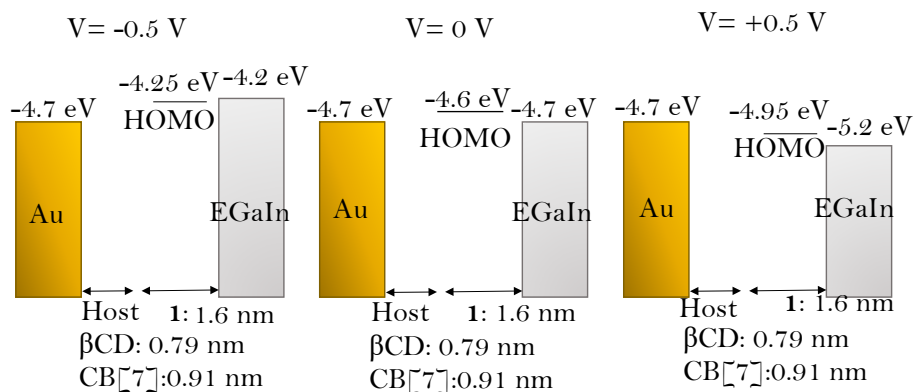


Figure 2.30. Proposed energy level diagram for the mechanism of charge transport across the supramolecular complexes immobilized on Au in EGaIn tunnelling junctions.

When a positive or negative bias of  $V=\pm 0.5$  V is applied to the system, the Fermi level of the EGaIn vary its initial value, 0.5 eV, with respect to the Au Fermi level. Likewise, the HOMO of compound **1** is slightly altered but not to the same degree as the fermi level of the electrode, probably due to a decreasing of the potential across the Van der Waals interface created between the Fc and the gallium oxide, which we estimate to be 0.15 eV. At a positive bias, the Fermi level of the EGaIn would decrease to -5.2 eV and the HOMO of compound **1** would decrease to -4.95 eV. At negative bias, the Fermi level of the EGaIn would increase to -4.2 eV and the HOMO of **1** to -4.25 eV. As the HOMO is between the Fermi levels of both electrodes in both scenarios, in theory it would be able to participate in the charge transport mechanism. To confirm the mechanism, the gathering of measurements at different temperatures and electrode distances will it be helpful, owing to the process of hopping is temperature dependent while tunnelling is a distance dependent mechanism.

Experimental EGaIn measurements were carried out to identify current changes between the host layer and the supramolecular complex, as well as, to check possible rectification processes in presence of the guest. Therefore  $\beta$ CD, CB[7] host SAMs and  $\beta$ CD@1 0.2, CB[7]@1 0.2 systems were contacted with the EGaIn tip and the current density (J) was recorded while sweeping the voltage (V) between  $\pm 0.5$  V. Specifically, for each sample, a different number of EGaIn junctions were formed recording 10 scans measured in the  $\pm 0.5$  V range, (1 scan is considered to be the entire cycle: from 0 to + 0.5 V, from + 0.5 V to 0, from 0 to -0.5 V and from -0.5 V to 0 V).

As Table 2.5 collects, high yields of EGaIn junctions were satisfactorily formed, with low percentages of shortcuts, indicating the presence of a layer between the two electrodes.

	N° Junctions	N° Good Junctions	Yield %
SH- $\beta$ CD	27	24	89
SH- $\beta$ CD@ <b>1</b> 0.2	30	26	87
CB[7]@ <b>1</b>	33	32	97
CB[7]@ <b>1</b> 0.2	48	35	73

Table 2.5. Statistic data of the EGaIn junctions formed with the different samples.

It is worth to mention that current intensity *vs.* bias plots are represented in logarithm scale. The current measured (*J*) depends exponentially on the distance between the electrodes <sup>52</sup>, which is determined by the SAM thickness, and it is not constant due to inevitable defects on the SAM and the bottom electrode, that results in a normal distribution of the distance values and therefore *J* is understood as a logarithm normally distributed function.

Figure 2.31. shows the obtained J-V curves in logarithm scales for the measured samples. In Figure 2.31 a, a non-significant increase of the current density is observed when compound **1** is present, compared to the  $\beta$ CD SAM sample, due to its detection between the error bars of the  $\beta$ CD SAM. Similar tendency is observed in Figure 2.31 b, when CB[7] is involved. In this case, a negligible increase of current density was detected after the formation of the supramolecular system. Additionally, similar but non reproducible current signals were obtained for different CB[7] SAMs, Figure 2.31 c, indicate possible slight differences in the host SAMs.



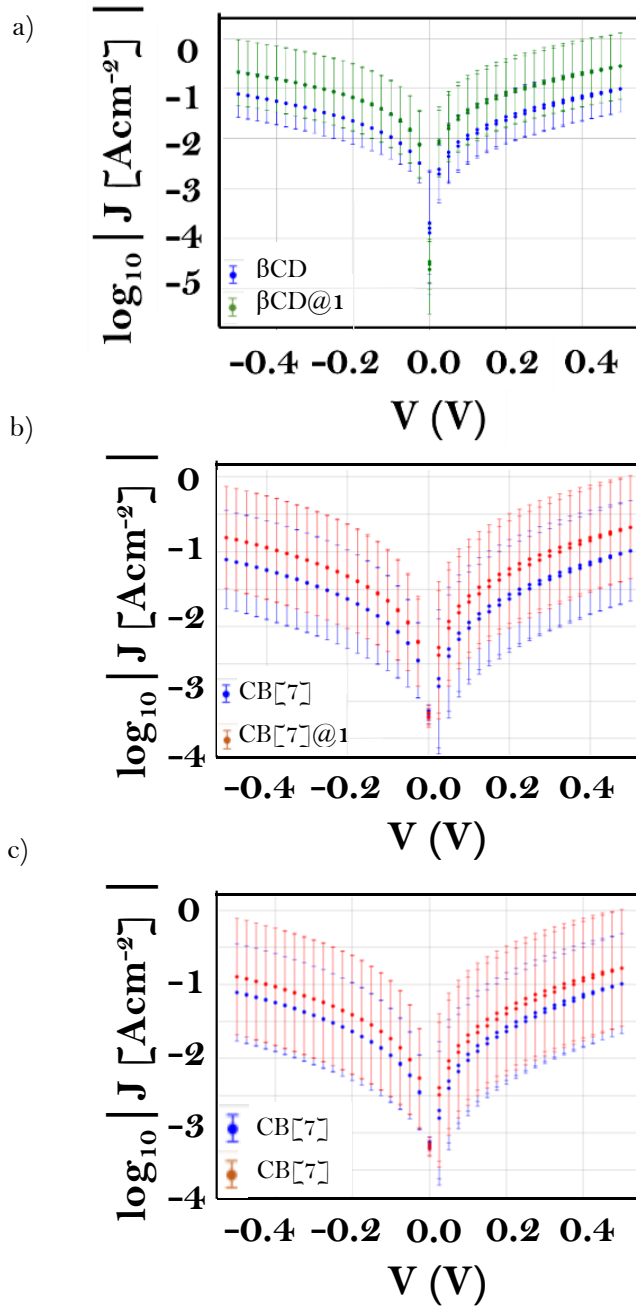


Figure 2.31. J-V plots for the a)  $\beta\text{CD}$ ,  $\beta\text{CD}@1$ , b)  $\text{CB}[7]$  and  $\text{CB}[7]@1$  and c) different  $\text{CB}[7]$  EGaIn junctions.

We could not detect differences in  $J$ , as initially expected upon the incorporation of the FcCCMoid. This is probably owing to a sum of factors including: solubility issues, the only partial surface coverage of compound **1** (estimated 50 %), the possible presence of compound **1** in a horizontal position interacting each Fc with two host cavities, and therefore leading to small difference between the electrode distances before and after the incubation, and the impossibility of using higher voltages, at which the rectification behaviour could be detected, due to the instability of the SAMs. In addition, AFM studies (not shown), suggested the presence of some aggregates of **1**, hindering a proper comparison between samples. In order to avoid the observed aggregation, lower concentrations of compound **1** could be analysed. However, the low surface coverage calculated by CV, would not be expected to provide better results.

Based on these results different alternative approaches can be proposed, such as improving the solubility of **1** by altering the pH to improve the host-guest SAM formation or, using longer chains in the  $\beta$ CD host to increase the electrodes separation and decoupling the Fc moiety from the bottom electrode.

## 2.4. Conclusions

- It has been demonstrated by UV-Vis and CV that the synthesized compound **1** is capable of forming supramolecular complexes with  $\beta$ CD and CB[7] in solution acting as a guest.
- From the three proposed methodologies to form the host-guest system on surfaces, the two-step approach involving the creation of the host SAM followed by the inclusion of the guest provided the best results.
- All the variations in the characterization experiments after the incubation of the host modified Au surfaces in a solution containing compound **1** indicate the presence of compound **1** in the supramolecular complex on surfaces.
- The lack of differences in J in the supramolecular complexes after the inclusion of **1**, observed when EGaIn junctions were formed, could be attributed to multiple factors such as the presence of aggregates together with the partial coverage of the SAM and the impossibility of using higher voltages due to the instability of the SAMs.

## 2.5. Experimental section

### Synthesis of FcCCMoid, 1

0.5 mL of acetylacetone (4.9 mmol) and 0.25 g of  $B_2O_3$  (3.59 mmol) were mixed in 5 mL EtOAc at 40 °C. 30 minutes later, a freshly prepared solution of 2 g ferrocenecarboxaldehyde (9.34 mmol) and 5.39 mL tributylborate (19.98 mmol) in 5 mL EtOAc was added, and the mixture was heated up at 40 °C for 3 h. After cooling down to RT, a solution of 0.25 mL butylamine (2.52 mmol) in 5 mL EtOAc, was introduced dropwise into the flask. The final reaction was stirred at room temperature for 2 days. Then, a solution of 10 % HCl was added, and the mixture stirred at 60 °C for 2 h. Finally, the reaction was filtered, washed with Milli-Q water and MeOH and dried with  $Et_2O$  to obtain the desired product as a purple solid in 77 %.  $^1H$  NMR (360 MHz,  $CDCl_3$ )  $\delta$ : 16.15 (1H, s), 7.56 (2H, d,  $^3J=14.6$  Hz), 6.23 (2H, d,  $^3J=14.9$  Hz), 5.63 (1H, s), 4.52 (s, 4H), 4.44 (s, 4H), 4.17, s (10 H). MS (MALDI - TOF): m/z calcd for FcCCMoid: 492.05 [M], found: 491.40 [M-1].

### Synthesis of Per -6- mesyl-B-cyclodextrin (Mesyl- $\beta$ CD)

After a drying process at 80 °C for 5 h under vacuum, 1.5 g (1.32 mmol) of  $\beta$ -cyclodextrin were dissolved in 5 mL of dry DMF maintaining both inert and temperature conditions. 3.7 mL (21.8 mmol) of mesyl chloride were dropwise added into the warm mixture and it was stirred for 2 days. Afterwards, the solvent was removed under vacuum, obtaining a wax which was dissolved in 7.5 mL of MeOH. Separately, 3 M sodium methylate solution was prepared by cutting 530 mg of Na and carefully washing them in hexane, EtOH and finally dissolving them in 7.5 mL of MeOH. The sodium methylate solution was added into the reaction residue. After stirring for 30 minutes, the mixture was poured onto ice and the precipitate

was filtered and washed with Milli-Q water to isolate the compound as a white solid in 94 % yield.  $^1\text{H}$  NMR (360 MHz,  $\text{CDCl}_3$ )  $\delta$ : 6.01 (7H, d,  $^3J=6.4$  Hz) 5.86 (7H, s), 4.96 (7H, s) 4.09 (7H, d,  $^3J=10.7$  Hz), 3.85 (m, 14H,  $^3J=8.92$  Hz), 3.65 (m, 7H,  $^3J=9.0$  Hz), 3.40, (m,  $^3J=8.2$  Hz).

### Synthesis of Per-6-thio-B-cyclodextrin (SH- $\beta$ CD)

372.2 mg (4.75 mmol) of thiourea were added into a solution of Mesyl  $\beta$ CD (1022.7 mg; 0.319 mmol) in 12.4 mL dry DMF. After 19 h at 70 °C under Ar atmosphere, the solvent was removed providing an oil which was dissolved in 62 mL of Milli-Q water. 312 mg of NaOH were introduced into the flask and the mixture was refluxed for 1h. Subsequently, the dispersion was acidified with  $\text{KHSO}_4$  and the precipitate was filtered and finally washed with Milli-Q water to isolate the product as a white solid in 91 % yield.  $^1\text{H}$  NMR (360 MHz,  $\text{CDCl}_3$ )  $\delta$ : 6.01 (7H, d,  $^3J=6.7$  Hz), 5.85 (7H, s), 4.96 (7H, s), 4.10 (7H, d,  $^3J=10.6$  Hz), 3.87 (14H, m,  $^3J=8.3$  Hz), 3.65 (7 H, t,  $^3J=9.3$  Hz), 3.40 (t,  $^3J=8.2$  Hz).

### Formation of the supramolecular complex in solution

- **Preparation of Host@1 2:1 complexes:** An aqueous solution 1 mM in the respective host (2  $\mu\text{mol}$  in 2 mL Milli-Q water) and 0.5 mM in compound **1** (0.49 mg; 1  $\mu\text{mol}$  in 2 mL Milli-Q water) was stirred for 14 days or 17 days for CB[7] or SH- $\beta$ CD, respectively.
- **Preparation of Host@1 1:1 systems,** same protocol as the complex 2:1 was applied but modifying the concentration of the involved host to 0.5 mM.

### **Fabrication of the template stripped gold electrodes <sup>53</sup>**

200 nm-thick layer of gold was deposited onto a Si wafer by evaporation at Institut de Nanociencia I Nanotecnologia (ICN2) Then, some drops of epoxy adhesive resin Epo-Tek 353ND (bought in Comercial Química Massó) were added on top of the gold layer. Some glass slides (size 2.5x0.5 cm) were apart rinsed with piranha, Milli-Q water, ethanol, acetone and dichloromethane. This prerinsed glass slides were carefully positioned on top of the resin drops which spread through the gold area contacted by the glass. To glue the glass to the gold, the glass/epoxy/gold/Si sandwich was air dried at room temperature for 5 h and 12 h at 80 °C. Finally, the glass/epoxy/gold assemblage was released from the Si wafer by applying pressure and moving a scalpel through the edges of the gold/epoxy interface. After the cleavage, the gold that had been in contact with the Si wafer was exposed and cleaned under N<sub>2</sub> flow before use.

### **Formation of the supramolecular complex on Au substrates**

- **Formation of CB[7] SAM**

CB[7] SAM was prepared by immersion of the Au<sup>TS</sup> substrate into a 1 mM aqueous solution of CB[7] for 24 h at room temperature. The surface was washed with Milli-Q water and dried in a stream N<sub>2</sub>.

- **Formation of SH-βCD SAM**

Au<sup>TS</sup> substrate was incubated in a 1 mM solution of per-6-thio-β-cyclodextrin in H<sub>2</sub>O:DMSO (2:3) for 18 h at room temperature under Ar atmosphere. Lastly, the surface was rinsed with Milli-Q water and dried in a stream of N<sub>2</sub>.

- **Formation of CB[7]@1 host-guest complex**

CB[7]-Au<sup>TS</sup> functionalised substrate was incubated in a 0.2 mM solution (DMSO:H<sub>2</sub>O 1:4) of **1** (4 mg, 40 mL) in a vertical position for 24 h stirring at room temperature. The substrate was rinsed with Milli-Q water and dried under N<sub>2</sub>.

- **Formation of SH-βCD@1 host-guest complex**

SH-βCD-Au SAMs were immersed in a 0.2 mM solution (DMSO:H<sub>2</sub>O 1:4) of **1** (4 mg, 40 mL) in a vertical position for 24 h stirring at RT. The surface was washed with Milli-Q water and dried in a stream of N<sub>2</sub>.

### **Alternative 1 for the formation of the supramolecular complex on Au surfaces: Precomplex**

Two aqueous solution, both 1 mM in SH-βCD and 0.5 mM in compound **1** were stirred for 24 h. After that time, an Au support was incubated in the mixtures for 24 h or 17 days. Then the substrate was rinsed with Milli-Q water and dried in a stream of N<sub>2</sub>.

### **Alternative 2 for the formation of the supramolecular complex on Au surfaces**

1mM aqueous solution of βCD and 0.5 mM of **1** was stirred for 24 h. In parallel, The SH-βCD SAM was formed in a Au substrate. Then, the SH-βCD modified Au substrate was incubated in the pre-prepared βCD@**1** solution stirring for 24 h. Finally, the surface was cleaned with Milli-Q water and dried with a N<sub>2</sub> flow.

## **Ultraviolet-Visible Absorption Spectroscopy (UV-Vis)**

For solution studies, the samples were measured in a 0.01 mM concentration solution in THF using 1 cm quartz cuvettes. For the solid measurements a mixture of 0.1 mg of CCMoid and 200 mg of KBr were milled and pressed to obtain thin pellets.

## **Cyclic Voltammetry (CV) and Differential Pulse Voltammetry (DPV)**

CV and DPV measurements of the CCMoids were conducted at 50 mV/s scan rate using 0.1 mM solutions of CCMoids in dry THF, 0.1 M solution of tetrabutylammonium hexafluorophosphate (TBAPF<sub>6</sub>) as electrolyte, Pt wires as counter and reference electrodes and glassy carbon (which was polished using granulated alumina on a microcloth pad) as working electrode. Fc was added as internal reference.

The supramolecular complexes were measured in 0.1 mM of Na<sub>2</sub>SO<sub>4</sub> aqueous solution at 50 mV/s using a glassy carbon working electrode, Pt counter electrode and Ag/AgCl reference electrode, at the moment of mixing the host and the guest, as well as 9 days later.

The measurements of the SAM on gold surfaces were carried out in 0.1 M aqueous solution of Na<sub>2</sub>SO<sub>4</sub> using the modified gold substrate now as working electrode, Pt wire as counter electrode and Ag/AgCl electrode as reference electrode at 50 mV/s.

## **Contact angle**

2-4  $\mu$ L of Milli-Q water were dropped onto the desired surface to identify the angle between the drop and the surface of the platform in a sessile drop method.



## Ellipsometry

Ellipsometry experiments were performed at UB with help of Dr. Alejandro Martin and Prof. Eliseo Ruiz. We measured psi ( $\Psi$ ), which is the ratio of the amplitudes of the p- and s-polarized light, and delta ( $\Delta$ ), which is the phase difference between them, of the reflected light for incident angles of  $65^\circ$ ,  $70^\circ$  and  $75^\circ$ . To obtain an experimental value of the thickness, the provided data was fitted to the Cauchy model by varying the refractive index and thickness set of parameters in CompleteEASE software.

## Theoretical calculations

Structural optimization calculations were performed in collaboration with Prof. Eliseo Ruiz with the fhi-aims program using the PBE functional including dispersion effects. We employed the “light” basis set due to the large number of atoms in these systems.

## Eutectic Gallium Indium (EGaIn)

The EGaIn measurements (current density vs voltage) were conducted in collaboration with Maria Elisabetta Giglio, Dr. J. Alejandro de Sousa, Dr. N ria Crivillers and Dr. Marta Mas (ICMAB) in a home-made set-up using a Keithley 2004B controlled by an in-house software developed with LabVIEW. During the measurements the bottom electrode was grounded, while the top EGaIn electrode was biased.

## Annex II

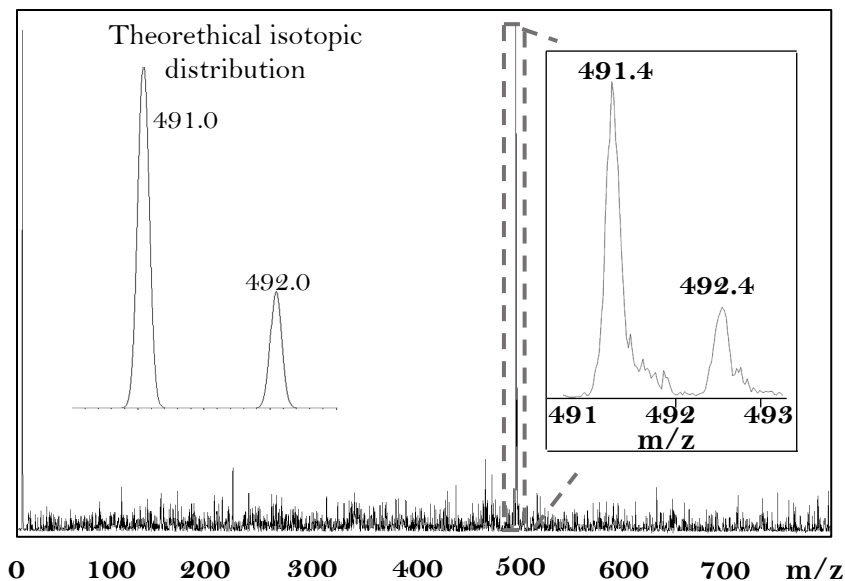


Figure A2.1. MALDI-TOF mass spectrum in negative mode of compound **1**.

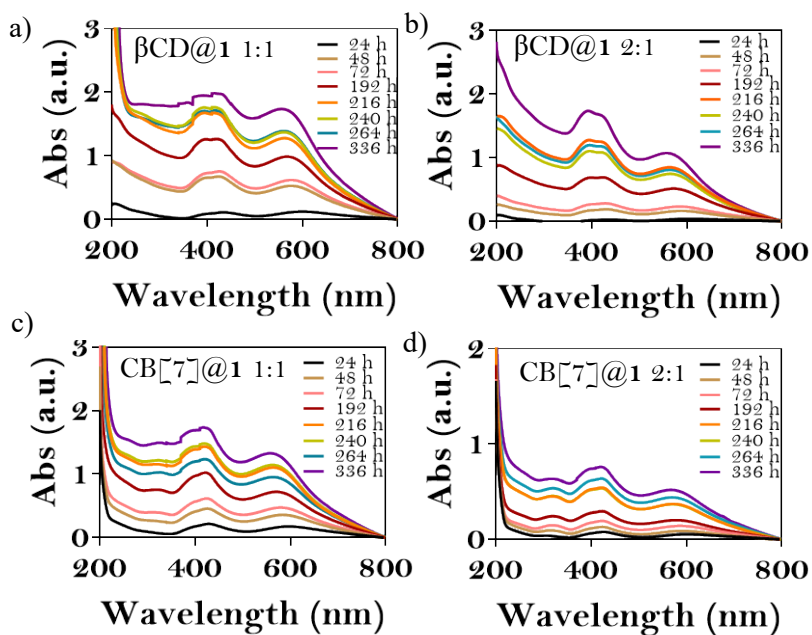


Figure A2.2. Variation of the UV-Vis absorption results of a)  $\beta\text{CD}@1$  1:1, b)  $\beta\text{CD}@1$  2:1, c)  $\text{CB}[7]@1$  1:1 and d)  $\text{CB}[7]@1$  2:1 in  $\text{Na}_2\text{SO}_4$  aqueous solution over 14 days period.

## References

- (1) Lenh, J.M. Supramolecular chemistry-Scope and perspectives- Molecules-Super molecules- Molecular device. *Nobel lecture*, **1987**, 444–491.
- (2) Ariga, K. *Biomaterials Nanoarchitectonics*; **2016**.
- (3) Jeon, W. S.; Moon, K.; Park, S. H.; Chun, H.; Ko, Y. H.; Lee, J. Y.; Lee, E. S.; Samal, S.; Selvapalam, N.; Rekharsky, M. V.; Sindelar, V.; Sobransingh, D.; Inoue, Y.; Kaifer, A. E.; Kim, K. Complexation of Ferrocene Derivatives by the Cucurbit[7]Uril Host: A Comparative Study of the Cucurbituril and Cyclodextrin Host Families. *J. Am. Chem. Soc.* **2005**, *127* (37), 12984–12989.
- (4) Supramolecular Cucurbit[7]uril@Ferrocene Complexation on Surface: From Nanostructure Differentiation to Guest Quantitation. Qi, L.; Wang, R.; Yu, H. *Acc. Mater. Res.* **2023**, *4* (5), 457–466.
- (5) Matsue, T.; Evans, D. H.; Osa, T.; Kobayashi, N. Electron-Transfer Reactions Associated with Host-Guest Complexation. Oxidation of Ferrocenecarboxylic Acid in the Presence of  $\beta$ -Cyclodextrin. *J. Am. Chem. Soc.* **1985**, *107* (12), 3411–3417.
- (6) Ong, W.; Kaifer, A. E. Unusual Electrochemical Properties of the Inclusion Complexes of Ferrocenium and Cobaltocenium with Cucurbit[7]Uril. *Organometallics* **2003**, *22* (21), 4181–4183.
- (7) 474349 and 396554 results obtained for the search in SciFinder of the key words: " beta cyclodextrin ,ferrocene, aqueous solution " and "cucurbit[7]uril, ferrocene, aqueous solution" vs 31082 and 7660 for the search of the key words: " beta cyclodextrin, ferrocene, gold " and "cucurbit[7]uril, ferrocene, gold.
- (8) Palma, G. Di; Kotowska, A. M.; Hart, L. R.; Scurr, D. J.; Rawson, F. J.; Tommasone, S.; Mendes, P. M. Reversible, High-A Ffi Nity Surface Capturing of Proteins Directed by Supramolecular Assembly. *ACS Appl. Mater. Interfaces*. **2019**, *11* (9), 8937–8944.

- (9) Young, J. F.; Nguyen, H. D.; Yang, L.; Huskens, J.; Jonkheijm, P.; Brunsveld, L. Strong and Reversible Monovalent Supramolecular Protein Immobilization. *Chem. Bio. Chem.* **2010**, *11* (2), 180–183.
- (10) Murray, J.; Sim, J.; Oh, K.; Sung, G.; Lee, A.; Shrinidhi, A.; Thirunarayanan, A.; Shetty, D.; Kim, K. Enrichment of Specifically Labeled Proteins by an Immobilized Host Molecule. *Angew. Chem. Int. Ed.* **2017**, *56* (9), 2395–2398.
- (11) Neirynck, P.; Brinkmann, J.; An, Q.; van der Schaft, D. W. J.; Milroy, L. G.; Jonkheijm, P.; Brunsveld, L. Supramolecular Control of Cell Adhesion via Ferrocene-Cucurbit[7]Uril Host-Guest Binding on Gold Surfaces. *Chem. Commun.* **2013**, *49* (35), 3679–3681.
- (12) Beulen, M. W. J.; Bugler, J.; De Jong, M. R.; Lammerink, B.; Huskens, J.; Schönherr, H.; Vancso, G. J.; Boukamp, B. A.; Wieder, H.; Offenhäuser, A.; Knoll, W.; Van Veggel, F. C. J. M.; Reinhoudt, D. N. Host-Guest Interactions at Self-Assembled Monolayers of Cyclodextrins on Gold. *Eur. J. Chem.* **2000**, *6* (7), 1176–1183.
- (13) Yang, S.; You, M.; Yang, L.; Zhang, F.; Wang, Q.; He, P. A Recyclable Electrochemical Sensing Platform for Breast Cancer Diagnosis Based on Homogeneous DNA Hybridization and Host-Guest Interaction between Cucurbit[7]Uril and Ferrocene-Nanosphere with Signal Amplification. *J. Electroanal. Chem.* **2016**, *783*, 161–166.
- (14) Lee, D. W.; Park, K. M.; Gong, B.; Shetty, D.; Khedkar, J. K.; Baek, K.; Kim, J.; Ryu, S. H.; Kim, K. A Simple Modular Aptasensor Platform Utilizing Cucurbit[7]Uril and a Ferrocene Derivative as an Ultrastable Supramolecular Linker. *Chem. Commun.* **2015**, *51* (15), 3098–3101.
- (15) Nakahata, M.; Takashima, Y.; Yamaguchi, H.; Harada, A. Redox-Responsive Self-Healing Materials Formed from Host Guest Polymers. *Nat. Commun.* **2011**, *2* (1) 511,

- (16) Ahn, Y.; Jang, Y.; Selvapalam, N.; Yun, G.; Kim, K. Supramolecular Velcro for Reversible Underwater Adhesion. *Angew. Chem. Int. Ed.* **2013**, *52* (11), 3140–3144.
- (17) Qi, L.; Tian, H.; Shao, H.; Yu, H. Z. Host-Guest Interaction at Molecular Interfaces: Binding of Cucurbit[7]Uril on Ferrocenyl Self-Assembled Monolayers on Gold. *J. Phys. Chem. C* **2017**, *121* (14), 7985–7992.
- (18) Wang, Y. H.; Zhou, Y. F.; Tong, L.; Huang, H.; Zheng, J. F.; Xie, W.; Chen, J. Z.; Shao, Y.; Zhou, X. S. Revealing Supramolecular Interactions and Electron Transport in Single Molecular Junctions of Cucurbit[n]Uril. *Adv. Electron Mater.* **2021**, *7* (9), 1–6.
- (19) Huang, M.; Sun, M.; Yu, X.; He, S.; Liu, S.; Nau, W. M.; Li, Y.; Wu, T.; Wang, Y.; Chang, S.; He, J. Reliably Probing the Conductance of a Molecule in a Cavity via van Der Waals Contacts. *J. Phys. Chem. C* **2020**, *124* (29), 16143–16148.
- (20) Sun, L.; Diaz-Fernandez, Y. A.; Gschneidtnr, T. A.; Westerlund, F.; Lara-Avila, S.; Moth-Poulsen, K. Single-Molecule Electronics: From Chemical Design to Functional Devices. *Chem. Soc. Rev.* **2014**, *43* (21), 7378–7411.
- (21) Nijhuis, C. A.; Reus, W. F.; Whitesides, G. M. Mechanism of Rectification in Tunneling Junctions Based on Molecules with Asymmetric Potential Drops. *J. Am. Chem. Soc.* **2010**, *132* (51), 18386–18401.
- (22) Chiechi, R. C.; Weiss, E. A.; Dickey, M. D.; Whitesides, G. M. Eutectic Gallium-Indium (EGaIn): A Moldable Liquid Metal for Electrical Characterization of Self-Assembled Monolayers. *Angew. Chem. Int. Ed.* **2008**, *47* (1), 142–144.
- (23) Wimbush, K. S.; Reus, W. F.; Van Der Wiel, W. G.; Reinhoudt, D. N.; Whitesides, G. M.; Nijhuis, C. A.; Velders, A. H. Control over Rectification in Supramolecular Tunneling Junctions. *Angew. Chem. Int. Ed.* **2010**, *49* (52), 10176–10180.
- (24) Yuan, L.; Nerngchamnong, N.; Cao, L.; Hamoudi, H.; Del Barco, E.; Roemer, M.; Sriramula, R. K.; Thompson, D.; Nijhuis, C. A. Controlling the

- Direction of Rectification in a Molecular Diode. *Nat Commun* **2015**, 6 (1), 6324.
- (25) Li, X.; Zhou, S.; Zhao, Q.; Chen, Y.; Qi, P.; Zhang, Y.; Wang, L.; Guo, C.; Chen, S. Supramolecular Enhancement of Charge Transport through Pillar 5 Arene-Based Self-Assembled. *Angew Chem Int Ed.* **2023**, e202216987a.
- (26) Lippincott, E. R.; Nelson, R. D. The Vibrational Spectra and Structure of Ferrocene and Ruthenocene. *J. Chem. Phys.* **1953**, 21 (7), 1307–1308.
- (27) Radhakrishnan, S.; Paul, S. Conducting Polypyrrole Modified with Ferrocene for Applications in Carbon Monoxide Sensors. *Sensors Actuators, B Chem.* **2007**, 125 (1), 60–65.
- (28) Nardo, L.; Andreoni, A.; Masson, M.; Haukvik, T.; Tønnesen, H. H. Studies on Curcumin and Curcuminoids. XXXIX. Photophysical Properties of Bisdemethoxycurcumin. *J. Fluoresc.* **2011**, 21 (2), 627–635.
- (29) Viezbicke, B. D.; Patel, S.; Davis, B. E.; Birnie, D. P. Evaluation of the Tauc Method for Optical Absorption Edge Determination: ZnO Thin Films as a Model System. *Phys. Status. Solidi. B. Basic. Res.* **2015**, 252 (8), 1700–1710.
- (30) Roy, G.; Gupta, R.; Ranjan Sahoo, S.; Saha, S.; Asthana, D.; Chandra Mondal, P. Ferrocene as an Iconic Redox Marker: From Solution Chemistry to Molecular Electronic Devices. *Coord. Chem. Rev.* **2022**, 473, 214816.
- (31) Gagne, R.R.; Koval, C.A.; Lisensky G.C. Ferrocene as an internal standard for electrochemical measurements. *Inorg. Chem.* **1980**, 19 (9), 2854–2855.
- (32) Etcheverry-Berríos, A.; Olavarría, I.; Perrin, M. L.; Díaz-Torres, R.; Jullian, D.; Ponce, I.; Zagal, J. H.; Pavez, J.; Vásquez, S. O.; van der Zant, H. S. J.; Dulić, D.; Aliaga-Alcalde, N.; Soler, M. Multiscale Approach to the Study of the Electronic Properties of Two Thiophene Curcuminoid Molecules. *J. Eur. Chem. A.* **2016**, 22 (36), 12808–12818.
- (33) Rojas, M. T.; Kaifer, A. E.; Königer, R.; Stoddart, J. F. Supported Monolayers Containing Preformed Binding Sites. Synthesis and Interfacial

- Binding Properties of a Thiolated  $\beta$ -Cyclodextrin Derivative. *J. Am. Chem. Soc.* **1995**, *117* (1), 336–343.
- (34) Weiss, E. A.; Chiechi, R. C.; Kaufman, G. K.; Kriebel, J. K.; Li, Z.; Duati, M.; Rampi, M. A.; Whitesides, G. M. Influence of Defects on the Electrical Characteristics of Mercury-Drop Junctions: Self-Assembled Monolayers of n-Alkanethiolates on Rough and Smooth Silver. *J. Am. Chem. Soc.* **2007**, *129* (14), 4336–4349.
- (35) Vogel, N.; Zieleniecki, J.; Köper, I. As Flat as It Gets: Ultrasoother Surfaces from Template-Stripping Procedures. *Nanoscale* **2012**, *4* (13), 3820–3832.
- (36) Whitesides, G. M.; Boncheva, M. Beyond Molecules: Self-Assembly of Mesoscopic and Macroscopic Components. *Proc. Natl. Acad. Sci.* **2002**, *99* (8), 4769–4774.
- (37) Li, G.; Lauer, M.; Schulz, A.; Boettcher, C.; Li, F.; Fuhrhop, J. H. Spherical and Planar Gold (0) Nanoparticles with a Rigid Gold(I)-Anion or a Fluid Gold (0)-Acetone Surface. *Langmuir* **2003**, *19* (16), 6483–6491.
- (38) An, Q.; Li, G.; Tao, C.; Li, Y.; Wu, Y.; Zhang, W. A General and Efficient Method to Form Self-Assembled Cucurbit[n]Urils Monolayers on Gold Surfaces. *Chem. Commun.* **2008**, *17*, 1989–1991.
- (39) Lam, C. N.; Wu, R.; Li, D.; Hair, M. L.; Neumann, A. W. Study of the advancing and receding contact angles: liquid sorption as a cause of contact angle hysteresis. *Adv. Colloid Int. Sci.*, **2002**, *96* (1–3), 169–191.
- (40) Law, K. Y. Definitions for hydrophilicity, hydrophobicity, and superhydrophobicity: getting the basics right. *J. Phys. Chem. Lett.* **2014**, *5* (4), 686–688.
- (41) Liu, W.; Zhang, Y.; Gao, X. Interfacial Supramolecular Self-Assembled Monolayers of C60 by Thiolated  $\beta$ -Cyclodextrin on Gold Surfaces via Monoanionic C60. *J Am Chem Soc* **2007**, *129* (16), 4973–4980.
- (42) Greczynski, G.; Hultman, L. X-Ray Photoelectron Spectroscopy: Towards Reliable Binding Energy Referencing. *Prog. Mat. Sci.* **2020**, *107*, 100591.

- (43) Moulder, J. F.; Stickle, W. F.; Sobol, P. E.; Bomben, K. D. Handbook of X-Ray Photoelectron Spectroscopy. **1992**. Perkin-Elmer Corporation.
- (44) Beulen, M. W. J.; Bügler, J.; Lammerink, B.; Geurts, F. A. J.; Biemond, E. M. E. F.; Van Leerdam, K. G. C.; Van Veggel, F. C. J. M.; Engbersen, J. F. J.; Reinhoudt, D. N. Self-Assembled Monolayers of Heptapodant  $\beta$ -Cyclodextrins on Gold. *Langmuir* **1998**, 14 (22), 6424–6429
- (45) Woodbridge, C. M.; Pugmire, D. L.; Johnson, R. C.; Boag, N. M.; Langell, M. A. HREELS and XPS Studies of Ferrocene on Ag (100). *J. Phys. Chem. B*. **2000**, 104 (14), 3085–3093.
- (46) Greenler, R. G. Infrared Study of Adsorbed Molecules on Metal Surfaces by Reflection Techniques. *J. Chem. Phys.* **1966**, 44 (1), 310–315.
- (47) Hollins, P. Infrared Reflection–Absorption Spectroscopy. *Encyclopedia of Analytical Chemistry*. **2006**. John Wiley & Sons.
- (48) Méndez-Ardoy, A.; Steentjes, T.; Kudernac, T.; Huskens, J. Self-Assembled Monolayers on Gold of  $\beta$ -Cyclodextrin Adsorbates with Different Anchoring Groups. *Langmuir* **2014**, 30 (12), 3467–3476.
- (49) McCrackin, F. L.; Passaglia, E.; Stromberg, R. R.; Steinberg, H. L. Measurement of the Thickness and Refractive Index of Very Thin Films and the Optical Properties of Surfaces by Ellipsometry. *J. Res. Natl. Bur. Stand. A. Phys. Chem.* **1963**, 67 (4), 363.
- (50) Nijhuis, C. A.; Reus, W. F.; Whitesides, G. M. Molecular Rectification in Metal-SAM-Metal Oxide-Metal Junctions. *J. Am. Chem. Soc.* **2009**, 131 (49), 17814–17827.
- (51) Nijhuis, C. A.; Reus, W. F.; Barber, J. R.; Dickey, M. D.; Whitesides, G. M. Charge Transport and Rectification in Arrays of SAM-Based Tunneling Junctions. *Nano Lett.* **2010**, 10 (9), 3611–3619.
- (52) Simmons, J. G. Generalized Formula for the Electric Tunnel Effect between Similar Electrodes Separated by a Thin Insulating Film. *J. Appl. Phys.* **1963**, 34 (6), 1793–1803.

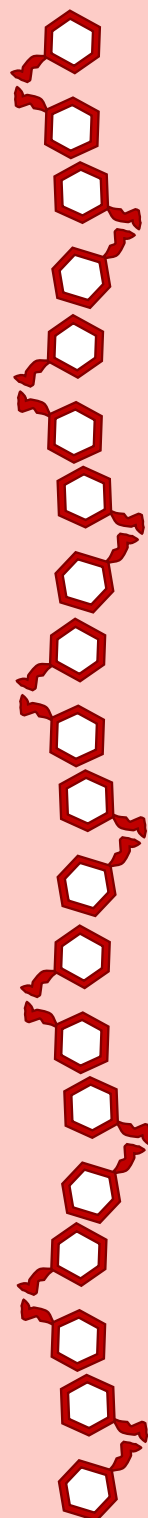


- (53) Weiss, E. A.; Kaufman, G.K.; Kriebel, J. K.; Li, Z.; Schalek, R.; Whitesides, G. M. Si/SiO<sub>2</sub>-Templated Formation of Ultraflat Metal Surfaces on Glass, Polymer, and Solder Supports: Their Use as Substrates for Self-Assembled Monolayers. *Langmuir* **2007**, *23* (19), 9686-9694.

# Chapter 3

## Development of new amino functionalized CCMoids

In this chapter, we investigate the optimal conditions for the achievement of a novel CCMoid that contains  $\text{-NH}_2$  functional groups as substituents in the terminal aromatic rings. This compound, named  $\text{NH}_2\text{CCMoid}$ , will be used as starting material for subsequent lateral reactions aimed at producing extended polycyclic aromatic hydrocarbon-based CCMoids, PAH-CCMoids.





### 3.1. Introduction

The keto-enol functionality of ACAC has been extensively studied in coordination chemistry, generally with metallic centres of the d-block in the periodic table, especially Cu(II), Ni(II), and Zn(II), among others, in the creation of coordination compounds (0D) <sup>1</sup>. This ability to coordinate metals, through the keto-enol unit, has been exploited with the analogous moiety present in the CCMoid skeletons <sup>2,3</sup>. This way, CCM has been coordinated to several metal centres mainly for medical applications, for instance to Zn(II) units in order to form Zn-curcumin nano-agents, for improving the stability and enhance the tumour accumulation and anticancer activity <sup>4</sup> (Figure 3.1 a). Although CCM has been the most studied molecule of the family, other CCMoids have also been examined, such as the diethyl amine terminated CCMoid bonded to Pd(II) and Cu(II) for photodynamic therapy <sup>5</sup> (depicted in Figure 3.1 b) or the so-called 9ACCMoid, which contains anthracene groups in the endings of the molecule, and whose coordination to Dy(III) ions has allowed the creation of  $[\text{Dy}(\text{9ACCM})_2(\text{NO}_3)_3]$  coordination compound that behaves as single molecule magnets (SMMs) in presence of an external magnetic field <sup>6</sup>. In a similar manner, additional SMMs were accomplished with this CCMoid when it is coordinated with Co(II) and two pyridines (Figure 3.1 c) or one bipyridine (Figure 3.1 d) to complete the coordination sphere of Co(II), having differences in the magnetic behaviour due to the variations in organization of the ligand substituents <sup>7</sup>.

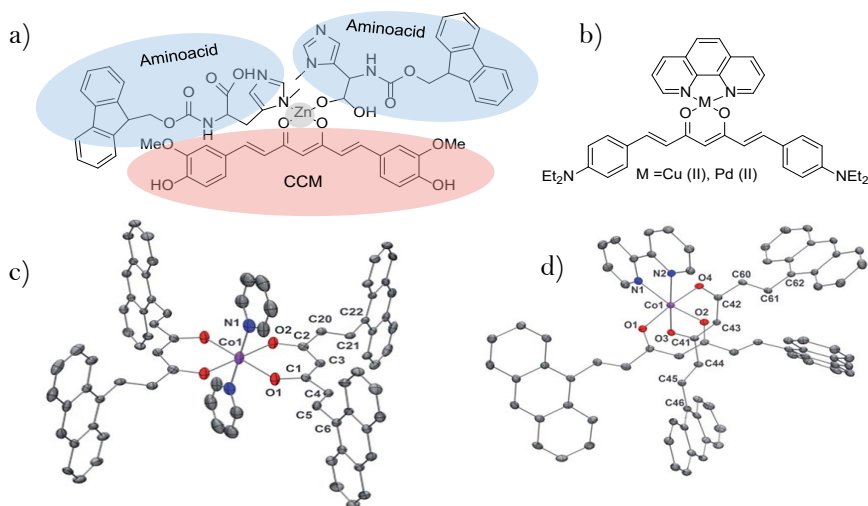


Figure 3.1. a) Chemical organization of CCM nanoagents described in Ref 4. b) Chemical structure of the diethyl amine-terminated CCMoid reported in Ref 5. c) d) Co(II) coordinated 9ACCMoid structure reported in Ref 7.

In addition to the keto-enol, each CCMoid could comprise extra components in its structure capable of interacting with other species, in order to explore new functionalities, properties and applications: the *arms* and the *leg* (see Chapter 1).

Regarding this matter, coordination polymers (CPs) rise from the different organizations resulting from the coordination of metal centres and organic ligands (linkers)<sup>8</sup>. CCMoid-based CPs, in particular, are formed by bonding metallic centres with a donor atom located in, and linked to the lateral aromatic rings of the CCMoid, the so-called *arms*. This bonding allows the formation of extended 1D, 2D or 3D structures with a range of different topologies and functionalities<sup>9–12</sup>.

The first CCMoid-based CP was dated on 2015 and is exhibited in Figure 3.2 a. Su *et al.*<sup>9</sup> described a porous polymer (MOF, metal organic framework) produced by the linking of Zn(II) ions with the three possible anchoring points of curcumin: the methoxy, hydroxyl and keto-enol groups. Some years later, Portolés-Gil *et al.*<sup>10</sup> reported a new CP also based on Zn(II) centres and CCM, as Figure 3.2 b shows. In this particular case, it was obtained by supercritical CO<sub>2</sub> and only one of the arms of curcumin were coordinated with the metal leaving the other arm unaffected. More recently, two novel coordination compounds employing Zn(II) as metal, and other CCMoids besides CCM, were published. One used 3pyCCMoid<sup>11</sup>, which contains 3-pyridine terminal rings, and it is shown in Figure 3.2 c, while the other used bisdemethoxycurcumin<sup>12</sup> as ligand, as Figure 3.2 d depicts.

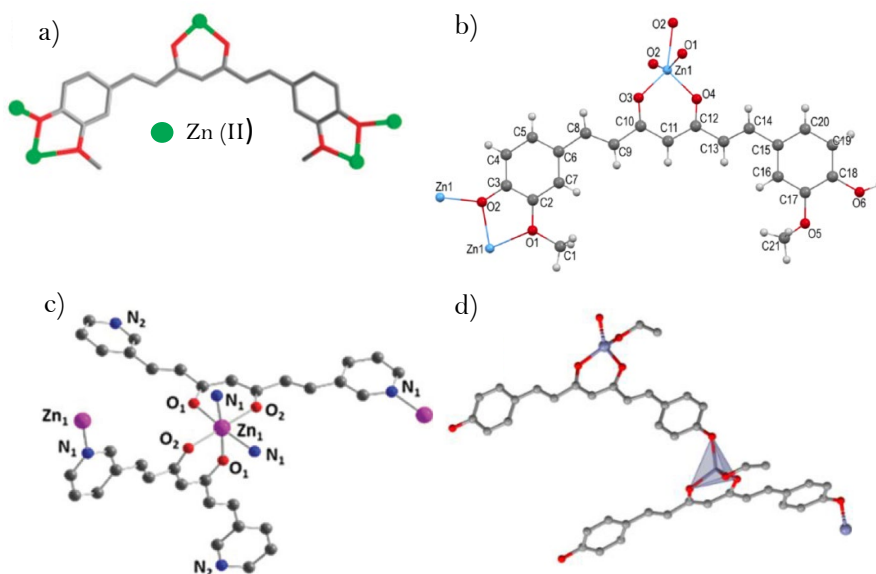


Figure 3.2. a) CCM based coordination polymer described in Ref 9. b) Crystalline structure of new CCM coordination polymer published in Ref 10. Zn (II) coordination compounds of c) 3pyCCMoid detailed in Ref. 11 and d) BDMC reported in Ref 12.

Focusing on CCMoids, it has been noted the interest of the organic coordination with metals, however, the lateral covalent modification of CCMoids has discretely started to be applied, predominantly for medical purposes. For instance, Wichitnithad *et al.*<sup>13</sup> synthesized several succinates derivative CCMoids by reacting the hydroxyl groups of CCM, DMC, and BDMC with different succinate acid chlorides in order to test their anticancer colon activity as Figure 3.3 a shows. The dual inhibition of some enzymes that participate in the production of specific species involved in Alzheimer disease was tested with newly designed CCMoids<sup>14</sup>. They were prepared following the Williamson ether synthesis between BDCM and benzyl bromide in presence of a base, as depicted in Figure 3.3 b. It implied the formation of an ether by a SN2 reaction between the deprotonated hydroxyl of the BDMC and the bromide. Most recently, the anticarcinogenic capacity of a set of curcumin and dichloroacetate hybrid conjugates against breast cancer was evaluated<sup>15</sup>. These CCMoids were isolated by an esterification reaction between the activated carboxylic acid of dichloroacetate functionalized amino acid and the hydroxyl group of CCM as it is represented in Figure 3.3 c.

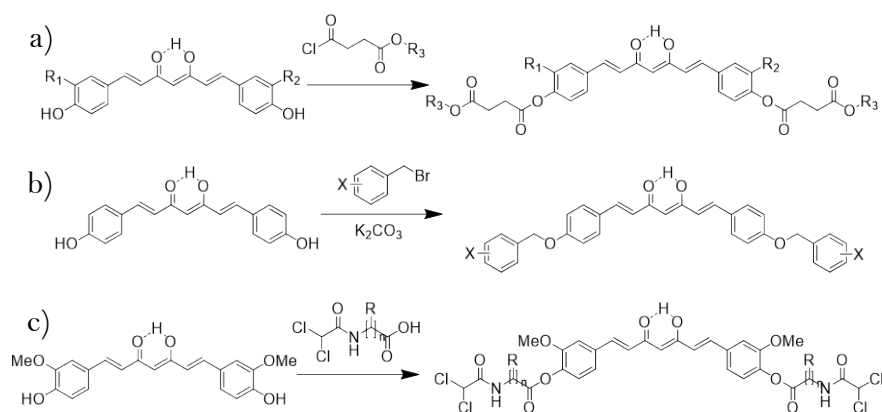


Figure 3.3 Examples of extended CCMoids published in references a) 13 b) 14 and c) 15.

Following this later approach, we conducted our research into the design of CCMoids with molecular endings that allow covalent attachments with a variety of organic compounds with the aim introduced in Chapter 1, of the creation of longer CCMoids for a better contact with graphene electrodes and the measure of their conductance through single CCMoid-graphene junctions.

One of many reactive functional groups available for this purpose is the amino group ( $-\text{NH}_2$ ). Amino derivatives can directly react with aldehydes or ketones giving rise to imines or with acids or acyl chloride to form amides, which are well described reactions <sup>16</sup>. Furthermore, amines can be transformed into diazonium salts, which can be substituted by cyano, alcohol or halide groups <sup>16</sup>. Additionally, they can be oxidised to nitro compounds, can be alkylated by alkyl halides, or transformed into sulphonamides <sup>16</sup>.

The introduction of reactive  $-\text{NH}_2$  groups, into the lateral aromatic rings of the CCMoid, offers the possibility of performing modifications as those mentioned above, for a subsequent extension of the molecule, for the further creation of more robust molecule-graphene interactions for conductance measurements.

## 3.2. Objectives

The main objective of this chapter is the synthesis and complete characterization of a novel CCMoid containing reactive terminal groups in the *para*- positions of the lateral aromatic rings. Therefore, the introduction of amino groups on those positions will be explored. These amino groups will allow future reactions with diverse functionalized molecules in order to enlarge the CCMoid for subsequent application in MEs.



### 3.3. Results and discussion

The use of benzaldehyde molecules is essential in the Pabon's reaction for the synthesis of common CCMoids. In order to achieve the amino terminated CCMoid,  $\text{NH}_2\text{CCMoid}$ , whose structure is shown in Figure 3.4, the *para*-amino benzaldehyde should be used as starting material in the above-mentioned reaction.

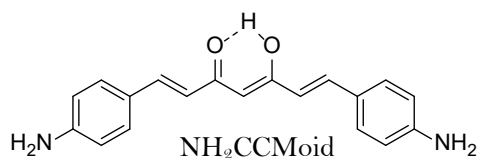
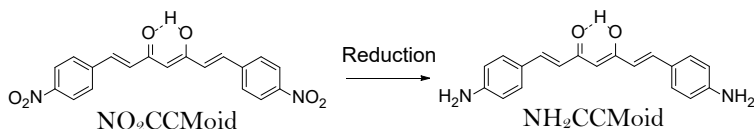


Figure 3.4. Chemical structure of  $\text{NH}_2\text{CCMoid}$ .

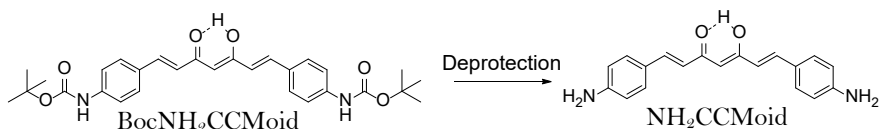
However, amine functional groups can react with aldehydes creating a Schiff base, so it was reasonable to think about the probable reaction between the aldehyde and the amine of the 4-aminobenzaldehyde potentially hindering the formation of the desired CCMoid. Due to this circumstance, together with the fact that regular conditions described in Chapter 1 for the Pabon's synthesis did not provide the desired amino terminated system,  $\text{NH}_2\text{CCMoid}$ , three different strategies represented in Scheme 3.1. were proposed and studied to isolate the amino terminated CCMoid.

The first strategy consisted on the reduction of the nitro-substituted CCMoid,  $\text{NO}_2\text{CCMoid}$ . The second approach involved the Pabon's reaction starting with the protected amine followed by a deprotection step. Finally, the third idea related to the analysis of the direct Pabon's reaction with the crude 4-aminobenzaldehyde but varying the usual conditions, among others, the reaction solvent using DMF instead of EtOAc.

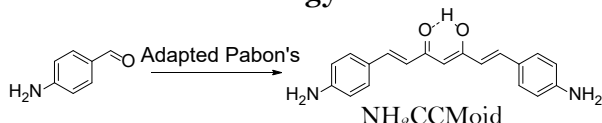
### Strategy 1



## Strategy 2



### Strategy 3



Scheme 3.1. Proposed synthetic routes to isolate NH<sub>2</sub>CCMoid.

### 3.3.1. Strategy 1: Reduction of $\text{NO}_2\text{CCMoid}$ , 2

### 3.3.1.1. Synthesis and characterization of NO<sub>2</sub>CCMoid, 2

NO<sub>2</sub>CCMoid, **2**, whose structure is shown in Figure 3.5, was synthesized by adapting the Pabon's protocol previously explained in Chapter 1 in a 2 % yield. The designed CCMoid comprises two terminal -NO<sub>2</sub> functional groups, that can be reduced to -NH<sub>2</sub> groups.

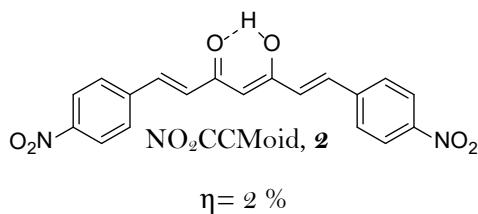


Figure 3.5. Chemical structure of NO<sub>2</sub>CCMoid, **2**.

The proper characterization of compound **2** was elucidated by  $^1\text{H}$  NMR, ATR-FTIR, UV-Vis absorption spectroscopy, elemental analysis and MALDI-TOF mass spectrometry (spectrum shown in Annex III, Figure A3.1).

The successful isolation of compound **2** was confirmed by its  $^1\text{H}$  NMR spectrum in  $\text{CDCl}_3$  depicted in Figure 3.6. It shows the characteristic signals related to the CCMoid skeleton, with the central proton appearing as a singlet close to 6 ppm ( $\text{H}_1$ ). In addition, the doublets related to the *trans* protons of the double bonds of the chain are observed approximately at 6.8 and 7.7 ppm ( $\text{H}_3$  and  $\text{H}_4$ ), with the latter overlapped with one signal corresponding to the aromatics ( $\text{H}_5$ ). The other doublet attributed to the aromatic groups is displayed at 8.3 ppm ( $\text{H}_6$ ). Finally, the proton of the enol is recognised at 15.5 ppm ( $\text{H}_2$ ).

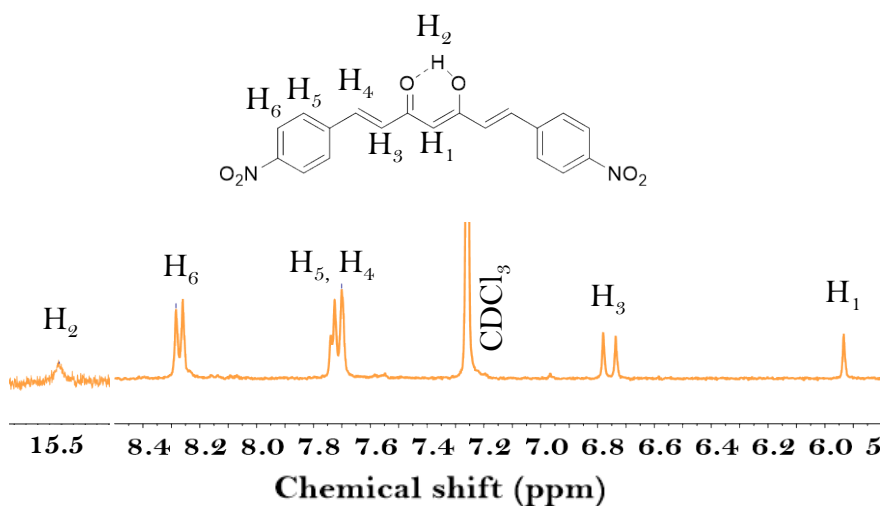


Figure 3.6.  $^1\text{H}$  NMR spectrum of **2** in  $\text{CDCl}_3$ .

The presence of the nitro groups in the CCMoid was corroborated by ATR-FTIR. The obtained spectrum for **2**, shown in Figure 3.7, reveals

the N-O stretching vibrations at  $1342\text{ cm}^{-1}$  and  $1529\text{ cm}^{-1}$  along with the C=O stretching attributed to the keto-enol of the backbone at  $1634\text{ cm}^{-1}$ .

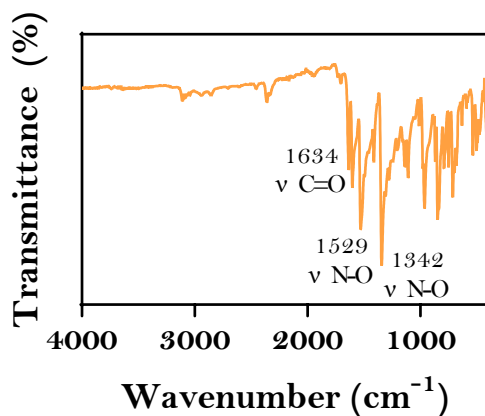


Figure 3.7. ATR-FTIR spectrum of **2**.

The UV-Vis spectrum of **2** in THF is plotted in Figure 3.8. The band related to the  $\pi$ - $\pi^*$  transitions of the CCMoid skeleton is centred at 395 nm, corroborating the CCMoid backbone. In addition, another band with two maxima at 311 nm and 187 nm, related to the substituted benzyl groups, are observed.

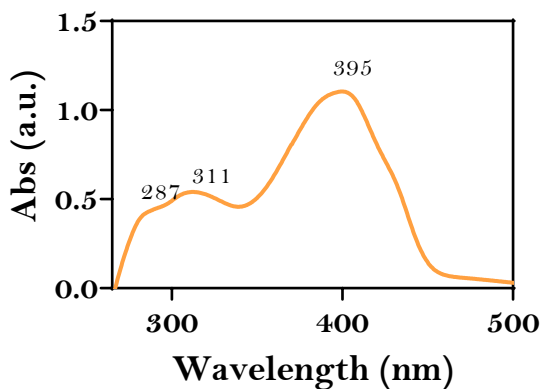


Figure 3.8. UV-Vis absorption spectrum of **2** in THF.

### 3.3.1.2 Reduction of compound **2**

Several methodologies have been reported to reduce  $\text{-NO}_2$  to  $\text{-NH}_2$  functional groups including transition metal catalysed hydrogenations <sup>17</sup>. However, the harsh conditions used could reduce other sensitive functional groups, apart from a possible metal coordination through the keto-enol of the CCMoid.

A free metal reduction procedure was published by Orlandi *et al.* <sup>18</sup> applicable to aliphatic and aromatic nitro compounds. They claimed an efficient reduction of numerous substituted 4-nitrotoluene derivatives by the combination of  $\text{HSiCl}_3$  and a tertiary amine, which leads into a nucleophilic silicon specie able to attack to the nitro group. However, when we applied this process to our  $\text{NO}_2\text{CCMoid}$ , using DCM as solvent and DIPEA as base, we collected pure  $\text{NO}_2\text{CCMoid}$  as product in all our reactions (performed by changing the order of the addition of the reactants). One possible reason for the failure of the procedure could have been the reaction of the chlorosilane through the enol group of the CCMoid, forming a silyl enol ether, which could have been hydrolyse to a carbonyl group, recovering the starting CCMoid.

A second widely used reducing agent for  $\text{-NO}_2$  groups in presence of other functionalities is  $\text{SnCl}_2$ . Until 1984, all the nitro reduction reactions involving  $\text{SnCl}_2$  were performed in acid catalysed media. That year, Bellamy *et al.* <sup>19</sup> found that  $\text{SnCl}_2$  transformed  $\text{-NO}_2$  in  $\text{-NH}_2$  in organic solvents as alcohol or ethyl acetate without any catalyst in yields higher than 90 %.

In spite of the poor solubility of compound **2** in EtOH, several reduction attempts were made in presence of an excess of  $\text{SnCl}_2$  under reflux <sup>20,21</sup> giving rise always to an impure amino substituted product. The  $^1\text{H}$  NMR spectra of  $\text{NO}_2\text{CCMoid}$  and the reduced  $\text{NO}_2\text{CCMoid}$  in  $\text{CDCl}_3$  are displayed in Figure A.3.2 (see Annex) It is noticeable the shift of all the

CCMoid signals to higher fields in the reduced NO<sub>2</sub>CCMoid, as expected due to the electron donating nature of the -NH<sub>2</sub> group, which increase the electron density giving rise to a higher shielding effect. Apart from the signals attributed to the reduced NO<sub>2</sub>CCMoid, numerous peaks were detected. The most recognisable one appears at 9.72 ppm, that along with the doublet at 7.68 ppm and the smallest overlapped at 6.69 ppm, corresponds to 4-aminobenzaldehyde. Due to the lack of 4-nitrobenzaldehyde signals in the initial NO<sub>2</sub>CCMoid <sup>1</sup>H NMR spectrum, the presence of 4-aminobenzaldehyde in the final mixture suggests the breaking of the NH<sub>2</sub>CCMoid under the conditions used, indicating the methodology employed was not the optimal one for the synthesis of NH<sub>2</sub>CCMoid. The rest of the peaks in the spectra could not be assigned.

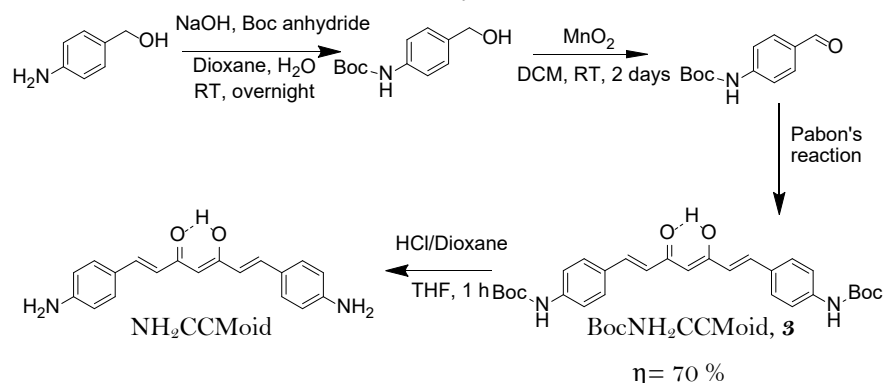
### **3.3.2. Strategy 2: Protection/Deprotection of -NH<sub>2</sub> groups**

#### **3.3.2.1. Synthesis and characterization of BocNH<sub>2</sub>CCMoid, **3****

The second strategy above mentioned, consisted on the study of the Pabon's reaction starting with the protected amine followed by a deprotection step to obtain NH<sub>2</sub>CCMoid. It was proposed in order to avoid the possible reaction between the free amino and aldehyde groups present in 4-aminobenzaldehyde.

t-Butyl carbamate, commonly known as Boc, is extensively used in the protection of amines owing to the easy formation and cleavage in acidic conditions expelling only t-BuOH and CO<sub>2</sub> as by-products <sup>22</sup>. Therefore, it was selected as protecting group to perform the desired reactions. The synthesis of the Boc protected CCMoid, BocNH<sub>2</sub>CCMoid, **3**, represented

in Scheme 3.2, was carried out in three steps <sup>23</sup>. The route started with the protection of the amino groups of 4-aminobenzyl alcohol with Boc anhydride under basic conditions. Subsequently, the alcohol group of the protected starting material was oxidised into aldehyde in presence of freshly synthesized  $\text{MnO}_2$ . Finally, compound **3** was isolated by applying a modified Pabon's reaction in a 70 % yield.



Scheme 3.2. Protocol applied for the synthesis of  $\text{NH}_2\text{CCMoid}$ , by deprotection of  $\text{BocNH}_2\text{CCMoid}$ , **3**.

The oxidation step using  $\text{MnO}_2$  was a critical stage in the process, as the efficiency of the reaction depends on several factors, such as the particle size, the solvent involved and the type of  $\text{MnO}_2$  used, mainly because the oxidation reaction takes places on the surface of the  $\text{MnO}_2$  <sup>24</sup>. To obtain a satisfactory reaction, the solvent should not deactivate the oxide, either by solubilising it or adsorbing its molecules onto the oxide surface, avoiding the adsorption of the alcohol, and therefore preventing the reaction. The importance regarding the kind of  $\text{MnO}_2$  used derives in the oxidising power which is affected by the formation methodology. The oxidation ability of a commercial  $\text{MnO}_2$  was tested twice: as received and after activation by drying it into the oven at 110 °C for 3 days, but no successful results were obtained. Finally, the  $\text{MnO}_2$  used in this thesis, which was reported as a suitable option <sup>25</sup>, was freshly synthesized by a redox reaction

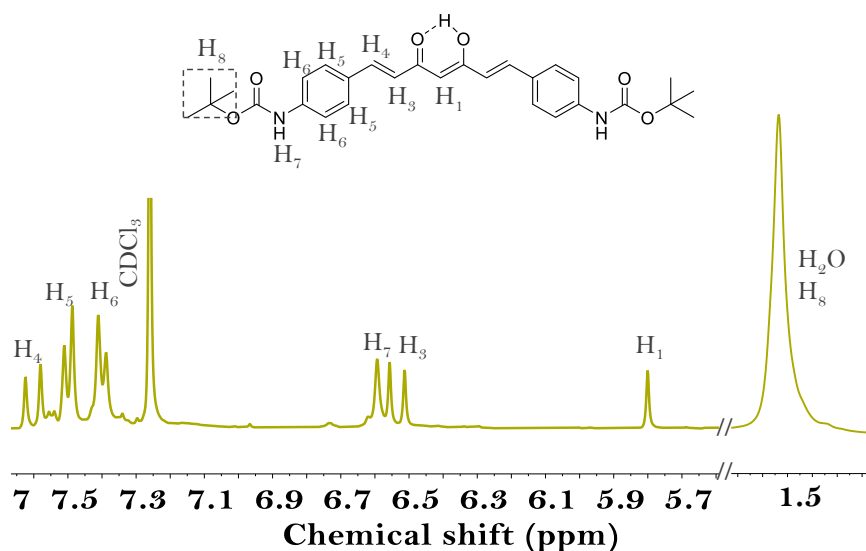
between  $\text{MnSO}_4$  and  $\text{KMnO}_4$  in a basic aqueous media followed by a drying process of 3 days at 110 °C.

After the achieving of the Boc-protected aldehyde, the next step was to synthesize the CCMoid. In his work related to the synthesis of CCM<sup>26</sup>, Pabon evaluated several solvents, bases and drying agents to reveal that the optimal conditions for the isolation of CCM was using EtOAc, *n*-butylamine and tributyl borate. The use of the same reactants has been demonstrated to be effective for the isolation of different CCMoids. Therefore, they were tested in the synthesis of compound **3**, obtaining Boc protected aldehyde as a product of the reaction in all the experiments carried out. Finally, the reaction worked successfully by changing the solvent from EtOAc to DMF due to better solubility of the reactants and by slightly modifying some ratios between the reagents 1.8:1 aldehyde:ACAC instead of 2:1, as Ferrari *et al.* reported<sup>27</sup>.

The chemical structure of compound **3** was confirmed by <sup>1</sup>H NMR, ATR-FTIR, UV-Vis, elemental analysis and MALDI-TOF mass spectrometry (spectrum shown in Figure A3.3, Annex III).

The formation of compound **3** was corroborated through the <sup>1</sup>H NMR spectrum in  $\text{CDCl}_3$ , represented in Figure 3.9, which displayed the distinctive signals related to the CCMoid structure. The central proton ( $\text{H}_1$ ) appears as a singlet at approximately 5.8 ppm. Furthermore, the doublets related to the *trans* protons of the double bonds of the chain ( $\text{H}_3$  and  $\text{H}_4$ ) are evidenced around 6.5 and 7.6 ppm, respectively. The doublets attributed to the aromatics ( $\text{H}_5$  and  $\text{H}_6$ ) are shown at 7.4–7.5 ppm. Finally, the proton of the amide group created in the protection step ( $\text{H}_7$ ) is observed as a singlet at 6.6 ppm and the methyl groups of the Boc were not identified due to its overlapping with the water signal at 1.56 ppm.



Figure 3.9.  $^1\text{H}$  NMR spectrum of compound **3** in  $\text{CDCl}_3$ .

The ATR-FTIR analysis evidenced the presence of the Boc group in compound **3** as demonstrated in Figure 3.10. The peaks at  $1154\text{ cm}^{-1}$ ,  $1713\text{ cm}^{-1}$  and  $2976\text{ cm}^{-1}$  were attributed to the tert-butyl group, the amide bond and the terminal methyl groups of the Boc respectively<sup>28</sup>. Besides, the  $\text{C}=\text{O}$  stretching assigned to the keto-enol of the backbone was distinguished at  $1623\text{ cm}^{-1}$ .

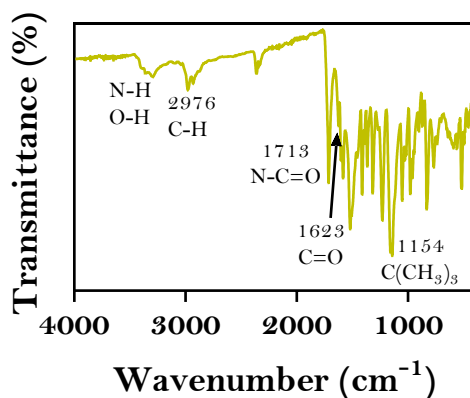
Figure 3.10. ATR-FTIR spectrum of CCMoid **3**.

Figure 3.11 displays the UV-Vis absorption spectrum of compound **3** in THF. The typical CCMoid pattern was observed with the band assigned to the  $\pi$ - $\pi^*$  transitions of the skeleton at 419 nm and the band corresponding to the substituted benzyl rings at 283 nm.

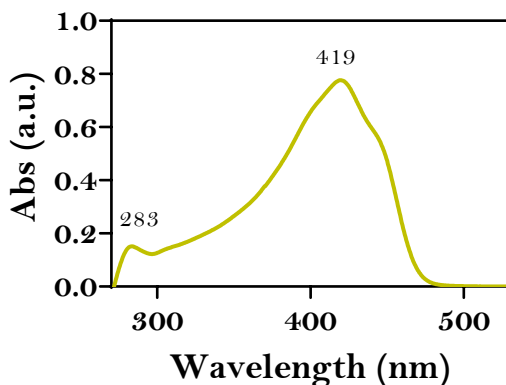


Figure 3.11. UV-Vis absorption spectrum of compound **3** in THF.

### 3.3.2.2. Deprotection of compound **3**

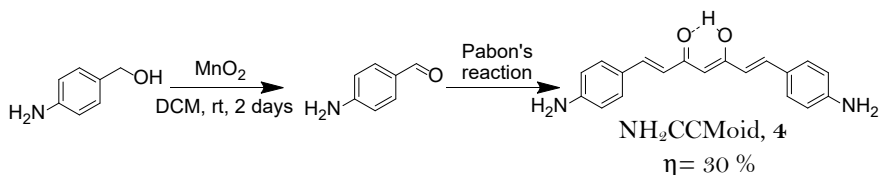
To remove the Boc group, HCl/dioxane was employed after dissolving compound **3** in THF. The reproducibility of the products from several reactions was analysed via  $^1\text{H}$  NMR and the spectrum is presented in Figure A3.4 (see Annex). Although some signals associated with the CCMoids were recognizable in the spectrum, such as the central proton at 5.62 ppm, a doublet of the *trans* protons, at 6.39 ppm, and finally a broad signal of the enol group at 15.47 ppm, the signals of the aromatics and the second doublet attributed to the *trans* protons were overlapped and undistinguishable in the region between 7.56 and 7.34 ppm. Additionally, what appear to be impurities containing aromatic and aliphatic groups were obtained as by-products of the reactions. TLC plates revealed several spots with similar  $R_f$  values in different mobile phases, being difficult the purification of the systems. As a consequence, the ambiguous and impure

spectrum obtained suggested the conditions employed were not favourable for these experiments.

### 3.3.3. Strategy 3: Direct synthesis of NH<sub>2</sub>CCMoid, **4**

#### 3.3.3.1 Synthesis and characterization of NH<sub>2</sub>CCMoid, **4**

The third alternative introduced at the beginning of this section included the investigation of the direct synthesis of NH<sub>2</sub>CCMoid, **4** using a variation of Pabon's method first reported by Ferrari *et al.* <sup>27</sup>. The achievement of the CCMoid was accomplished following the Pabon's reaction using 4-aminobenzaldehyde after the oxidation of the alcohol group of 4-aminobenzyl alcohol into an aldehyde in presence of freshly synthesized MnO<sub>2</sub> <sup>23</sup>, as Scheme 3.3 indicates.



Scheme 3.3. Synthetic route of compound **4**.

Here, the synthetic pathway of compound **4** requires careful consideration of two crucial parameters: the MnO<sub>2</sub> used for the oxidation (as it has been explained in detail above) and the solvent of the Pabon reaction. Identically as in strategy 2, the MnO<sub>2</sub> was freshly synthesized before every oxidation reaction and the choice of solvent for the Pabon reaction proved to be critical.

When using EtOAc, the resulting mixture was very contaminated with several products, including ACAC, aldehyde and two other unidentified structures that presents a keto-enol moiety in their structure due to the observance of three different broad signals around 16 ppm in the  $^1\text{H}$  NMR spectrum (Figure A3.5, Annex III). Besides, the aromatic region displays six doublets attributed to aromatic protons and three doublets assigned to *trans* protons. Furthermore, several signals were also observed in the area where the central proton of the CCMoid appears, suggesting the possible existence of various CCMoids. Finally, the reaction between the aldehyde and the amino groups of the molecule was not discarded due to the presence of a weak singlet at 10.20 ppm that could be assigned to the amide bond created after their reaction. Recrystallization and washing processes with MeOH and ACN were conducted in order to isolate some compounds, with no successful results.

While EtOAc results in a messy combination of compounds, the use of DMF as solvent, as Ferrari *et al.* employed in their synthesis <sup>27</sup>, together with an excess of aldehyde (5:1 aldehyde: ACAC) successfully gave rise to the desired compound **4**, due to a better solubility of the aldehyde in DMF. Following these modifications in the methodology it was possible to achieve compound **4** in a 30 % yield. The system was characterized by  $^1\text{H}$  NMR and  $^{13}\text{C}$  NMR, ATR-FTIR, UV-Vis absorption spectroscopy, electrochemistry (CV, and DPV), elemental analysis and MALDI TOF mass spectrometry (spectrum shown in Figure A3.6, Annex III).

The  $^1\text{H}$  NMR spectrum of **4** in  $\text{CDCl}_3$ , depicted in Figure 3.12, exhibits the usual set of signals distinctive for CCMoids, corroborating its chemical structure. The central proton  $\text{H}_1$  appears as a sharp singlet at 5.73 ppm. The pair of doublets attributed to the double bonds of the conjugated chain,  $\text{H}_3$  and  $\text{H}_4$ , are shown at 7.59 and 6.45 ppm, in that order. Close to these signals, the peaks of the aromatic protons  $\text{H}_5$  and  $\text{H}_6$  of the arms emerged at 7.40 ppm and 6.67 ppm, respectively. Additionally, the proton

related to the enol form,  $H_2$  is observed at 16.22 ppm. Finally, the amino protons of the structure,  $H_7$ , are observed at 3.95 ppm.

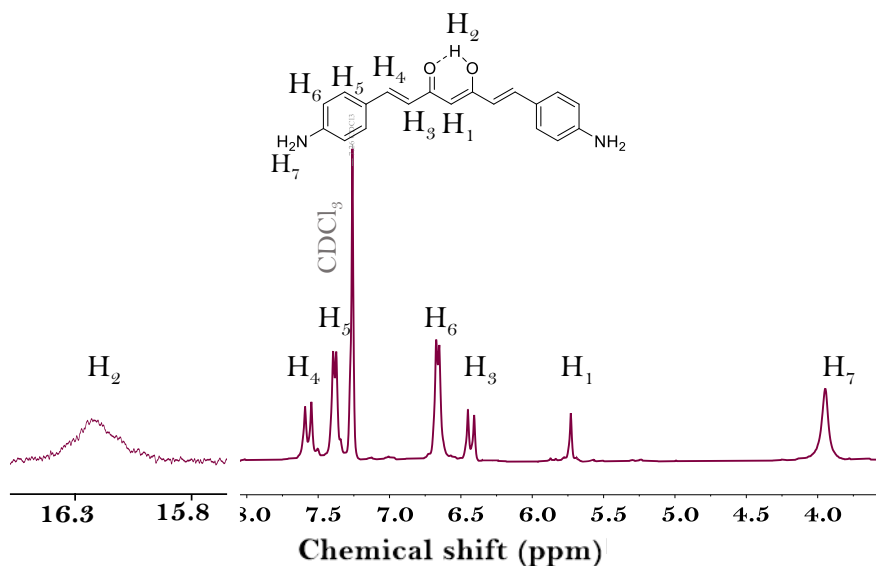


Figure 3.12.  $^1H$  NMR spectrum, in  $CDCl_3$ , of **4** obtained by the modified version of Pabon's reaction in DMF.

The displacements observed in the  $^{13}C$  NMR spectra for CCMoids are also very informative and characteristic of this family of molecules. The presence of the keto-enol form is revealed by the detection of the signal attributed to the central carbon ( $C_1$ ) approximately at 100 ppm. The other most recognizable signal is the one attributed to the carbonyl region of the keto-enol ( $C_2$ ), which appears at lower fields, between 180 and 200 ppm. Both carbons show a unique signal due to the efficient interconversion of the diketone and keto-enol form. The rest of signals which correspond to the double bonds in the chain ( $C_3$  and  $C_4$ ) and aromatic carbons of the arms ( $C_5$ - $C_8$ ) are shown between 110 and 170 ppm being the aromatic ones the most intense.

In the particular case of compound **4**, whose  $^{13}\text{C}$  NMR in  $\text{CDCl}_3$  is assigned in Figure 3.13, all the signals appear in the expected areas but, the peak of the central carbon  $\text{C}_1$ , was not distinguishable from the baseline noise, probably due to the partial solubility of the big amount needed for the analysis. The possibility of having the diketo tautomer of the CCMoid was also discarded due to the absence of the signal corresponding to  $\text{C}_1$ , which is estimated to appear for the diketo form around 50–60 ppm.

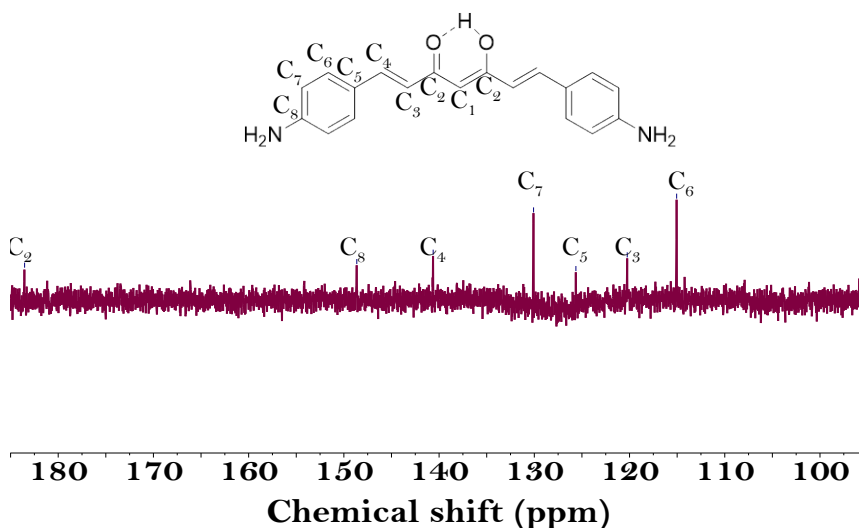


Figure 3.13.  $^{13}\text{C}$  NMR spectrum of **4** in  $\text{CDCl}_3$ .

The ATR-FTIR spectrum of **4** is shown in Figure 3.14. The characteristic stretching vibration of the carbonyl moiety  $\text{C}=\text{O}$  of the keto-enol component was observed at  $1617\text{ cm}^{-1}$ . In addition, the presence of primary amine moieties in the product was confirmed by the exhibition of the double band at  $3457$  and  $3347\text{ cm}^{-1}$  attributed to the  $\text{N-H}$  stretching vibration, together with the signal at  $1279\text{ cm}^{-1}$  corresponding to the  $\text{C-N}$  vibrations.

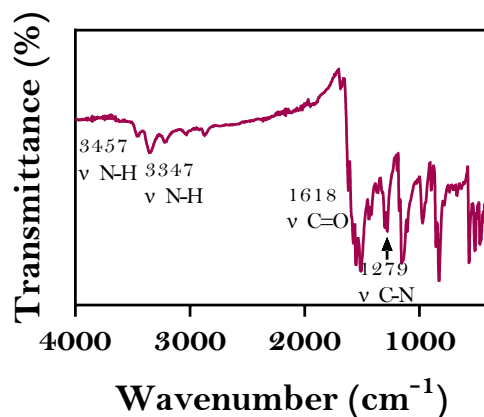


Figure 3.14. ATR-FTIR spectrum of compound **4**.

To extract the electronic information of the CCMoid including the band gap of compound **4**, UV-Vis absorption and electrochemical experiments were carried out.

The UV-Vis spectrum of compound **4** was measured in THF and is displayed in Figure 3.15. The maximum absorbance of the band related to the  $\pi$ - $\pi^*$  transition assigned to the backbone was reached at 452 nm. At higher energies, three weak bands appeared at 254, 283 and 315 nm, respectively, which correspond to the amino substituted phenyl groups.

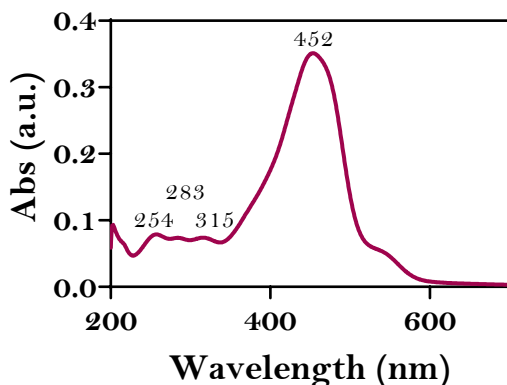


Figure 3.15. UV-Vis absorption spectrum of **4** in THF.

As CCMoids present solvochromic character, the optical bandgap of **4** was calculated from the Tauc's equation (Eq 2.2 in Chapter 2) applied to the UV-Vis absorption spectrum obtained in solid state by measuring a pellet of 0.1 mg of the CCMoid mixed with 200 mg of KBr.

As Figure 3.16 a shows, the solid-state spectrum of **4** displays negligible shifts on the maximum absorbance wavelength compared to the solution spectrum. By applying the Tauc's equation and plotting the Tauc's chart in Figure 3.16 b,  $E_{\text{gop}}$  of compound **4** was determined to be 1.96 eV indicating a semiconductor behaviour.

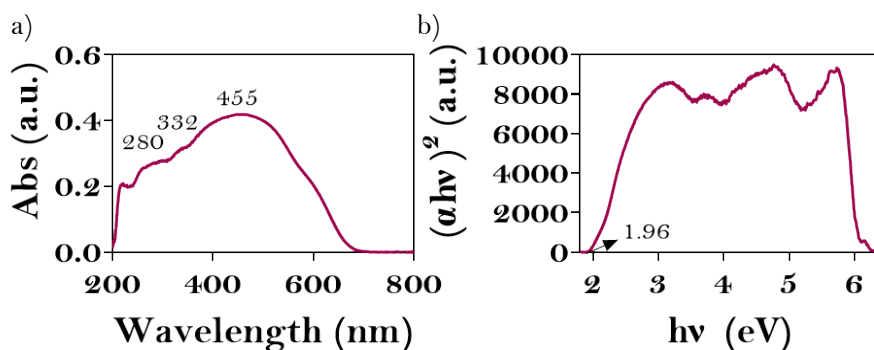


Figure 3.16. a) UV-Vis absorption spectrum of **4** in solid state. b) Tauc's representation of the UV-Vis spectrum of **4** in solid state.



CV and DPV experiments were conducted in order to analyse the redox behaviour of compound **4** and to obtain information about its bandgap, HOMO and LUMO levels. The experiments were carried out with the conditions detailed in Chapter 2.

Figure 3.17 a presents the CV of compound **4** which exhibit a series of four reduction processes and one irreversible oxidation wave in the voltammogram. In order to study the possible reversibility of the reduction processes, a set of experiments were performed at different scan rates, from 50 to 1000 mV/s.

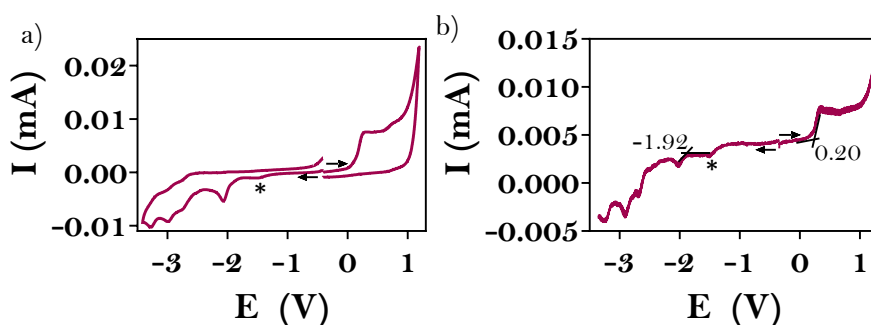


Figure 3.17. Oxidation and reduction CVs (a) and DPVs (b) voltammogram of compound **4**. \* Impurity.

For the reduction processes, several parameters of the resulting voltammogram were analysed as: (i) the ratio between the anodic to cathodic intensities ( $I_{pa}/I_{pc}$ ), (ii) the difference among the redox potential ( $\Delta E_p$ ) and (iii) the relationship of the maximum current and the square root of the scan rate. A process is considered as a reversible if the ratio between  $I_{pa}/I_{pc}$  is close to 1,  $\Delta E_p$  is smaller than 59 mV, for aqueous solutions, or finally, whether there is a linear regression between the maximum current reached and the square root of scan rate, according to the Randles-Sevcik equation <sup>29</sup>.

The graph of the first reduction wave of **4** at different scan rates is displayed in Figure 3.18 a. The calculated parameters  $\Delta E_p$  deviate from the references values as Table 3.1 shows. However, since the studies were carried out in an organic media, the ideal 59 mV separation between the redox potential cannot be considered a reliable requirement to be fulfilled. Despite of these results,  $I_{pa}/I_{pc}$  ratio is close to 1 for the common scan rates used ( from 50 to 250) and the Randles-Sevcik equation displays a linear relationship between the plotted parameters in Figure 3.18 b. Therefore, the first reduction process of  $NH_2CCMoid$  can be described as a quasi-reversible step under the explored conditions. Unfortunately, the next reduction process did not fulfil any criteria for a reversible process.

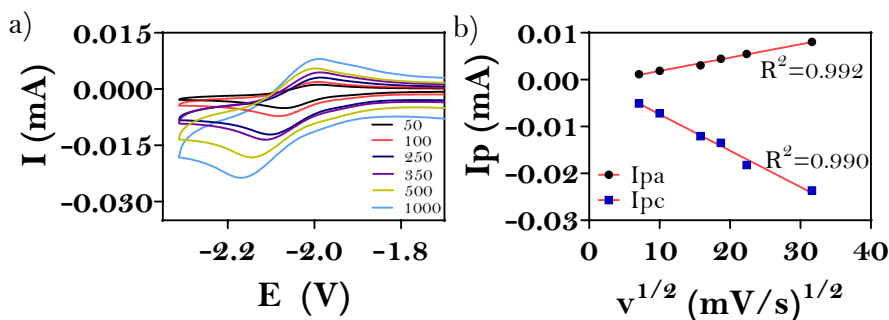


Figure 3.18. a) First reduction wave of compound **4** recorded at several scan rates. b) Graphical representation of the maximum intensity *vs.* the square root of the scan rate for the anodic and cathodic peaks.

Scan rate (mV/s)	I <sub>pa</sub> /I <sub>pc</sub>	ΔE <sub>p</sub> (mV)
<b>50</b>	1.03	90
<b>100</b>	1.12	90
<b>250</b>	1.21	110
<b>350</b>	1.30	140
<b>500</b>	1.39	150
<b>1000</b>	1.66	180

Table 3.1. Division of the anodic and cathodic maximum intensities and potential values differences for the oxidation and reduction processes at different scan rates.

The DPV graph, depicted in Fig 3.17 b, was used to calculate the approximated values of the HOMO and LUMO levels according to the Equations indicated in Chapter 2.

Table 3.2 collects the HOMO, LUMO and the E<sub>g</sub> estimated values. The extracted bandgap for **4** was 2.12 eV, which roughly coincides with the optical bandgap value of 1.96 eV obtained from the UV-Vis absorption experiment. These two values indicate that the HOMO-LUMO energy may be estimated at around 2.0-2.1 eV corroborating its semiconducting behaviour.

<b>E onset ox</b> (V)	<b>Eonset red</b> (V)	<b>E HOMO</b> (eV)	<b>E LUMO</b> (eV)	<b>E<sub>g</sub></b> (eV)
0.20	-1.92	-5.00	-2.88	2.12

Table 3.2. Potential values for oxidation and reduction, HOMO, LUMO and electrochemical bandgap of compound **4**.

### 3.3.3.2 Synthesis and characterization of hemiNH<sub>2</sub>CCMoid, **5**

Our studies, and others, show that the ratio between the aldehyde and the ACAC in the CCMoid formation is a decisive parameter in the symmetry of the resulting CCMoid <sup>13,26,27,30–32</sup>. In the synthesis of symmetric CCMoids, stoichiometrically 4 equivalents of aldehyde are needed for 2 equivalents of ACAC according to the reaction mechanism, although it was demonstrated that 3.6:2 ratio is enough to obtain the desired symmetric CCMoid <sup>27</sup>.

Theoretically, decreasing the proportion aldehyde:ACAC in the reaction to 2:2, it should be possible to achieve hemiCCMoids, that possess only one arms of the conjugated skeleton, remaining the other side as a -CH<sub>3</sub> group. These compounds are also interested because they can serve as starting materials in the preparation of assymetric CCMoids, which have different moieties in both arms, and therefore to combine two functionalities in one CCMoid. Kim *et al.* <sup>30</sup> isolated boron difluoride complexes of hemiCCMoids with 1:1 ratio of the reactants and Pedersen *et al.* <sup>31</sup> employed the same proportion for the synthesis of asymmetric CCMoids. Other studies <sup>13</sup> have reported lower rates of equivalents, 1:4 (aldehyde:ACAC) or even 1:5, to obtain hemi or asymmetric CCMoids in good yields.

However, in this work, hemiNH<sub>2</sub>CCMoid, **5**, shown in Figure 3.19, was extracted during the workup of the symmetric NH<sub>2</sub>CCMoid reaction, where 5 equivalents of aldehyde were mixed with 1 equivalent of ACAC in DMF. When the reaction was finished, after the water addition to break the boron complex, a filtration step was required to isolate the symmetric NH<sub>2</sub>CCMoid. In that step, NH<sub>2</sub>CCMoid remained as a solid on the filtering paper whereas in the filtered solution, a fine solid was observed, which was isolated by centrifugation in a 8 % yield and identified as

hemiNH<sub>2</sub>CCMoid, **5**, opening the possibilities for new extended asymmetric CCMoids.

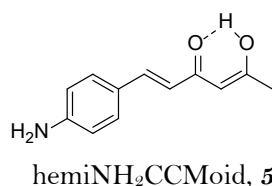


Figure 3.19. Chemical structure of compound **5**.

The identification of **5** was accomplished by <sup>1</sup>H and <sup>13</sup>C NMR, ATR-FTIR, UV-Vis, electrochemistry, elemental analysis and MALDI-TOF experiments (spectrum shown in Figure A3.7, Annex III).

<sup>1</sup>H NMR verified the formation of compound **5**, whose spectrum in CDCl<sub>3</sub> is displayed in Figure 3.20. The spectrum provided by the hemiCCMoid (in blue) is similar to the obtained for compound **4** (in garnet color). However, the main difference which is important to highlight is the noticeable presence of an intense singlet at 2.14 ppm attributed to the methyl terminal groups of the monosubstituted compound. Furthermore, there is a modest shift of the backbone pattern to higher fields in the spectrum of **5** owing to the lack of conjugation on one side compared to the symmetric CCMoid that implies a high shielding of the molecules protons.

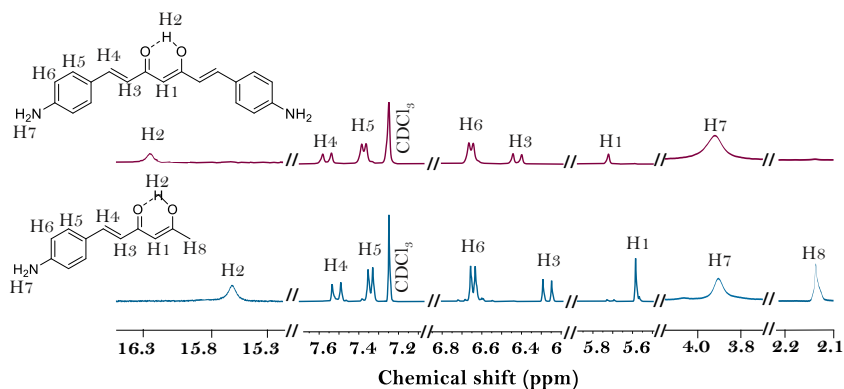


Figure 3.20. Comparison between  $^1\text{H}$  NMR spectra of **4** and **5** in  $\text{CDCl}_3$ .

The  $^{13}\text{C}$  NMR spectra in  $\text{CDCl}_3$  of the hemi and symmetric  $\text{NH}_2\text{CCMoid}$  are compared in Figure 3.21. Both present many similarities although there are some noticeable changes. The most significant one which confirms the presence of the hemiCCMoid, is the appearance of the signal around 30 ppm, corresponding to the carbon of the methyl terminal group,  $\text{C}_9$ , in compound **5**. Another important change, is the upshift of the carbonyl  $\text{C}_2$  signal over 190 for the hemiCCMoid. The non-substituted aromatic carbons,  $\text{C}_6$  and  $\text{C}_7$ , do not suffer any significant difference, whereas the aromatic carbon bonded to the conjugated chain,  $\text{C}_5$ , along with  $\text{C}_3$ , are downshifted. In this case, the carbon linked to the amine group,  $\text{C}_8$  is not distinguishable.

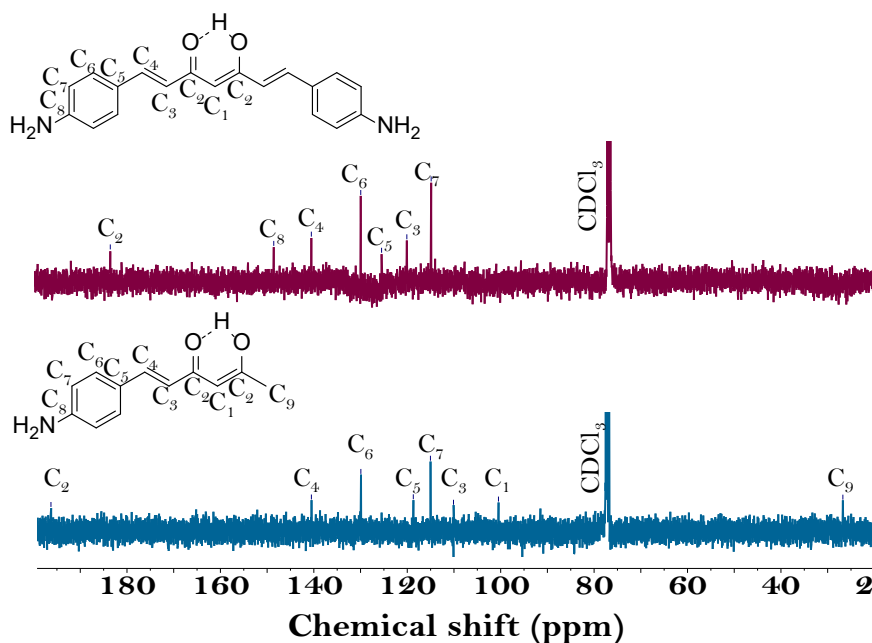


Figure 3.21. Comparison of the  $^{13}\text{C}$  NMR spectra of **4** and **5** in  $\text{CDCl}_3$ .

The ATR-FTIR spectrum of compound **5**, displayed in Figure 3.22, closely resembles that of **4**. The characteristic vibrations identified for **4** were equally detected for system **5**, which is not surprising because all the functional groups presented in **4** are also comprised in the latter. However, the recognition of the methyl terminal group in **5**, which is the only distinct group between **4** and **5** was not achieved by ATR-FTIR, probably overlapped in the area of  $2900\text{ cm}^{-1}$ .

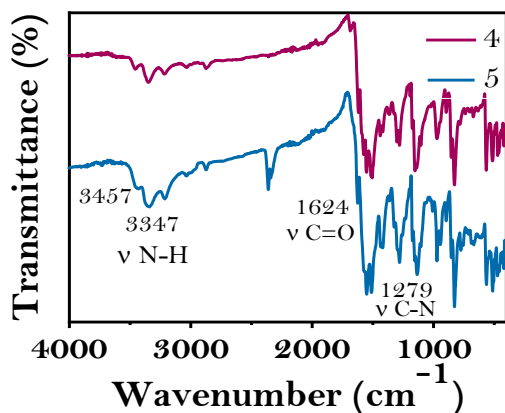
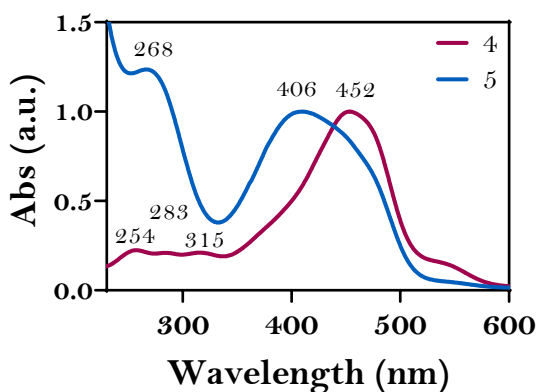
Figure 3.22. ATR-FTIR spectrum of compound **5**.

Figure 3.23 shows a comparison between the UV-Vis absorption spectra of compound **4** and **5** in THF. The spectrum of **5** is characterized by a hypsochromic shift of the band related to the backbone from 452 nm, for **4**, to 406 nm, for **5**. This trend attributed to the missing effect of the extended  $\pi$  conjugated part (symmetric CCMoids), coincides with previous works reported <sup>30</sup>. At higher energies, 268 nm respectively, the bands which correspond to the amino substituted phenyl group appeared.

Figure 3.23. Comparison of the UV-Vis spectra of **4** and **5** in THF.



Similar to some previous examples, the solid-state UV-Vis absorption spectrum data is used to calculate and represent the Tauc's plot for estimating the optical bandgap of the compound. Figure 3.24 a, shows the solid-state UV-Vis plot for **5** which displays the two bands slightly displaced compared to the solution spectrum. Applying the Tauc's equation (Eq 2.2 in Chapter 2) we obtained the Tauc's graph (Figure 3.24 b) and consequently the  $E_g$  value, which is 1.94 eV. This value is similar to the obtained for compound **4**, 1.96 eV, which implies that both compounds can be categorized as semiconductor systems as well.

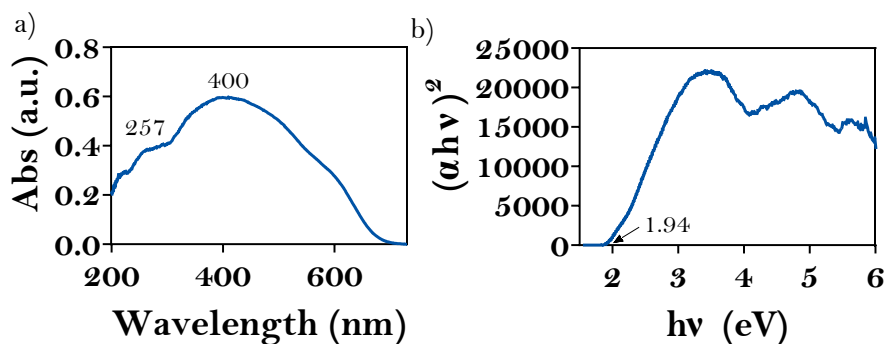


Figure 3.24. a) UV-Vis absorption spectrum of **5** in solid state. b) Tauc's representation of the UV-Vis spectrum in solid state of **5**.

CV and DPV measurements were conducted under the same conditions as for compound **4** to acquire data on the bandgap, HOMO and LUMO levels of compound **5**.

Two reduction and one oxidation processes are observed in the CV voltammogram of compound **5**, exhibited in Figure 3.25 a. The reversible reduction behaviour of compound **5** was analysed estimating the previously mentioned parameters.

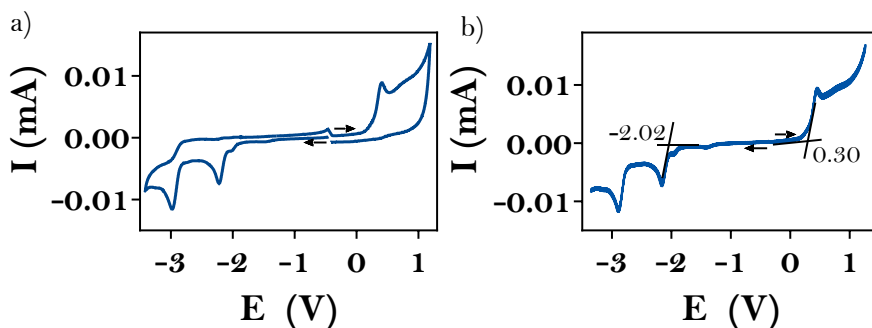


Figure 3.25. Oxidation and reduction CVs (a) and DPVs (b) voltammogram of compound **5**.

The first intense reduction wave of compound **5** at different scan rates is represented in Figure 3.26 a. The determined parameters for  $I_{pa}/I_{pc}$  and  $\Delta E_p$  do not approach the ideal values as Table 3.3 collects. Nevertheless,  $I_{pa}$  and  $I_{pc}$  present a linear dependence on the scan rate, as Figure 3.26 b shows. Hence, the first reduction process of hemiNH<sub>2</sub>CCMoid can be described as a quasi-reversible step under the explored conditions, as it happens with the symmetric homologous. However, the next reduction process fails to meet the requirements to be considered as a reversible process.

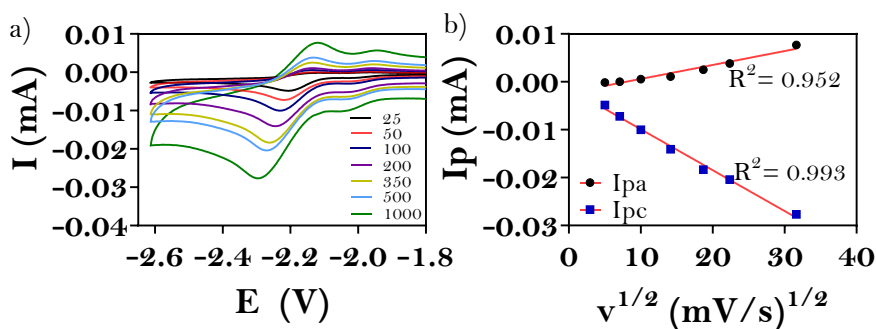


Figure 3.26. a) First reduction wave of compound **5** recorded at several scan rates. b) Graphical representation of the maximum intensity *vs.* the square root of the scan rate for the anodic and cathodic peaks.

Scan rate (mV/s)	I <sub>pa</sub> /I <sub>pc</sub>	ΔE <sub>p</sub> (mV)
<b>25</b>	0.44	90
<b>50</b>	0.40	90
<b>100</b>	0.38	90
<b>200</b>	0.47	120
<b>350</b>	0.47	120
<b>500</b>	0.47	140
<b>1000</b>	0.66	180

Table 3.3. Division of the anodic and cathodic maximum intensities and potential values differences for the oxidation and reduction processes at different scan rates.

The DPV graph, shown in Fig 3.25 b, was utilized to estimate the HOMO and LUMO levels according to the equations outlined in Chapter 2. The values are collected in Table 3.4. The bandgap calculated for **5** was 2.32 eV, which is not approximately consistent with the optical bandgap value estimated from the UV-Vis experiment that was 1.94 eV, however the electrochemical gap is more in the line with the changes observed in the NMR experiments, where the displacement of the signals indicates that the hemiCCMoid, **5** presents lower conjugation features than NH<sub>2</sub>CCMoid, **4**.

E onset ox (V)	Eonset red (V)	E HOMO (eV)	E LUMO (eV)	E <sub>g</sub> (eV)
0.30	-2.02	-5.10	-2.78	2.32

Table 3.4. Potential values for oxidation and reduction, HOMO, LUMO and electrochemical bandgap of compound **5**.

Nevertheless, according to the electrochemical estimation, compounds **4** and **5** present a similar gap being slightly smaller for NH<sub>2</sub>CCMoid. Besides, the representation of the energy distribution for **4** and **5**, shown in Figure 3.27, implies a similar donor-acceptor behaviour of both systems. One could expect higher variations regarding the value and wide of the energy gap between the two molecules. However, their similarity shows the relevance of the nature of the arms of the CCMoids, and how it can modulate their electronic behaviour. From our results we observed that the -NH<sub>2</sub> group provides smaller HOMO-LUMO gaps than other systems reported in the literature <sup>33,34</sup>, pointing out this fact.

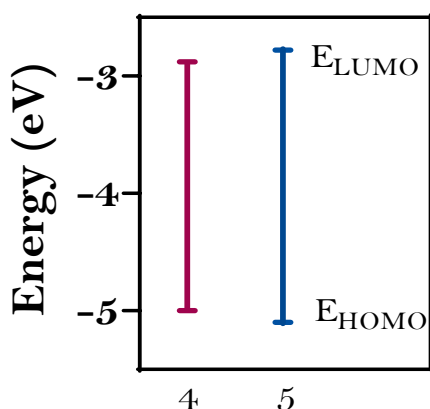


Figure 3.27. Schematic diagram for HOMO and LUMO energy levels of compound **4** and **5**.

## 3.4. Conclusions

- Two new amino CCMoids were isolated and characterized, the symmetric  $\text{NH}_2\text{CCMoid}$ , **4**, and the hemi $\text{NH}_2\text{CCMoid}$ , **5**.
- Three different strategies were explored for the achievement of compound **4**, however, only the varied Pabon's reaction using 5 equivalents of aldehyde and DMF as solvent allowed to obtain the desirable CCMoid.
  - The low yield of the nitro derivative  $\text{NO}_2\text{CCMoid}$ , **2**, together with the impure compound **4**, obtained after reduction of **2**, caused the development of different routes to prepare the final CCMoid.
  - The impossibility of the Boc cleavage with the tested conditions resulted on the abandon of the second protocol, which implied the Pabon's reaction with Boc protected 4-aminobenzaldehyde.
- The synthetic process employed for the preparation of compound **4** allowed the obtention of the hemiCCMoid, compound **5**.
- The lack of one conjugated side in the hemi $\text{NH}_2\text{CCMoid}$ , affects to the appearance of the signals in  $^1\text{H}$  NMR and UV-Vis spectra, shifted to higher fields in the former and blue shifted in the latter, respectively, compared to the symmetric  $\text{NH}_2\text{CCMoid}$ .
- The absence of one arm in the hemi $\text{NH}_2\text{CCMoid}$  seems not to influence significantly in the electrical behaviour of the CCMoid, presenting both CCMoids, **4** and **5**, a reasonable semiconductor behaviour, with the electrochemical bandgap of compound **4** being slightly smaller.

## 3.5. Experimental section

### Synthesis of NO<sub>2</sub>CCMoid, 2

0.34 mL of ACAC (3.31 mmol) and 0.16 g of B<sub>2</sub>O<sub>3</sub> (2.31 mmol) were mixed in 1.4 mL EtOAc at 60 °C. In parallel, to dissolve the aldehyde, 1.00 g of 4-nitrobenzaldehyde (6.62 mmol) was mixed with 3 mL of EtOAc and stirred at 60 °C. 1 hour later, the aldehyde solution and 3.57 mL tributylborate (13.23 mmol) were added into the initial mixture, and the temperature maintained for 2 h. After cooling down to RT, a solution of 0.25 mL of butylamine (2.48 mmol) in 2 mL EtOAc was added into the flask. The final reaction was stirred at room temperature for 2 days. Then, the precipitate was filtered and washed with EtOAc. Next, the isolated solid was mixed with Milli-Q and stirred overnight. Finally, the NO<sub>2</sub>CCMoid product was obtained as a yellow solid in 2% after filtration, washing with Milli-Q water and drying with Et<sub>2</sub>O. <sup>1</sup>H NMR (360 MHz, CDCl<sub>3</sub>) δ: 15.55 (1H, s) 8.28 (4H, d, <sup>3</sup>J=8.7 Hz), 7.74 (6H, m) 6.78 (2H, d, <sup>3</sup>J= 15.9 Hz), 5.93 (1H, s). Elemental analysis calcd for C<sub>19</sub>H<sub>14</sub>N<sub>2</sub>O<sub>6</sub> · 0.1 C<sub>4</sub>H<sub>8</sub>O<sub>2</sub> · 0.15 H<sub>2</sub>O: C: 61.67 %; H: 4.03 %; N 7.41%; O: 26.89 %, found: C 61.67 %; H 3.97 %; N: 7.44 %; O: 26.92 %; MS MALDI-TOF (m/z) calcd for NO<sub>2</sub>CCMoid: 366.3 [M<sup>+</sup>]; found: 365.2 [M-1].

### Synthesis of MnO<sub>2</sub><sup>35</sup>.

MnSO<sub>4</sub> (11.5 g, 68.0 mmol in 20 mL Milli-Q water) and NaOH (14 g, 350 mmol in 16.5 mL Milli-Q water) aqueous solutions were simultaneously added dropwise into a heated solution of KMnO<sub>4</sub> (13.0 g, 85.2 mmol in 80 mL Milli-Q water) at 40 °C. After 1 h at 60 °C, the reaction was cooled down to ambient temperature, filtered through a filter plate and

thoroughly washed with Milli-Q water. Finally, the product was dried in an oven at 100 °C over 3 nights. Yield 60%.

### Synthesis of 4- (Boc-amino) benzylaldehyde

A solution of NaOH (0.65 g, 16.0 mmol) in 40 mL of water was added into a solution of 4-aminobenzyl alcohol (2.00 g, 16.2 mmol) in 10 mL of dioxane. Di-tert-butyl di-carbonate (4.95 g, 22.7 mmol) was introduced into the mixture and it was stirred over two nights at room temperature. Then, 50 mL of diethyl ether were added and the mixture was extracted with 1M HCl, saturated NaHCO<sub>3</sub> and brine. Finally, the organic layer was dried with MgSO<sub>4</sub>, filtered and the solvent evaporated to obtain 4-(Boc-amino)benzylalcohol. The obtained solid was dissolved in 48 mL of DCM and mixed with 9 g of freshly synthesized MnO<sub>2</sub> (103.5 mmol). After 2 days at room temperature, the mixture was filtered through celite and the solvent removed under vacuum to isolate the product in 72% yield. <sup>1</sup>H NMR (360 MHz, CDCl<sub>3</sub>,) δ: 9.89 (1H, s) 7.84 (2H, d, <sup>3</sup>J=8.6 Hz), 7.54 (2H, d, <sup>3</sup>J=8.3 Hz) 6.74 (2H, s). Elemental analysis calcd for C<sub>12</sub>H<sub>15</sub>NO<sub>3</sub>·0.1 H<sub>2</sub>O: C: 64.62%; H: 6.87 %; N 6.28 %; O: 22.24 %, found: C 64.85 %; H 6.80 %; N: 6.11 %; O: 22.24%.

### Synthesis of BocNH<sub>2</sub>CCMoid, 3

51 µL of ACAC (0.50 mmol) were mixed with 35.0 mg of B<sub>2</sub>O<sub>3</sub> (0.50 mmol) in 0.2 mL of DMF. After 30 minutes heating at 80 °C, 0.54 mL of tributylborate (2.00 mmol) and a solution of 200 mg of 4-(Boc-amino) benzaldehyde (0.90 mmol) in 0.6 mL of DMF were added at an interval of 30 min. 30 minutes later, 19.7 µL of butylamine (0.20 mmol) were dissolved in 0.2 mL DMF and added dropwise into the mixture. Then, the reaction was kept at 80 °C for a total of 4 h and subsequently 6 mL of

Milli-Q water were added allowing the mixture to cool down to RT and stirring for 1 extra hour. Finally, the reaction was filtered off, washed with Milli-Q water and dried with Et<sub>2</sub>O. Yield 70%. <sup>1</sup>H NMR (400 MHz, CDCl<sub>3</sub>) δ: 15.98 (1H, s) 7.62 (2H, d, <sup>3</sup>J= 15.8 Hz) 7.51 (4H, d, <sup>3</sup>J=8.6 Hz), 7.41 (4H, d, <sup>3</sup>J=8.6 Hz) 6.59 (2H, s), 6.55 (2H, d, <sup>3</sup>J=15.8 Hz). Elemental analysis calcd: C: 68.76%; H: 6.77 %; N 5.53 %; O: 18.95 %, found: C 68.46 %; H 7.00 %; N: 5.63 %; O: 18.91%; MS MALDI-TOF (m/z) calcd for BocNH<sub>2</sub>CCMoid: 506.6 [M]; found: 505.6 [M-1].

### Synthesis of 4-aminobenzaldehyde.

9 g of freshly synthesized MnO<sub>2</sub> (103.5 mmol) were introduced into a round bottom flask containing a solution of 4-aminobenzyl alcohol (2.00 g, 16.2 mmol) in 48 mL of dry DCM. After being stirred for 2 days, the mixture was filtered through celite and the solvent was evaporated under vacuum to provide pure 4-aminobenzaldehyde in 94% yield. <sup>1</sup>H NMR (360 MHz, CDCl<sub>3</sub>) δ: 9.73 (1H, s) 7.68 (2H, d, <sup>3</sup>J=8.5 Hz), 6.69 (2H, d, <sup>3</sup>J=8.5 Hz) 4.35 (2H, s). <sup>13</sup>C NMR (90 MHz, CDCl<sub>3</sub>) δ: 190.6, 152.7, 132.4, 127.5, 114.2. MS MALDI-TOF (m/z) calcd for 4-aminobenzaldehyde: 121.0 [M]; found: 122.0 [M+1].

### Synthesis of NH<sub>2</sub>CCMoid, 4.

78 µL of ACAC (0.77 mmol) and 53.7 mg of B<sub>2</sub>O<sub>3</sub> (0.77 mmol) in 0.5 mL of DMF were heated at 80 °C for 30 min. Then sequentially, at an interval of 30 min, 0.83 mL of tributylborate (3.07 mmol) and a solution of 425 mg of 4-aminobenzaldehyde (3.50 mmol) in 1 mL of DMF were added. The mixture was allowed to evolve at 80 °C for another half hour and then 30 µL of butylamine (0.30 mmol) dissolved in 0.4 mL DMF was added



dropwise. 4 h later, 6 mL of Milli-Q water were added allowing the mixture to cool to RT for 1 hour. Finally, the reaction was filtered off, rinsed with Milli-Q water and dried with Et<sub>2</sub>O to obtain a garnet solid in 30% yield. <sup>1</sup>H NMR (360 MHz, CDCl<sub>3</sub>) δ: 16.20 (1H, s) 7.59 (2H, d, <sup>3</sup>J=15.9 Hz), 7.40 (4H, d, <sup>3</sup>J=8.1 Hz) 6.67 (4H, d, <sup>3</sup>J= 8.2 Hz), 6.45 (2H, d, <sup>3</sup>J= 15.8 Hz), 5.73 (1H, s), 3.94 (4 H, s). <sup>13</sup>C NMR (90 MHz, CDCl<sub>3</sub>) δ: 183.6, 148.7, 140.7, 130.1, 125.7, 120.3, 115.1. Elemental analysis calcd for C<sub>19</sub>H<sub>18</sub>N<sub>2</sub>O<sub>2</sub> · 0.55 H<sub>2</sub>O: C: 72.16 %; H: 6.09 %; N: 8.86 %; O: 12.90 %, found: C 72.20 %; H 5.66 %; N: 9.00 %; O: 13.14 %; MS MALDI - TOF (m/z) calcd for NH<sub>2</sub>CCMoid: 306.1 [M<sup>+</sup>]; found: 304.9 [M-1<sup>+</sup>]

### Synthesis of hemiNH<sub>2</sub>CCMoid, **5**:

HemiNH<sub>2</sub>CCMoid, **5** was obtained as byproduct in the previous reaction in an 8 % yield. The mother liquid from the final filtration described for **4** contained **5** as a thin precipitated that was isolated by centrifugation, washed with Milli-Q water and dried with Et<sub>2</sub>O. <sup>1</sup>H NMR (360 MHz, CDCl<sub>3</sub>) δ: 15.58 (1H, s) 7.55 (1H, d, <sup>3</sup>J=15.9 Hz), 7.37 (2H, d, <sup>3</sup>J=8.6 Hz) 6.67 (2H, d, <sup>3</sup>J= 8.4 Hz), 6.30 (1H, d, <sup>3</sup>J= 15.8 Hz), 5.59 (1H, s), 3.94 (2 H, s), 2.14 (3H, s). <sup>13</sup>C NMR (90 MHz, CDCl<sub>3</sub>) δ: 196.3, 140.6, 130.0, 118.7, 115.1, 110.13, 100.5, 26.8. Elemental analysis calcd for C<sub>12</sub>H<sub>13</sub>NO<sub>2</sub> · 0.4 H<sub>2</sub>O · 0.05 C<sub>3</sub>H<sub>7</sub>NO: C 68.16 %; H: 6.66 %; N: 6.87 %; O: 18.31 %, found: C 67.98 %; H: 6.33%; N: 7.23 %; O: 18.46 %; MS MALDI- TOF (m/z) calcd for HemiNH<sub>2</sub>CCMoid: 203.1 [M<sup>+</sup>]; found: 202.1 [M-1<sup>+</sup>].

## Annex III

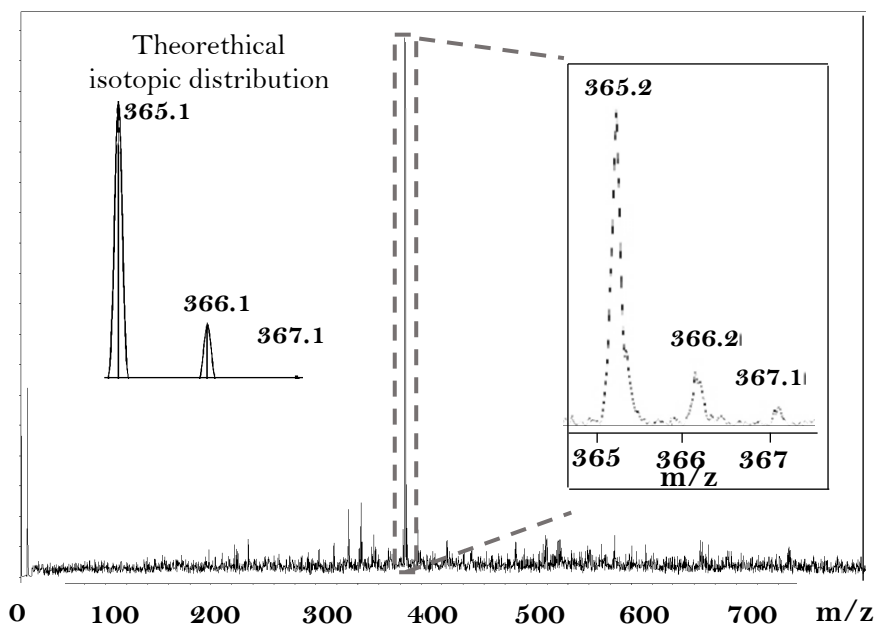


Figure A3.1. MALDI-TOF mass spectrum in negative mode of **2**.

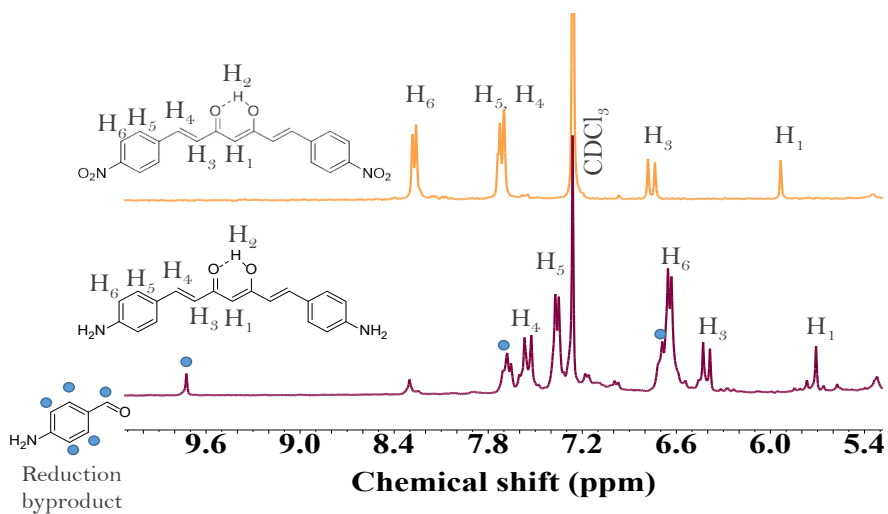


Figure A3.2. Comparison between <sup>1</sup>H NMR spectra of compound **2** and its product after the reduction reaction of NO<sub>2</sub>CCMoid.

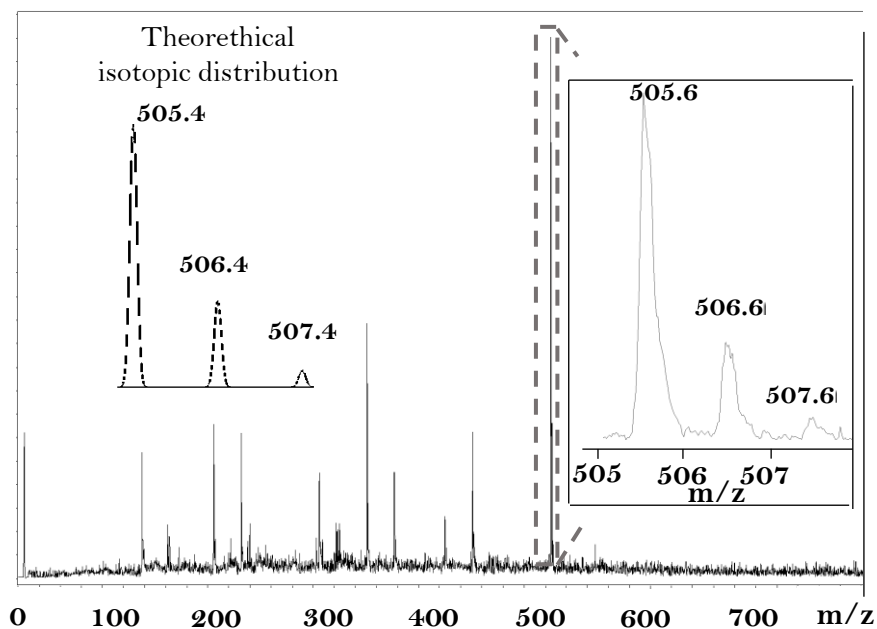


Figure A3.3. MALDI-TOF mass spectrum in negative mode of **3**.

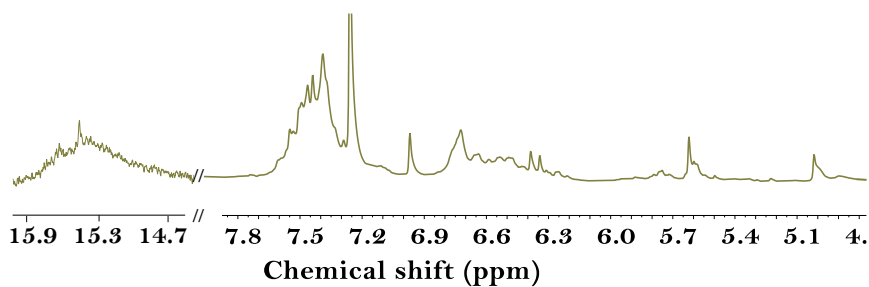


Figure A3.4.  $^1\text{H}$  NMR spectrum in  $\text{CDCl}_3$  obtained after the Boc deprotection of  $\text{BocNH}_2\text{CCMoid}$  with  $\text{HCl}$ /dioxane in THF.

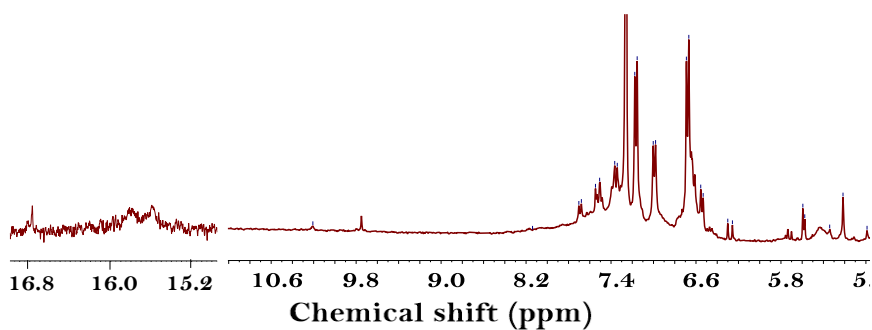


Figure A3.5.  $^1\text{H}$  NMR spectrum in  $\text{CDCl}_3$  of the adapted Pabon reaction with 4-aminobenzaldehyde in EtOAc.

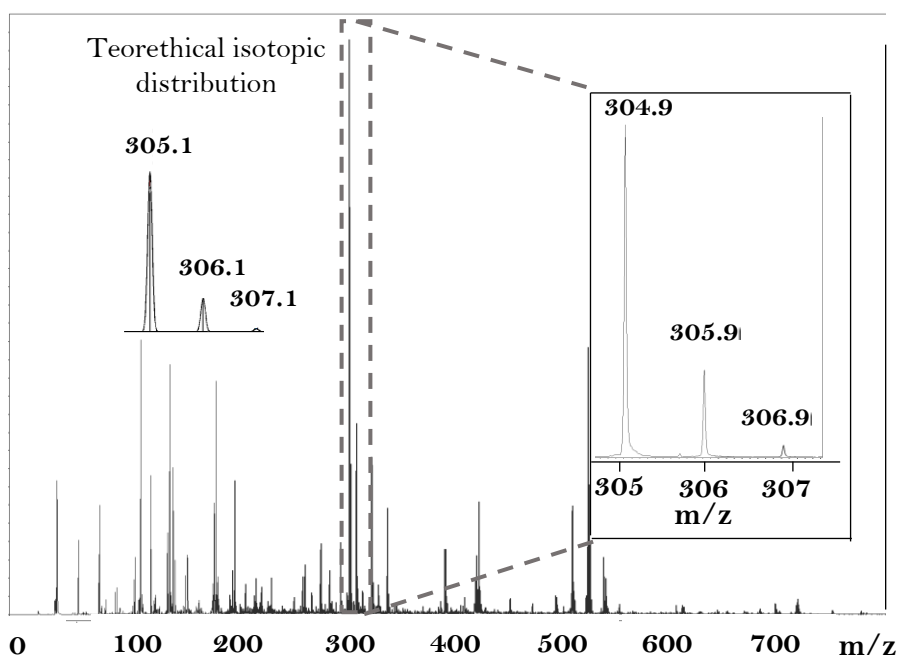


Figure A3.6. MALDI-TOF mass spectrum in negative mode of **4**.

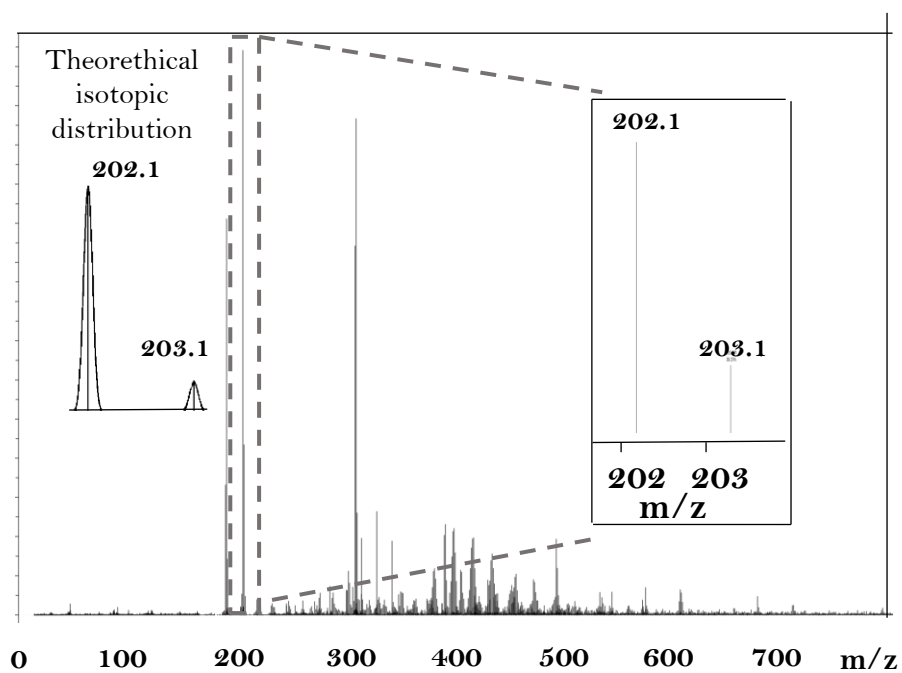


Figure A3.7. MALDI-TOF mass spectrum in negative mode of **5**.

## References

- (1) Bray, D. J.; Clegg, J. K.; Lindoy, L. F.; Schilter, D. Self-Assembled Metallo-Supramolecular Systems Incorporating  $\beta$ -Diketone Motifs as Structural Elements. *Adv. Inorg. Chem.* **2006**, *59*, 1–37.
- (2) Zhang, Y.; Khan, A. R.; Fu, M.; Zhai, Y.; Yu, A.; Zhai, G. The Progresses in Curcuminoids-Based Metal Complexes: Especially in Cancer Therapy. *Future Med. Chem.* **2019**, *11* (9), 1035–1056.
- (3) Khorasani, M. Y.; Langari, H.; Sany, S. B. T.; Rezayi, M.; Sahebkar, A. The Role of Curcumin and Its Derivatives in Sensory Applications. *Mat. Sci. Eng. C.* **2019**, *103*, 109792.
- (4) Li, Y.; Zou, Q.; Yuan, C.; Li, S.; Xing, R.; Yan, X. Amino Acid Coordination Driven Self-Assembly for Enhancing Both the Biological Stability and Tumor Accumulation of Curcumin. *Angew. Chem. Int. Ed.* **2018**, *130* (52), 17330–17334.
- (5) de França, B. M.; Oliveira, S. S. C.; Souza, L. O. P.; Mello, T. P.; Santos, A. L. S.; Bello Forero, J. S. Synthesis and Photophysical Properties of Metal Complexes of Curcumin Dyes: Solvatochromism, Acidochromism, and Photoactivity. *Dyes Pigments* **2022**, *198*, 110011.
- (6) Menelaou, M.; Ouharrou, F.; Rodríguez, L.; Roubeau, O.; Teat, S. J.; Aliaga-Alcalde, N. DyIII- and YbIII-Curcuminoid Compounds: Original Fluorescent Single-Ion Magnet and Magnetic near-IR Luminescent Species. *Chem. Eur. J.* **2012**, *18* (37), 11545–11549.
- (7) Díaz-Torres, R.; Menelaou, M.; Roubeau, O.; Sorrenti, A.; Brandariz-De-Pedro, G.; Sañudo, E. C.; Teat, S. J.; Fraxedas, J.; Ruiz, E.; Aliaga-Alcalde, N. Multiscale Study of Mononuclear CoII SMMs Based on Curcuminoid Ligands. *Chem. Sci.* **2016**, *7* (4), 2793–2803.

- (8) Hoskins, B. F.; Robson, R. Infinite Polymeric Frameworks Consisting of Three Dimensionally Linked Rod-like Segments. *J. Am. Chem. Soc.* **1989**, *111* (15), 5962–5964.
- (9) Su, H.; Sun, F.; Jia, J.; He, H.; Wang, A.; Zhu, G. A Highly Porous Medical Metal-Organic Framework Constructed from Bioactive Curcumin. *Chem. Commun.* **2015**, *51* (26), 5774–5777.
- (10) Portolés-Gil, N.; Lanza, A.; Aliaga-Alcalde, N.; Ayllón, J. A.; Gemmi, M.; Mugnaioli, E.; López-Periago, A. M.; Domingo, C. Crystalline Curcumin BioMOF Obtained by Precipitation in Supercritical CO<sub>2</sub> and Structural Determination by Electron Diffraction Tomography. *ACS Sustain. Chem. Eng.* **2018**, *6* (9), 12309–12319.
- (11) Rodríguez-Cid, L.; Qian, W.; Iribarra-Araya, J.; Etcheverry-Berríos, Á.; Martínez-Olmos, E.; Choquesillo-Lazarte, D.; Sañudo, E. C.; Roubeau, O.; López-Periago, A. M.; González-Campo, A.; Planas, J. G.; Soler, M.; Domingo, C.; Aliaga-Alcalde, N. Broadening the Scope of High Structural Dimensionality Nanomaterials Using Pyridine-Based Curcuminoids. *Dalton Trans.* **2021**, *50* (20), 7056–7064.
- (12) Rodríguez-Cid, L.; Sañudo, E. C.; López-Periago, A. M.; González-Campo, A.; Aliaga-Alcalde, N.; Domingo, C. Novel Zn (II) Coordination Polymers Based on the Natural Molecule Bisdemethoxycurcumin. *Cryst. Growth Des.* **2020**, *20* (10), 6555–6564.
- (13) Wichitnithad, W.; Nimmannit, U.; Wacharasindhu, S.; Rojsitthisak, P. Synthesis, Characterization and Biological Evaluation of Succinate Prodrugs of Curcuminoids for Colon Cancer Treatment. *Molecules* **2011**, *16* (2), 1888–1900.
- (14) Di Martino, R. M. C.; De Simone, A.; Andrisano, V.; Bisignano, P.; Bisi, A.; Gobbi, S.; Rampa, A.; Fato, R.; Bergamini, C.; Perez, D. I.; Martinez, A.; Bottegoni, G.; Cavalli, A.; Belluti, F.

Versatility of the Curcumin Scaffold: Discovery of Potent and Balanced Dual BACE-1 and GSK-3 $\beta$  Inhibitors. *J. Med. Chem.* **2016**, *59* (2), 531–544.

- (15) Panda, S. S.; Tran, Q. L.; Rajpurohit, P.; Pillai, G. G.; Thomas, S. J.; Bridges, A. E.; Capito, J. E.; Thangaraju, M.; Lokeshwar, B. L. Design, Synthesis, and Molecular Docking Studies of Curcumin Hybrid Conjugates as Potential Therapeutics for Breast Cancer. *Pharmaceuticals* **2022**, *15* (4), 451.
- (16) Wade, L. G. Química orgánica. *Pearson*, **2017**.
- (17) Blaser, H. U.; Steiner, H.; Studer, M. Selective Catalytic Hydrogenation of Functionalized Nitroarenes: An Update. *Chem. Cat. Chem.* **2009**, *1* (2), 210–221.
- (18) Orlandi, M.; Tosi, F.; Bonsignore, M.; Benaglia, M. Metal-Free Reduction of Aromatic and Aliphatic Nitro Compounds to Amines: A HSiCl<sub>3</sub>-Mediated Reaction of Wide General Applicability. *Org. Lett.* **2015**, *17* (16), 3941–3943.
- (19) Bellamy, F. D.; Ou, K. Selective Reduction of Aromatic Nitro Compounds with Stannous Chloride in Non Acidic and Non Aqueous Medium. *Tetrahedron Lett.*, **1984**, *25* (8) 839–842.
- (20) Sonmez, F.; Sevmezler, S.; Atahan, A.; Ceylan, M.; Demir, D.; Gencer, N.; Arslan, O.; Kucukislamoglu, M. Evaluation of New Chalcone Derivatives as Polyphenol Oxidase Inhibitors. *Bioorg. Med. Chem. Lett.* **2011**, *21* (24), 7479–7482.
- (21) Cui, M.; Ono, M.; Kimura, H.; Liu, B.; Saji, H. Synthesis and Structure-Affinity Relationships of Novel Dibenzylideneacetone Derivatives as Probes for  $\beta$ -Amyloid Plaques. *J. Med. Chem.* **2011**, *54* (7), 2225–2240.
- (22) Wuts, P. G. M.; Greene, T. W. *Greene's Protective Groups in Organic Synthesis*; John Wiley & Sons, **2006**.



- (23) Takahashi, T.; Hijikuro, I.; Sugimoto, H.; Kihara, T.; Shimmyo, Y.; Niidome, T. Preparation of Novel Curcumin Derivatives as Bsecretase Inhibitors. WO 2008066151 A1, June 5, **2008**.
- (24) Evans, R. M. Oxidations by Manganese Dioxide in Neutral Media. *Q. Rev. Chem. Soc* **1959**, *13*, 61–70.
- (25) Pratt, E. F.; Van De Castle, J. F. Oxidation By Solids.I. Oxidation of Selected Alcohols by Manganese Dioxide. *J. Org. Chem.***1960**, *26*, 2973–2975.
- (26) Pabon, H. J. J. A Synthesis of Curcumin and Related Compounds. *Recl. Trav. Chim. Pays-Bas* .**1964**, *83*, 379–386.
- (27) Ferrari, E.; Lazzari, S.; Marverti, G.; Pignedoli, F.; Spagnolo, F.; Saladini, M. Synthesis, Cytotoxic and Combined CDDP Activity of New Stable Curcumin Derivatives. *Bioorg. Med. Chem* .**2009**, *17* (8), 3043–3052.
- (28) Berns, B.; Tieke, B. Electrochromic Polyiminocarbazolylenes with Latent Hydrogen Bonding. *Polym. Chem.* **2015**, *6* (27), 4887–4901.
- (29) Bard, A. J.; Faulkner, L. R. *Electrochemical Methods: Fundamentals and Applications*. John Wiley & Sons, **2001**.
- (30) Kim, E.; Felouat, A.; Zaborova, E.; Ribierre, J. C.; Wu, J. W.; Senatore, S.; Matthews, C.; Lenne, P. F.; Baffert, C.; Karapetyan, A.; Giorgi, M.; Jacquemin, D.; Ponce-Vargas, M.; Guennic, B. Le; Fages, F.; D'Aléo, A. Borondifluoride Complexes of Hemicurcuminoids as Bio-Inspired Push-Pull Dyes for Bioimaging. *Org. Biomol. Chem.* **2016**, *14* (4), 1311–1324.
- (31) Pedersen, U.; Rasmussen, P. B.; Lawesson, S. O.; Pedersen, U.; Rasmussen, P. B.; Lawessont, S.-O. Synthesis of Naturally Occurring Curcuminoids and Related Compounds. *Liebigs Annalen der Chemie*, **1985** *8*, 1557-1569.

- (32) More, A. B.; Sekar, N. Nonlinear Optical Properties of Pyrene Based Fluorescent Hemicurcuminoid and Their BF<sub>2</sub> Complexes –Spectroscopic and DFT Studies. *J. Fluoresc.* **2017**, 27 (5), 1777–1792.
- (33) Etcheverry-Berrios, A.; Olavarría, I.; Perrin, M. L.; Díaz-Torres, R.; Jullian, D.; Ponce, I.; Zagal, J. H.; Pavez, J.; Vásquez, S. O.; van der Zant, H. S. J.; Dulić, D.; Aliaga-Alcalde, N.; Soler, M. Multiscale Approach to the Study of the Electronic Properties of Two Thiophene Curcuminoid Molecules. *Chem. Eur. J.* **2016**, 22 (36), 12808–12818.
- (34) Riba-López, D.; Zaffino, R.; Herrera, D.; Matheu, R.; Silvestri, F.; Ferreira da Silva, J.; Sañudo, E. C.; Mas-Torrent, M.; Barrena, E.; Pfattner, R.; Ruiz, E.; González-Campo, A.; Aliaga-Alcalde, N. Dielectric Behavior of Curcuminoid Polymorphs on Different Substrates by Direct Soft Vacuum Deposition. *iScience* **2022**, 25 (12), 105686.
- (35) Torres, R. D. Synthesis, Characterization and Deposition on Surfaces of Curcuminoids-Based Systems. PhD Thesis, University of Barcelona, **2018**.



## Chapter 4

# Preparation of extended carbon nanotubes and polycyclic aromatic hydrocarbon-based CCMoids as functional units in graphene-based three-terminal devices

In this chapter, we study the extension of the previously synthesized  $\text{NH}_2\text{CCMoid}$  through the incorporation of functionalised CNTs and perylene units, resulting in the creation of elongated CNTs and polycyclic aromatic hydrocarbon-based CCMoids, named here CCMoidfCNTs and peICCMoid, respectively. Additionally, we anchor peICCMoid to nanogap graphene-based three-terminal devices and analyse its electrical conductance within a single molecule regime.





## 4.1. Introduction

Nowadays, the fabrication of robust and efficient three-terminal devices for electron transport studies of single molecules is still a challenge <sup>1</sup>. The most basic conformation consists on the immobilization of individual molecules that will act as nanowires, within an electrical circuit composed by three electrodes: named as source (S), drain (D) and, separated from them by an insulator, the third one called gate (G), as Figure 4.1 shows. Taking into account the average dimension of molecules, the gaps between S-D may be at the nm scale (nanogaps, of the order of 1- 2 nm).

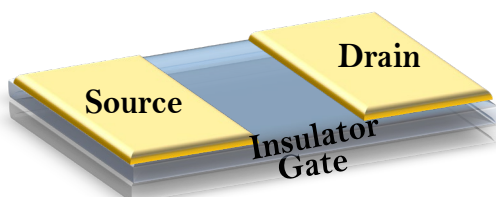


Figure 4.1. Basic three-terminal device architecture.

Traditionally, the creation of single molecule junctions has primarily involved nanogapped metallic electrodes, particularly gold, using different techniques such as mechanically controlled break junctions or electromigration, among others <sup>2</sup>. However, due to the high atom mobility, Au nanoelectrodes tend to be unstable at room temperature <sup>3</sup>, in the regime where the device should work <sup>4</sup>. A suitable alternative is the use of two-dimensional planar graphene electrodes resulting in hybrid graphene-based three-terminal devices, as represented in Figure 4.2, where S and D are made of graphene supported on Si (G) and separated by a thick layer of SiO<sub>2</sub>. Graphene-based S and D electrodes can be separated by nanometer distances applying the previously described (in Chapter 1) gap opening

techniques, lithography <sup>5</sup>, mechanically controllable break junction <sup>6</sup> or electroburning <sup>4</sup>, being the latter applied for the obtaining of 1-2 nm separation between the graphene electrodes.

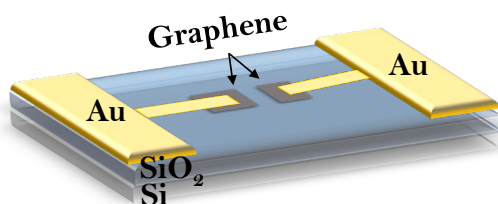


Figure 4.2. Example of a graphene-based three-terminal device.

The  $sp^2$  carbon lattice offers this material stability at both low and high temperatures (10 K to 300 K). Moreover, it opens the possibility to couple single molecules through  $\pi$ - $\pi$  stacking or covalent bonding <sup>7</sup>. As the gap opening experiments usually involves the presence of oxygen, because the use of oxygen plasma ion etching, or because the experiment is performed in air, the edges of the broken graphene are functionalised, with hydroxyl, aldehyde and/or acid groups, among others. These groups can react, optimizing them, with amino groups comprised in the single molecule leading to the creation of amide covalent junctions <sup>5</sup>.

On the other hand, looking at the  $\pi$ - $\pi$  stacking interactions between the molecule and the electrodes, CNTs and polycyclic aromatic hydrocarbons (PAHs) are ideal candidates to locate in the extremes of single molecules to act as anchoring points with graphene.

CNTs have widely been explored as electrodes in three terminal devices <sup>7</sup>. However, in most of the cases, where a single molecule was attached, particularly by covalent modification <sup>8,9</sup>, the cutting of the nanotubes was mostly performed by oxygen plasma ion etching <sup>10</sup> leading into a nanometer

separation higher than 1-2 nm obtained by electroburning. Additional gap formation techniques were studied, such as, electrical breakdown creating a gap down to 7 nm, where the molecule was attached by  $\pi$ - $\pi$  interaction between terminal phenantrene moieties and CNTs <sup>11</sup> or by helium ion etching where the gap formed was around 3 nm size <sup>12</sup>.

Although the use of CNTs as electrodes in three terminal devices has been intensively studied, their role as single wires in carbon-based devices, has attract less attention, due to the challenging control of the density and separation of CNTs to connect only one tube to each device <sup>13</sup>.

Regarding PAHs, this specific family of molecules, represented some of them in Figure 4.3, are composed by the fusion of a number of benzene rings. They are considered cut-outs of graphene, therefore they are able to interact by  $\pi$ - $\pi$  staking with similar materials <sup>14,15</sup>.

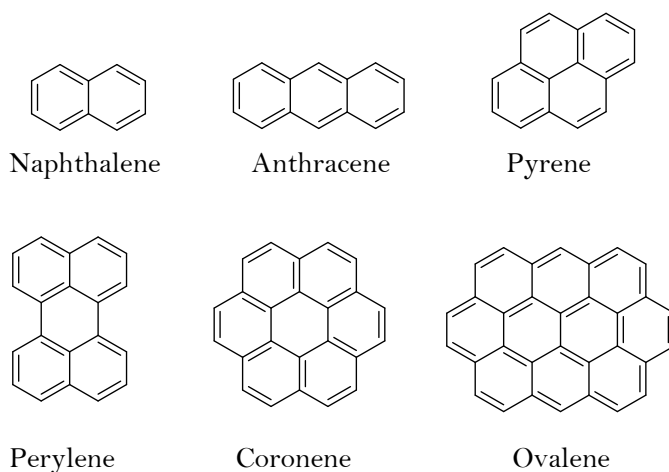


Figure 4.3. Examples of PAHs.

Perylene is the five fused ring structure shown in Figure 4.3, whose derivative perylene tetracarboxylic diimide, named PDI (represented in Figure 4.4) and PDI-based compounds have been measured in single



molecule break junctions attached by different anchoring groups to Au electrodes <sup>16,17,18,19</sup>. This family of compounds present some attractive features to act as active unit in electronics, such as the easiest functionalization of the bay area to increase the solubility or to tune the redox properties of the compound and the modification of the N-substitution without variation in the HOMO-LUMO orbital due to the presence of nodes in that position <sup>17</sup>.

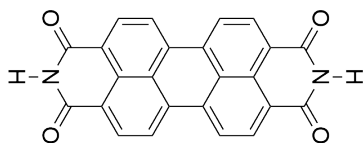


Figure 4.4. Structure of perylene tetracarboxylic diimide (PDI).

To date, there is not any graphene-based three-terminal device incorporating a single molecule containing basic perylene as anchoring points, although a related investigation was reported by El Abbassi *et al.* <sup>20</sup> fabricating the first and unique electroburned graphene-based field effect transistor including a nanoribbon formed by fused perylene units.

Although perylene has not been extensively introduced as terminal points for electrical single molecule measurements, smaller PAHs have, such as pyrene <sup>21</sup> (four fused rings) or anthracene <sup>4</sup> (three fused rings).

The conductance of a family of CCMoids incorporating anthracene moieties have been investigated. In 2011, Prins *et al.* <sup>4</sup> developed the first stable graphene CCMoid junction at room temperature. 9ACCMoid whose structure is shown in Figure 4.5, was the elected candidate to be deposited onto the device.

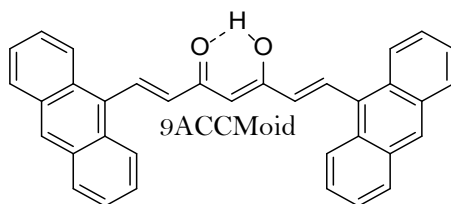


Figure 4.5. Representation of the structure of 9ACCMoid.

9ACCMoid exhibits terminal anthracene units, providing two conjugated parts to the molecule: the conjugated chain that can manage the charge transport and the terminal aromatic rings capable of interacting through  $\pi$ - $\pi$  stacking with the graphene electrodes. After performing electroburning, to open the gap in the few layer graphene electrodes, reaching 1-2 nm separation, the CCMoid was deposited and finally the conductance at room temperature was measured, as Figure 4.6 a displays. The intensity *vs* current curve (I-V curve) (Figure 4.6 b) collected by applying a source drain voltage ( $V_{sd}$ ) and zero gate voltage ( $V_g$ ), reveals an increase of the current after the deposition of the molecule. To verify that the increase was indeed due to molecular effects, the same measurements were repeated, this time with the application of a gate voltage ranging from -10 to +10 V at room temperature (Figure 4.6 c) and at 10 K (not shown) <sup>4</sup>. Consistently, a similar current increment was observed, corroborating the successful creation of the molecular junction at RT.

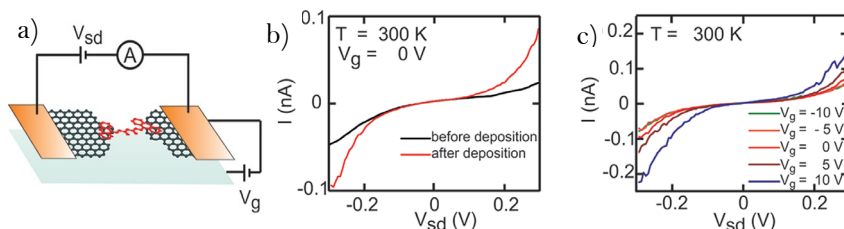


Figure 4.6. a) Representation of 9ACCMoid anchored to a nanogap graphene-based device. b) I-V curve conducted at room temperature and zero gate voltage.

c) I-V curves performed at different voltage gates. Figures extracted from reference 4.

Apart from the creation of 1-2 nm gap through electroburning, the process performed at room temperature, led to the oxidation and functionalization of the edges of the graphene electrodes with most probably -OH, -CHO and -COOH groups, which hindered a profitable molecular contact with the graphene. To minimize the influence of these functionalities and enhance the coupling with the electrodes, in 2016, Burzuri *et al.*<sup>22</sup> used a longer CCMoid, 9ALCCCMoid, whose structure is shown in Figure 4.7, that was added, in a similar manner than before, into a hybrid-graphene three-terminal device.

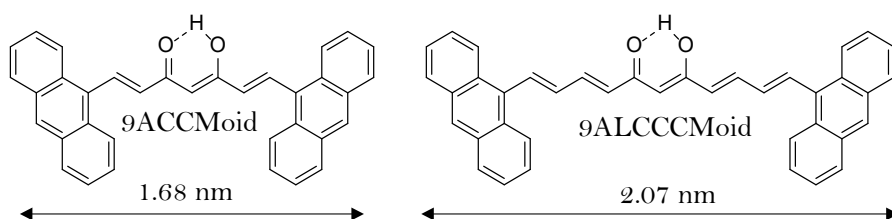


Figure 4.7. Chemical structures of 9ACCMoid and 9ALCCCMoid, comparing lengths.

The strategy they followed consisted on the extension of the conjugated backbone of the previously explored 9ACCMoid from 7 to 11 carbon atoms, increasing the length of the molecule from 1.68 nm to 2.07 nm, allowing the anchoring far from the functionalized edges of the graphene. They conducted I-V measurements at low temperatures, below 10 K reporting an increase of the conductance about 2 orders of magnitude with respect to the empty device, which was an analogous result to that observed with the shorter molecule. Despite the longer length of 9ALCCCMoid, which would result in lower conductance, they observed similar conductance values at low temperature compared to the initial CCMoid, 9ACCMoid, suggesting an improved anchoring as the reason for the comparable conductance.

2.07 nm, which is the size of the longer active CCMoid investigated, is still close to the gap limit. To overcome that barrier and anchor the molecule farther from the graphene edges, we proposed the design of extended CCMoids in a different way. While in the past our group enlarged the conjugated chain, now we put emphasis on the extension of the arms using as starting material the  $\text{NH}_2\text{CCMoid}$  **4**, described in Chapter 3, taking advantage of its capacity to further react. Furthermore, we aimed to strengthen more the interaction between the molecule and graphene by the introduction of CNTs or, in the case of PAH groups, two additional rings, using perylene, instead of anthracene moieties, as anchoring groups in our investigation.

## 4.2. Objectives

The objective of this chapter is to study the reactivity of  $\text{NH}_2\text{CCMoid}$  for the formation of longer CCMoid systems, containing CNTs and PAH arms, respectively, in order to strengthen their anchoring to graphene electrodes for the exploration of the single-molecule electronic properties over three-terminal nanogap graphene-based devices. In order to exploit the final goal, it is necessary to accomplish the following aims:

- Covalent functionalization of CNTs with the  $\text{NH}_2\text{CCMoid}$ , **4**, for the obtaining of extended CCMoids.
- Synthesis of a PAH-CCMoid based on modified perylene moieties and  $\text{NH}_2\text{CCMoid}$ , **4** for its use as nanowire in three terminal devices.

## 4.3. Results and discussion

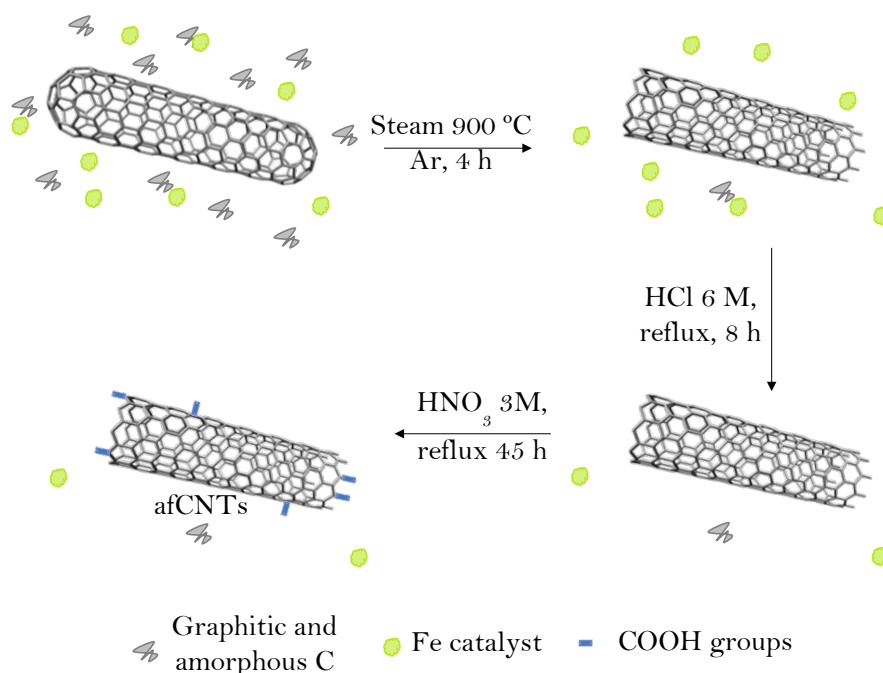
### 4.3.1. Covalent functionalization of CNTs with NH<sub>2</sub>CCMoid.

#### 4.3.1.1. Preparation of the covalent modified CCMoidfCNTs

The commercially available single walled carbon nanotubes (SWCNTs) from Sigma Aldrich used in this thesis were growth by chemical vapor deposition. This methodology generates also carbon impurities in the sample, such as amorphous carbon or graphitic nanoparticles. Therefore, before using them, a purification process is needed, followed by a functionalization step to introduce functional groups in the SWCNTs (giving rise to fCNTs) capable of reacting with the previously described NH<sub>2</sub>CCMoid, **4**.

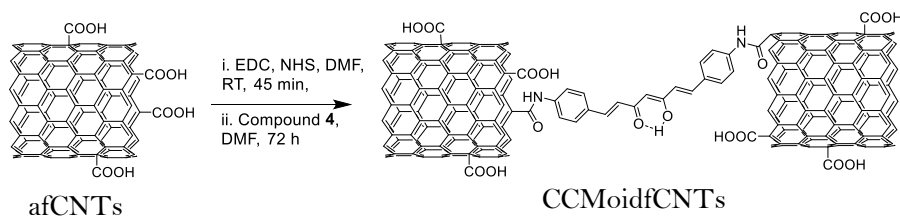
As scheme 4.1. outlines, the purification process comprised two steps <sup>23</sup>. In the initial one SWCNTs were exposed to water steam at 900 °C under argon atmosphere for 4 h, to remove the carbon-based impurities. This methodology implies the avoidance of defects, by oxidation with O<sub>2</sub> and also the opening of the ends of the nanotubes. Subsequently, the sample was refluxed in presence of HCl (6 M) for 8 h, for the removal of the iron catalyst employed in the synthetic procedure, and finally was filtered, washed (until neutral pH) and dried.

Then, acid functionalities, capable of reacting with the amino groups of compound **4**, were introduced on the edges and walls of the opened SWCNTs by an acid treatment of the sample with HNO<sub>3</sub> (3 M) under reflux for 45 h, obtaining acid functionalized CNTs, called here afCNTs <sup>23</sup>.



Scheme 4.1. Purification and acid functionalization process of SWCNTs.

After a thermogravimetric analysis to know the percentage of acid groups in the sample (shown in Figure A4.1 Annex IV), we performed the reaction between the acid functionalised CNTs and compound **4**, as displayed in Scheme 4.2. First, the acid groups were preactivated by a well-known protocol with 1-ethyl-3-(3-dimethylaminopropyl)carbodiimide (EDC) and N-hydroxysuccinimide (NHS) in DMF for 45 minutes <sup>24</sup>. Afterwards, in order to optimize the coupling with NH<sub>2</sub>CCMoid, **4**, three different amounts of NH<sub>2</sub>CCMoid were studied, 1:1 ratio between acid:diamine groups, 2:1 and 10:1 in DMF for 72 h. By UV-Vis absorption spectroscopy it was possible to found out that there was an excess of NH<sub>2</sub>CCMoid in the 1:1 and 2:1 ratio sample, being the optimal conditions the 10:1 mixture, ideally resulting in the named CCMoidfCNTs exposed in scheme 4.2.



Scheme 4.2. Route followed for the preparation of CCMoidfCNTs.

This scheme depicts the final goal with the methodology described above, although this may be one of the possible products, having also a range of  $\text{NH}_2\text{CCMoids}$  attached to the same afCNT, in a lateral manner, for example, and others in the apical positions of the functionalized CNTs, as exemplified in Figure 4.8.

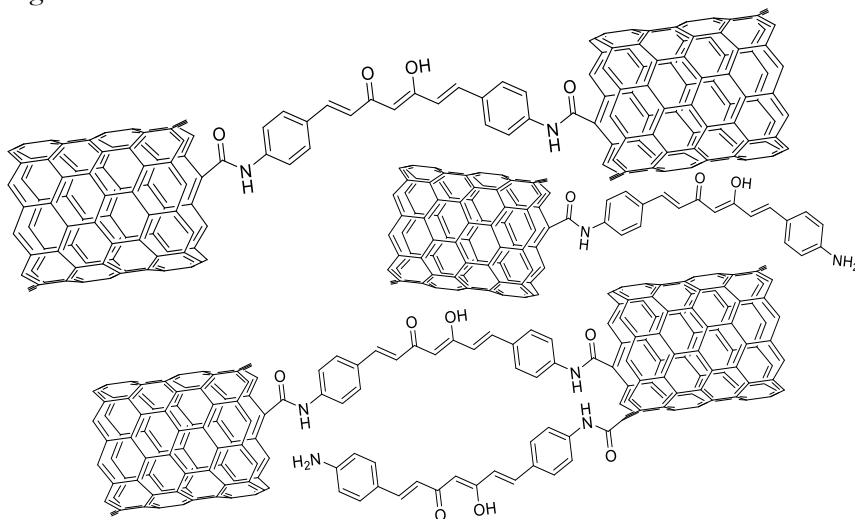


Figure 4.8. Examples of a mixture of CCMoidfCNTs systems.

Our total CCMoidfCNT sample was characterised by UV-Vis absorption spectroscopy, transmission electron microscopy (TEM), FTIR spectroscopy, and Raman spectroscopy.

#### 4.3.1.2. UV-Vis absorption spectroscopy of CCMoidfCNTs

For the UV-Vis analysis, a solution of **4** in isopropanol and two dispersions, of the afCNTs and CCMoidfCNTs, using the same solvent were measured and compared. The spectra obtained are shown in Figure 4.9. The CCMoidfCNTs exhibit two absorption bands at 326 nm and 466 nm, respectively, equally than compound **4**, indicating its presence in the mixture. However, we could not confirm the type of interaction, chemical or physical, between the CCMoid and the afCNTs due to the absence of the  $\pi$  plasmon absorbance wave assigned to the CNTs in the CCMoidfCNTs, which appears at 255 nm in the acid functionalised CNTs <sup>25, 26</sup>.

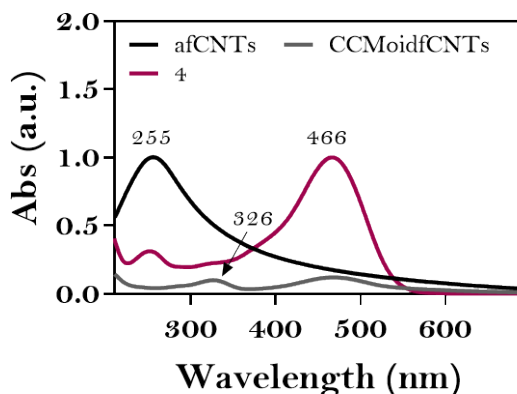


Figure 4.9. UV-Vis absorption spectra of **4**, afCNTs and CCMoidfCNTs in isopropanol.

#### 4.3.1.3. TEM of CCMoidfCNTs

TEM images, observed in Figure 4.10, do not show any significant changes in the morphology of the tubes for the acid or CCMoid functionalised systems, as it was expected.



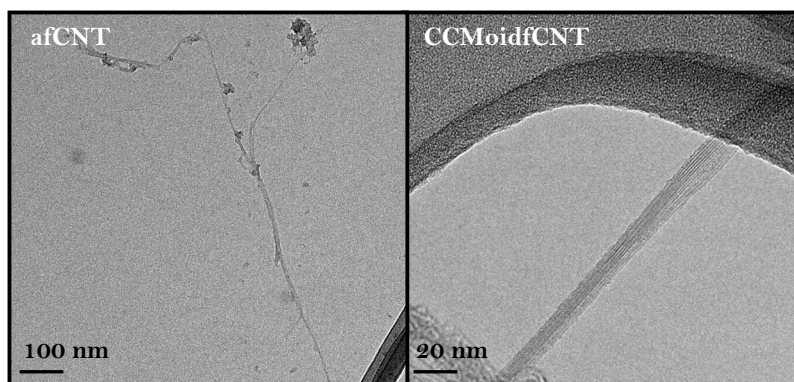


Figure 4.10. TEM images of afCNTs and CCMoidfCNTs.

#### 4.3.1.4. FTIR spectroscopy of CCMoidfCNTs

CNTs samples were deposited onto zinc selenide (ZnSe) pellets by drop casting of an isopropanol dispersion followed by solvent evaporation heating the pellet at 80 °C for FTIR experiments. Figure 4.11 displays the comparison of the spectra for afCNTs and CCMoidfCNTs. It is not observed any remarkable change between them, but the diminishing of the intensity of the C=O signal related to the acid groups at 1728  $\text{cm}^{-1}$  for the CCMoidfCNTs, which is not missing owing to the presence of remaining non-modified acid groups in the sample. However, the C=O signal of the created amide bond or any peak attributed to the CCMoid are not detected, probably because of the low proportion of CCMoid in the sample compared to the CNTs presence, which agrees with reported literature <sup>27</sup>.

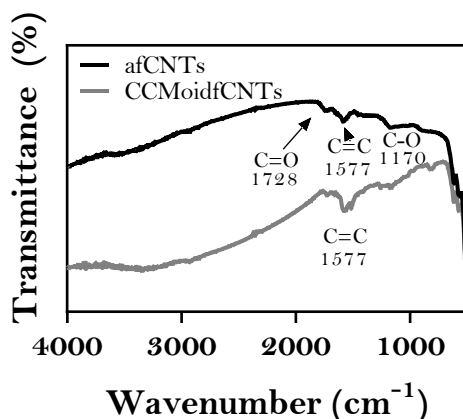


Figure 4.11. ATR-FT-IR spectra of afCNTs and CCMoidfCNTs in ZnSe pellets.

#### 4.3.1.5. Raman spectroscopy of CCMoidfCNTs

Raman spectroscopy has been demonstrated to be a powerful tool to analyse diverse aspects of CNTs<sup>28</sup>. Therefore, we conducted Raman spectroscopy measurements in an equipment with a solid state laser emitting at 532 nm. In Figure 4.12 the comparison of the Raman spectra for afCNTs and CCMoidfCNTs are represented. The CCMoidfCNTs graph is characterised by the lack of signals regarding the CCMoid structure, with all the peaks identified corresponding to the CNT architecture. Probably due to the low ratio of CCMoid in comparison to the CNT, the CCMoid signals are not detectable.

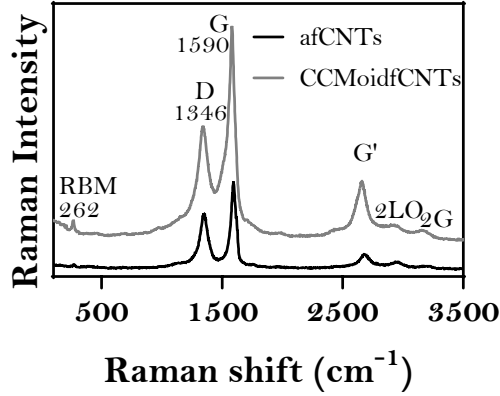


Figure 4.12. Compared Raman spectra of afCNTs and CCMoidfCNTs.

CNTs present an exclusive signal in the Raman spectrum in the region between 100 and 500  $\text{cm}^{-1}$ , the so-called radial breathing mode (RBM), which correspond with the vibration of the C atoms in the radial direction. This frequency of the band is inversely related to the diameter of the nanotubes, whose dependence is mathematically expressed by Equation 4.1.

$$\omega_{RBM} = \frac{A}{d_t} + B \quad \text{Eq. 4.1.}$$

A and B are experimentally extracted and differ in the literature, being the most extended values  $A=248 \text{ cm}^{-1}$  and  $B=0$  which correspond to isolated SWCNTs on a  $\text{SiO}_2$  substrate <sup>29</sup>.

Applying Eq 4.1, with the previously values exposed, for  $\omega_{RBM} = 262 \text{ cm}^{-1}$ , the employed CNTs are estimated to have a diameter  $d_t$  value of 0.90 nm.

In the region between 1300 and 1600  $\text{cm}^{-1}$  two intense bands appear, the D and G band. The former is displayed at 1346  $\text{cm}^{-1}$  and is related to the defects on the  $\text{sp}^2$  layer. The latter, G band is exhibited at 1590  $\text{cm}^{-1}$  and is present in all the  $\text{sp}^2$  carbon systems attributed to the graphitic network. Owing to

the attribution of the D band, to the defects on the  $sp^2$  layer, the relation between the intensity of the D ( $I_D$ ) and G ( $I_G$ ) band is a key factor to analyse the covalent functionalization of the CNTs. The  $I_D/I_G$  values of the as received SWCNTs, the afCNTs and the CCMoidfCNTs are collected in Table 4.1. The afCNTs present an  $I_D/I_G$  value of 0.67, which is higher than the obtained for the as received one, 0.30, most probably due to the acid modification of the edges and walls of the CNTs altering the C  $sp^2$  structure. The intensities ratio for CCMoidfCNTs, 0.60 is similar to the afCNTs, because the defects on the  $sp^2$  layer do not increase, due to the covalent reaction through the already attached acid groups.

	$I_D/I_G$
As received	0.30
afCNTs	0.67
CCMoidfCNTs	0.60

Table 4.1.  $I_D/I_G$  values calculated for the functionalised CNTs.

The G band allows the distinction of the semiconducting or metallic character of the CNTs within the sample. Both present two components of the G band, with a similar linewidth of  $6\text{--}15\text{ cm}^{-1}$  <sup>30</sup> for the components of the semiconducting tubes and for the higher frequency component of the metallic, being much broader for the lower frequency of the metallic. In our specific case, there is not clear distinction of two components of the G band, due to an overlapping of both, hindering the determination of the linewidth. However, the supplier's specifications of the pristine SWCNT (Sigma Aldrich) revealed a mixture of semiconducting and metallic with a higher ratio of semiconducting.

Finally above  $2500\text{ cm}^{-1}$  several overtones of the D and G band appears such as G', 2LO and 2G <sup>28</sup>.

The characterization results for the CCMoidfCNTs suggested low or negligible amount of CCMoid. Moreover, any of them offered any contribution about the disposition of the CCMoid in the sample, which could yield, as mentioned before, into a huge mixture of products, as exemplified in Figure 4.8. In order to obtain a system where the CCMoid bridges two CNTs, which would be the ideal for the single molecule measurements in the three-terminal devices, the combination of structures generated, must be purified. A suitable technique for the isolation of CNTs is ultracentrifugation and it should be taken into account in future analyses of the samples <sup>31</sup>.

Despite of the attractive systems and possibilities, it was decided to stop this field of investigation, owing to the difficult control of the isolation and characterization of the ideal CCMoidfCNTs system (shown in Scheme 4.2), the complicated anchoring of single or few molecules on the device due to the extensive aggregation and stacking of the CNTs and the variability of electrical measurements generated also by the mixture of semiconducting and metallic CNTs present in the sample. Therefore, we focused our research in the isolation of CCMoid-based systems containing smaller C sp<sup>2</sup> organizations, including perylene.

### **4.3.2. Synthesis and characterization of perylene-based CCMoid, peICCMoid, 6.**

#### **4.3.2.1. Synthesis of peICCMoid, 6**

Imines (-C=N-), also known as Schiff bases or azomethines, are commonly synthesized by a condensation reaction between an aldehyde with an

aromatic amine, under reflux, with the consequent liberation of a molecule of water <sup>32</sup> .

PeICCMoid, **6**, whose chemical structure is displayed in Figure 4.13, exhibits two terminal perylene moieties linked to the CCMoid skeleton through imine functional groups, which can interact with the graphene electrodes by  $\pi$ - $\pi$  stacking.

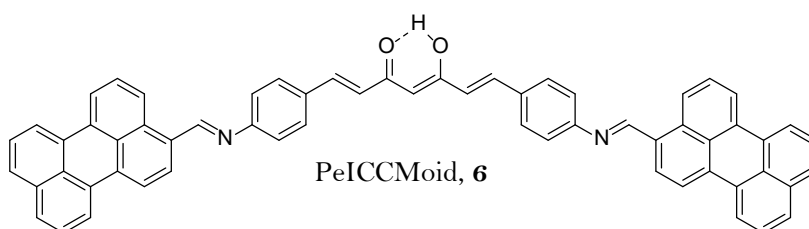
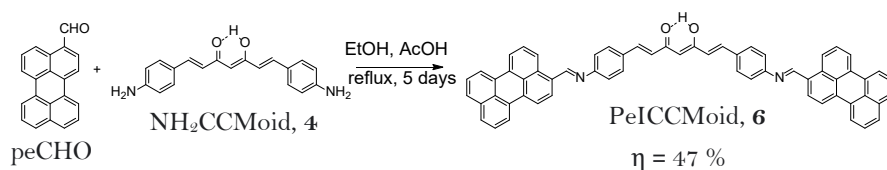


Figure 4.13. Structural scheme of compound **6**.

Different conditions were tested to obtain compound **6**. For instance, THF,  $\text{CHCl}_3$ , DMF, and mixtures of them, were used as solvents to finally found out, that the optimal conditions to isolate **6** in 47 % yield, was in an acid catalysed condensation between 3-perylenecarboxaldehyde (peCHO) and the amino containing CCMoid, **4** under reflux for 5 days using EtOH as solvent, as outlined in Scheme 4.3. This experiment yielded in a mixture of the product along with the starting 3-perylenecarboxaldehyde, which was removed after several washing processes with hot  $\text{CHCl}_3$ . The most critical and disturbing parameter in all the cases was the insolubility of the perylenecarboxaldehyde (peCHO), hindering most of the tested reactions. The insolubility factor of the initial perylene derivative, affects also to the final compound **6**, which is not soluble in the common solvents found in the laboratory.



Scheme 4.3. Synthetic pathway described for the preparation of **6**.

Although **6** is not soluble in most of the usual solvents, in tetrachloroethane (TCE) is reasonable soluble and this way it was characterized by using <sup>1</sup>H NMR and UV-Vis absorption spectroscopy. Additional solid-state techniques were used to confirm the creation of compound **6**, such as ATR-FTIR, Raman spectroscopy and MALDI-TOF mass spectrometry.

#### 4.3.2.2. <sup>1</sup>H NMR of compound **6**

The <sup>1</sup>H NMR spectra of peICCMoid and compound **4** in TCE-d<sub>2</sub> are shown in Figure 4.14. Its low solubility made difficult a complete characterization and assignment of all the signals. However, the creation of a new imine bond is clearly demonstrated by the appearance of the proton H<sub>7</sub> as a singlet at 9.06 ppm together with the disappearance of the aldehyde signal, corresponding to the 3-perylenecarboxaldehyde starting material. Next to the singlet, a doublet attributed to the closest proton of the perylene (H<sub>8</sub>) appears, while the rest of the protons of the PAH appear between 8.4 and 7.5 ppm, approximately. Remarkably, the only detectable signal related to the CCMoid skeleton is the one observed at 7.39 ppm, which corresponds with one aromatic proton (H<sub>5</sub>).

Further characterization was made to confirm the CCMoid structure owing to the limited information <sup>1</sup>H NMR could reveal which was restricted to the presence of the new imine and perylene moieties.

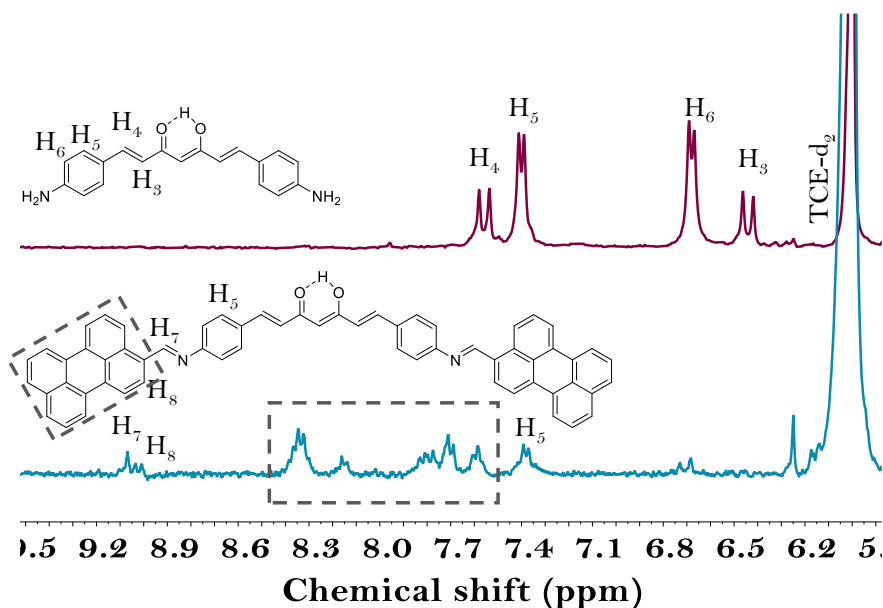


Figure 4.14. Comparison of the  $^1\text{H}$ NMR spectra of **4** and **6** in TCE- $\text{d}_2$ .

#### 4.3.2.3. ATR-FTIR spectroscopy of compound **6**

ATR-FTIR spectrum of **6** is compared with the one for **4** in Figure 4.15. At  $1619\text{ cm}^{-1}$  appears a signal in both spectra, being broader for compound **6** due to the overlapping of two contributions: the new imine bond created<sup>33</sup> and the keto-enol component of the CCMoid skeleton. Additionally, two characteristic signals of perylene corresponding to the bending C-C and C-H out of plane vibrations are observed at  $807$  and  $762\text{ cm}^{-1}$ <sup>34</sup>, with no intense signals in  $2850\text{--}2950\text{ cm}^{-1}$  related to the stretching C-H vibrations.



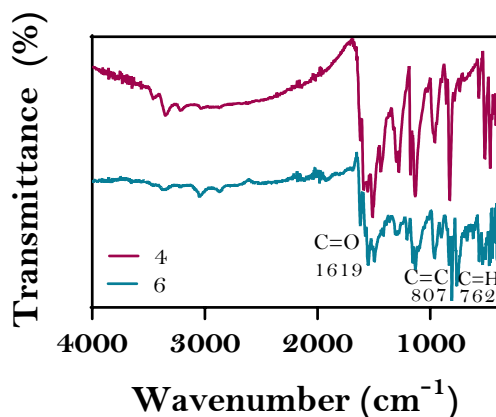


Figure 4.15. ATR-FTIR spectra of **4** and **6**.

#### 4.3.2.4. Raman spectroscopy of compound **6**

Due to the specific and well-described fingerprint that PAHs display in Raman spectra, this technique has been widely used for their identification<sup>35</sup>. Besides, it can be employed for the recognition and comparison of additional functional groups present in NH<sub>2</sub>CCMoid, **4**, and peICCMoid, **6**. Therefore, the Raman spectra obtained with the laser emitting at 785 nm for **4** and **6** are compared in Figure 4.16. The most characteristic signals appear in the windows of 1150-1200 cm<sup>-1</sup> and 1550-1650 cm<sup>-1</sup> for both compounds, slightly shifted to higher frequencies for **4**. At 1155 cm<sup>-1</sup> is observed the in-plane bending C-H vibrations of the phenyl rings of peICCMoid and the signals at 1553 and 1577 cm<sup>-1</sup> are attributed to the C=C and C=O stretching vibrations, respectively. The C=N bond is not detected but it could be overlapped with the C=C signal<sup>36</sup>.

The description provided for compound **6** is applicable to compound **4** due to the presence of almost every functional group comprised in **6**. The vibration related to the amino group was prevented to be detected by this technique because of the high fluorescence interference<sup>37</sup>.

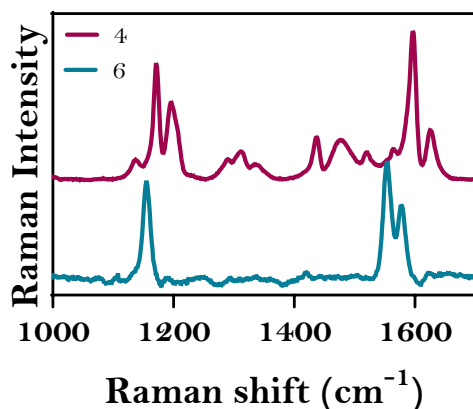


Figure 4.16. Raman spectra of **4** and **6**.

#### 4.3.2.5. UV-Vis absorption spectroscopy of **6**

UV-Vis absorption experiments were conducted in both, solution and in solid state, due to the solvochromic behaviour of the CCMoids, in order to extract electronic information of the system <sup>38</sup>.

The UV-Vis spectra of **4** and **6** in TCE are compared in Figure 4.17. Compound **6** displays an intense band at 486 nm, which is bathochromic shifted compared to the bands related to the starting materials. This band is the result of the overlapping of the  $\pi$ -  $\pi^*$  transition attributed to the CCMoid backbone and the signal related to the perylene moieties <sup>39</sup>. Furthermore, two additional bands appeared in between 240 and 260 nm, probably attributed to the substituted benzene rings.

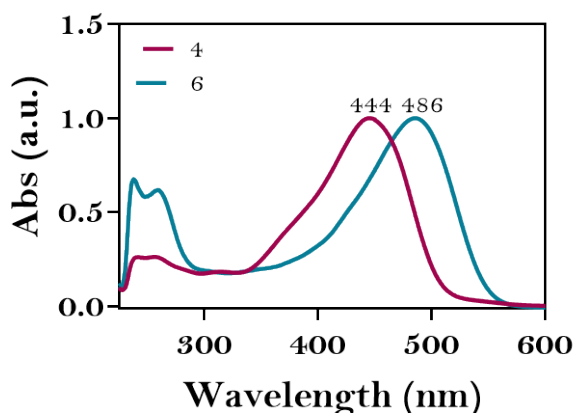


Figure 4.17. UV-Vis spectra of **4** and **6** in TCE.

For the solid state analysis, a pellet of the CCMoid was prepared by mixing compound **6** and KBr. In Figure 4.18 the spectrum of **6** and the Tauc's plot applying the Tauc's equation (Chapter 2, Eq. 2.2) are exhibited. The optical bandgap  $E_{g_{op}}$  reveals a value of 1.87 eV, indicating a better semiconducting behaviour of **6** compared to **4**, whose optical  $E_g$  value was 1.96 eV.

In this thesis, the  $E_{g_{op}}$  estimation is always coupled with the electrochemical bandgap for comparative reasons. However, due to the insolubility of compound **6** in the available dry solvents, we could not estimate the corresponding electrochemical values. As a result, with no further corroboration of the bandgap, we performed DFT calculations (comparing **4** and **6**) that show that **6** has a better semiconducting behaviour than compound **4**, displaying values of 2.12 eV (**6**) and 2.27 eV (**4**), correspondingly, in agreement with our  $E_{g_{op}}$  estimations.

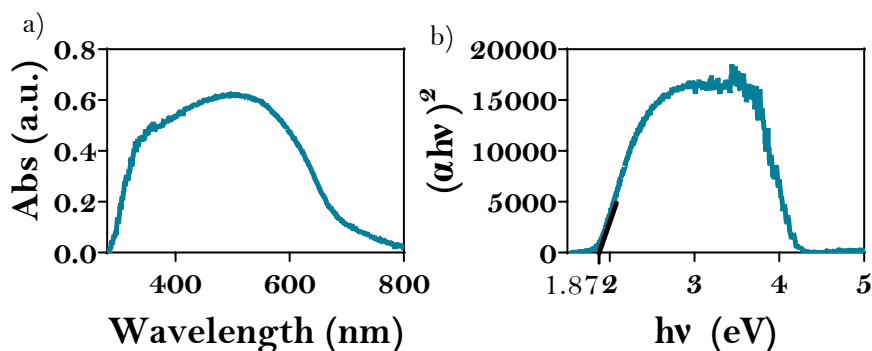


Figure 4.18. a) Solid state UV-Vis absorption spectrum of **6**. b) Tauc's plot of the solid state spectrum of **6**.

Finally, MALDI-TOF spectrometry experiments were carried out to corroborate the successful formation of peICCMoid, whose exact mass is 830.3 m/z. A peak at 829.2 m/z was detected in negative mode (See Figure A4.2 Annex IV), which agrees well with the presence of compound **6**.

Once compound **6** was characterized, its electrical properties were measured by its deposition over graphene-based three-terminal devices.

### 4.3.3. Electrical characterization of peICCMoid on graphene- based three- terminal devices

In this section we detail the fabrication processes of the creation of hybrid nanogapped graphene-based devices, the deposition of the molecule on the device and finally its electrical characterization.

### 4.3.3.1. Device fabrication

The device fabrication is not included as an objective of this thesis project, however, we want to briefly describe it, for a better understanding of the following results.

The developed devices used in this doctoral thesis adopt a basic field effect transistor architecture, which include three electrodes: the source, drain, and gate, correspondingly. In our case, S and D, are single layer graphene electrodes, separated from G, which is silicon, by a 300 nm insulator film of  $\text{SiO}_2$ .

The production of the three-terminal devices is conducted in a 4-step process, as illustrated in Figure 4.19. Initially, a micropatterning of the commercially available (graphenea.com) monolayer graphene/ $\text{SiO}_2$ /Si platform is carried out by photolithography, (Figure 4.19, step 1). Subsequently, a second photolithography is used to define the pattern for the electrical contacts finally obtained after evaporating a 5 nm adhesion Cr layer and 50 nm Au (step 2). Then, a further patterning is done to reduce the graphene area between the gold electrodes below to 1  $\mu\text{m}$  features in order to simplify, and increase the success rate, of the final feedback-controlled electroburning step, used to define graphene nanogaps below 5 nm<sup>40,41</sup> (step 3). The feedback-controlled electroburning process (step 4) opens a nanogap of approximately 1-2 nm on the graphene by the applications of a series of consecutive voltage ramps, between the S and the D, while recording the current intensity and monitoring abrupt decrease. Current intensity dropping indicates breaking-down of the graphene layer and the voltage applied is automatically backed to zero by the feedback-control. Then a new voltage ramp is applied up to an adjusted target voltage used to prevent excessive burning of the graphene resulting in larger nanogaps. The cycle finishes when there is no more current intensity signal

from the device, suggesting a complete nanogap opening in the graphene layer.

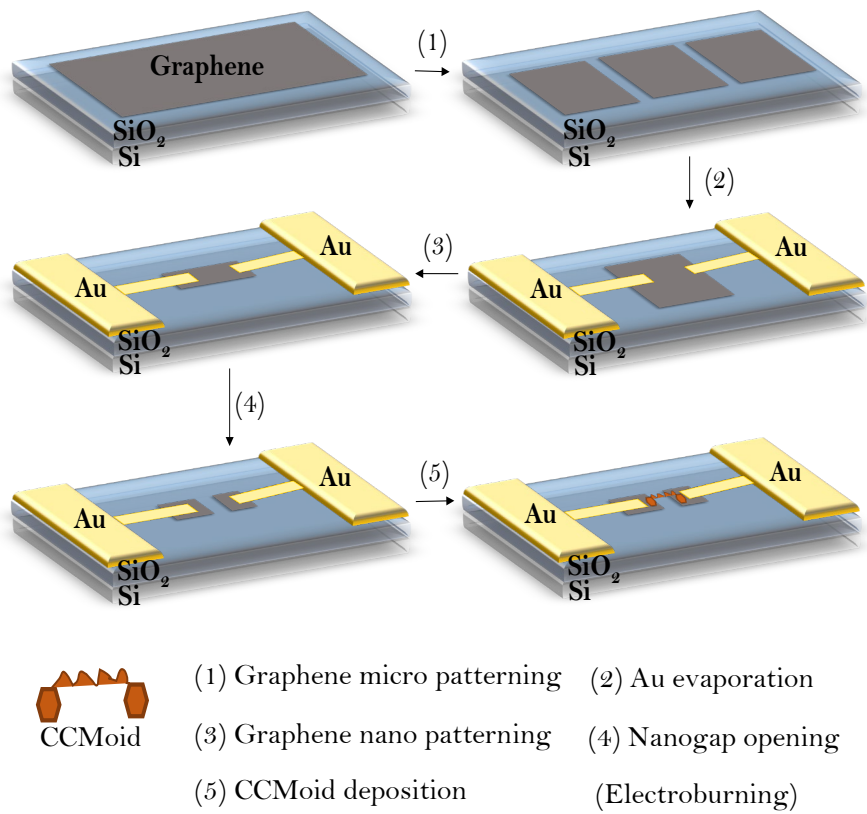


Figure 4.19. Protocol for the fabrication of nanogap graphene-based three-terminal devices.

The electroburning process can be performed both at room conditions in the presence of air or under vacuum <sup>42</sup>, being the former the employed in our case. After the electroburning, I-V curves between  $\pm 1$  V between source and drain are measured, as the one represented in Figure 4.20 to select nanogaps useful for single molecules analysis. Only nanogaps with a low bias resistance greater than 1 G $\Omega$  are considered for the following analysis.

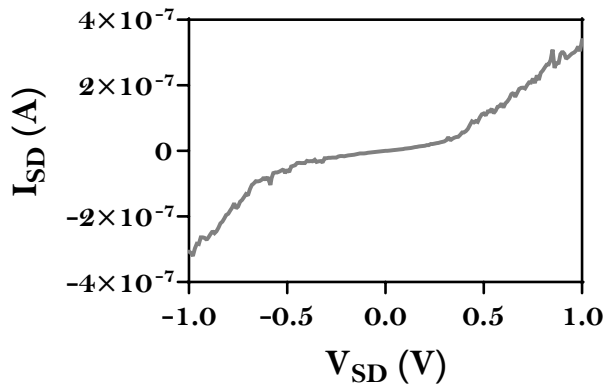


Figure 4.20. Typical I-V curve recorded for bare graphene electrodes separated by a nanometer size gap.

I-V curves obtained for nanogap opened devices display a characteristic “S” shape, as Figure 4.20. shows. This is observed for high negative and positive voltage, as a consequence of the electron tunnelling current detected between the graphene electrodes due to their close proximity (1-2 nm). An estimation of the gap size can be obtained by applying the Simmons model<sup>43</sup>, which suggests a nanogap value of only few nm width.

Besides the thoroughly electrical characterization, SEM and AFM experiments, observable in Figure 4.21 before a) and after b), c) electroburning, are performed to visualise the gap.

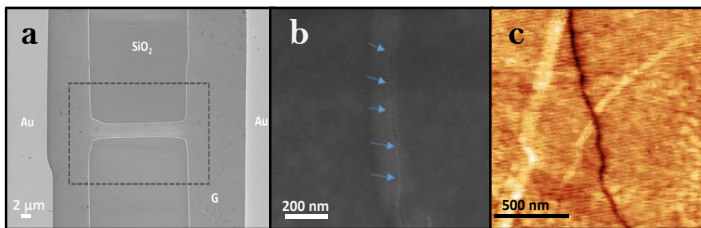


Figure 4.21. SEM images of the device a) before electroburning and b) after electroburning. c) AFM picture of the nanogap.

#### 4.3.3.2. Deposition of **6** over three terminal devices

Prior molecular deposition over the device, two different techniques were investigated in order to optimise the single-molecule anchoring conditions of compound **6** onto graphene substrates: dip coating and drop casting. Initially a 2 mM solution of PeICCMoid in TCE was prepared. However, due to the insolubility of the compound, we filtered the dispersion after sonication reaching an unknown concentration solution. Subsequently, two graphene substrates were functionalised with compound **6**, one by drop casting and the other by dip coating. While the drop casting technique consist on the deposition of a drop on the substrate, dip coating involves the complete immersion of the substrate in a solution of the desired compound. In both cases, hence, 1 h after the deposition of the drop or the immersion of the substrate, the graphene surface was rinsed with TCE and dried at room temperature for 30 minutes. Finally, it was dried under vacuum for other 30 minutes to remove any remaining traces of the solvent.

The morphology of the surfaces was explored by SEM and AFM which images are shown in Figure 4.22. It is observed the aggregation of the molecule in the AFM and SEM pictures of the drop casted surface (Figure 4.22 a and c) while the modified by dip coating (b and d) exhibit less aggregation and cleaner surfaces, closer to what should be expected in the single molecule regime. Therefore, the further depositions of **6** on the three-terminal device were performed by dip coating.



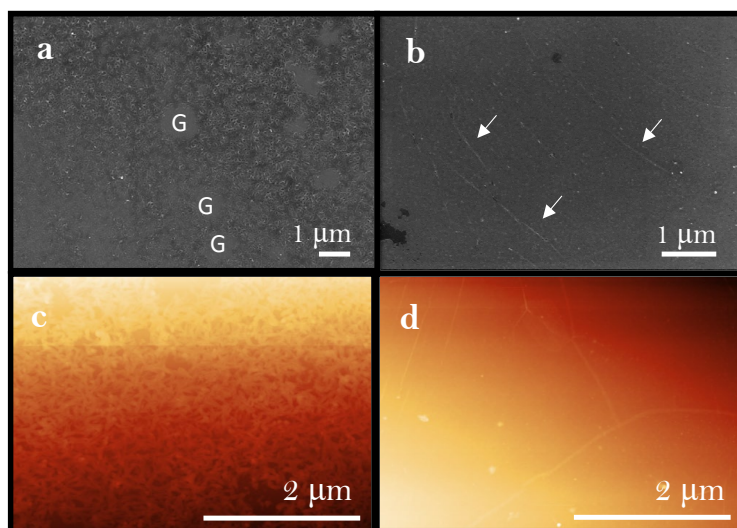


Figure 4.22. SEM and AFM images of drop casted (a,c) and dip coated (b,d) graphene surfaces with solutions of compound **6** in TCE.

The functionalization process of the three-terminal device was conducted in a similar manner than the deposition of peICCMoid on the graphene surfaces. The device was immersed in a solution of **6** (resulting from the filtration of the 2 mM dispersion) for 1 h. Afterwards it was dried for 30 minutes in air and for 30 minutes in vacuum. Finally, it was electrically characterised at room temperature. Usually, two types of electrical measurements are conducted after the anchoring of the molecule. The first series of measurements includes the application of a voltage between the source and drain, to analyse changes in the current, while the second set of experiments consist on the exploration of the source-drain current dependence with the gate, in order to confirm that the changes in the current can be attributed to molecular effects.

The I-V curves of the device before and after the incubation of the molecule are shown in Figure 4.23. There is a clear increase in the current, about 2 orders of magnitude, after the introduction of the CCMoid. However, the

second set of experiments involving of the gate voltage were not carried out and we could not confirm the current increase was related to compound **6**.

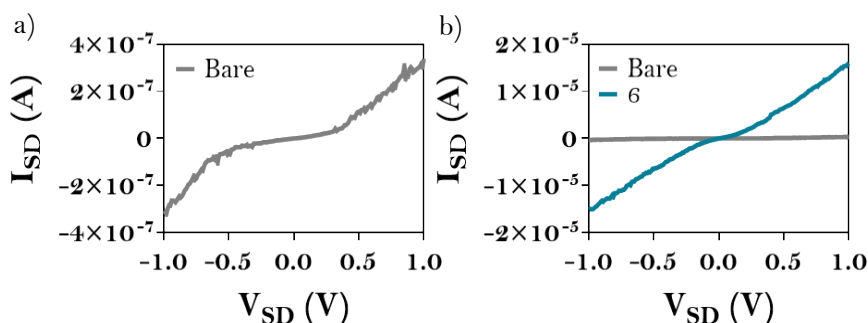


Figure 4.23. I-V curve performed at room temperature and zero gate voltage for the device a) before the molecular deposition and b) after the deposition.

The gate dependence measurements were planned to be conducted, however, in the process, several deposition experiments by dip coating were performed onto graphene substrates and the surface investigated by AFM and SEM. Surprisingly, the pictures collected, displayed in Figure 4.24, differed from the initial obtained, by the appearance of long tangled wires and aggregates. To discard any change in the state of the molecule (solid state), we performed UV-Vis absorption measurements in TCE and now it was observed a splitting and shift of the absorption band compared to the initial peICCMoid. The new bands were hypsochromic shifted to 451 and 475 nm, which coincide with the band of peCHO. Additionally, a shoulder at 444 nm appeared, in agreement with the NH<sub>2</sub>CCMoid band, as Figure 4.25 reveals. These changes indicate the fragmentation of the imide bond of peICCMoid giving as a result the starting materials of the reaction, peCHO and NH<sub>2</sub>CCMoid, and showing that with our methodology compound **6** was unstable after a short period of time in solid state. As a possibility, the knotted wires observed in the microscopes, could be the result of Van der Waals interactions between the amine and the aldehyde resulting from the decomposition.

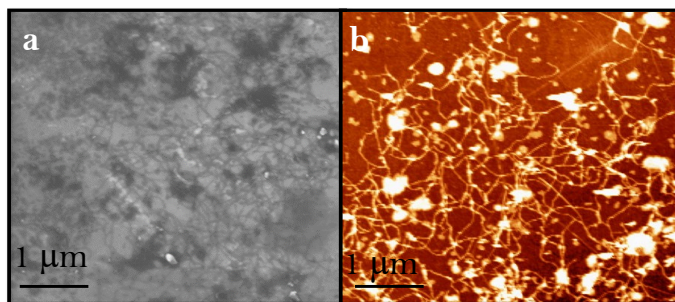


Figure 4.24. SEM and AFM of old **6** anchored onto graphene surfaces.

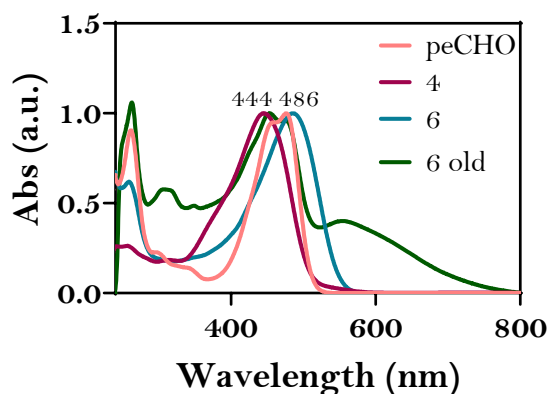
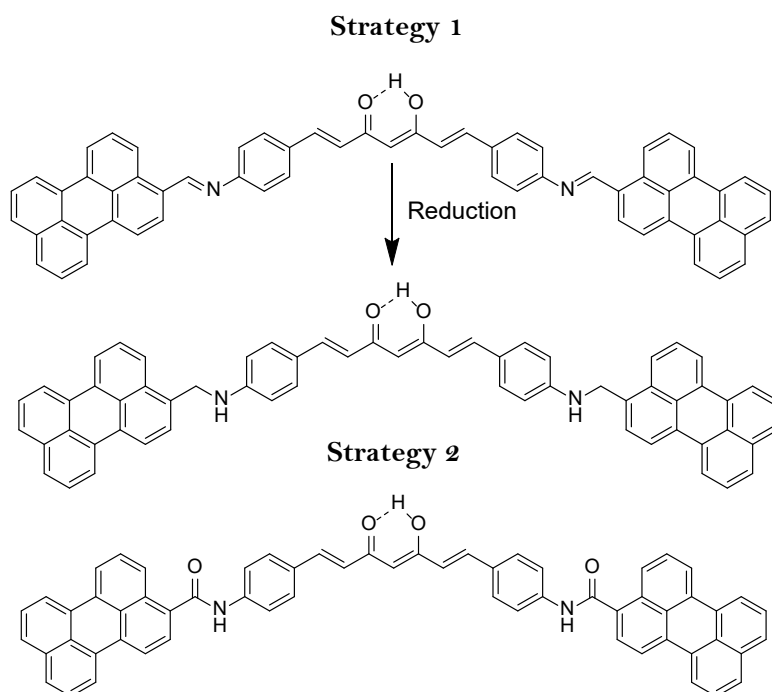


Figure 4.25. UV-Vis spectra comparison of peCHO, **4**, fresh and old **6**.

The instability of peICCMoid was also observed in solution, specifically in TCE- $d_2$  with time, detected by  $^1H$  NMR. Owing to this unstable behaviour, we did not proceed with any further electrical characterization until the achievement of a more stable compound.

In order to synthesize a stable CCMoid comprising perylene arms, we proposed two alternatives, displayed in Scheme 4.4. On the one hand we explored chemical reduction of the imine group present in **6** to an amine group. On the other hand, the second strategy included the creation of an amide bond instead of the imine functional group.



Scheme 4.4. Proposed strategies for the isolation of stable perylene containing CCMoids.

#### 4.3.3.3. Strategy 1 for the obtaining of stable perylene-based CCMoids: Reduction of compound 6

Due to the limited solubility of compound **6**, the first approach we tested, for reducing the imine group, was in presence of  $\text{NaBH}_3\text{CN}$ , a common reducing agent used in the transformation of imines to amines <sup>44</sup>, in TCE, where the compound was partially soluble, ideally leading to the structure shown in Figure 4.26. However, the resulting product of the reaction one day after, whose  $^1\text{H}$  NMR is shown in Figure A4.3. Annex IV, was a mixture of peCHO, compound **4**, and peICCMoid, indicating the hydrolysis of the

imide bond, corroborating one more time the low stability of the product in this organic solvent.

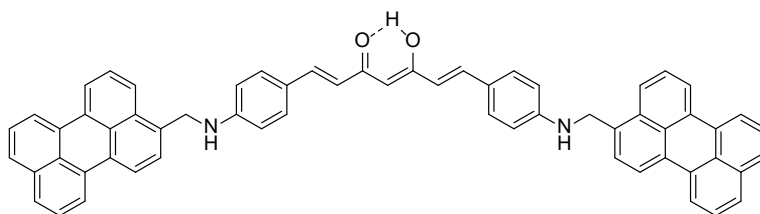


Figure 4.26. Structural representation of reduced compound **6**.

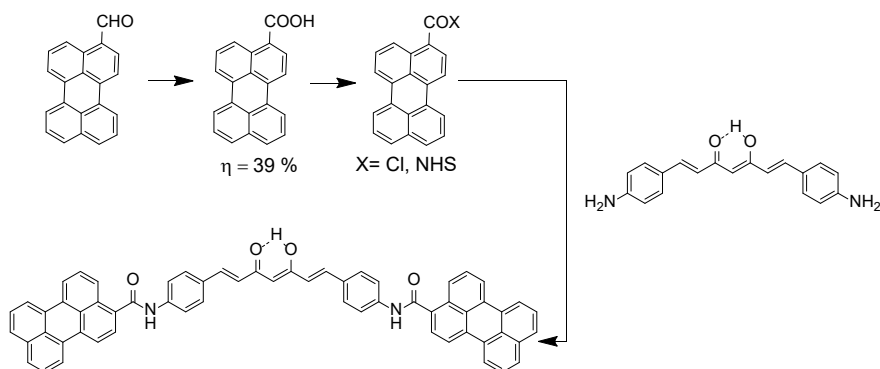
Taking advantage of the solubility of  $\text{NaBH}_3\text{CN}$  in MeOH and EtOH,<sup>45</sup> the second synthetic procedure followed did not involve the isolation of peICCMoid as before, but the addition of  $\text{NaBH}_3\text{CN}$  in the reaction mixture once compound **6** has been formed. Hereby, 3-perylenecarboxyaldehyde was mixed with compound **4** in presence of AcOH using EtOH as solvent for 5 days under reflux and afterwards  $\text{NaBH}_3\text{CN}$  was introduced in the reaction mixture, leaving it for 1 more day. The structures of the final compounds were elucidated by  $^1\text{H}$  NMR (Annex IV, Figure A4.4) revealing the presence of perylene-3-yl-methanol as a new compound, owing to the reduction of the aldehyde group of 3-perylenecarboxyaldehyde into alcohol.

The insufficient stability of **6** prevented the modification of the imine bond by the proposed methodology, leading to the research of additional alternatives to design stable perylene-based CCMoids.

#### 4.3.3.4. Strategy 2 for the obtaining of stable perylene-based CCMoids: Creation of amide bond

Amide bonds are known to be more stable and harder to hydrolyse than imines, therefore the second strategy suggested for creating a robust perylene based CCMoid, was the introduction of an amide linkage in the

final product. The isolation of the compound implied three steps, outlined in Scheme 4.5, the oxidation of the aldehyde contained in 3-perylenecarboxaldehyde into an acid group, followed by the activation of the acid for the subsequent nucleophilic substitution with the amino groups of the  $\text{NH}_2\text{CCMoid}$ , which act as nucleophiles in the reaction to obtain the desired formation of the amide bond.



Scheme 4.5. Proposed synthetic pathway for the synthesis of amide perylene based CCMoid.

Regarding the transformation of the aldehyde into the acid functionality in the position 3 of perylene, the optimal oxidation conditions were found after several failed attempts owing to the low solubility of 3-perylenecarboxaldehyde, using  $\text{NaOCl}$  in pyridine<sup>46</sup>, bromine in basic media<sup>47</sup> or potassium permanganate in presence of a base in a mixture of  $\text{H}_2\text{O}$ :acetone which led into the unintended achievement of 4-(perylene-3-yl)but-3-en-2-one, exposed in Figure A4.5 (See Annex IV). Finally, the most suitable conditions for the obtaining of 3-perylenecarboxylic acid in 39% was in presence of  $\text{KMnO}_4$  in a mixture of acetone: Milli-Q water (1:1) adding almost 22 equivalents more of solvent than the reported for similar compounds<sup>48</sup>.

For the following step, distinct molecules have been typically analysed as coupling agents for the condensation reaction between the acid and the amine <sup>49,50</sup>, being dicyclohexyl carbodiimide (DCC) and thionyl chloride the most used ones <sup>51</sup>. Instead of DCC, the commonly known as EDC, has been employed with non-soluble bulkier conjugated systems, such as carbon nanotubes in presence of the stabilizer NHS <sup>24,52</sup>. Due to similar behaviour in terms of composition and insolubility, we tried the activation of the acid under the former conditions, with EDC, NHS in DMF for the subsequent reaction with NH<sub>2</sub>CCMoid. The <sup>1</sup>H NMR of the reaction reveals the presence of the intermediate product after the activation with EDC, NHS (see Figure A4.6. Annex IV). However, there was no sign of further reaction with the NH<sub>2</sub>CCMoid, suggesting that the low basicity of the amine (pK<sub>a</sub> aniline = 4.7) makes NH<sub>2</sub>CCMoid a weak nucleophile, not strong enough to attack the carbonyl functionality.

More drastic conditions, involving the use of SOCl<sub>2</sub>, were tested to trigger the nucleophilic reaction. The acid group was transformed, in presence of an excess of thionyl chloride (SOCl<sub>2</sub>), into an acid chloride <sup>53</sup>. This step was necessary because the chloride ion acts as an excellent leaving group in the subsequent nucleophilic substitution with the amino groups of the NH<sub>2</sub>CCMoid, which was carried out in presence of triethylamine in dry DCM, THF and also in anhydrous DMF to increase the solubility, all dry to avoid the hydrolysis of the freshly formed acyl chloride.

While DMF resulted incompatible with the possible traces of SOCl<sub>2</sub> remained in the mixture leading into undesired reactions between SOCl<sub>2</sub> and DMF <sup>54</sup>, DCM and THF produced similar mixtures of compounds. The <sup>1</sup>H NMR spectrum exposed in Figure A4.7. Annex IV demonstrates the presence of peCOOH, NH<sub>2</sub>CCMoid, and other compound difficult to elucidate its structure due to the overlapping of the signals. However, the appearance of the signal at 10.89 suggested the presence of an amide bond, although no more peaks attributed to a new CCMoid skeleton were detected

specially because of the insolubility of the compound in the deuterated solvents, which prevent an easy recognition of the NMR signals.

On the other hand, the use of microwave (MW) radiation in organic synthesis has been extensively studied owing to its advantages, such as faster reactions, successful solventless reactions or higher yields derived from the selective and homogeneous heating of the organic species due to their ability to absorb the MW radiation <sup>55,56,57</sup>.

In this specific case, our purpose was to find out whether the MW radiation would help to the accomplishment of the reaction overcoming the limitations of the low solubility of the reactants. First, the acid was modified with SOCl<sub>2</sub>, with conventional heating and afterwards, it was placed in a MW vial with NH<sub>2</sub>CCMoid and triethylamine in THF. The reaction was conducted at 60 °C for 90 minutes and characterized by <sup>1</sup>H NMR, shown in Figure A4.8. in Annex IV. The obtained spectrum was comparable with the previously characterized under conventional conditions, being the MW one cleaner than the former. Both show the proton corresponding to the amide bond, non-well defined overlapped aromatic signals with no presence of CCMoid backbone signals. According to the results, in this specific case, due to the insolubility of the perylene derivatives, the perylene containing CCMoid was not possible to be isolated and characterized by conventional or MW heating.

As it has been expressed along this chapter, experiments involving perylene CCMoid derivatives have been governed by the insolubility and instability of the compounds. These facts evolved into a reconsideration and improvement of the design of PAH-based CCMoid incorporating stable linkages with smaller soluble PAHs exposed in the next chapter.



## 4.4. Conclusions

- First attempts suggested no-significant modifications of acid functionalised SWCNTs with the specific amino terminal CCMoid, **4**. Additionally, due to the challenging control on the isolation of a single CNT-CCMoid-CNT junction as well as the complicate deposition of the single system on the device, no further studies were performed.
- The freshly isolated PAH-CCMoid based on perylene, peICCMoid was tested as nanowire in the graphene-based devices with a consequent increase in conductivity about two orders of magnitude compared with the bare device. Gate dependence measurements were not carried out owing to the instability of the compound caused by the reversible imine linkage.
- Dip coating deposition technique promoted the obtaining of cleaner graphene surfaces, closer to the single-molecule regime than drop casting graphene surfaces demonstrated by SEM and AFM images.
- The instability of compound **6** produced long entangled wires on graphene substrates detected by SEM and AFM differing from the morphology of the freshly synthesized PeICCMoid deposited on the same surfaces.
- The unstable character along with the insolubility of **6** in the analysed solvents hampered the synthesis and proper characterization of stable compounds containing perylene, by the proposed strategies, either for reduction of the imine into amide bond or through the creation of an amide bond.
- MW heating seems to work more favourable for the creation of stable amide bonds than conventional heating, with no confirmation of the isolation of the desired final CCMoid owing to the difficult characterization due to its insolubility.

## 4.5. Experimental section

### Purification CNTs

400 mg of commercially available CNTs, previously milled, were treated in in collaboration with Dr. Stefania Sandoval and Dr. Gerard Tobias in a purged with Ar tubular furnace with water steam at 900 °C for 4 h. Afterwards, when the sample was cooled down at room temperature, it was extracted from the furnace and refluxed at 110 °C in 100 mL of 6 M HCl for 8 h. Finally, the mixture was filtered through polycarbonate filters, rinsed with Milli-Q water until neutral pH and dried in the oven at 60 °C.

### Acid functionalization of CNTs, afCNTs

The purified CNTs obtained in the step explained above were added into a 150 mL of 3 M HNO<sub>3</sub> solution. Subsequently, the mixture was heated up at 130 °C for 45 h. Finally, when cooled down to ambient temperature, it was filtered through PC filter, washed with Milli-Q water until reaching pH 7 and dried in the oven at 60 °C to obtain 238 mg of afCNTs.

### CCMoid functionalization of CNTs

20 mg of afCNTs were mixed with 19.17 mg EDC and 17.26 mg NHS (0.1 mmol; 0.15 mmol) in 5 mL of anhydrous DMF for 45 minutes at room temperature. Afterwards, 1.21 mg of NH<sub>2</sub>CCMoid, **4** (3.95 μmol) were added into the mixture flask. After 72 h at room temperature, the solvent was evaporated and the mixture dispersed in 10 mL of MeOH and left stirring for 1 h. Finally, it was filtered over polycarbonate filter and washed vigorously with MeOH and CHCl<sub>3</sub>.

## FT-IR CNTs

CNTs were deposited onto ZnSe pellets by drop casting of an isopropanol dispersion followed by solvent evaporation heating the pellet at 80 °C.

## TEM sample preparation

A dispersion of CNTs in isopropanol was prepared and some drops were deposited on a Cu grid with holes and a C membrane, used as support. The solvent was evaporated at open air.

## Synthesis of peICCMoid, **6**.

A solution of 191.3 mg of NH<sub>2</sub>CCMoid, **4** (0.62 mmol) in 60 mL of EtOH were added into a dispersion of 350 mg 3-perylenecarboxaldehyde (1.25 mmol) in 60 mL of EtOH previously heated at 60 °C. Subsequently, 6 drops of AcOH were poured into the mixture, and refluxed for 5 days. Finally, the reaction was filtered off, washed several times with hot CHCl<sub>3</sub> and dried with Et<sub>2</sub>O to obtain **6** as red solid in 47 % yield. <sup>1</sup>H NMR (400 MHz, TCE-d<sub>2</sub>)  $\delta$ : 9.07 (s) 9.03 (d, <sup>3</sup>J=9.9 Hz), 8.37 (m) 8.16 (m), 7.83 (m), 7.72 (m), 7.60 (m), 7.39 (d, <sup>3</sup>J=7.25 Hz), 6.73 (d, <sup>3</sup>J=16.52 Hz). MS MALDI - TOF (m/z) calcd for peICCMoid: 830.3 [M<sup>+</sup>]; found: 829.2 [M-1].

## Synthesis of 3-perylenecarboxylic acid

A solution of KMnO<sub>4</sub> (540 mg, 3.4 mmol) in 60 mL of Milli-Q water was mixed with a dispersion of 1-perylenecarboxaldehyde (250 mg, 0.89 mmol) in 60 mL acetone. After being refluxed for 24 h, the mixture was filtered off and washed several times with DCM. Finally, the aqueous phase was

acidified until reaching  $\text{pH} = 2$  and centrifuged to isolate the product in 39% yield.  $^1\text{H}$  NMR (400 MHz,  $\text{DMSO-d}_6$ )  $\delta$ : 13.13 (b, 1H) 8.82 (1H, d,  $^3J=8.5$  Hz), 8.49 (4H, m,  $^3J=7.9$  Hz) 8.16 (1H, d,  $^3J=7.9$  Hz), 7.92 (1H, d,  $^3J=8.1$  Hz), 7.87 (1H, d,  $^3J=8.2$  Hz) 7.70 (1H, t,  $^3J=7.9$  Hz), 7.63 (2H, m,  $^3J=5.0$  Hz).

## Annex IV

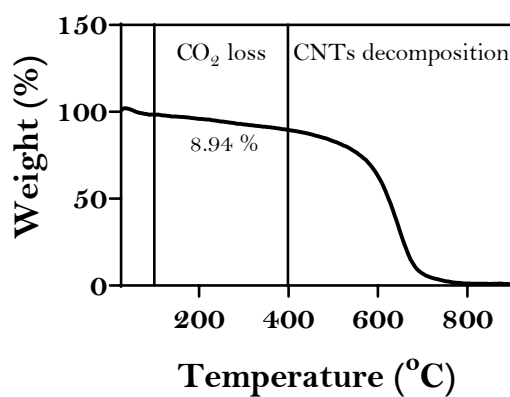


Figure A4.1. TGA of afCNTs.

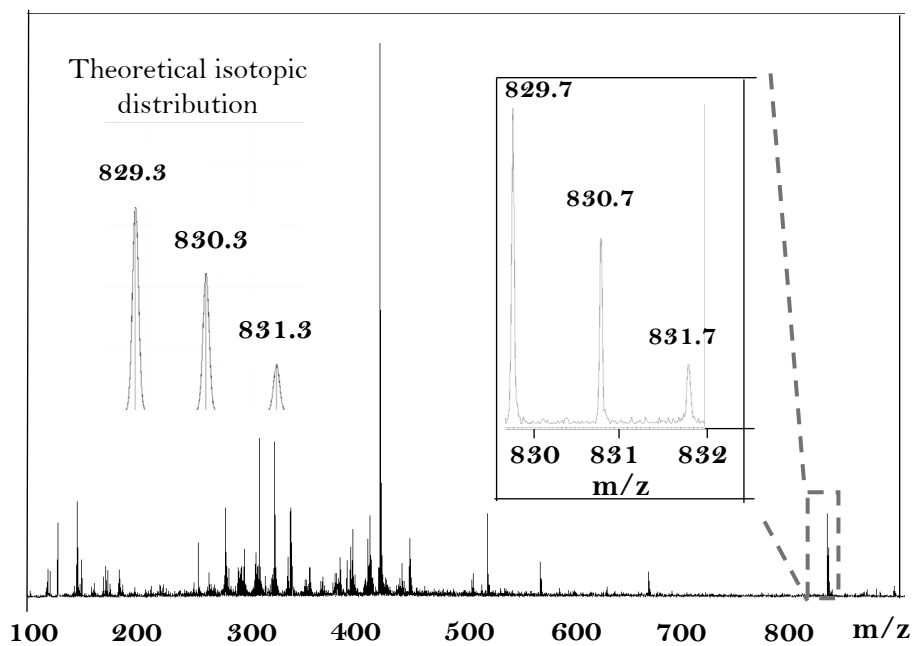


Figure A4.2. MALDI-TOF spectrum of compound 6 in negative mode.

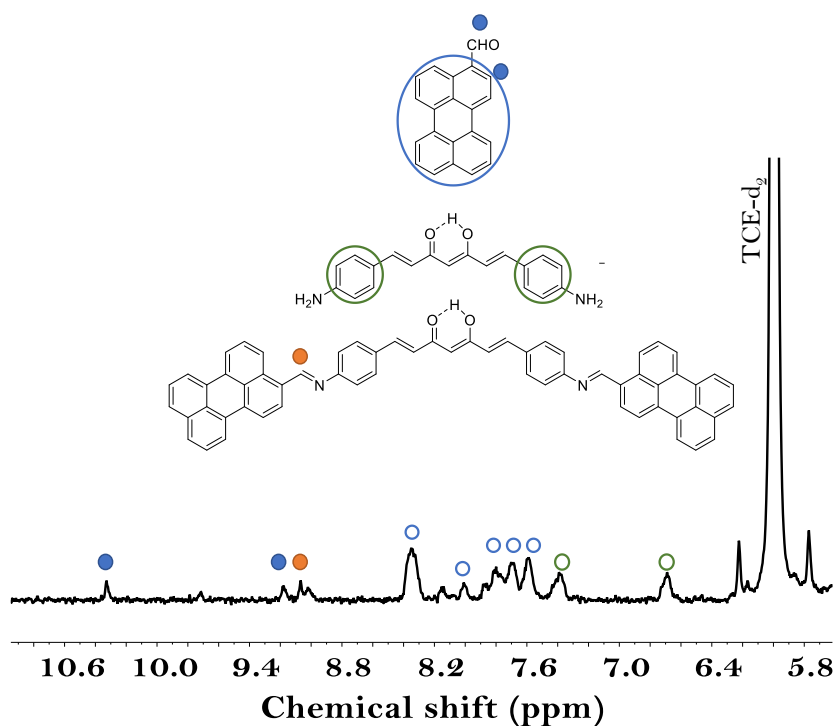


Figure A4.3.  $^1\text{H}$  NMR spectrum in  $\text{TCE-d}_2$  of the product obtained in the 24 h reduction reaction of **6** in TCE in presence of  $\text{NaBH}_3\text{CN}$ .

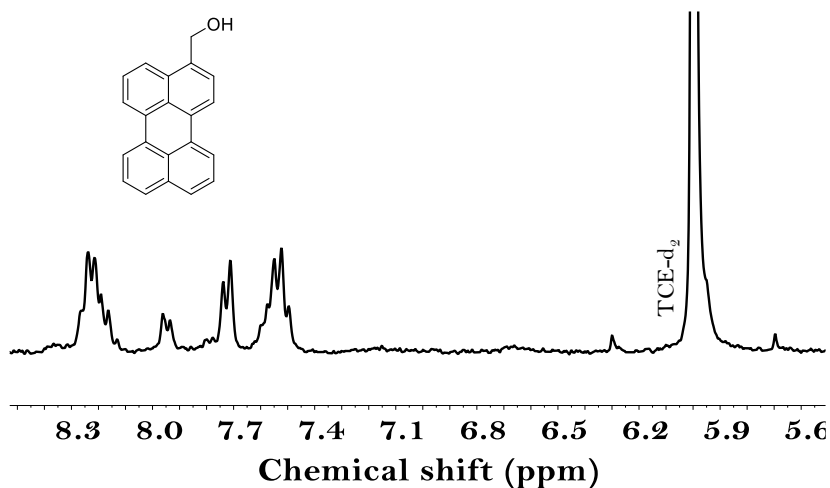


Figure A4.4.  $^1\text{H}$  NMR spectrum of perylene-3-yl-methanol in  $\text{TCE-d}_2$ , synthesised in the reduction reaction of non-isolated **6** in EtOH with  $\text{NaBH}_3\text{CN}$ .

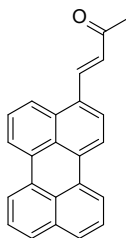


Figure A4.5. Chemical structure of 4-(perylene-3-yl)but-3-en-2-one isolated by the oxidation of 3-perylenecarboxaldehyde with potassium permanganate in presence of a base in a mixture of  $\text{H}_2\text{O}$ : acetone.

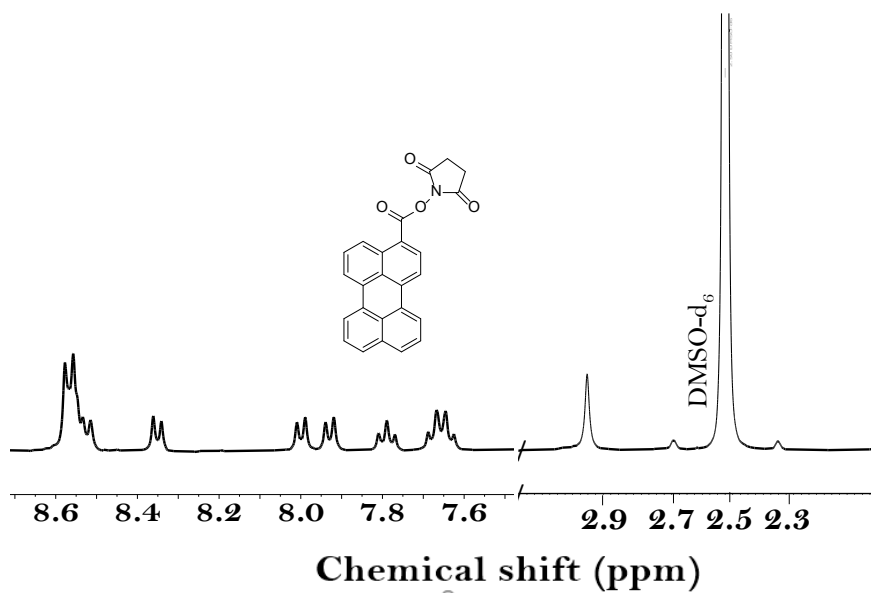


Figure A4.6.  $^1\text{H}$  NMR in  $\text{DMSO-d}_6$  of the compound isolated in the activation with EDC, NHS of 3-perylenecarboxylic acid.

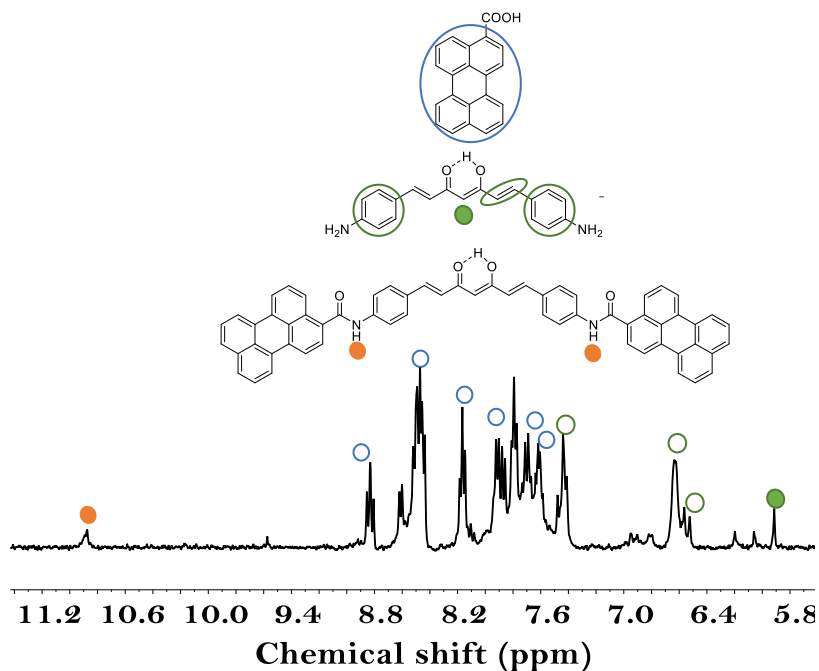


Figure A4.7.  $^1\text{H}$  NMR spectrum in  $\text{DMSO-d}_6$  of the mixture in the creation of the amide derivative compound by the reaction of  $\text{SOCl}_2$  preactivated 3-perylenecarboxylic acid and  $\text{NH}_2\text{CCMoid}$  by conventional heating in THF.

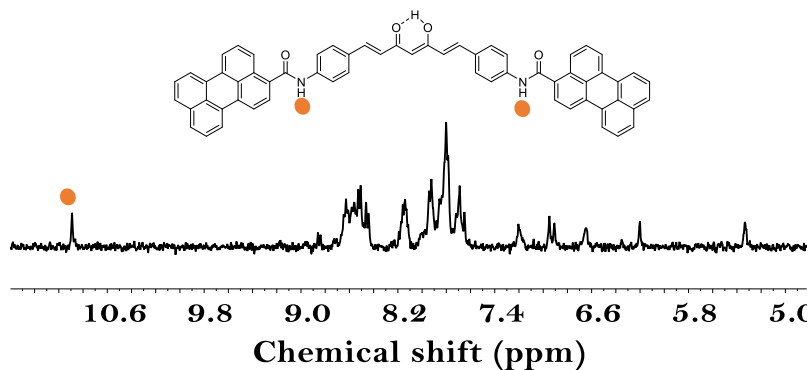


Figure A4.8.  $^1\text{H}$  NMR spectrum in  $\text{DMSO-d}_6$  of the amide derivative compound formed in the reaction of  $\text{SOCl}_2$  preactivated 3-perylenecarboxylic acid and  $\text{NH}_2\text{CCMoid}$  by MW heating in THF.



## References

- (1) Zhao, S.; Chen, H.; Qian, Q.; Zhang, H.; Yang, Y.; Hong, W. Non-Covalent Interaction-Based Molecular Electronics with Graphene Electrodes. *Nano, Res.* **2023**, *16* (4), 5436–5446
- (2) Li, Y.; Yang, C.; Guo, X. Single-Molecule Electrical Detection: A Promising Route toward the Fundamental Limits of Chemistry and Life Science. *Acc. Chem. Res.* **2020**, *53* (1), 159–169.
- (3) O'Neill, K.; Osorio, E. A.; Van Der Zant, H. S. J. Self-Breaking in Planar Few-Atom Au Constrictions for Nanometer-Spaced Electrodes. *Appl Phys Lett* **2007**, *90* (13), 133109
- (4) Prins, F.; Barreiro, A.; Ruitenbergh, J. W.; Seldenthuis, J. S.; Aliaga-Alcalde, N.; Vandersypen, L. M. K.; Van Der Zant, H. S. J. Room-Temperature Gating of Molecular Junctions Using Few-Layer Graphene Nanogap Electrodes. *Nano Lett* **2011**, *11* (11), 4607–4611.
- (5) Cao, Y.; Dong, S.; Liu, S.; He, L.; Gan, L.; Yu, X.; Steigerwald, M. L.; Wu, X.; Liu, Z.; Guo, X. Building High-Throughput Molecular Junctions Using Indented Graphene Point Contacts. *Angew. Chem. Int. Ed.* **2012**, *51* (49), 12228–12232.
- (6) Caneva, S.; Gehring, P.; García-Suárez, V. M.; García-Fuente, A.; Stefani, D.; Olavarria-Contreras, I. J.; Ferrer, J.; Dekker, C.; van der Zant, H. S. J. Mechanically Controlled Quantum Interference in Graphene Break Junctions. *Nat. Nanotechnol.* **2018**, *13*(12), 1126–1131.
- (7) Ghasemi, S.; Moth-Poulsen, K. Single Molecule Electronic Devices with Carbon-Based Materials: Status and Opportunity. *Nanoscale*, **2021**, *13*(2), 659–671.
- (8) Guo, X.; Small, J. P.; Klare, J. E.; Wang, Y.; Purewal, M. S.; Tam, I. W.; Hong, B. H.; Caldwell, R.; Huang, L.; O'brien, S.; Yan, J.;

- Breslow, R.; Wind, S. J.; Hone, J.; Kim, P.; Nuckolls, C. Covalently Bridging Gaps in Single-Walled Carbon Nanotubes with Conducting Molecules. *Science*, **2006**, *311*(5759), 356–359.
- (9) Whalley, A. C.; Steigerwald, M. L.; Guo, X.; Nuckolls, C. Reversible Switching in Molecular Electronic Devices. *J. Am. Chem. Soc.* **2007**, *129* (42), 12590–12591.
- (10) Guo, X.; Nuckolls, C. Functional Single-Molecule Devices Based on SWNTs as Point Contacts. *J. Mater. Chem.* **2009**, *19* (31), 5470–5473.
- (11) Marquardt, C. W.; Grunder, S.; Błaszczuk, A.; Dehm, S.; Hennrich, F.; Löhneysen, H. V.; Mayor, M.; Krupke, R. Electroluminescence from a Single Nanotube-Molecule-Nanotube Junction. *Nat. Nanotechnol.* **2010**, *5* (12), 863–867.
- (12) Thiele, C.; Vieker, H.; Beyer, A.; Flavel, B. S.; Hennrich, F.; Muñoz Torres, D.; Eaton, T. R.; Mayor, M.; Kappes, M. M.; Löhneysen, H. V.; Krupke, R. Fabrication of Carbon Nanotube Nanogap Electrodes by Helium Ion Sputtering for Molecular Contacts. *Appl. Phys. Lett.* **2014**, *104* (10), 103102.
- (13) Seo, M.; Kim, H.; Kim, Y. H.; Na, J.; Lee, B. J.; Kim, J. J.; Lee, I.; Yun, H.; McAllister, K.; Kim, K. S.; Jeong, G. H.; Kim, G. T.; Lee, S. W. Fabrication and Electrical Properties of Single Wall Carbon Nanotube Channel and Graphene Electrode Based Transistors Arrays. *Appl. Phys. Lett.* **2015**, *107* (3), 033103.
- (14) Wu, J.; Pisula, W.; Müllen, K. Graphenes as Potential Material for Electronics. *Chem. Rev.* **2007**, *107* (3), 718–747.
- (15) Rieger, R.; Müllen, K. Forever Young: Polycyclic Aromatic Hydrocarbons as Model Cases for Structural and Optical Studies. *J. Phys. Org. Chem.* **2010**, *23* (4), 315–325.

- (16) Li, X.; Hihath, J.; Chen, F.; Masuda, T.; Zang, L.; Tao, N. Thermally Activated Electron Transport in Single Redox Molecules. *J. Am. Chem. Soc.* **2007**, *129* (37), 11535–11542.
- (17) Li, C.; Mishchenko, A.; Li, Z.; Pobelov, I.; Wandlowski, T.; Li, X. Q.; Würthner, F.; Bagrets, A.; Evers, F. Electrochemical Gate-Controlled Electron Transport of Redox-Active Single Perylene Bisimide Molecular Junctions. *J. Condens. Matter Phys.* **2008**, *20* (37), 374122.
- (18) Frisenda, R.; Parlato, L.; Barra, M.; van der Zant, H. S. J.; Cassinese, A. Single-Molecule Break Junctions Based on a Perylene-Diimide Cyano-Functionalized (PDI8-CN<sub>2</sub>) Derivative. *Nanoscale Res. Lett.* **2015**, *10* (1) 1-7.
- (19) Zhou, J.; Wang, K.; Xu, B.; Dubi, Y. Photoconductance from Exciton Binding in Molecular Junctions. *J. Am. Chem. Soc.* **2018**, *140* (1), 70–73.
- (20) El Abbassi, M.; Perrin, M. L.; Barin, G. B.; Sangtarash, S.; Overbeck, J.; Braun, O.; Lambert, C. J.; Sun, Q.; Pechtl, T.; Narita, A.; Müllen, K.; Ruffieux, P.; Sadeghi, H.; Fasel, R.; Calame, M. Controlled Quantum Dot Formation in Atomically Engineered Graphene Nanoribbon Field-Effect Transistors. *ACS Nano* **2020**, *14* (5), 5754–5762.
- (21) Limburg, B.; Thomas, J. O.; Holloway, G.; Sadeghi, H.; Sangtarash, S.; Hou, I. C. Y.; Cremers, J.; Narita, A.; Müllen, K.; Lambert, C. J.; Briggs, G. A. D.; Mol, J. A.; Anderson, H. L. Anchor Groups for Graphene-Porphyrin Single-Molecule Transistors. *Adv. Funct. Mater.* **2018**, *28* (45), 1803629.
- (22) Burzurí, E.; Island, J. O.; Díaz-Torres, R.; Fursina, A.; González-Campo, A.; Roubeau, O.; Teat, S. J.; Aliaga-Alcalde, N.; Ruiz, E.; Van Der Zant, H. S. J. Sequential Electron Transport and Vibrational Excitations in an Organic Molecule Coupled to Few-Layer Graphene Electrodes. *ACS Nano* **2016**, *10* (2), 2521–2527.

- (23) Kierkowicz, M.; Pach, E.; Santidrián, A.; Sandoval, S.; Gonçalves, G.; Tobías-Rossell, E.; Kalbáč, M.; Ballesteros, B.; Tobias, G. Comparative Study of Shortening and Cutting Strategies of Single-Walled and Multi-Walled Carbon Nanotubes Assessed by Scanning Electron Microscopy. *Carbon* **2018**, *139*, 922–932.
- (24) Sung, Y. H.; Tobias, G.; Ballesteros, B.; El Oualid, F.; Errey, J. C.; Doores, K. J.; Kirkland, A. I.; Nellist, P. D.; Green, M. L. H.; Davis, B. G. Atomic-Scale Detection of Organic Molecules Coupled to Single-Walled Carbon Nanotubes. *J. Am. Chem. Soc.* **2007**, *129* (36), 10966–10967.
- (25) Rance, G. A.; Marsh, D. H.; Nicholas, R. J.; Khlobystov, A. N. UV-Vis Absorption Spectroscopy of Carbon Nanotubes: Relationship between the  $\pi$ -Electron Plasmon and Nanotube Diameter. *Chem. Phys. Lett.* **2010**, *493* (1–3), 19–23.
- (26) Hu, C.; Chen, Z.; Shen, A.; Shen, X.; Li, J.; Hu, S. Water-Soluble Single-Walled Carbon Nanotubes via Noncovalent Functionalization by a Rigid, Planar and Conjugated Diazo Dye. *Carbon* **2006**, *44* (3), 428–434.
- (27) Cabana, L.; González-Campo, A.; Ke, X.; Van Tendeloo, G.; Núñez, R.; Tobias, G. Efficient Chemical Modification of Carbon Nanotubes with Metallacarboranes. *Chem. Eur. J.* **2015**, *21* (47), 16792–16795.
- (28) Dresselhaus, M. S.; Dresselhaus, G.; Saito, R.; Jorio, A. Raman Spectroscopy of Carbon Nanotubes. *Phys. Rep.* **2005**, *409*(2), 47–99.
- (29) Jorio, A.; Saito, R.; Hafner, J. H.; Lieber, C. M.; Hunter, M.; McClure, T.; Dresselhaus, G.; Dresselhaus, M. S. Structural (n, m) Determination of Isolated Single-Wall Carbon Nanotubes by Resonant Raman Scattering. *Phys. Rev. Lett.* **2001**, *86* (6), 1118–1121.

- (30) Dresselhaus, M. S.; Dresselhaus, G.; Jorio, A.; Filho, A. G. S.; Saito, R. R. Raman Spectroscopy on Isolated Single Wall Carbon Nanotubes. *Carbon*, **2002**, 40(12), 2043–2061.
- (31) Arnold, M. S.; Green, A. A.; Hulvat, J. F.; Stupp, S. I.; Hersam, M. C. Sorting Carbon Nanotubes by Electronic Structure Using Density Differentiation. *Nat. Nanotechnol.* **2006**, 1 (1), 60–65.
- (32) Qin, W.; Long, S.; Panunzio, M.; Biondi, S. Schiff Bases: A Short Survey on an Evergreen Chemistry Tool. *Molecules*. **2013**, 18(10), 12264–12289.
- (33) Ascherl, L.; Evans, E. W.; Gorman, J.; Orsborne, S.; Bessinger, D.; Bein, T.; Friend, R. H.; Auras, F. Perylene-Based Covalent Organic Frameworks for Acid Vapor Sensing. *J. Am. Chem. Soc.* **2019**, 141 (39), 15693–15699.
- (34) Ding, L.; Schulz, P.; Farahzadi, A.; Shportko, K. V.; Wuttig, M. Investigation of Intermolecular Interactions in Perylene Films on Au(111) by Infrared Spectroscopy. *Chem. Phys.* **2012**, 136 (5), 054503.
- (35) Maddams, W. F.; Royaud, I. A. M. The Characterization of Polycyclic Aromatic Hydrocarbons by Raman Spectroscopy. *Spectrochim. Acta A: Mol. Spectrosc.* **1990**, 46 (2), 309–314
- (36) Dai, W.; Shao, F.; Szczerbiński, J.; McCaffrey, R.; Zenobi, R.; Jin, Y.; Schlüter, A. D.; Zhang, W. Synthesis of a Two-Dimensional Covalent Organic Monolayer through Dynamic Imine Chemistry at the Air/Water Interface. *Angew. Chem. Int. Ed.* **2016**, 55 (1), 213–217.
- (37) Wei, D.; Chen, S.; Liu, Q. Review of Fluorescence Suppression Techniques in Raman Spectroscopy. *Appl. Spectrosc. Rev.* **2015**, 50 (5), 387–406.
- (38) Nardo, L.; Andreoni, A.; Masson, M.; Haukvik, T.; Tønnesen, H. H. Studies on Curcumin and Curcuminoids. XXXIX. Photophysical

- Properties of Bisdemethoxycurcumin. *J. Fluoresc.* **2011**, *21* (2), 627–635.
- (39) Garcia, M. P. B.; Martin, C. S.; Kavazoi, H. S.; Maximino, M. D.; Alessio, P. Perylene Nanostructured Films Optimization for Organic Electronics: Molecular, Structural, and Electrochemical Characterization. *Thin Solid Films* **2023**, 777, 139895.
- (40) Lau, C. S.; Mol, J. A.; Warner, J. H.; Briggs, G. A. D. Nanoscale Control of Graphene Electrodes. *Phys. Chem. Chem. Phys.* **2014**, *16* (38), 20398–20401.
- (41) Briggs, G. A. D.; Mol, J. A. Method for Forming Nano-Gaps in Graphene. WO 2016/005726 A1, January 14, **2016**.
- (42) El Abbassi, M.; Pósa, L.; Makk, P.; Nef, C.; Thodkar, K.; Halbritter, A.; Calame, M. From Electroburning to Sublimation: Substrate and Environmental Effects in the Electrical Breakdown Process of Monolayer Graphene. *Nanoscale* **2017**, *9* (44), 17312–17317.
- (43) Simmons, J. G. Generalized Formula for the Electric Tunnel Effect between Similar Electrodes Separated by a Thin Insulating Film. *J. Appl. Phys.* **1963**, *34* (6), 1793–1803.
- (44) Borch, R. F., Bernstein, M. D., & Durst, H. D. Cyanohydridoborate anion as a selective reducing agent. *J. Am. Chem. Soc.* **1971**, *93*(12), 2897–2904.
- (45) Zhu, X.; Yang, Y.; Xiao, G.; Song, J.; Liang, Y.; Deng, G. Double C-S Bond Formation: Via C-H Bond Functionalization: Synthesis of Benzothiazoles and Naphtho[2,1-d] Thiazoles from N-Substituted Arylamines and Elemental Sulfur. *Chem. Commun.* **2017**, *53* (87), 11917–11920.
- (46) Babu, P.; Sangeetha, N. M.; Vijaykumar, P.; Maitra, U.; Rissanen, K.; Raju, A. R. Pyrene-Derived Novel One- and Two-Component Organogelators. *Chem. Eur. J.* **2003**, *9* (9), 1922–1932.

- (47) Takaishi, K.; Iwachido, K.; Takehana, R.; Uchiyama, M.; Ema, T. Evolving Fluorophores into Circularly Polarized Luminophores with a Chiral Naphthalene Tetramer: Proposal of Excimer Chirality Rule for Circularly Polarized Luminescence. *J. Am. Chem. Soc.* **2019**, *141* (15), 6185–6190.
- (48) Liu, T.; Huang, Z.; Feng, R.; Ou, Z.; Wang, S.; Yang, L.; Ma, L. J. An Intermolecular Pyrene Excimer-Based Ratiometric Fluorescent Probes for Extremely Acidic PH and Its Applications. *Dyes Pigm.* **2020**, *174*, 108102.
- (49) Montalbetti, C. A. G. N.; Falque, V. Amide Bond Formation and Peptide Coupling. *Tetrahedron*. 2005, *61*(46), 10827–10852.
- (50) Valeur, E.; Bradley, M. Amide Bond Formation: Beyond the Myth of Coupling Reagents. *Chem. Soc. Rev.* **2009**, *38* (2), 606–631.
- (51) Sabatini, M. T.; Boulton, L. T.; Sneddon, H. F.; Sheppard, T. D. A Green Chemistry Perspective on Catalytic Amide Bond Formation. *Nat. Catal.* **2019**, *2* (1), 10–17.
- (52) Xu, Q.; Scuri, G.; Mathewson, C.; Kim, P.; Nuckolls, C.; Bouilly, D. Single Electron Transistor with Single Aromatic Ring Molecule Covalently Connected to Graphene Nanogaps. *Nano Lett.* **2017**, *17* (9), 5335–5341.
- (53) Tehfe, M. A.; Dumur, F.; Contal, E.; Graff, B.; Morlet-Savary, F.; Gigmes, D.; Fouassier, J. P.; Lalevée, J. New Insights into Radical and Cationic Polymerizations upon Visible Light Exposure: Role of Novel Photoinitiator Systems Based on the Pyrene Chromophore. *Polym. Chem.* **2013**, *4* (5), 1625–1634.
- (54) Knunyants, I. L.; Cheburkov, Y. A.; Aronov, Y. E. Reactions of Carboxylic Acid Chlorides with Dimethylformamide. *Russ. Chem. Bull.* **1966**, *15*, 992–996
- (55) Torres-Moya, I.; Harbuzaru, A.; Donoso, B.; Prieto, P.; Ortiz, R. P.; Díaz-Ortiz, Á. Microwave Irradiation as a Powerful Tool for the

- Preparation of N-Type Benzotriazole Semiconductors with Applications in Organic Field-Effect Transistors. *Molecules* **2022**, *27* (14), 4340.
- (56) Díaz-Ortiz; Prieto, P.; de la Hoz, A. A Critical Overview on the Effect of Microwave Irradiation in Organic Synthesis. *Chem. Rec.* **2019**, *19* (1), 85–97.
- (57) Nain, S.; Singh, R.; Ravichandran, S. *Adv. J. Chem. A.* **2019**, *2* (2), 94–104.

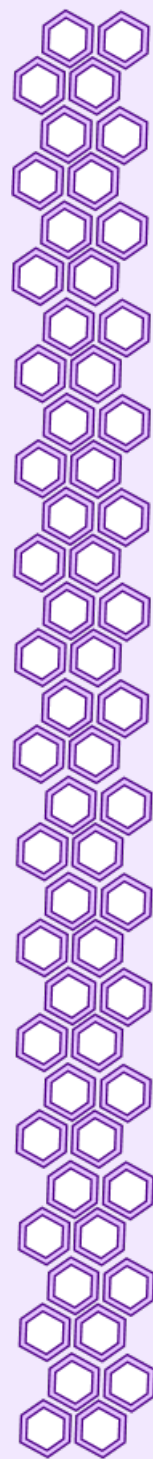




# Chapter 5

## Design of stable pyrene-based CCMoid to be used as nanowire in graphene-based three-terminal devices

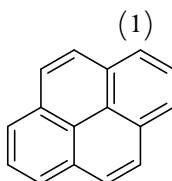
In this chapter, we describe the formation of an elongated stable PAH-based CCMoid comprising pyrene units as anchoring groups labelled as pyACCMoid. In addition, we explore the electron transport behavior of the molecule once incorporated into three-terminal devices of the type: graphene-pyACCMoid-graphene/SiO<sub>2</sub>/Si.





## 5.1. Introduction

Pyrene, the PAH unit containing 4 fused aromatic rings through more than one side, as depicted in Figure 5.1, has gathered significant attention in organic electronics due to its easier chemical mono substitution (favoured in position 1, Figure 5.1), its manageable solubility and its optical properties <sup>1</sup>.



Pyrene

Figure 5.1. Chemical structure of pyrene.

Specifically, in nanometer separated graphene-based devices, pyrene has been the preferred carbon-based group for  $\pi$ - $\pi$  interactions with graphene. For instance, Sadeghi *et al.* <sup>2</sup> did theoretical studies on the effect of different terminal coupling groups on the conductance of zinc porphyrin derivatives, including direct C-C bond, amide coupling resulting from amine functional groups,  $\pi$ -  $\pi$  interactions through substituted 1-pyrene and 2-pyrene, as illustrated in Figure 5.2. They concluded that, as expected, the covalent C-C bonding between molecule and electrodes, exhibited the highest electrical conductance, followed by  $\pi$ -  $\pi$  interactions through substituted 1-pyrene and 2-pyrene being the less conductive the amide-based anchoring system (Figure 5.2). The explanation offered was attributed to the favourable HOMO-LUMO position for the direct C-C anchoring with respect to the Fermi level of the electrodes, and a conjugation breaking when the amide bond is present placing the  $\pi$ - $\pi$  interaction in an intermediate position. The theoretical study, although thorough and necessary, is limited to

conductance-related conditions but does not take into account factors such as solubility, flexibility or stability of the ligands for real implementation focusing exclusively in the best fit between the electrodes and molecules.

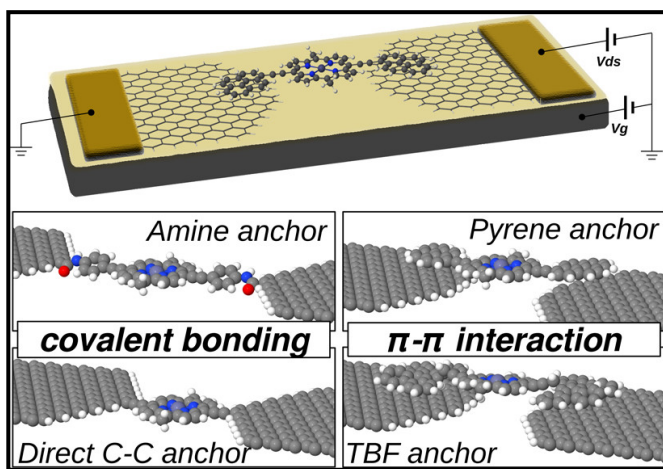


Figure 5.2. Deposition of Zn porphyrin derivatives functionalised with several anchoring groups from reference 2.

Several experimental studies with pyrene terminal groups have demonstrated their coupling with graphene electrodes involving a variety of cores, including mono- or tri-porphyrins <sup>3,4,5</sup>, fullerene units <sup>6</sup> and coordination compounds based on pyrazolyl pyridine derivative ligands <sup>7</sup>.

Li *et al.* <sup>8</sup> performed theoretical calculations regarding the binding energy between graphene and PAH units. They demonstrated a direct correlation between the number of carbons in PAHs and the binding energy, with PAHs containing higher number of benzene rings exhibiting stronger binding. However, the number of rings is inversely related to the solubility, hindering the molecular deposition of large PAH derivatives for real applications.

Due to the instability and insolubility discussed for compound **6** in Chapter 4, and with the identical purpose of enlargement of the CCMoid arms for the strengthening of the interaction between the molecule and graphene electrodes, here, we address this investigation focusing on the use of pyrene, a smaller soluble PAH than perylene but larger than anthracene, as terminal anchoring groups for the extension of the CCMoid.

## 5.2. Objectives

The aim of this chapter is the validation that starting from  $\text{NH}_2\text{CCMoid}$  we can create longer, stable, and soluble CCMoid systems reinforcing the anchoring to graphene electrodes. The final objective is the electronic study of nanogapped graphene-based device including a robust PAH-CCMoid as nanowire. In order to accomplish this general objective, the following goals were needed:

- Chemical modification of the  $\text{NH}_2\text{CCMoid}$ , **4**, with functionalized pyrene derivatives for the preparation of a longer PAH-CCMoid.
- Deposition and subsequent electronic characterization of the reliable PAH-CCMoid in the device.

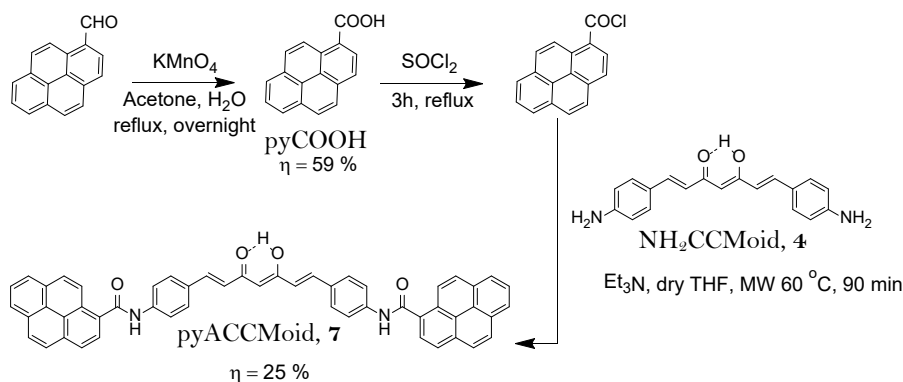
## 5.3. Results and discussion

### 5.3.1. Synthesis and characterization of pyACCMoid, **7**

#### 5.3.1.1. Synthesis of pyACCMoid, **7**

To improve the  $\pi$ - $\pi$  attachment of CCMoids with the graphene electrodes, NH<sub>2</sub>CCMoid, **4** was chemically modified, slightly adjusting the optimized conditions described in Chapter 4, by reacting the amino groups with the preactivated acid group of 1-pyrenecarboxylic acid (pyCOOH) in a microwave (MW) reactor as outlined in Scheme 5.1.

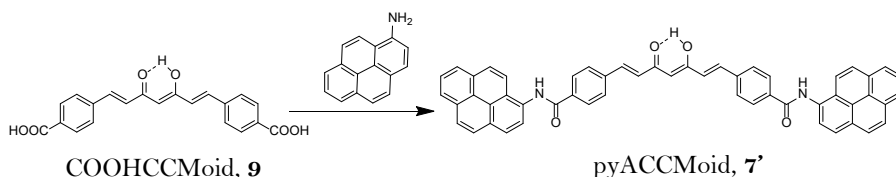
In a first reaction, pyCOOH was obtained in 59 % yield by the oxidation of the aldehyde contained in 1-pyrenecarboxaldehyde under reflux, using KMnO<sub>4</sub> as oxidising specie<sup>9</sup>, and its MALDI-TOF mass spectrum is shown in Figure A5a.1 (See Annex Va). Consequently, the acid group was transformed, in presence of an excess of thionyl chloride (SOCl<sub>2</sub>), into an acid chloride<sup>10</sup>. This intermediate compound was able to react with NH<sub>2</sub>CCMoid under MW radiation using dry THF as solvent (needed to avoid the hydrolysis of the acid chloride intermediate in presence of water) and triethylamine as base at 60 °C for 90 minutes, achieving the extended CCMoid, pyACCMoid, **7**, as a product of the reaction after a washing process with hot ACN in a 25% yield.

Scheme 5.1. Synthetic route followed for the preparation of pyACCMoid, **7**.

It is worth pointing out some special conditions involved in the last reaction. Owing to the high reactivity of the activated carbonyl compound, in general, it is well-established that the condensation between the acid and the amine is carried out at room temperature, or slightly above, in dry DCM, THF or DMF, in order to increase the solubility of the reactants <sup>9,10,11,12</sup>. However, due to the better results using MW heating observed in the <sup>1</sup>H NMR spectrum in the previous Chapter, and the MW ability to accomplish reactions between non soluble reagents <sup>13–15</sup>, we decided to conduct the NH<sub>2</sub>CCMoid coupling under MW conditions in dry THF.

An analogous version of pyACCMoid could be also designed by using 1-aminopyrene and a CCMoid with carboxylic endings in the *para*- position of the benzene arms (COOHCCMoid, **9**), which was prepared by deprotection of the corresponding ester curcuminoid (COOMeCCMoid, **8**). The reaction between **9** and 1-aminopyrene is shown in Scheme 5.2. The main difference with compound **7** would it be the disposition of the amide group (-NH(CO)-, in **7**, *vs.* the -(CO)NH-) of the analogue. Unfortunately, the compound was not isolated, nevertheless, the path taken is described in Appendix Vb of this Chapter.





Scheme 5.2. Proposed pathway for the synthesis of the analogous pyACCMoid.

### 5.3.1.2. $^1\text{H}$ NMR of compound **7**

The  $^1\text{H}$  NMR spectrum of pyACCMoid in  $\text{DMSO-d}_6$  is shown in Figure 5.3. The achievement of the new product **7** is confirmed by the presence of the amide proton  $\text{H}_7$ , together with the central proton,  $\text{H}_1$ , and with the enol one,  $\text{H}_2$ , observed the two first as a sharp singlet and the latter as a broad singlet at 10.98 ppm, 6.20 ppm and 16.28 ppm, respectively (the latter not shown). The signals attributed to the double bonds of the conjugated chain,  $\text{H}_3$  and  $\text{H}_4$ , appeared at 6.95 and 7.70 ppm, respectively. All the aromatics peaks were distinguished in the region from 8.80 to 7.80 ppm, being the peaks corresponding to the rings bonded to the  $-\text{NH}$  group the ones displayed between 7.99 and 7.82 ppm ( $\text{H}_5$  and  $\text{H}_6$ , respectively). Therefore, the signals attributed to the pyrene moieties ( $\text{H}_p$ ) appeared at lower fields, between 8.0 and 8.8 ppm. Compared to the  $^1\text{H}$  NMR of CCMoid **4** it is remarkable (and expected) the loss of the signal related to the amino groups  $\text{H}_7$  and the shift to lower field of the whole spectrum due to the presence of the lower donating amide groups, with an overall lower shielding effect of the molecule protons than the amino groups.

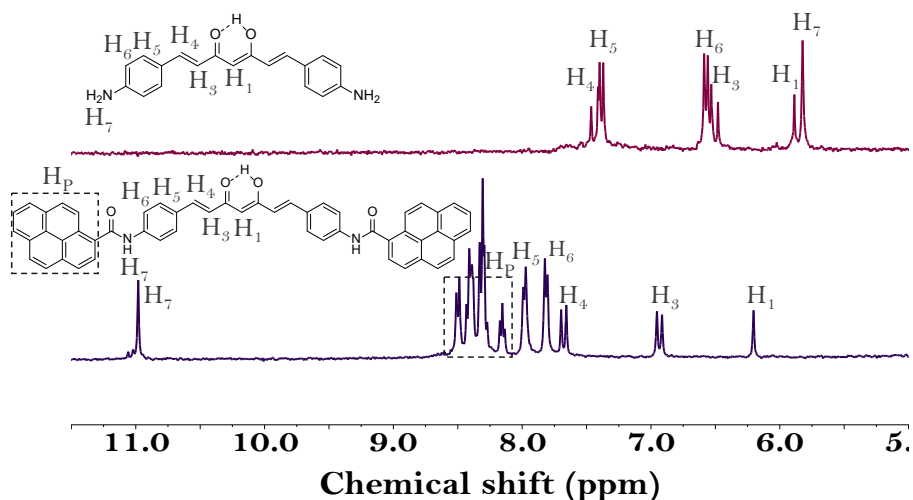


Figure 5.3. Comparison of the <sup>1</sup>H NMR spectra of **4** and **7** in DMSO-d<sub>6</sub>.

### 5.3.1.3. ATR- FTIR spectroscopy of compound **7**

In Figure 5.4, the ATR-FTIR spectrum of **7** is displayed. The keto-enol functionality of the CCMoid skeleton was evidenced by the specific stretching vibration of the carbonyl moiety C=O at 1618 cm<sup>-1</sup>. Additionally, the presence of the carbonyl from the amide was also confirmed by the appearance of a band at 1648 cm<sup>-1</sup> corroborating the formation of the new bond. Some pyrene vibration frequencies were identified at 824 cm<sup>-1</sup> and 707 cm<sup>-1</sup> related to the *out of plane* C=C and C-H bending, while the C=C stretching of the pyrene aromatic rings or C-H were not identified owing to overlapping around the 1550 cm<sup>-1</sup> and 3100 cm<sup>-1</sup> regions, respectively <sup>16</sup>.

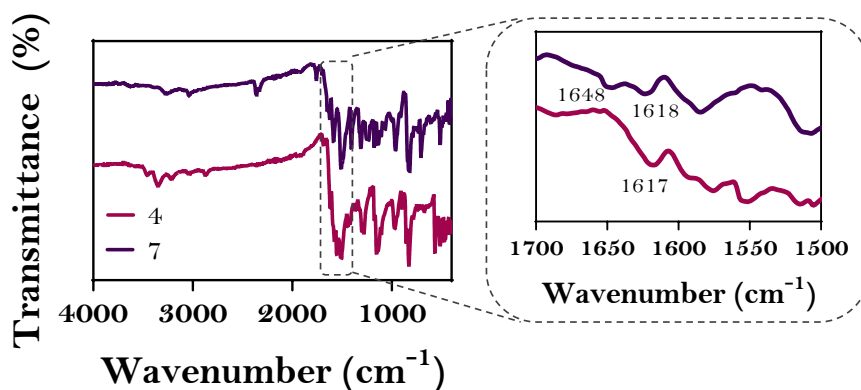


Figure 5.4. Comparison of the ATR-FTIR spectra of **4** and **7**.

#### 5.3.1.4. Raman spectroscopy of compound **7**

Raman spectra of **4** and **7** obtained with the laser emitting at 785 nm are displayed in Figure 5.5. The *in-plane* bending C-H vibrations of the pyrene aromatic rings of **7** appeared at 1181 cm<sup>-1</sup> while the signals at 1606 and 1632 cm<sup>-1</sup> are assigned to the C=C and C=O stretching vibrations. Although **7** presents two C=O types of bonds, the keno-enol and the amide, however, only one signal is observed due to the overlapping of both.

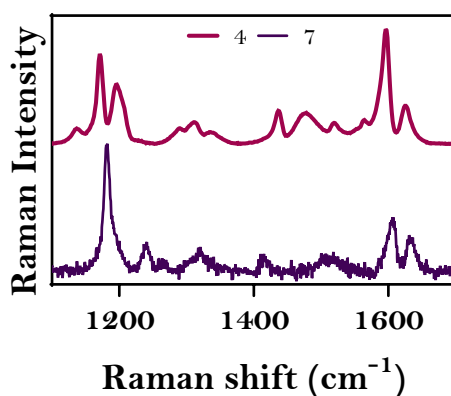


Figure 5.5. Comparison of the Raman spectra of **4** and **7**.

### 5.3.1.5. UV-Vis absorption spectroscopy of compound **7**

As explained in previous chapters, UV-Vis absorption experiments were performed in solution and in solid state for the analysis of electronic properties of the compound such as the bandgap.

The UV-Vis spectrum of **7** in THF is shown in Figure 5.6. It exhibits the  $\pi$ - $\pi^*$  transition related to the CCMoid skeleton centred at 422 nm, which is hypsochromic shifted compared to the spectrum of **4** owing to the lower donor character of the amide group. In this case, two additional intense bands attributed to the pyrene species are observed at lower wavelengths<sup>17</sup>.

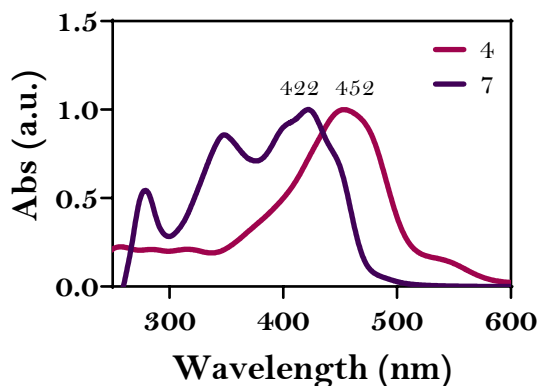


Figure 5.6. Comparison of the UV-Vis absorption spectra in THF of CCMoids **4** and **7**.

For the solid-state UV-Vis absorption analysis, compound **7** and KBr were mixed and pressed to create the pellet which was measured. Figure 5.7 exhibits the spectrum of **7** and the Tauc's representation applying the Tauc's equation (described in Chapter 2, Eq. 2.2). The optical bandgap  $E_{gop}$  is now 2.45 eV, which is higher and implies a less semiconducting behaviour of **7** compared to **4**, the latter with an optical  $E_g$  value of 1.96 eV. DFT calculations performed by Prof. Eliseo Ruiz (UB) confirmed this

semiconducting behaviour for **7**, providing a bandgap value of 2.63 eV, higher as well when comparing to 2.27 eV for compound **4**.

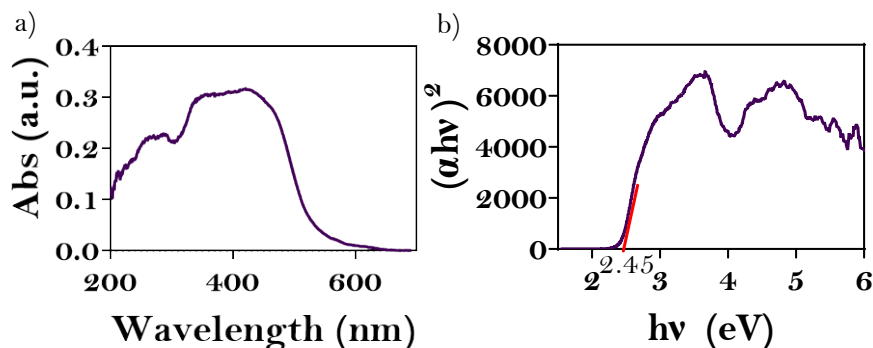


Figure 5.7. a) UV-Vis absorption spectrum of **7** in solid state. b) Tauc's representation of the UV-Vis spectrum in solid state of **7**.

### 5.3.1.6. Electrochemistry of compound **7**: CV and DPV

CV and DPV experiments, were carried out to explore the redox behaviour of compound **7** and obtain information about its bandgap, HOMO and LUMO levels; this study was performed with the same conditions used in previous chapters using THF as a solvent, for comparative reasons.

The oxidation and reduction processes obtained in the CV experiment of compound **7** are displayed in Figure 5.8 a. It is observed one irreversible oxidation wave and 3 reduction ones, whose reversibility processes were studied. The criteria to identify reversible processes was exposed in Chapter 3. To summarize,  $I_{pa}/I_{pc}$  must be close to 1,  $\Delta E_p$  should be small (approximately 59 mV for aqueous solutions) and a linear regression should

appear by plotting the maximum current reached *vs* the square root of scan rate explored.

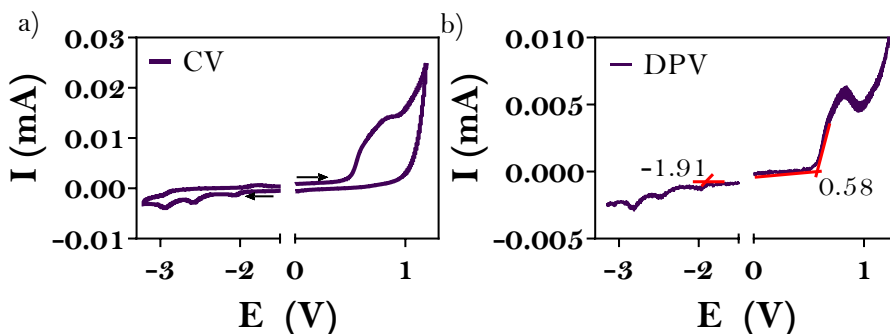


Figure 5.8. Oxidation and reduction CVs (a) and DPVs (b) voltammogram of compound **7**.

The voltammogram of the first reduction process at different scan rates is represented in Figure 5.9 and the consequent  $I_{pa}/I_{pc}$  and  $\Delta E_p$  parameters are collected in Table 5.1.  $I_{pa}/I_{pc}$  values differ from the unity, being grouped from 0.58, for the smallest speed, to 0.91, for the highest scan rate. In terms of difference between the voltage where the peaks are centred,  $\Delta E_p$ , the results differ less than 10 mV from the ideal 59 mV for the scan rates included from 25 mV/s to 350 mV/s, presenting a major different for the highest speeds. Taking into account the ideal 59 mV value is considered for the experiments performed in water, we could contemplate this requirement is fulfilled. In Figure 5.9, the maximum of the current for the anodic and cathodic peak are close to the linear fit. Therefore, one can conclude that the first reduction process is quasi-reversible due to the accomplishment of most of the reversibility criteria. The application of such criteria in the second reduction process showed that the latter was irreversible.

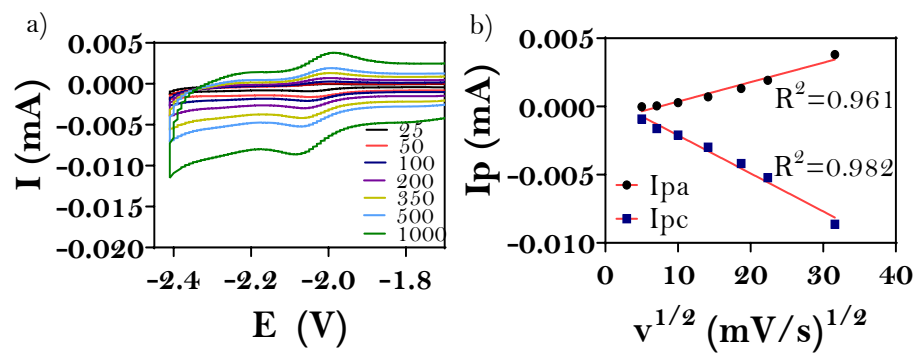


Figure 5.9. a) First reduction wave of compound **7** recorded at several scan rates. b) Graphical representation of the maximum intensity *vs.* the square root of the scan rate for the anodic and cathodic peaks.

Scan rate (mV/s)	I <sub>pa</sub> /I <sub>pc</sub>	ΔE <sub>p</sub> (mV)
<b>25</b>	0.58	60
<b>50</b>	0.61	55
<b>100</b>	0.67	56
<b>250</b>	0.70	63
<b>350</b>	0.76	69
<b>500</b>	0.75	76
<b>1000</b>	0.91	94

Table 5.1. Division of the anodic and cathodic maximum intensities and potential values differences for the oxidation and reduction processes at different scan rates.

The DPV plot, depicted in Fig 5.8 b, was used to estimate the approximated values of the HOMO, LUMO and electrochemical bandgap by applying Eq. 2.3 and Eq. 2.4 and Eq 2.5 (described in Chapter 2). Table 5.2 collects the mentioned values and reveals a semiconductor character of compound **7**,

which presents an electrochemical  $E_g$  of 2.49 eV matching very well with the value obtained for optical bandgap.

<b>E onset ox (V)</b>	<b>Eonset red (V)</b>	<b>E HOMO (eV)</b>	<b>E LUMO (eV)</b>	<b>E<sub>g</sub> (eV)</b>
0.58	-1.91	-5.38	-2.89	2.49

Table 5.2. Potential values for oxidation and reduction, HOMO, LUMO and electrochemical bandgap of compound **7**.

The electrochemical calculation reveals a relatively large bandgap for compound **7**, which is in agreement with the optical estimation. The bandgap difference is visually appreciated in Figure 5.10. which includes the energy values of the HOMO and LUMO levels for the two systems, **4** and **7**, correspondingly. For a similar energetically LUMO, compound **4** exhibits a shorter gap, indicating a more donating behaviour than compound **7**, demonstrated also by the easier oxidation of  $\text{NH}_2\text{CCMoid}$  comparing with  $\text{pyACCMoid}$ . The comparison between both systems clearly shows the impact of coordination on the energy gap.

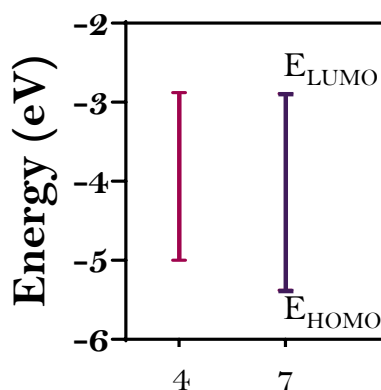


Figure 5.10. Schematic diagram for HOMO and LUMO energy levels of compound **4** and **7**.



CCMoid **7**, whose MALDI-TOF spectrum is shown in Figure A5a.2 in Annex Va, is a promising candidate to study as a single molecule in the previously introduced nanogapped graphene devices, due to its conjugated structure which manage the charge transport and its estimated length, 3.06 nm, which allow the  $\pi$ - $\pi$  interaction with the graphene electrodes farther from the functionalized electrodes edges <sup>18</sup>.

### 5.3.2. Deposition of compound **7** on the device

The molecular deposition over the graphene substrates is described in detail in Chapter 4. Briefly, dip-coated and drop-casted graphene surfaces were analysed by SEM and AFM techniques recommending dip coating as a more suitable deposition technique owing to the cleanest surfaces obtained (Figure 4.22, Chapter 4). Prior to the molecular attachment to the device, we investigated by AFM the morphology of the molecular functionalization of a graphene substrate after its immersion in a 0.1 mM solution of compound **7** in THF. Interestingly, a sort of spontaneous ordering of molecules assembled on graphene is observed and represented by a parallel pattern, in Figure 5.11, suggesting the formation of long wires probably owing to  $\pi$ - $\pi$  stacking between pyrene units and between pyrene and graphene.

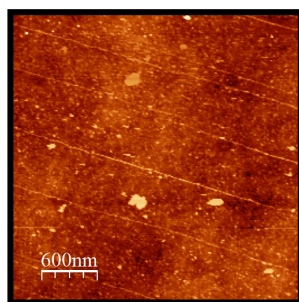


Figure 5.11. AFM image of a graphene surface functionalised by immersion in 0.1 mM solution of **7** in THF.

Subsequently, a chip with several devices was immersed in a filtered 0.1 mM solution of compound **7** in THF for 1 h. Afterwards, it was rinsed with THF and dried at room temperature for 30 minutes. Finally, it was dried under vacuum for another half an hour to remove the remaining THF traces.

As explained in Chapter 4, two types of electrical measurements were carried out after the deposition of pyACCMoid, with or without the operation of the gate voltage to corroborate that the changes in the current were related with the presence of **7**.

Figure 5.12 illustrates the I-V curves of a) the bare nanogap and b) the nanogap after the deposition of compound **7**. There is a clear increase in the current, about several orders of magnitude, after the deposition of the CCMoid. Theoretical calculations performed by Prof. Eliseo Ruiz (UB) provides a value of conductance for **7** of  $8 \times 10^{-4} G_0$ , similar to the experimental current values observed so far. These calculations suggest a planar disposition of the pyrene moieties included in compound **7** over the graphene electrodes, as Figure 5.13 represents, allowing a strong molecule-electrodes  $\pi$ - $\pi$  stacking.

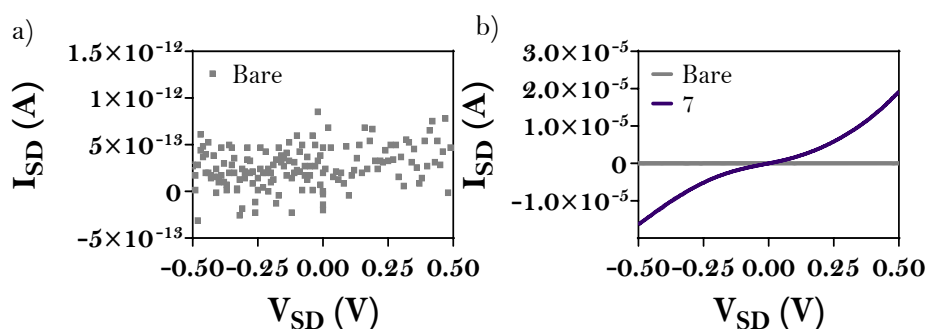


Figure 5.12. I-V curve conducted at room temperature and zero gate voltage for the device a) before the molecular deposition and b) after the deposition of **7**.

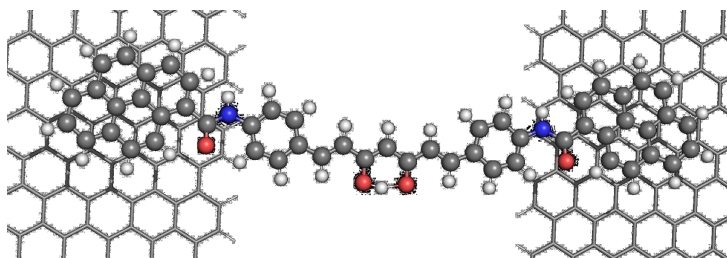


Figure 5.13. Representation of the theoretically calculated disposition of **7** over graphene electrodes.

To corroborate that the increase of the current is due to molecules acting as nanowires within the nanogap, we studied the dependence of the source-drain current by the gate voltage, first at room temperature and then progressively lowering the temperature until reaching 10 K. These experiments, which are performed in the installations of our collaborator, Prof. Herre van der Zant, at TUDelft, in The Netherlands are currently in progress, which is why it has not been possible to add them in the present chapter.

An update of the electrical results can be found in Annex VII (pg 287).

## 5.4. Conclusions

- A novel extended PAH-CCMoid, pyACCMoid, **7**, was isolated by the reaction, under MW conditions, of the starting NH<sub>2</sub>CCMoid, **4**, and an acyl chloride activated pyrene unit.
- The presence of a less donating group (amide) in compound **7**, compared to the amine of compound **4**, promoted a shift of the proton signals to lower fields in <sup>1</sup>H NMR or the hypsochromic shift in the UV-Vis absorption band.
- The estimated optical and electrochemical bandgap for compound **7** are bigger than the ones calculated for compound **4**, including both in the semiconductor range. Additionally, electrochemical measurements suggested a lower position of the HOMO level of compound **7** indicating a less donor behaviour than compound **4**.
- $\pi$ - $\pi$  interactions between pyrene units of molecule **7** deposited by dip coating on graphene substrates seems to promote a spontaneous order of the molecules indicated by a parallel pattern observed by AFM.
- A current increase measured at room temperature about eight orders of magnitude (higher than other CCMoids measured in the past) is experimented after the anchoring of molecule **7** on the graphene-based device, in agreement with the theoretical calculations performed in a similar model system. Repetition of such types of experiments and further low temperature electrical characterizations are needed to attribute the increment to the molecular effect.

## 5.5. Experimental section

### Synthesis of pyCOOH.

An aqueous solution of  $\text{KMnO}_4$  (664 mg, 4.2 mmol) in 50 mL of Milli-Q water was refluxed with a solution of 1- pyrenecarboxaldehyde (250 mg, 0.108 mmol) in 50 mL acetone for 24 h. Subsequently, the mixture was filtered and extracted with DCM. Afterwards, the aqueous phase was acidified until pH=2 and centrifuged to isolate the pale brownish product in 59% Yield.  $^1\text{H}$  NMR (400 MHz,  $\text{DMSO-d}_6$ )  $\delta$ : 13.30 (b, 1H) 9.24 (1H, d,  $^3\text{J}=9.4$  Hz), 8.62 (1H, d,  $^3\text{J}=8.1$  Hz) 8.43 (5H, m), 8.27 (1H, d,  $^3\text{J}= 8.7$  Hz), 8.18 (1H, t,  $^3\text{J}=7.8$  Hz). MS MALDI - TOF (m/z): calcd for PyCOOH: 246.1  $[\text{M}]$ ; found: 244.9  $[\text{M}-1]$ .

### Synthesis of pyACCMoid, 7.

30 mg pyCOOH (0.12 mmol) were dissolved in 0.8 mL of  $\text{SOCl}_2$  (11.2 mmol) and refluxed for 3 h. Subsequently, the excess of  $\text{SOCl}_2$  was removed under vacuum, and the remaining precipitate was dissolved in 5 mL of dry THF and transferred into a MW vial, together with 16  $\mu\text{L}$  of  $\text{Et}_3\text{N}$  (0.11 mmol), and a dispersion of  $\text{NH}_2\text{CCMoid}$ , **4** (18.4 mg, 0.06 mmol) in 12 mL of dry THF. The mixture was placed into the microwave at 60 °C for 90 minutes. After that time, the mixture was filtrated off, the solvent evaporated, and the product washed with hot ACN to obtain the pure product as a red solid in 25% yield.  $^1\text{H}$  NMR (400 MHz,  $\text{DMSO-d}_6$ )  $\delta$ : 16.28 (1H, s), 10.98 (2H, s), 8.51 (3H, d,  $^3\text{J}=9.1$  Hz), 8.43 (7H, m) 8.33 (9H, m), 8.17 (2H, t,  $^3\text{J}= 7.4$  Hz), 7.99 (4H, d,  $^3\text{J}=8.2$  Hz), 7.82 (4 H, d,  $^3\text{J}= 8.8$  Hz), 7.70 (2H, d,  $^3\text{J}= 16.1$  Hz), 6.95 (2H, d,  $^3\text{J}= 16.6$  Hz), 6.20 (1H, s); MS MALDI - TOF (m/z): calcd for PyACCMoid: 762.2  $[\text{M}]$ ; found: 761.3  $[\text{M}-1]$ .

### Synthesis of COOMeCCMoid, 8.

0.3 mL of acetylacetone (2.90 mmol) and 155 mg of  $B_2O_3$  (2.22 mmol) were mixed in 4 mL EtOAc at 60 °C for 1 h. Afterwards, a prepared solution of 1 g methyl 4-formylbenzoate (6.09 mmol) and 3.3 mL tributylborate (12.24 mmol) in 4.5 mL EtOAc was introduced, and the mixture was heated up at 60 °C for 2 h. After cooling down to RT, a solution of 0.20 mL butylamine (2.02 mmol) in 1 mL EtOAc, was added dropwise to the mixture. The final reaction was stirred at room temperature for 2 days. Then, water was added, and the mixture was stirred overnight. Finally, the reaction was filtered off, washed with Milli-Q water and dried with  $Et_2O$  to obtain the product as a yellow solid in 19% yield.  $^1H$  NMR (360 MHz,  $CDCl_3$ )  $\delta$ : 15.75 (1H, s) 8.07 (2H, d,  $^3J=6.9$  Hz), 7.71 (2H, d,  $^3J=15.6$  Hz), 7.63 (2H, d,  $^3J=6.9$  Hz), 6.74 (2H, d,  $^3J=15.9$  Hz), 5.89 (1H, s), 3.94 (s, 6H). Elemental analysis calcd for  $C_{23}H_{20}O_6 \cdot 0.05$  EtOAc: C: 70.22 %; H: 5.18 %; O: 24.60 %, found: C 69.78 %; H 5.04 %; O: 24.24 % MS (MALDI - TOF):  $m/z$  calcd for COOMeCCMoid: 392.4  $[M^-]$ , found: 393.5  $[M+1^-]$ .

### Synthesis of COOHCCMoid, 9.

140 mg of LiOH (5.84 mmol) dissolved in 4 mL  $H_2O$  were mixed with a solution of 8 (109 mg, 0.27 mmol) in 11 mL of THF stirring overnight. Subsequently, THF was removed under vacuum and the reaction was acidified to pH = 1 by adding 20 % HCl dropwise. After 24 h, the yellow precipitate was isolated in 49% yield by centrifugation and washed with MeOH.  $^1H$  NMR (360 MHz,  $DMSO-d_6$ )  $\delta$ : 15.97 (1H, s), 13.13 (1H, s), 8.00 (2H, d,  $^3J=8.2$  Hz), 7.87 (2H, d,  $^3J=8.2$  Hz), 7.73 (2H, d,  $^3J=15.9$  Hz), 7.13 (2H, d,  $^3J=16.2$  Hz), 6.28 (1H, s).  $^{13}C$  NMR (100 MHz,  $DMSO-d_6$ )  $\delta$ : 183.5, 167.2, 139.7, 139.2, 132.3, 130.3, 128.9, 126.9, 103.1; MS MALDI - TOF ( $m/z$ ) calcd for COOHCCMoid: 364.1  $[M^-]$ ; found: 365.5  $[M+1^-]$ .

# Annex Va

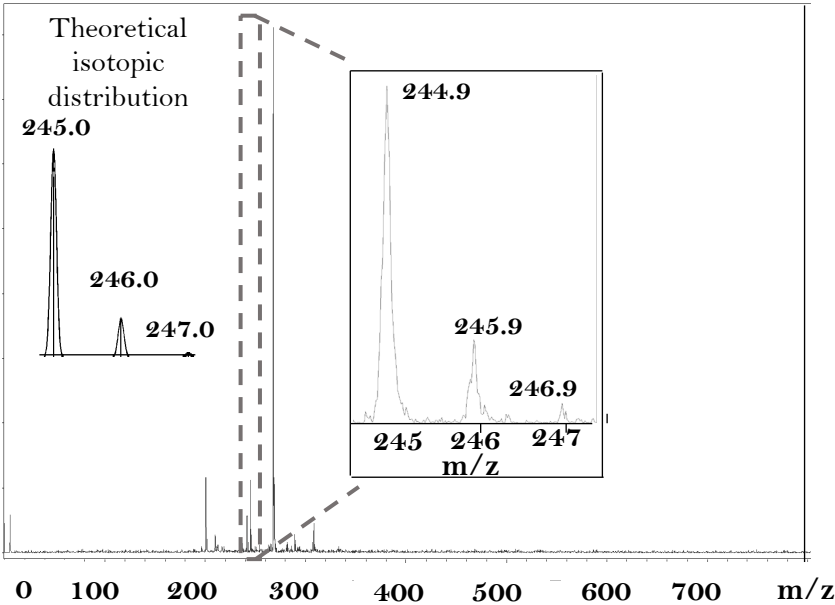


Figure A5a.1. MALDI-TOF mass spectrum in negative mode of pyCOOH.

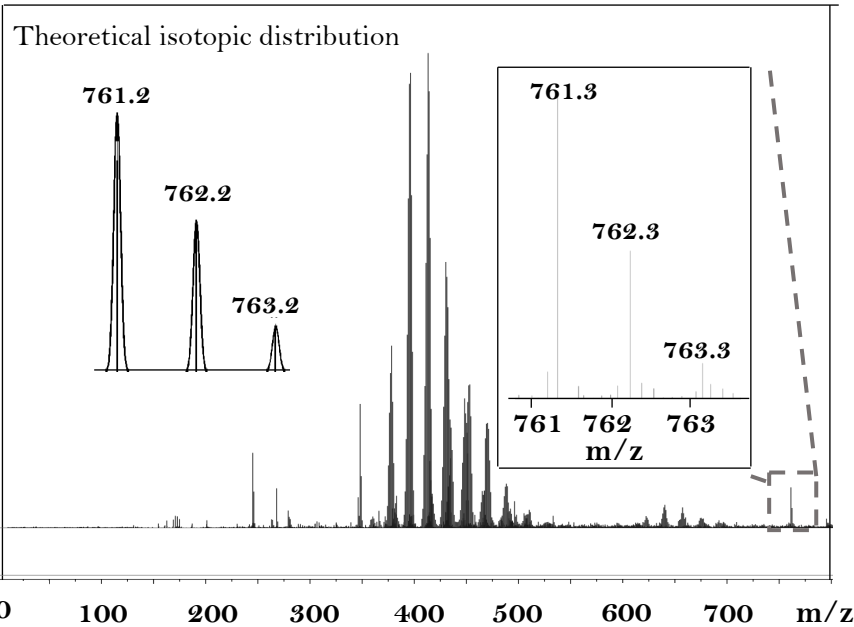
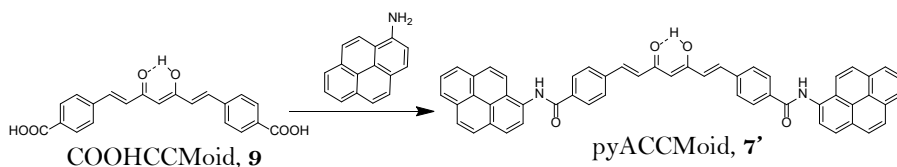


Figure A5a.2. MALDI-TOF mass spectrum in negative mode of 7.

## Annex Vb

### A5b.1. Synthesis of analogue pyACCMoid, 7'

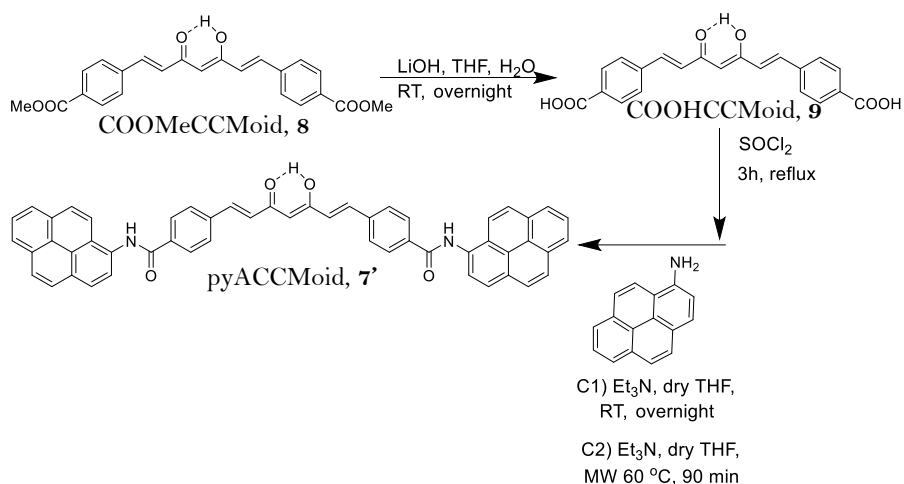
The synthesis of a similar system as pyACCMoid was also suggested by the reaction between the CCMoid containing acid groups ( $-\text{COOH}$ ) in *para*-positions and 1-aminopyrene units (Scheme A5b.1). The unique difference with compound **7** would be the N-H and C=O groups disposition within the molecule.



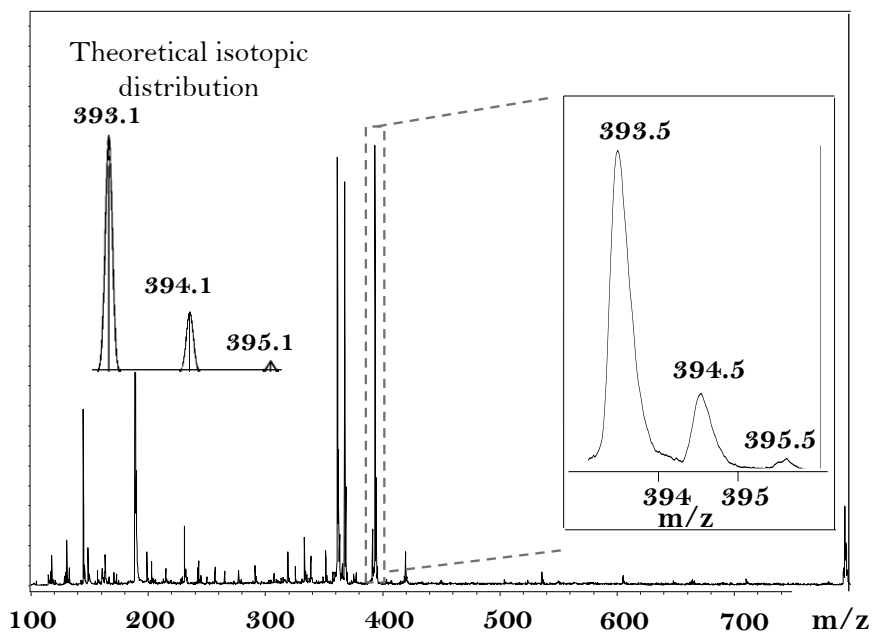
Scheme A5b.1. Reactants employed for the synthesis of the analogous pyACCMoid.

In order to compare both pyACCMoid systems, several attempts to isolate **7'** were carried out. The synthetic route followed is shown in Scheme A5b.2. The first step involved the hydrolysis with LiOH of the ester CCMoid, COOMeCCMoid, **8** obtained through the usual modified Pabon's reaction in EtOAc, to obtain the acid CCMoid, COOHCCMoid, **9**. Afterwards, the acid group was activated by  $\text{SOCl}_2$ , and the amino coupling reactions were tested under two different conditions: at room temperature overnight and applying MW radiation for 1.30 h at 60 °C, respectively.



Scheme A5b.2. Alternative chemical pathway tested for the isolation of **7'**.

The chemical structure of **8** and **9** was confirmed by <sup>1</sup>H NMR, ATR-FTIR, UV-Vis absorption spectroscopy, elemental analysis and MALDI-TOF (Figure A5b.1 and A5b.2).

Figure A5b.1. MALDI-TOF mass spectrum in positive mode of **8**.

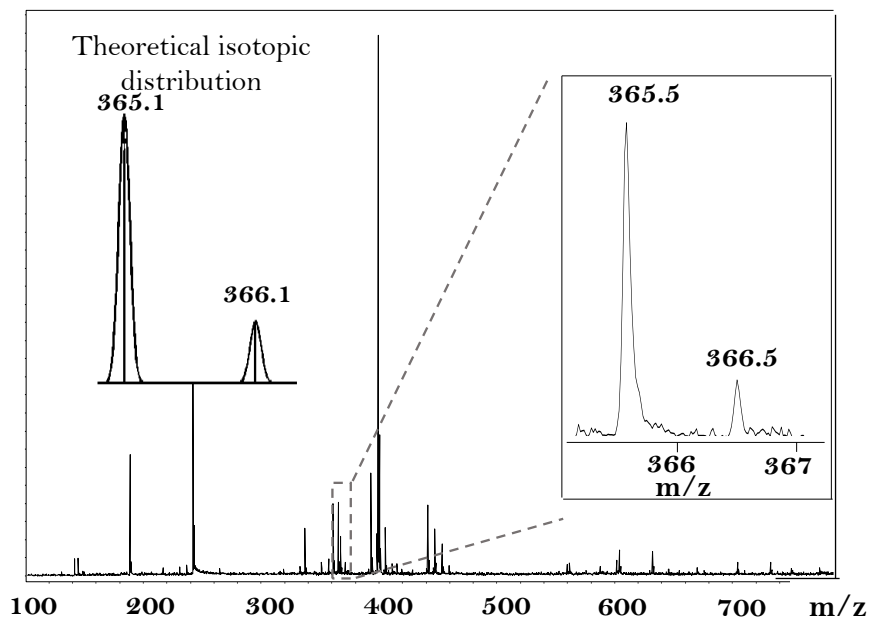
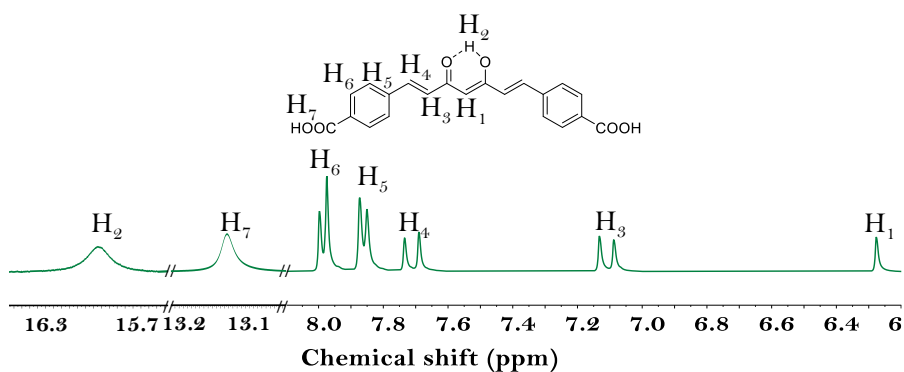
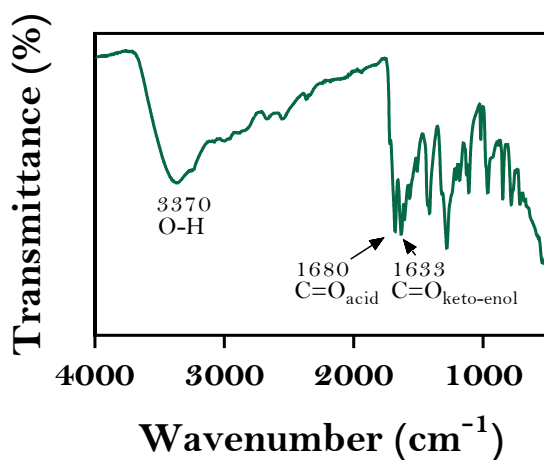


Figure A5b.2. MALDI-TOF mass spectrum in positive mode of **9**.

The  $^1\text{H}$  NMR spectrum of COOHCCMoid in  $\text{DMSO-d}_6$  is presented in Figure A5b.3. It demonstrates the successful obtaining of **9** by the appearance of the specific signals related to the CCMoid skeleton and the acid groups. The central proton ( $\text{H}_1$ ) singlet appears at higher fields, at 6.27 ppm specifically. The doublets attributed to the *trans*- protons of the double bonds of the backbone are identified approximately at 7.73 and 7.13 ppm ( $\text{H}_3$  and  $\text{H}_4$ , respectively). The aromatics signals are detected at 7.99 and 7.87 ppm ( $\text{H}_5$  and  $\text{H}_6$ , in that order). Finally, the proton of the acid and the enol groups are recognised at 13.13 ppm ( $\text{H}_7$ ) and 15.93 ppm ( $\text{H}_2$ ), correspondingly.

Figure A5b.3.  $^1\text{H}$  NMR spectrum of **9** in  $\text{DMSO-d}_6$ .

The ATR-FTIR spectrum of **9**, represented in Figure A5b.4, corroborated the presence of the acid, which is evidenced by the broad intense band at  $3370\text{ cm}^{-1}$  attributed to the stretching vibration of the O-H and the signal related to the C=O bond at  $1680\text{ cm}^{-1}$ , respectively. Additionally, at  $1633\text{ cm}^{-1}$  the stretching vibration of the carbonyl moiety C=O of the keto-enol unit was detected.

Figure A5b.4. ATR-FTIR spectrum of **9**.

The UV-vis absorption spectrum obtained for compound **9** in THF is plotted in Figure A5b.5. It displays two absorbance bands, the one attributed to the  $\pi$ - $\pi^*$  transition related to the skeleton centred, at 390 nm, and the assigned to the acid substituted aromatic rings, at 279 nm, corroborating the CCMoid structure of the product.

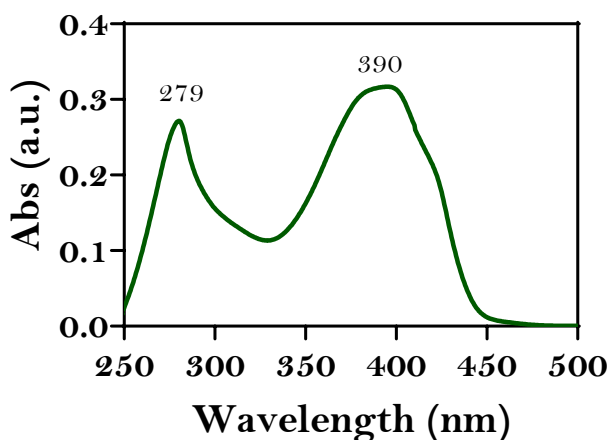


Figure A5b.5. UV-vis absorption spectrum of **9** in THF.

As mentioned earlier, compound **9** was isolated and then transformed into an acyl chloride by reacting with  $\text{SOCl}_2$  under reflux. Subsequently, the reaction with 1-aminopyrene was tested using two different conditions: (i) under ambient conditions overnight and (ii) using MW radiation for 1.30 h at 60 °C.

The comparison of the products obtained under both conditions was carried out by the analysis of their  $^1\text{H}$  NMR spectra in  $\text{DMSO-d}_6$ , which are displayed in Figure A5b.6. Both exhibit two signals at 10.93 ppm that could be attributed to the new amide bond ( $\text{H}_7$ ) and some overlapped aromatic signals corresponding to pyrene groups. However, while the conventional methodology displays two additional peaks attributed to the aromatics of

the CCMoid ( $H_5$  and  $H_6$ ), the MW assisted reaction shows the presence of 1-aminopyrene as impurity. Furthermore, both spectra lack the signals expected for the CCMoid backbone, including the central proton ( $H_1$ ), the *trans* ( $H_3$  and  $H_4$ ) and the one related to the keto-enol moiety ( $H_2$ ).

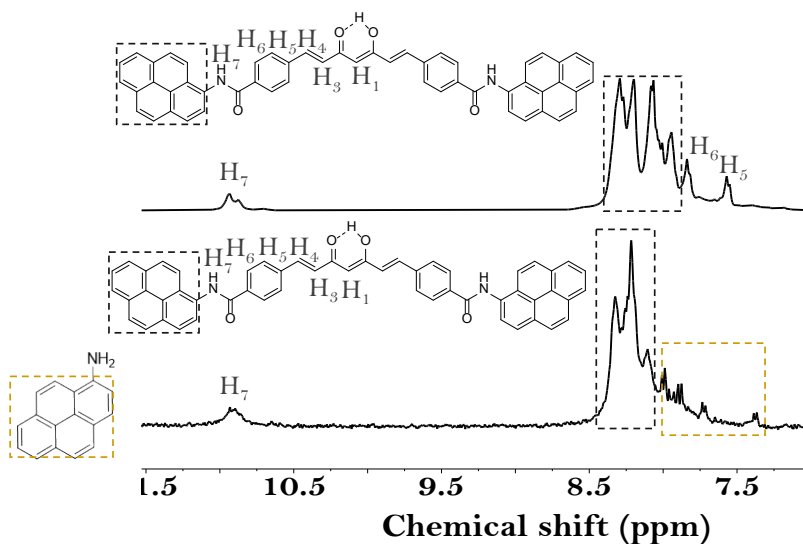


Figure A5b.6. Comparison of the  $^1\text{H}$  NMR spectra of the products of the reaction between acyl chloride CCMoid and 1-aminopyrene (i) under ambient conditions overnight and (ii) under MW radiation for 1.30 h at 60 °C.

Repeated attempts of both reactions yielded same results, failing to provide any clarifying contribution about the CCMoid structure. Therefore, the unique extended CCMoid selected for further characterization and application was the initially described pyACCMoid, **7**.

## References

- (1) Figueira-Duarte, T. M.; Müllen, K. Pyrene-Based Materials for Organic Electronics. *Chem. Rev.* **2011**, *111* (11), 7260–7314.
- (2) Sadeghi, H.; Sangtarash, S.; Lambert, C. Robust Molecular Anchoring to Graphene Electrodes. *Nano Lett.* **2017**, *17* (8), 4611–4618.
- (3) Limburg, B.; Thomas, J. O.; Holloway, G.; Sadeghi, H.; Sangtarash, S.; Hou, I. C. Y.; Cremers, J.; Narita, A.; Müllen, K.; Lambert, C. J.; Briggs, G. A. D.; Mol, J. A.; Anderson, H. L. Anchor Groups for Graphene-Porphyrin Single-Molecule Transistors. *Adv Funct Mater* **2018**, *28* (45), 1803629.
- (4) Thomas, J. O.; Limburg, B.; Sowa, J. K.; Willick, K.; Baugh, J.; Briggs, G. A. D.; Gauger, E. M.; Anderson, H. L.; Mol, J. A. Understanding Resonant Charge Transport through Weakly Coupled Single-Molecule Junctions. *Nat Commun* **2019**, *10* (1), 4628.
- (5) Thomas, J. O.; Sowa, J. K.; Limburg, B.; Bian, X.; Evangelì, C.; Swett, J. L.; Tewari, S.; Baugh, J.; Schatz, G. C.; Briggs, G. A. D.; Anderson, H. L.; Mol, J. A. Charge Transport through Extended Molecular Wires with Strongly Correlated Electrons. *Chem. Sci.* **2021**, *12* (33), 11121–11129.
- (6) Gehring, P.; Harzheim, A.; Spièce, J.; Sheng, Y.; Rogers, G.; Evangelì, C.; Mishra, A.; Robinson, B. J.; Porfyrakis, K.; Warner, J. H.; Kolosov, O. V.; Briggs, G. A. D.; Mol, J. A. Field-Effect Control of Graphene-Fullerene Thermoelectric Nanodevices. *Nano Lett.* **2017**, *17* (11), 7055–7061.
- (7) Burzurí, E.; García-Fuente, A.; García-Suárez, V.; Senthil Kumar, K.; Ruben, M.; Ferrer, J.; Van Der Zant, H. S. J. Spin-State Dependent Conductance Switching in Single Molecule-Graphene Junctions. *Nanoscale* **2018**, *10* (17), 7905–7911.
- (8) Li, Y.; Tu, X.; Wang, H.; Sanvito, S.; Hou, S. First-Principles Investigation on the Electronic Efficiency and Binding Energy of the Contacts Formed by Graphene and Poly-Aromatic Hydrocarbon Anchoring Groups. *J. Chem. Phys.* **2015**, *142* (16), 164701.

- (9) Liu, T.; Huang, Z.; Feng, R.; Ou, Z.; Wang, S.; Yang, L.; Ma, L. J. An Intermolecular Pyrene Excimer-Based Ratiometric Fluorescent Probes for Extremely Acidic PH and Its Applications. *Dyes Pigm.* **2020**, *174*, 108102.
- (10) Tehfe, M. A.; Dumur, F.; Contal, E.; Graff, B.; Morlet-Savary, F.; Gigmes, D.; Fouassier, J. P.; Lalevée, J. New Insights into Radical and Cationic Polymerizations upon Visible Light Exposure: Role of Novel Photoinitiator Systems Based on the Pyrene Chromophore. *Polym Chem* **2013**, *4* (5), 1625–1634.
- (11) Wrona-Piotrowicz, A.; Zakrzewski, J.; Métivier, R.; Brosseau, A.; Makal, A.; Woźniak, K. Efficient Synthesis of Pyrene-1-Carbothioamides and Carboxamides. Tunable Solid-State Fluorescence of Pyrene-1-Carboxamides. *RSC Adv.* **2014**, *4* (99), 56003–56012.
- (12) Xie, X.; Reznichenko, O.; Chaput, L.; Martin, P.; Teulade-Fichou, M. P.; Granzhan, A. Topology-Selective, Fluorescent “Light-Up” Probes for G-Quadruplex DNA Based on Photoinduced Electron Transfer. *Chem. Eur. J.* **2018**, *24* (48), 12638–12651.
- (13) Nain, S.; Singh, R.; Ravichandran, S. *Adv. J. Chem. A.* **2019**, *2* (2), 94–104.
- (14) Díaz-Ortiz; Prieto, P.; de la Hoz, A. A Critical Overview on the Effect of Microwave Irradiation in Organic Synthesis. *Chem. Rec.* **2019**, *19* (1), 85–97.
- (15) Torres-Moya, I.; Harbuzaru, A.; Donoso, B.; Prieto, P.; Ortiz, R. P.; Díaz-Ortiz, Á. Microwave Irradiation as a Powerful Tool for the Preparation of N-Type Benzotriazole Semiconductors with Applications in Organic Field-Effect Transistors. *Molecules* **2022**, *27* (14), 4340.
- (16) Zhang, Y.; Yuan, S.; Zhou, W.; Xu, J.; Li, Y. Spectroscopic Evidence and Molecular Simulation Investigation of the  $\pi$ - $\pi$  Interaction between Pyrene Molecules and Carbon Nanotubes. *J. Nanosci. Nanotechnol.* **2007**, *7* (7), 2366–2375.
- (17) Feng, X.; Qi, C.; Feng, H. T.; Zhao, Z.; Sung, H. H. Y.; Williams, I. D.; Kwok, R. T. K.; Lam, J. W. Y.; Qin, A.; Tang, B. Z. Dual Fluorescence of

Tetraphenylethylene-Substituted Pyrenes with Aggregation-Induced Emission Characteristics for White-Light Emission. *Chem. Sci.* **2018**, *9* (25), 5679–5687.

- (18) Burzurí, E.; Island, J. O.; Díaz-Torres, R.; Fursina, A.; González-Campo, A.; Roubeau, O.; Teat, S. J.; Aliaga-Alcalde, N.; Ruiz, E.; Van Der Zant, H. S. J. Sequential Electron Transport and Vibrational Excitations in an Organic Molecule Coupled to Few-Layer Graphene Electrodes. *ACS Nano*. **2016**, *10* (2), 2521–2527.





# Chapter 6

## T-shaped CCMoids

In this chapter, we present two methodologies for the synthesis of T-shaped CCMoids, one related to the inclusion of an additional group in the central carbon of the CCMoid skeletons and the other by the modification of the keto-enol moiety of new CCMoids, respectively. Such units (called “*leg*” and “*hat*”, in that order) end with triethoxysilane groups, to be used as anchoring sites to immobilize the CCMoid molecules, in a further step, over the SiO<sub>2</sub> layer of the graphene-based device.





## 6.1. Introduction

At present, it is a great challenge to fabricate reliable three terminal graphene-based devices comprising single molecule junctions in terms of reproducibility and robustness <sup>1</sup>. To date, two different approaches have been employed for the creation of graphene-molecule-graphene junctions taking into account the molecular design and interactions with the electrodes: supramolecular interactions ( $\pi$ - $\pi$  stacking) <sup>2</sup> and covalent attachments <sup>3</sup>. From those,  $\pi$ - $\pi$  stacking at the molecular electrode interface could result into mechanical instability, due to weak molecule-electrodes coupling, leading into the sliding of the molecules over the electrodes surface <sup>4,5</sup>. This situation could be overcome by the introduction of covalent linkages between the molecule and the functionalised edges of the graphene electrodes. However, the measured conductance would be dependent on the electrode geometry together with the nature of the covalent attachment by itself, generating non-electrically reproducible systems <sup>6</sup>. The alternative solution to create stable devices that we propose in this Chapter (as it was similarly reported by El Abbassi *et al.* <sup>7</sup> during the course of this thesis project) focuses on the covalent anchoring of an active molecule onto the SiO<sub>2</sub> layer (in order to immobilize it on the platform) avoiding possible molecular translations while maintaining the  $\pi$ - $\pi$  interactions with the graphene electrodes. While El Abbassi *et al.* <sup>7</sup> explored the conductance through a number of fixed molecules interacting between them by  $\pi$ - $\pi$  stacking (Figure 6.1 a), our approach is based on the study of a single molecule, in concordance with the previous chapters, and as Figure 6.1 b shows.

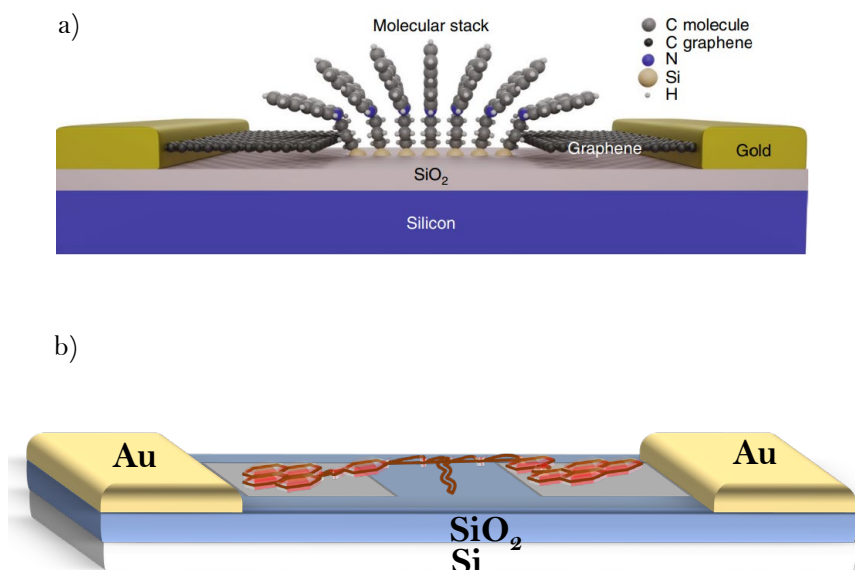


Figure 6.1. Comparison of the molecular immobilization proposed by a) El Abbassi *et al* (Ref. 7) and b) our research group, (representation of a T-shaped CCMoid (in orange) over an idealized three-terminal device (graphene in grey)).

For that purpose, in this Chapter, our design includes now a terminal alkoxy-silane group attached to the central moiety (C atom, *leg*, or keto-enol group, *hat*, Figure 6.2.) in extended pyrene terminal CCMoids, called in previous chapter pyACCMoid, **7**, to anchor the final compound (T-shaped CCMoid) covalently through the ending alkoxy-silane unit to the SiO<sub>2</sub> insulator layer of the device, and via  $\pi$ - $\pi$  interaction with the graphene electrodes, as exemplified in Figure 6.1b.

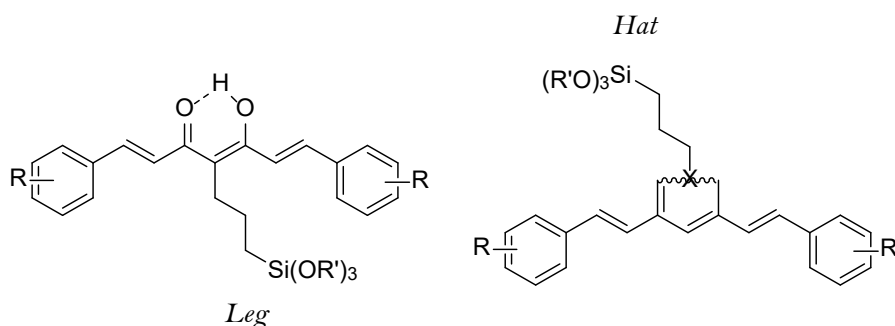


Figure 6.2. General structures of CCMoids containing terminal alkoxy silane groups in the *leg* or *hat* positions.

## 6.2. Objectives

The main objective of this chapter, as it was previously mentioned, is the synthesis of T-shaped PAH-based CCMoids for the fabrication of robust molecular graphene-based three-terminal devices. In order to accomplish this general goal, an individual aim must be fulfilled:

- Finding reliable methodologies for the synthesis of T-shaped pyrene-based CCMoids, via introduction of a terminal anchoring group (alkoxysilane) in the central part (*leg* and *hat*) of the molecule.

## 6.3. Results and discussion

The general structure of CCMoids already described in Chapter 1 and depicted now in Figure 6.3, comprises four different parts which can be modified according to the desired applications: the keto-enol group (*head*, green), the conjugated chain (*body*, yellow), and what we refer as *arms* (cyclic aromatic groups that can be functionalized, R, orange) and *leg* (a great variety of functional groups, Y, blue).

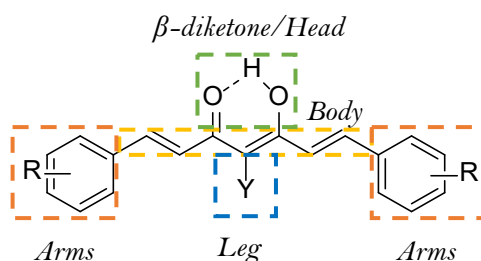


Figure 6.3. Different parts comprised in the CCMoid structure.

In order to attach covalently the extended CCMoid on the surface of the  $\text{SiO}_2$  layer of the devices (while keeping non-covalent anchoring of the pyrene units over the graphene electrodes), we propose the introduction of an alkoxy silane terminal *leg*, on the central C atom of the CCMoid skeleton, or an alkoxy silane terminal *hat*, by capping the keto-enol moiety of the same CCMoid, respectively, as displayed in Figure 6.4.

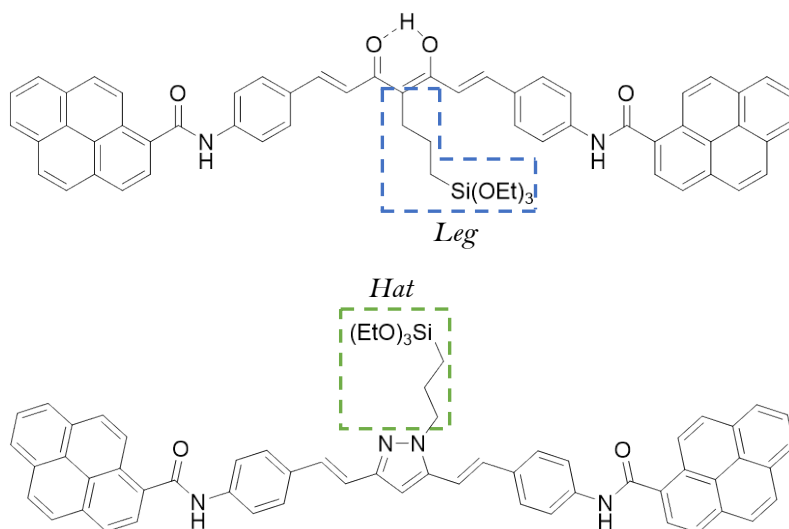


Figure 6.4. Chemical structure of the proposed T-shaped CCMoids for their anchoring on the device.

Taking advantage of this  $\text{SiO}_2$  layer within the platform, the new features inserted in the CCMoid were designed to contain an alkoxy silane reactive terminal group for unification, affinity and specially, reactivity reasons, being capable of creating a covalent Si-O-Si bond with the hydroxyl activated  $\text{SiO}_2$  layer anchoring the molecule on the surface <sup>8</sup>.

It is important to stress that, in a similar manner that happens on surface reactions, in solution, the alkoxy silanes of different molecules can form Si-O-Si bonds among them, leading into a polymerization triggered by water molecules which catalysed the hydrolysis of the alkoxy silanes, leading to undesired condensation products <sup>9</sup>.

Due to the incompatibility of the Pabon reaction with the alkoxy silane functionality (because of the use of water in the CCMoid formation to break the boron complex), and the impossibility of the anchoring of the molecule on the device once the silane polymerizes, the synthesis of the extended

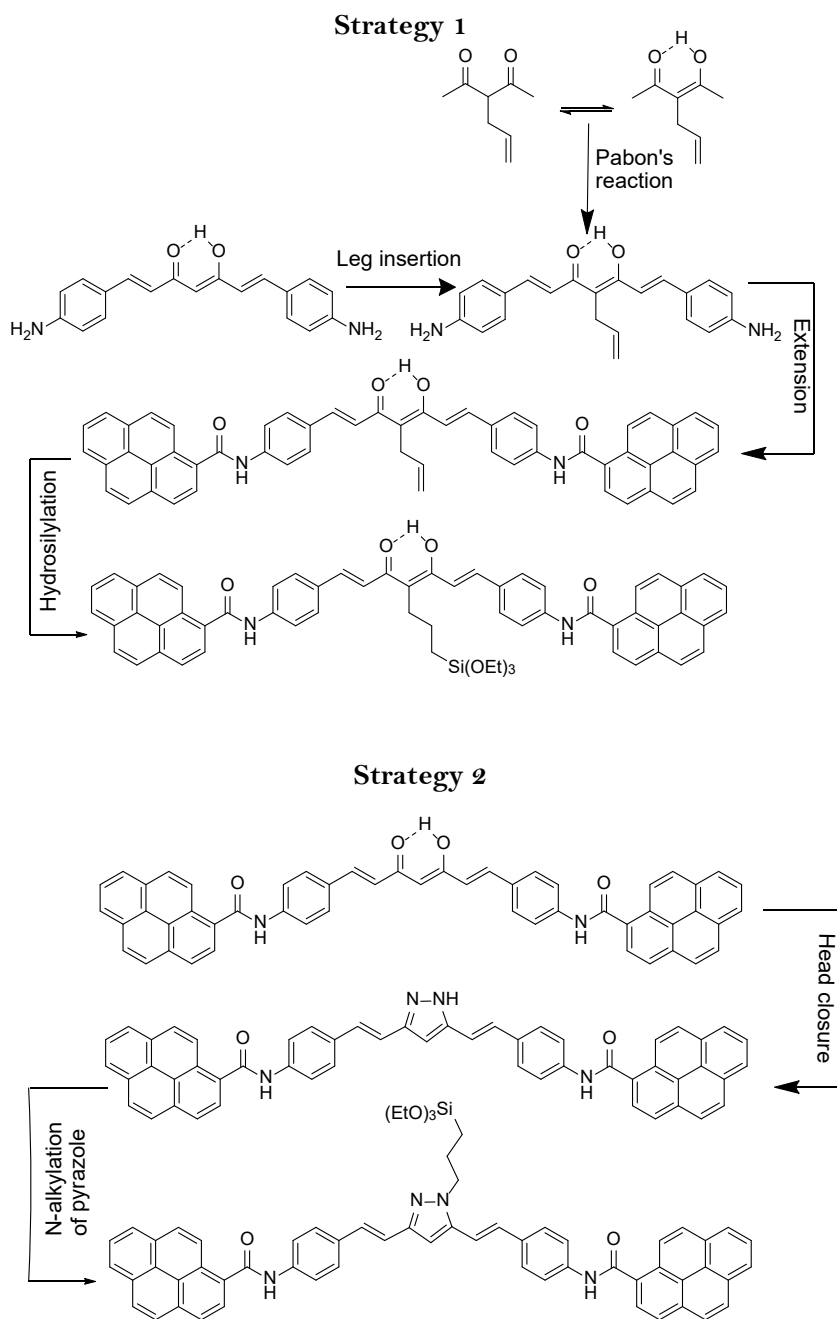


CCMoid was silane free, which implied the introduction of a silane group in the *leg* or in the *hat* in the last steps of the synthetic routes.

As it was mentioned earlier, two strategies were proposed for the achievement of the T-shaped molecules involving the addition of a *leg* or *hat*, both depicted in Scheme 6.1.

The first which involved the *leg*, implied the creation of a terminal alkene (or alkyne) *leg*-based NH<sub>2</sub>CCMoid derivative through (i) the direct insertion of the *leg* in the NH<sub>2</sub>CCMoid or through (ii) the Pabon's reaction, starting with 3-allylpentane-2,4-dione instead of acetylacetone; followed by the addition of pyrene units for the arms extension, to finish with the hydrosilylation of the double bond (or triple bond) ending group. In the second approach (*hat*), the keto-enol moiety of the pyACCMoid is transformed into a pyrazole core followed by the alkylation of the N atom of the pyrazole.

As the *leg* and the *hat* are located in the middle of the molecule separating two equal long arms, we named these types of molecules T-shaped molecules.



Scheme 6.1. Synthetic routes suggested for the achievement of terminal silane anchoring groups T-shaped pyrene-based CCMoids.

### 6.3.1. T-shaped CCMoid through the *leg*

#### 6.3.1.1. *Leg* introduction: synthesis and characterization of NH<sub>2</sub>L2bCCMoid, **10**

NH<sub>2</sub>L2bCCMoid, **10**, which contains -NH<sub>2</sub> terminal arms and a double bond terminal *leg*, as Figure 6.5 shows, was synthesized by two different methodologies.

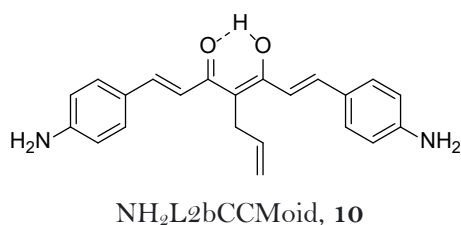
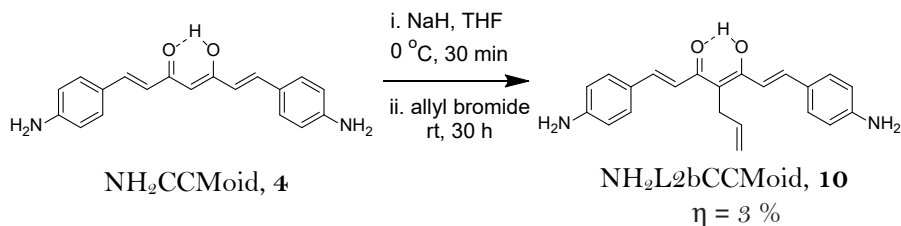


Figure 6.5. Chemdraw representation of compound **10**.

The first one, shown in Scheme 6.2, involved two steps: (i) the deprotonation of the central carbon of the NH<sub>2</sub>CCMoid skeleton, with NaH under inert atmosphere (in an ice bath using dry THF as solvent for 30 minutes), and (ii) its subsequent nucleophilic reaction with allyl bromide (for 30 h at room temperature)<sup>10</sup>. The ratio between the three reagents was 1:1:1, however not all the starting CCMoid reacted, yielding into a mixture of several products identified by TLC. The purification of the new T-shaped CCMoid was performed using a preparative thin layer chromatography, with EtOAc:Hex (2:1) as mobile phase, giving a final yield of 3%.



Scheme 6.2. Initial strategy tested for the synthesis of compound **10**.

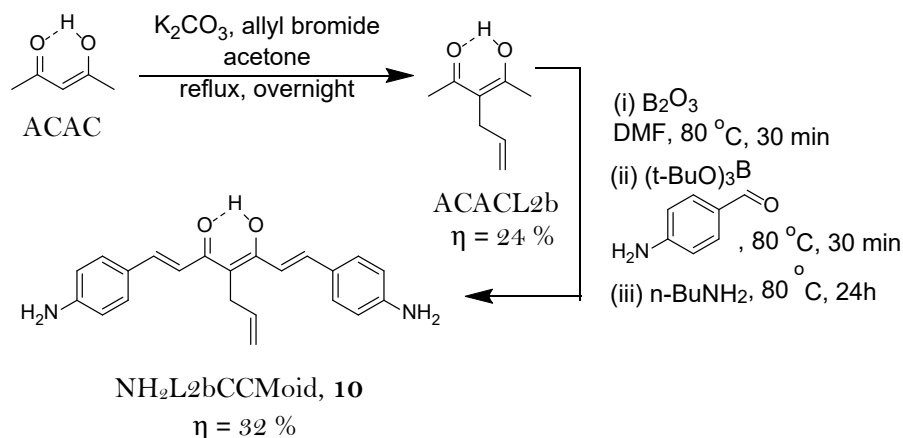
The special conditions of the initial deprotonation step were mandatory because of the possible vigorous reaction of the generated  $\text{H}_2$  with water and the fire risk if heated.

To improve the yield of the reaction, some modifications such as the use of 2 equivalents of NaH, or variations in the time given for the deprotonation process, were checked finding out the presence of 4-aminobenzaldehyde in the  $^1\text{H}$  NMR spectrum, and suggesting the degradation of the CCMoid under those conditions.

Owing to the difficulties finding the optimal conditions for this reaction, we moved from the direct introduction of the *leg* in the CCMoid to the second methodology, based on the insertion of the *leg* first in ACAC units to use them latter in modified Pabon's reactions.

The introduction of a *leg* into ACAC molecules, as it is shown in Scheme 6.3, was carried out in a similar manner as the introduction on the  $\text{NH}_2\text{CCMoid}$ . First, the central proton of the ACAC was removed using  $\text{K}_2\text{CO}_3$  as base. This was followed by its nucleophilic attack to allyl bromide in anhydrous acetone under reflux overnight <sup>11</sup>. To purify the reaction mixture, the desired monosubstituted product, ACACL2b, was separated from the byproducts, as for example the di-substituted ACAC (two double bond *legs* linked to central carbon of the ACAC units), by distillation under vacuum

giving as a result the desired system in a 24 % yield. The  $^1\text{H}$  NMR spectrum is shown in Figure A6.1, in Annex VI. Interestingly, the two tautomers, diketo and keto-enol forms of the monosubstituted ACACL2b were detected by this technique.



Scheme 6.3. Optimized strategy for the synthesis of **10**.

Once the ACACL2b was isolated, the next step was its use as a starting material in the adapted Pabon's reaction for the synthesis of  $\text{NH}_2\text{L2bCCMoid}$ , **10**. First, equal conditions as those used for the synthesis of  $\text{NH}_2\text{CCMoid}$  were applied, hence, DMF was added as solvent, and the reaction was carried out for 5 h. In agreement with the previous  $\text{NH}_2\text{CCMoid}$ , **4**, synthesis, two different products were distinguished by  $^1\text{H}$  NMR, the symmetric  $\text{NH}_2\text{L2bCCMoid}$ , **10** and the hemi- $\text{NH}_2\text{L2bCCMoid}$ , whose molecular scheme and  $^1\text{H}$  NMR are displayed in Figure A6.2 (See Annex VI).

In order to avoid the achievement of the hemi-CCMoid and improve the yield of the symmetric  $\text{NH}_2\text{L2bCCMoid}$ , **10**, different parameters were slightly varied such as the amount of solvent, the equivalents of 4-aminobenzaldehyde, the amount of n-butylamine and the reaction time. Finally, optimization of the reaction was accomplished by adding double

amount of solvent, incrementing three times the initial quantity of *n*-butylamine and keeping the reaction for a total of 24 h, which allowed the achievement of NH<sub>2</sub>L2bCCMoid, **10**, as the unique product (32% yield), without the need of further purification.

The structure of NH<sub>2</sub>L2bCCMoid was identified by <sup>1</sup>H NMR (in CDCl<sub>3</sub>, Figure 6.6) and MALDI-TOF (See Annex VI, Figure A6.3).

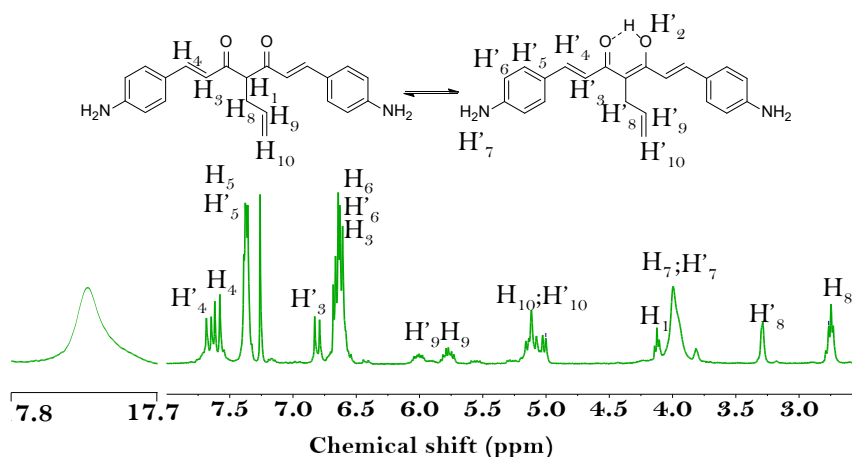


Figure 6.6. <sup>1</sup>H NMR spectrum of compound **10** in CDCl<sub>3</sub>.

In general, the keto-enol form of the CCMoids predominates above the diketo tautomer, therefore, in the <sup>1</sup>H NMR spectra, we only detect the earlier. However, in this case, both forms of the equilibrium were identified by the presence of 3 doublets attributed to 3 pairs of the *trans* protons of both tautomers (H'<sub>4</sub>, H<sub>4</sub> and H<sub>3</sub>). Here, the *trans* signal (H'<sub>3</sub>) is overlapped with the signal of the aromatics (H'<sub>6</sub> and H<sub>6</sub>), which appears together with the other aromatic doublets (H<sub>5</sub> and H'<sub>5</sub>) between 7.5 and 6.5 ppm, respectively. At approximately 6 ppm, two multiplets, assigned to the non-terminal double bond protons of the *leg* (H'<sub>9</sub> and H<sub>9</sub>), were detected followed by a third multiplet around 5 ppm, corresponding to the terminal protons

( $H'_{10}$  and  $H_{10}$ ) of the allyl group in the *leg*. The rest of the signals exclusively related to the diketo tautomer,  $H_1$  and  $H_8$ , were represented by a triplet close to 4 ppm, assigned to the central proton of the CCMoid backbone ( $H_1$ ), and the triplet of the closer proton of the *leg* ( $H_8$ ) at higher fields. The specific signals of the keto-enol form,  $H'_2$  and  $H'_8$ , are the ones shown at the lowest and highest fields, confirming the existence of the tautomeric equilibrium under these conditions. The ratio between the two tautomers (1.5:1; diketo:keto-enol), regarding the integrals found, suggest a predominant presence of the diketo form.

The ATR-FTIR spectrum of compound **10** is displayed in Figure 6.7. It shares similarities with the vibrational bands found for  $NH_2CCMoid$ , **4** (the same CCMoid without the *leg*), such as the stretching vibration of the amino terminal groups at 3357 and 3347  $cm^{-1}$  or the carbonyl moiety  $C=O$  of the keto-enol component at 1618  $cm^{-1}$ , respectively. However, additional signals corresponding to the *leg* were observed at 2927  $cm^{-1}$ , and in the region between 1500–1400  $cm^{-1}$  and 1300–1200  $cm^{-1}$ , correspondingly, that could be attributed to the stretching of the C-H from the vinyl and methylene groups and their bending modes <sup>12</sup>, in that order, confirming their presence in **10**.

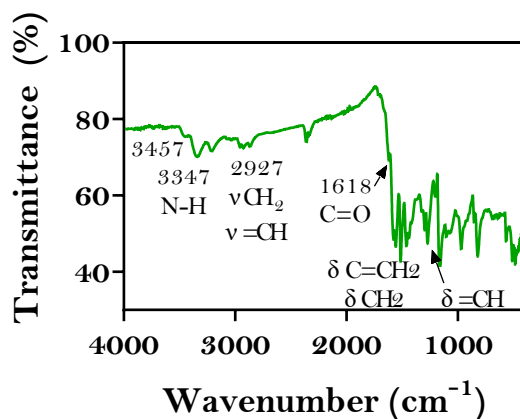


Figure 6.7. ATR-FTIR spectrum of compound **10**.

The UV-Vis absorption spectra in THF of compounds **4** and **10** are compared in Figure 6.8. The maximum absorbance band related to the CCMoid skeleton in compound **4**, NH<sub>2</sub>CCMoid, appeared at 452 nm and the ones related to the amino terminal phenyl rings at 283 and 315 nm, respectively. Compound **10**, NH<sub>2</sub>L2bCCMoid, also exhibited a similar pattern at 315 nm than **4**, displaying a slightly bathochromic shift to 458 nm for the band assigned to the skeleton, showing the latter an additional shoulder at 483 nm. However, a new and intense band appears at 387 nm, absent in compound **4**, which could be assigned to the backbone of diketo tautomer of the CCMoid, in agreement with the reported literature <sup>13</sup>. According to the bands intensities seen in the spectrum, the diketo form seems to be predominant in the sample, which agrees with the higher ratio extracted by the integrals of <sup>1</sup>H NMR analysis.

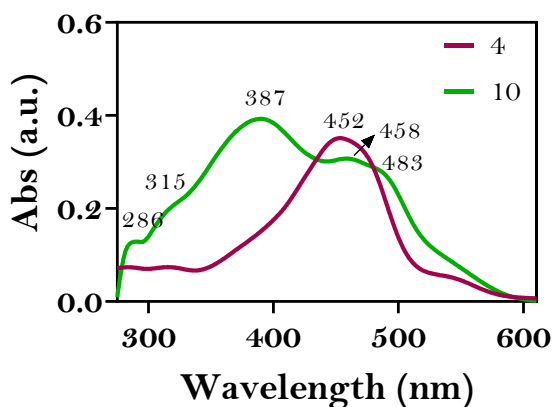


Figure 6.8. UV-Vis absorption spectra of compound **4** and **10** in THF.

The solid-state UV-Vis absorption spectrum of **10** and its Tauc's representation (detailed in Chapter 2, Eq. 2.2) are shown in Figure 6.9. As in other Chapters, they were used to extract electronic information of the compounds, due to the solvochromic character of CCMoids in solution <sup>14</sup>.



The solid-state spectrum depicted in Figure 6.8 a, differs from the obtained in solution due to the appearance of only one broad wave, appearing at an intermediate position between the diketo and keto-enol signals in solution. From the Tauc's graph (Figure 6.9 b), we conclude that the bandgap  $E_{g,op}$  for **10** is 2.00 eV, which is very similar to the  $E_{g,op}$  for **4** of 1.96 eV, indicating the same semiconducting behaviour for both compounds, suggesting that the introduction of the *leg* does not affect significantly the energy gap of the CCMoid systems.

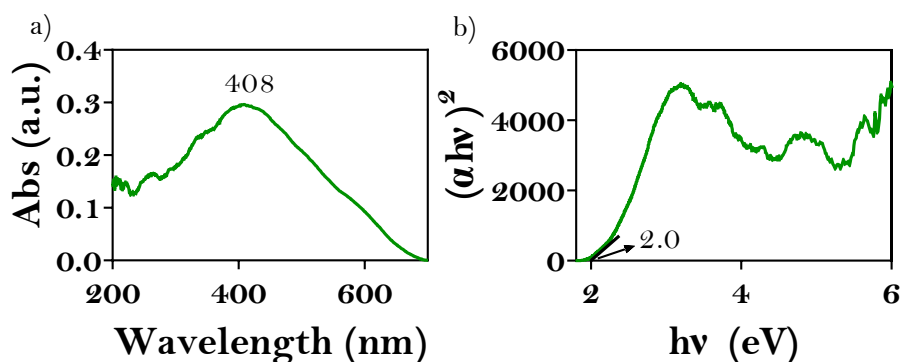


Figure 6.9. a) UV-Vis absorption spectrum of **10** in solid state. b) Tauc's representation of the UV-Vis spectrum in solid state of **10**.

The oxidation and reduction processes of compound **10** were studied by CV. The obtained voltammogram in THF with the parameters detailed in Chapter 2, is shown in Figure 6.10. Two irreversible oxidation waves and a total of seven reduction processes were identified, from which the three first appearing at -1.69, -2.04 and -2.29 V seemed, by shape, quasi-reversible, (see Annex VI, Figure A6.4 a) although proper characterization was not performed because it was found that THF was unstable after long periods time (Figure A6.4 b, Annex VI).

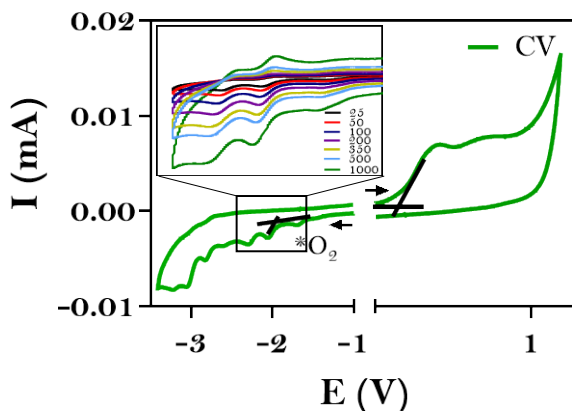


Figure 6.10. Oxidation and reduction CVs voltammogram of compound **10** in THF.

In this specific case, the calculations of the approximated values of the HOMO-LUMO and energy dispositions (with the equations described in Chapter 2) were made directly from the CV plot, instead of using the DPV (shown in Figure A6.5, Annex VI), due to the appearance of additional reduction processes attributed to small impurities.

Table 6.1 collects the HOMO, LUMO and the electrochemical  $E_g$  values of compound **10**. The estimated bandgap for **10** was 2.11 eV, which agrees with the optical bandgap value extracted from the UV-Vis absorption analysis.

<b>E onset ox</b> (V)	<b>Eonset red</b> (V)	<b>E HOMO</b> (eV)	<b>E LUMO</b> (eV)	<b>E<sub>g</sub></b> (eV)
0.15	-1.96	-4.95	-2.84	2.11

Table 6.1. HOMO, LUMO and electrochemical bandgap of **10** extracted from electrochemical analysis.

Compounds **4** (with a  $E_g$  of 2.12 eV) and **10** present almost identical gaps. Additionally, the representation of the energy level distribution for **4** and

**10**, depicted in Figure 6.11 implies a similar donor-acceptor behaviour of both systems, without being able to distinguish differences in their nature and confirming that the introduction of the *leg* does not affect the electronic properties of the CCMoid system.

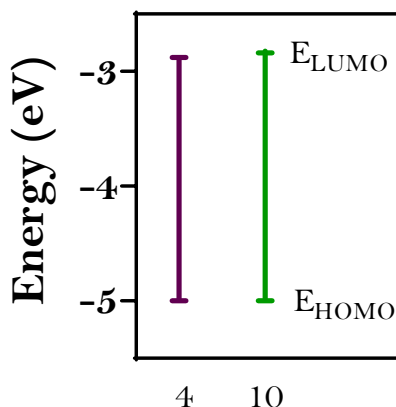
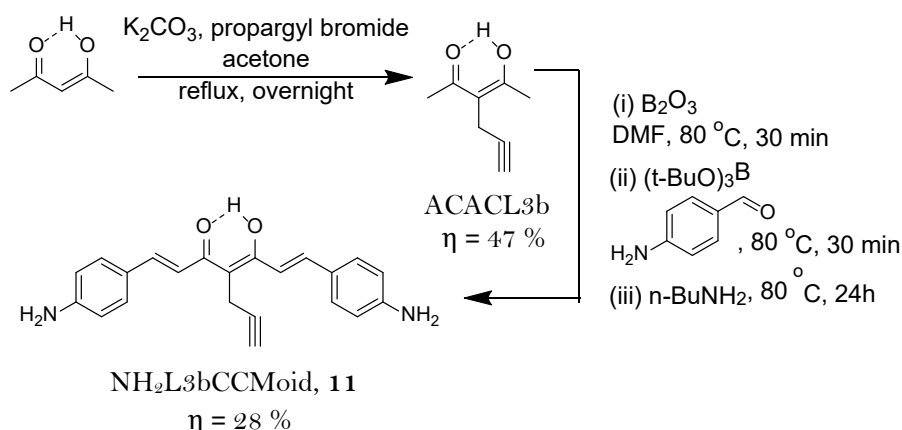


Figure 6.11. Comparison of the HOMO and LUMO energy levels diagram of compound **4** and **10**.

Same methodology starting from ACACL3b<sup>15</sup> (<sup>1</sup>H NMR spectrum in Figure A6.6) was applied for the achievement of NH<sub>2</sub>L3bCCMoid, **11**, which contains a terminal alkyne in the *leg*, as represented in Scheme 6.4.



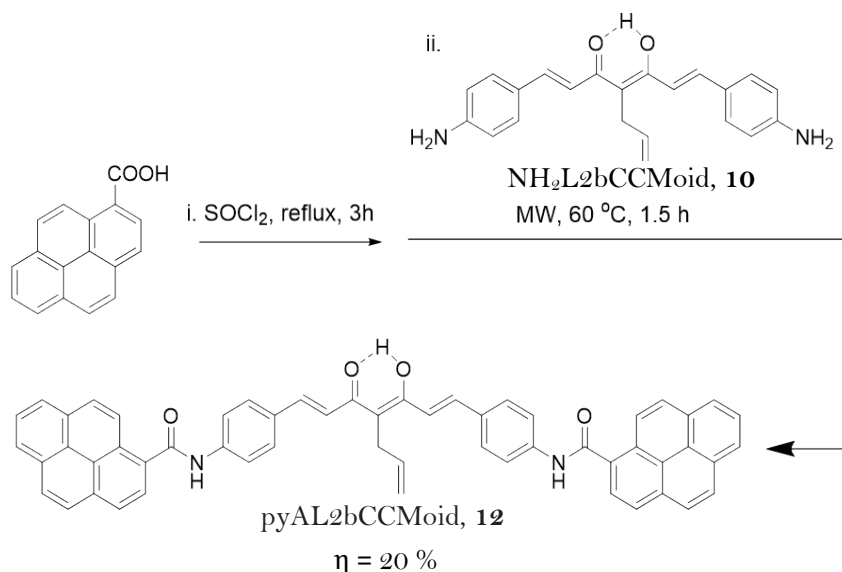
Scheme 6.4. Optimized methodology for the synthesis of compound **11**.

Compound **11** was characterized with the same techniques employed for compound **10** (Figure A6.7-A6.11 Annex VI) and as expected,  $^1\text{H}$  NMR and IR spectra confirmed the presence of the alkyne *leg*. Moreover, together with the UV-Vis spectra the predominance of the diketo tautomer of the equilibrium in solution was also observed, as it happens for **10**. Furthermore, the optical bandgap was extracted from the solid-state absorption UV-Vis data giving a value of 1.90 eV, similar to the alkene *leg*. This value could not be compared with the electrochemical one due to the limited solubility of the system.

### 6.3.1.2. Extension of the arms: synthesis and characterization of pyAL2bCCMoid, **12**

The next step, in the process to isolate the final silane-based T-shaped compound, was the incorporation of the pyrene arms. As scheme 6.5 displays, 1-pyrenecarboxylic acid was activated by  $\text{SOCl}_2$  under reflux for 3 h, and the intermediate compound was reacted with compound **10**, by the

use of microwave radiation, for 2 h at 60 °C, to obtain compound **12**, which was simply purified after washing with hot ACN (20 % yield).



Scheme 6.5. Synthetic pathway proposed for the isolation of compound **12**.

The <sup>1</sup>H NMR spectrum of compound **12** in DMSO-d<sub>6</sub> is shown in Figure 6.12. The evidence of the successful reaction was confirmed by the presence of the amide proton H<sub>7</sub>, together with the enol proton, H<sub>2</sub>, appearing both as sharp singlets at 10.99 and 17.91 ppm, respectively. Only two pairs of signals corresponding to the *trans* protons of the conjugated chain, H<sub>4</sub> and H<sub>3</sub>, appeared at 7.74 and 7.28 ppm, in that order, showing now the existence of only the keto-enol tautomer in the sample. All the aromatics peaks were distinguished in the region from 7.80 to 8.50 ppm, being the peaks corresponding to the rings bonded to the -NH group, H<sub>5</sub> and H<sub>6</sub>, the ones exhibited between 7.97 and 7.86 ppm, appearing the signals attributed to the pyrene moieties (H<sub>p</sub>) at lower fields, between 8.0 – 8.5 ppm. Only two of the protons of the *leg* were detected due to the overlapping of H<sub>8</sub> with the

solvent signal, being both, H<sub>9</sub> and H<sub>10</sub>, identified as broad mountains at 6.02 and 5.11 ppm, respectively.

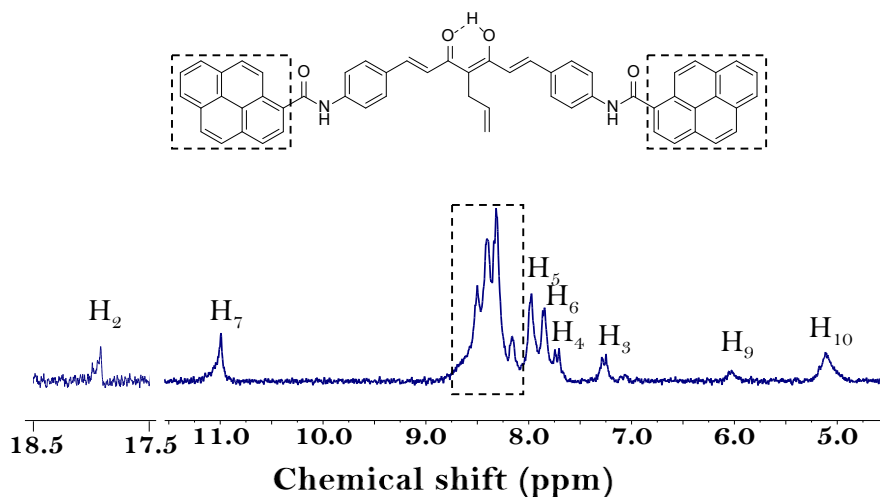


Figure 6.12. <sup>1</sup>H NMR spectrum of compound **12** in DMSO-d<sub>6</sub>.

The ATR-FTIR spectrum of compound **12** is depicted in Figure 6.13. It displays two stretching vibrations related to carbonyl bonds, one of the C=O of the keto-enol functionality at 1619 cm<sup>-1</sup>, and the other from the carbonyl of the amide at 1645 cm<sup>-1</sup>, demonstrating the formation of the new bond. Additionally, some pyrene vibrations were detected at 710 cm<sup>-1</sup> related to the C-H bending, while the rest of the signals ( $\nu$  C=C) of pyrene could be overlapped around 1500 cm<sup>-1</sup>. Finally, some peaks could be assigned to the *leg* part, such as the signals at 2970 cm<sup>-1</sup>, corresponding to the stretching of the C-H from the vinyl and methylene groups. Some in the regions of 1500–1400 and 1300–1200 cm<sup>-1</sup> were attributed to the bending modes of the methylene and vinyl groups, respectively.

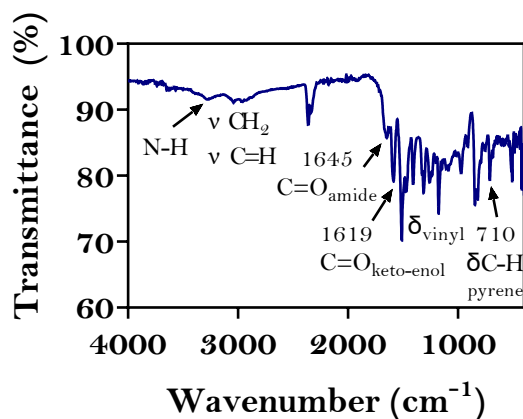
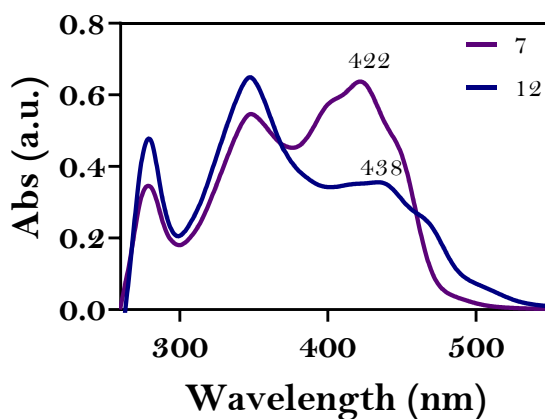
Figure 6.13. ATR-FTIR spectrum of compound **12**.

Figure 6.14 depicts the UV-Vis absorption spectrum in THF of **12**. It exhibits two typical bands attributed to the pyrene units at lower wavelengths, and the  $\pi$ - $\pi^*$  transition related to the CCMoid backbone at 438 nm. It shows a bathochromic shift of 16 nm in comparison to system **7**, which corresponds to the pyACCMoid without the *leg*. A possible explanation for this fact is related with the donor character of the allyl *leg*, which helps to the charge localization in the central part of the backbone, promoting a lower energetic transition.

Figure 6.14. UV-Vis absorption spectra of compounds **7** and **12** in THF.

The UV-Vis absorption spectrum was collected as well in solid-state in order to provide an estimation of the optical bandgap of compound **12**. The spectrum, in Figure 6.15 a, shows the band related to the CCMoid skeleton centred at 459 nm, presenting a dramatic shift from the obtained in solution, found at 438 nm. Additionally, the Tauc's plot of the solid-state data, Figure 6.15 b, provided an optical bandgap value of 2.38 eV for the same system. Compared to the optical bandgap of compound **7**, pyACCMoid without the *leg*, which is 2.45 eV, both present a similar semiconducting behaviour, corroborating again the small variations in the electronic properties due to the presence of the *leg*.

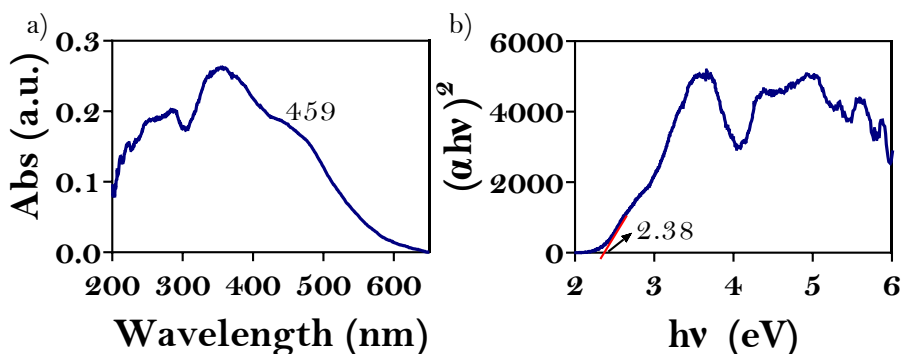


Figure 6.15. a) UV-Vis absorption spectrum of **12** in solid state. b) Tauc's representation of the UV-Vis spectrum in solid state.

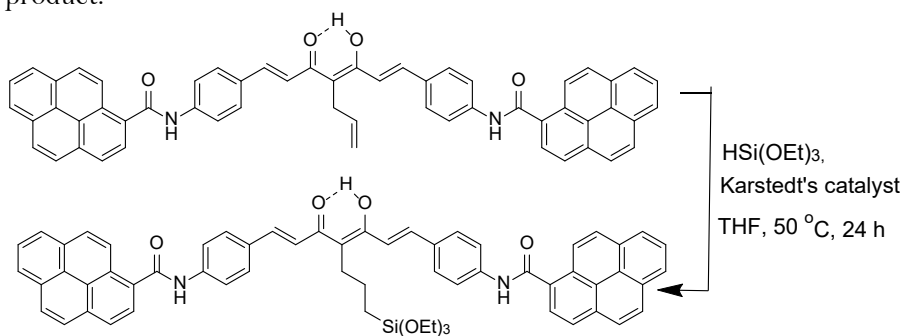
The electrochemical bandgap and the energy of the HOMO and LUMO levels of pyAL2bCCMoid were not estimated owing to the low intensity of the reduction bands in CV and DPV experiments because of the poor solubility of the compound under such conditions.



### 6.3.1.3. Hydrosilylation of pyAL2bCCMoid, **12**

Hydrosilylation is a widely recognized, and used, chemical reaction based on the addition of a silicon derivative to a carbon atom which initially was forming part of a double (or triple) bond; the reaction takes place with the simultaneous introduction of a hydrogen atom onto the other carbon atom, from the same double/triple bond unit under attack, in presence of a catalyst<sup>16</sup>.

The synthetic route employed for the hydrosilylation of compound **12** is depicted in Scheme 6.6. Initially, the reaction was tested using triethoxysilane,  $\text{HSi}(\text{OEt})_3$ , as reagent and solvent, in presence of the Karstedt catalyst. However, it did not dissolved compound **12**, hindering the reaction. Finally, the reaction was performed using dry THF to dissolve compound **12**, in presence of an excess of  $\text{HSi}(\text{OEt})_3$  and adding some drops of the Karstedt's catalyst; afterwards, the reaction was heated to activate the catalyst.<sup>17,18</sup> Generally, this transformation is considered a fast reaction, although in our case, the reaction did not finish after 1 h (or even 3 h), being left for a total of 24 h at 50 °C. Further attempts, including reactions with long periods of time (48 h), promoted the appearance of unidentified signals in the aromatic part of the  $^1\text{H}$  NMR spectrum, as well as polymerization of the silane, considering the conditions not suitable for achieving the desired product.



Scheme 6.6. Purposed hydrosilylation reaction of compound **12**.

All the  $^1\text{H}$  NMR spectra in  $\text{DMSO-d}_6$ , after 24 h of reaction (shown in Figure A6.12, Annex VI), provided similar and complex pattern, with a number of unidentified signals. Nevertheless, changes were detected, compared to the spectrum of compound **12**. The most remarkable ones include the shift of the signal attributed to the amide protons ( $\text{H}_7$ ) to higher fields, also the shift of the peaks related to the aromatic ring bonded to the N, ( $\text{H}_5$  and  $\text{H}_6$ ) and the lack of signal related *trans* protons ( $\text{H}_3$  and  $\text{H}_4$ ) as well as the disappearance of the bands assigned to the alkene bond of the *leg* ( $\text{H}_9$  and  $\text{H}_{10}$ ), being only the latest expected. Focused on the aliphatic region of the spectrum, apart from an excess of  $\text{HSi}(\text{OEt})_3$  that could not be removed under vacuum, additional signals could be guessed, at 4.20, 2.82 and 0.47 ppm, which could be related to the new silane *leg*<sup>19,20</sup>. In the end, the low intensity of these signals, the impurities present and the excess of  $\text{HSi}(\text{OEt})_3$  hampered the clear identification and therefore confirmation of the final transformation.

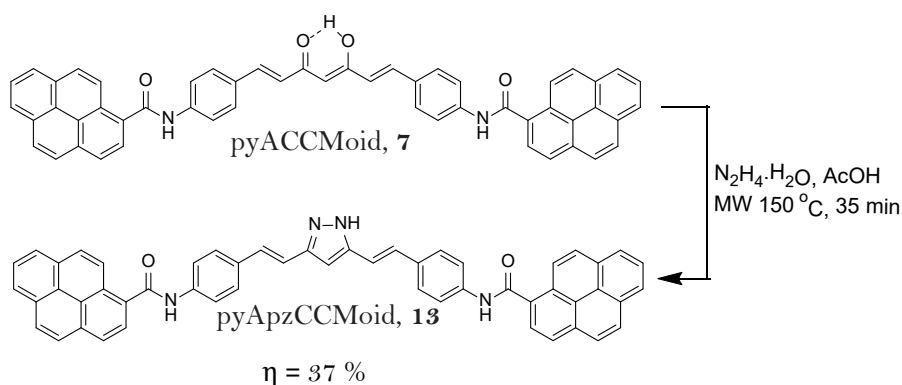
With no further elucidation of the structure, owing to the low amounts manipulated, we focused our investigation in the second strategy, mentioned at the beginning of the chapter, which implied the introduction of the *hat* in the CCMoid.

Compound **11** ( $\text{NH}_2\text{L3bCCMoid}$ ) which comprises the terminal amino groups and the alkyne terminal *leg* was prepared with the same purpose as compound **10**, as starting material for the extension of the arms with pyrene and the final hydrosilylation. In the light of the above hydrosilylation results together with the lack of new synthetic routes to avoid the found problems, no reaction attempts were tried with this compound either.

### 6.3.2. T-shaped CCMoid by customizing the keto-enol moiety

#### 6.3.2.1. Keto-enol capping: synthesis and characterization of pyrazole-based CCMoid, pyApzCCMoid, **13**

The first step, in this second methodology, is based on the creation of a pyrazole moiety by an adapted Paal-Knorr condensation where a dinucleophile (diamine) attacks the carbonyl moiety of the central keto-enol group in the CCMoid skeleton <sup>21</sup>. Specifically, as represented in Scheme 6.7, the functionalization of the keto-enol moiety of the extended CCMoid **7** was conducted with an excess of hydrazine in the microwave at 150 °C, for 35 minutes using AcOH as solvent <sup>22</sup>. After the isolation of compound **13**, the traces of AcOH were removed by stirring the compound overnight in a dispersion of K<sub>2</sub>CO<sub>3</sub> in methanol, in order to avoid polymerization processes of the silane derivative in the following step.



Scheme 6.7. Synthetic route for the achievement of compound **13**.

The  $^1\text{H}$  NMR spectra of compound **7** and **13** in  $\text{DMSO-d}_6$  are compared in Figure 6.16. All the expected signals for compound **13** appeared in the 13.0 - 6.0 ppm range. From lower to higher field, one could identify the singlet for the pyrazole proton ( $\text{H}_2$ ), the amide protons ( $\text{H}_7$ ), followed by the protons of the pyrene units ( $\text{H}_\text{p}$ ), the aromatics bonded to the N atom ( $\text{H}_5$  and  $\text{H}_6$ ), and the *trans* protons ( $\text{H}_3$  and  $\text{H}_4$ ), to end with the central proton of the pyrazole ( $\text{H}_1$ ) at higher fields, in that order. There are relevant variations in the spectrum for **13** compared to the spectrum for **7**, being the most drastic the shift of the central proton,  $\text{H}_1$ , to lower fields, and the overlapping of the two pairs of *trans* protons ( $\text{H}_3$  and  $\text{H}_4$ ) giving rise to a one false quadruplet. The formation of the heterocycle implies the increase of aromaticity of the central part of the molecule which improves the deshielding effect of the closest protons mainly  $\text{H}_1$ , appearing at lower fields.

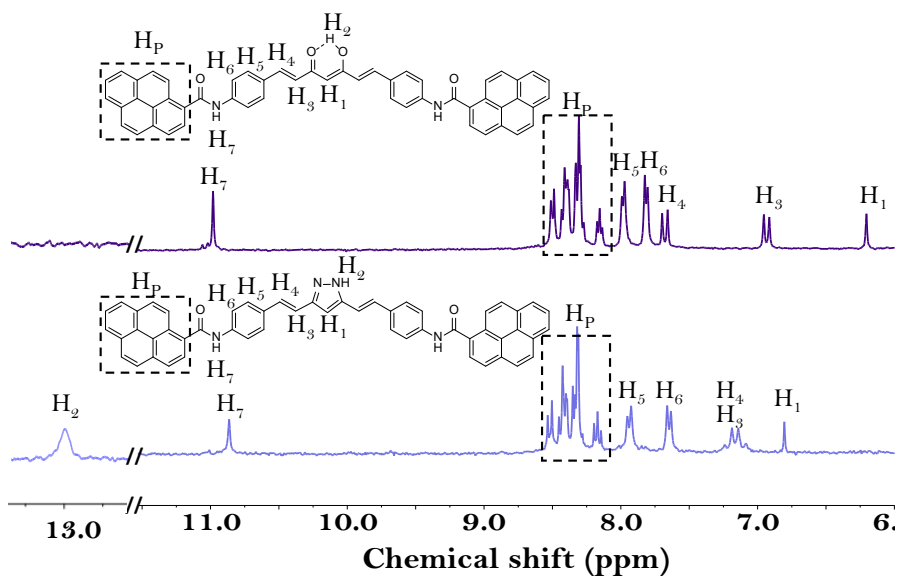


Figure 6.16. Comparison of  $^1\text{H}$  NMR spectra of compounds **7** and **13** in  $\text{DMSO-d}_6$ .

UV-Vis absorption analysis in solid-state was performed to estimate the optical bandgap of pyApzCCMoid, **13**. The spectrum, exhibited in Figure 6.17 a, shows the band related to the CCMoid backbone at 461 nm, in a similar manner as it happens with compound **12**, which present the alkene *leg* and shows a band at 459 nm, shifted both from the one of compound **7** (pyACCMoid) that appear at 438 nm. Additionally, the Tauc's plot in, Figure 6.17 b, provides an estimated value for the optical bandgap of 2.47 eV (compound **13**). Compared to the optical bandgap of compound **7**, which is 2.45 eV, both present almost the same semiconducting behaviour, suggesting the aromaticity of the pyrazole unit does not affect significantly in the overall electronic properties.

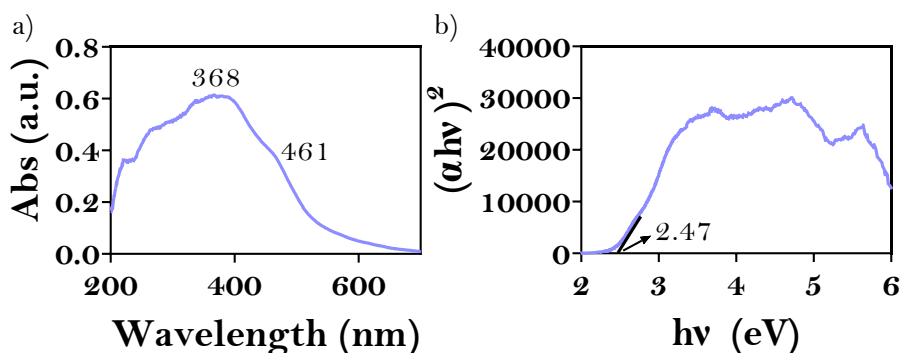


Figure 6.17. a) UV-Vis spectrum of **13** in solid state. b) Tauc's representation of the UV-Vis spectrum of **13** in the solid-state.

CV and DPV experiments of compound **13** were measured in THF with the approach described in previous Chapters in order to obtain electronic information and be able to compare with the rest of systems. The voltammograms are shown in Figure 6.18. CV exhibit one irreversible oxidation wave and two reduction processes whose reversibility was studied, and it is shown below.

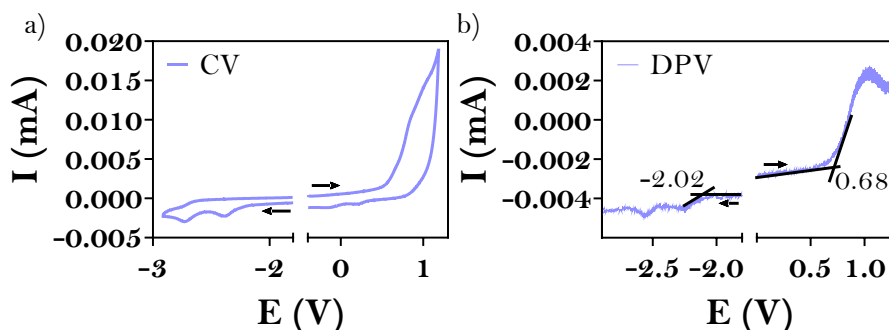


Figure 6.18. Oxidation and reduction CVs (a) and DPVs (b) voltammogram of compound **13** in THF.

Figure 6.19 a depicted the voltammogram of the first reduction wave at different scan rates and Figure 6.19 b the relationship between the anodic and cathodic current intensity *vs* the square root of the involved scan rate. In the latest, it is observed an acceptable linear fitting, suggesting a quasi-reversible process. The other analysed conditions,  $I_{pa}/I_{pc}$  and  $\Delta E_p$  are grouped in Table 6.2.  $I_{pa}/I_{pc}$  values are close to the unity, differing a maximum of 0.35 units for the lowest and highest scan rates, being 0.14 the maximum difference for the intermediate speeds. Regarding the difference between the voltage where the peaks appeared,  $\Delta E_p$ , the results deviate considerably for the three highest speeds, being less than 10 mV the difference from the ideal 59 mV for the scan rates included from 25 mV/s to 200 mV/s. Taking into account the previous results, we suggest that the first reduction process is quasi-reversible. However, the second reduction wave observed did not accomplish these criteria, concluding that it is an irreversible process.

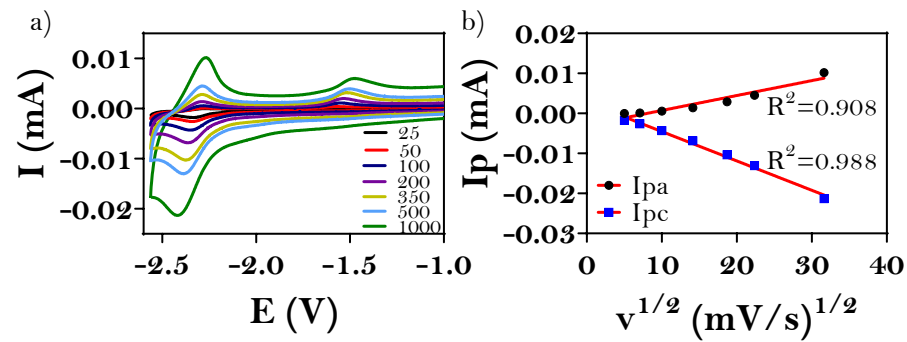


Figure 6.19. a) 1<sup>st</sup> reduction process of compound **13** at different scan rates. b) Graphical representation of the maximum intensity *vs.* the square root of the scan rate for the anodic and cathodic peaks.

Scan rate (mV/s)	Ipa/Ipc	$\Delta E_p$ (mV)
25	0.74	48
50	0.89	55
100	0.86	56
200	0.88	66
350	0.86	80
500	1.05	94
1000	1.35	142

Table 6.2. Division of the anodic and cathodic maximum intensities and potential values differences for the oxidation and reduction processes at different scan rates.

The DPV plot shown in Figure 6.18 b was used to extract the electronic information such as the HOMO and LUMO energy and the electrochemical bandgap of compound **13**, applying the equations described in Chapter 2. The values are compiled in Table 6.3. The calculated bandgap for **13** is 2.70

eV, which differ in 0.22 eV with the optical bandgap value extracted from the UV-Vis absorption analysis (2.48 eV). These electrochemical values denote that the energy gap of system **13** is bigger than that of compound **7**, where the effect of the capping is slightly emphasized in comparison with the analysis of the UV-Vis absorption features of both CCMoids.

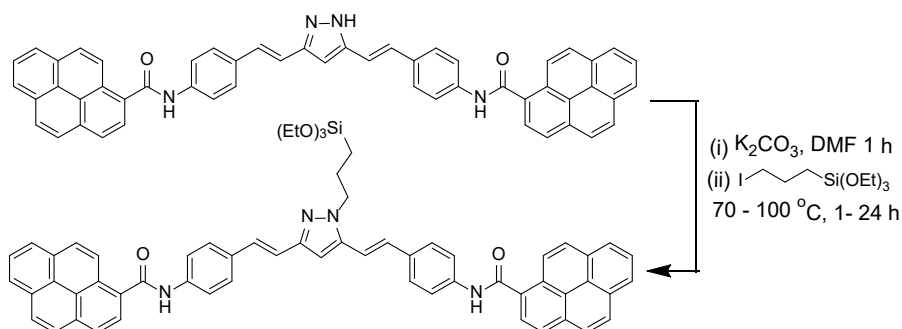
<b>E onset ox</b> (V)	<b>Eonset red</b> (V)	<b>E HOMO</b> (eV)	<b>E LUMO</b> (eV)	<b>Eg</b> (eV)
0.68	-2.02	-5.48	-2.78	2.70

Table 6.3. HOMO, LUMO and estimated electrochemical bandgap extracted from electrochemical analysis for compound **13**.

### 6.3.2.2. *Hat* introduction: alkylation of the pyrazole-based CCMoid

pyApzCCMoid, **13** was alkylated with a propyltriethoxysilane chain in a N atom of the pyrazole moiety, in a two-step process, as illustrated in Scheme 6.8. Initially, the proton of the pyrazole unit was removed using dry  $K_2CO_3$  (1 equivalent) in anhydrous DMF under inert conditions for 1 h, with a subsequent nucleophilic reaction with 3-iodopropyl triethoxysilane (1.8 equivalents). Several temperatures (RT, 70 °C, 100 °C) and reaction times (1 h, 24 h, 48 h) were tested without finding out the optimized conditions for the obtaining of the pure CCMoid being 70 °C and 1 h the best ones achieved so far.



Scheme 6.8. Suggested alkylation conditions for compound **13**.

Due to solubility reasons, the  $^1\text{H}$  NMR spectrum of the reaction was conducted in  $\text{DMSO}-d_6$ , which contains a high percentage of water, and despite of the efforts made to remove it, it was always observed in the spectrum, which can affect the stability of the final compound due to the presence of the  $-\text{Si}(\text{OEt})_3$  groups.

The  $^1\text{H}$  NMR spectrum depicted in Figure A6.13 (Annex VI) evidenced the presence of the starting CCMoid and 3-iodopropyltriethoxysilane indicating a partial conversion of the reactants. However, a small singlet appeared at 6.96 ppm which corresponds with the central proton of the new *hat*-derivative CCMoid formed. Besides, another important difference compared to the spectrum of the CCMoid of the starting material is the change in shape and splitting of the multiplet assigned to the *trans* protons. Regarding the aliphatic region of the spectrum, several signals, apart from the ones of the 3-iodopropyl-triethoxysilane were observed in the expected region, not being possible to identify the ones corresponding to the new product, which should appear around 0.8, 2.1 and 4.2 ppm <sup>23</sup>.

Although it has not been possible to optimize the reaction and separate the desired T-shaped CCMoid during the course of this thesis, future

adjustments on the reaction parameters will allow it for the consecutive exploration of its electrical properties over the device.

## 6.4. Conclusions

- Compound **10**, named NH<sub>2</sub>L2bCCMoid, which contains amino substituted aromatic rings as arms and an alkene terminal *leg*, was achieved by two different protocols either by starting with the deprotonation of NH<sub>2</sub>CCMoid, **4**, with NaH in THF, followed by the reaction with allyl bromide, or by conducting the Pabon's reaction starting with the ACAC containing the vinyl terminal *leg*, resulting the latest in higher yields.
  - The hemi-NH<sub>2</sub>L2bCCMoid which comprises only one substituted arm, was obtained using the initial conditions tested for the synthesis of compound **4**, NH<sub>2</sub>CCMoid without the *leg*.
  - The use of double amount of solvent and three times more equivalents of n-butylamine allowed the isolation of a cleaner compound **10** in high yield without further purification.
  - With that fruitful route, a similar compound, containing alkyne *leg*, **11**, was synthesized.
- <sup>1</sup>H NMR and UV-Vis analysis demonstrated the presence of the two tautomers of the equilibrium, diketo and keto-enol for compound **10**.
- The introduction of the *leg* does not affect significantly to the electronic properties of NH<sub>2</sub>L2bCCMoid, which presents similar estimated optical and electrochemical bandgaps than compound **4**, a similar CCMoid without the *leg*, providing both of them a semiconducting behaviour.

- Two synthetic strategies for the achievement of triethoxysilane terminated T-shaped pyrene based CCMoids through the *leg* or through the  $\beta$ -diketone have been developed, although not optimized, being unable to isolate any novel silane terminal pyrene extended CCMoid in a pure way.
  - Regarding the modification through the *leg*: pyAL2bCCMoid, **12** was achieved by the reaction of compound **10** with preactivated 1-pyrenecarboxylic acid, but the suitable parameters for its hydrosilylation reaction were not found out.
  - The tautomer equilibrium was not observed for compound **12** by  $^1\text{H}$  NMR or UV-Vis experiments. UV-vis analysis in solid state determined a semiconducting behaviour of pyAL2bCCMoid, with not considerable electronic alterations compared to the compound without the *leg*.
  - The closure of the keto-enol unit with hydrazine gave rise to the achievement of the pyrazole derivative CCMoid, pyApzCCMoid, **13**.
  - The average bandgap value from the optical and electrochemical calculations was slightly bigger for the pyrazole derivative **13** compared to the compound exhibiting the keto-enol moiety, **7**, suggesting a less semiconducting behaviour for the former.
  - New tests of the alkylation reaction of the pyrazole unit in presence of  $\text{K}_2\text{CO}_3$ , anhydrous DMF and iodopropyltriethoxysilane must be conducted to determine the proper temperature and time conditions for the isolation of the silane-terminal pyrene CCMoid.

## 6.5. Experimental section

### Synthesis of NH<sub>2</sub>L2bCCMoid, 10. Strategy 1

4.32 mg (0.18 mmol) of NaH (purity 60%) were dissolved in 0.5 mL of dry THF in an ice bath. Subsequently, a solution of 32.2 mg of compound **4** (0.10 mmol) in 0.3 mL dry THF was added dropwise, and the mixture was stirred 0.5 h in an ice bath and 2 h more at room temperature. Afterwards, 9  $\mu$ L of allyl bromide (0.10 mmol) was introduced into the mixture. After 30 h, the mixture was quenched with Milli-Q water and washed several times with EtOAc. The organic layer was purified by preparative TLC using EtOAc:Hex (2:1) as mobile phase to isolate the product as a dark garnet solid in 3% Yield. <sup>1</sup>H NMR (360 MHz, CDCl<sub>3</sub>)  $\delta$ : 17.76 (1H, s, keto-enol form), 7.68 (2H, d, <sup>3</sup>J=15.5 Hz), 7.62 (2H, d, <sup>3</sup>J=15.8 Hz), 7.39 (8H, m, <sup>3</sup>J= 8.3Hz), 6.83 (2H, d, <sup>3</sup>J= 15.3 Hz), 6.68 (10H, m), 6.05 (1H, m), 5.83 (1H, m), 5.16 (5H, m), 4.14 (2H, t, <sup>3</sup>J= 7.2 Hz, diketo) 4.00 (8H, s, broad), 3.30 (2H, d, <sup>3</sup>J= 4.8 Hz, keto-enol), 2.77 (3H, t, <sup>3</sup>J=7.2 Hz, diketo).

### Synthesis of ACACL2b <sup>11</sup>

5.16 mL of acetylacetone (5.00 g, 50 mmol) and 6.43 g of pre-dried K<sub>2</sub>CO<sub>3</sub> (46.5 mmol) were stirred in 40 mL of anhydrous acetone. Immediately, 5.31 mL of allyl bromide (61.5 mmol) were added, and the mixture refluxed overnight. Afterwards, Et<sub>2</sub>O was added, the mixture was filtered and the solvent of evaporated under vacuum. The product was purified by distillation under vacuum reaching a 24% yield. <sup>1</sup>H NMR (360 MHz, CDCl<sub>3</sub>)  $\delta$ : 16.73 (1H, s, keto-enol form), 5.89 (1H, m), 5.76 (1H, m), 5.14 (5H, m), 3.74 (1H, t, <sup>3</sup>J= 7.4 Hz, diketo), 2.99 (2H, d, <sup>3</sup>J=5.0 Hz, keto-enol), 2.61 (2H, t, <sup>3</sup>J=7.4 Hz, diketo), 2.18 (6H, s), 2.10 (6H, s).

### Synthesis of ACACL3b <sup>15</sup>

In a similar manner than ACACL2b, a mixture of 5.16 mL of acetylacetone (5.00 g, 50 mmol), 8.30 g of pre-dried K<sub>2</sub>CO<sub>3</sub> (60.1 mmol) and 0.87 mL of propargyl bromide (10.1 mmol) in 112 mL of anhydrous acetone were heated up to 60 °C for 24 h. Afterwards, the mixture was filtered and the solvent removed to purify the compound by column chromatography using Hex:EtOAc (2:1) as mobile phase in a 47% yield. <sup>1</sup>H NMR (360 MHz, CDCl<sub>3</sub>) δ: 16.52 (1H, s, keto-enol form), 3.87 (1H, t, <sup>3</sup>J=7.5 Hz, diketo), 3.10 (2H, d, <sup>4</sup>J=2.4, keto-enol), 2.70 (2H, dd, <sup>3</sup>J=7.5 Hz, <sup>4</sup>J= 2.58 Hz, diketo), 2.24 (6H, s), 2.21 (6H, s), 2.03 (2H, t, <sup>4</sup>J = 2.5 Hz).

### Synthesis of NH<sub>2</sub>L2bCCMoid, 10. Strategy 2

115.7 mg of ACACL2b (0.83 mmol) and 115.71 mg of B<sub>2</sub>O<sub>3</sub> (1.66 mmol) in 0.5 mL of DMF were heated at 80 °C for 30 min. Then sequentially, at an interval of 30 min, 0.88 mL of tributylborate (3.27 mmol) and a solution of 200 mg of 4-aminobenzaldehyde (1.65 mmol) in 2 mL of DMF were added. The mixture was allowed to evolve at 80 °C for another half hour and then 108 µL of butylamine (1.09 mmol) dissolved in 1 mL DMF were added dropwise. Subsequently, the reaction was kept at 80 °C for a total of 24 h and subsequently 4 mL of Milli-Q water were added allowing the mixture to cool to RT and stirring for 1 extra hour. Finally, the reaction was filtered off, washed with Milli-Q water and dried with Et<sub>2</sub>O. Yield for NH<sub>2</sub>L2bCCMoid: 32%. <sup>1</sup>H NMR (400 MHz, TCE-d<sub>2</sub>) δ: 17.72 (1H, s, keto-enol form), 7.66 (2H, d, <sup>3</sup>J=15.3 Hz), 7.59 (2H, d, <sup>3</sup>J=15.9 Hz), 7.41 (8H, d, <sup>3</sup>J= 7.8 Hz), 6.83 (2H, d, <sup>3</sup>J= 15.8 Hz), 6.69 (10H, m), 5.16 (4H, m), 4.16 (1H, t, <sup>3</sup>J= 7.3 Hz, diketo) 4.08 (4H, s, broad), 3.30 (2H, d, <sup>3</sup>J= 4.8 Hz, keto-enol), 2.72 (2H, t, <sup>3</sup>J=7.0 Hz, diketo). MS MALDI-TOF (m/z) calcd for NH<sub>2</sub>L2bCCMoid: 346.2 [M<sup>+</sup>]; found: 344.9 [M-1].

### Hemi-NH<sub>2</sub>L2bCCMoid

115.7 mg of ACACL2b (0.83 mmol) and 115.71 mg of B<sub>2</sub>O<sub>3</sub> (1.66 mmol) in 0.3 mL of DMF were heated at 80 °C for 30 min. Then progressively, at 30 min intervals, 0.88 mL of tributylborate (3.27 mmol) and a solution of 200 mg of 4-aminobenzaldehyde (1.65 mmol) in 1 mL of DMF were added. The mixture was kept at 80 °C for 30 more minutes and then 36 µL of butylamine (0.36 mmol) dissolved in 0.5 mL DMF were added dropwise. After 24 h at 80 °C, 4 mL of Milli-Q water were added allowing the mixture to cool down to RT while stirring for another one hour. Subsequently, the reaction was filtered off and the liquid centrifuged, washed with Milli-Q water, and dried with Et<sub>2</sub>O. Finally, the product was purified by preparative TLC to obtain the hemi-CCMoid as dark garnet solid in <1%. <sup>1</sup>H NMR (400 MHz, CDCl<sub>3</sub>) δ: 16.88 (1H, s, keto-enol form), 7.63 (1H, d, <sup>3</sup>J=15.5 Hz), 7.61 (1H, d, <sup>3</sup>J=15.8 Hz), 7.40 (4H, d, <sup>3</sup>J= 8.4 Hz), 6.66 (6H, m), 5.98 (1H, m), 5.80 (1H, m) 5.13 (4H, m), 4.08 (4H, s, broad), 3.98 (1H, t, <sup>3</sup>J= 7.1 Hz, diketo), 3.16 (2H, d, <sup>3</sup>J=6.9, keto-enol), 2.69 (2H, t, <sup>3</sup>J= 6.7, diketo), 2.20 (3H, s), 2.16 (3H, s).

### Synthesis of NH<sub>2</sub>L3bCCMoid, 11

Same procedure followed for NH<sub>2</sub>L2bCCMoid but using ACACL3b. Yield 28%. <sup>1</sup>H NMR (360 MHz, CDCl<sub>3</sub>) δ: 17.64 (1H, s, keto-enol form), 7.71 (2H, d, <sup>3</sup>J=15.6 Hz), 7.64 (4H, d, <sup>3</sup>J=15.2 Hz), 7.42 (3H, d, <sup>3</sup>J= 8.4 Hz), 7.36 (8H, d, <sup>3</sup>J= 7.8 Hz), 6.95 (2H, d, <sup>3</sup>J=15.6), 6.66 (16H, m), 4.31 (2H, t, <sup>3</sup>J= 7.6 Hz, diketo), 4.09 (10H, s, broad), 3.40 (2H, d <sup>4</sup>J= 2.3 Hz, keto-enol) 2.88 (4H, dd, <sup>3</sup>J= 6.9 Hz, <sup>4</sup>J=2.6 Hz, diketo), 2.17 (2H, t, <sup>4</sup>J= 2.7 Hz, keto-enol), 2.00 (3H, t, <sup>4</sup>J=2.81 Hz, diketo). MS MALDI-TOF (m/z) calcd for NH<sub>2</sub>L3bCCMoid: 344.2 [M]; found: 342.9 [M-1].

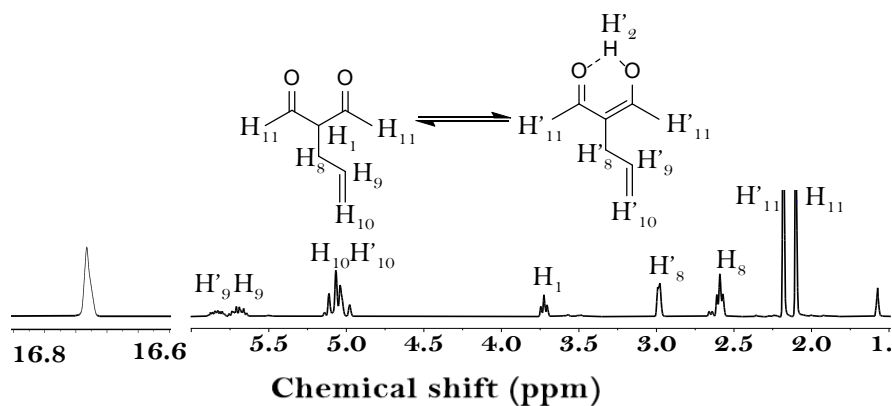
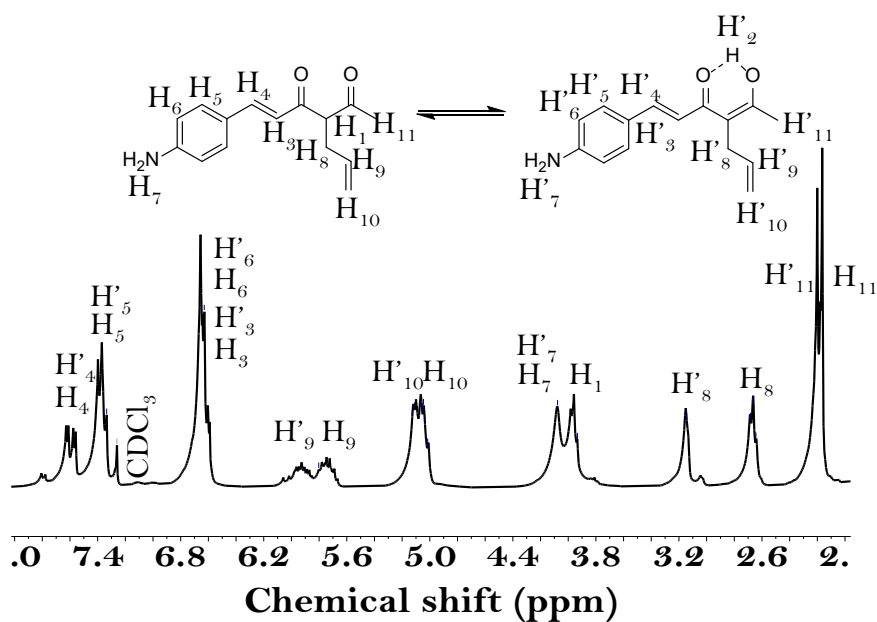
### Synthesis of PyAL2bCCMoid, 12

30 mg pyCOOH (0.12 mmol) and 0.8 mL of SOCl<sub>2</sub> (11.2 mmol) were refluxed for 3 h. Afterwards, the excess of SOCl<sub>2</sub> was removed under vacuum. A solution of the product in 5 mL of dry THF was transferred into a MW vial, together with 16 µL of Et<sub>3</sub>N (0.11 mmol), and a dispersion of NH<sub>2</sub>L2bCCMoid (20.8 mg, 0.06 mmol) in 12 mL of dry THF. The vial was introduced in the microwave at 60 °C for 2 h. When the MW reaction finished, the mixture was filtered off, the solvent removed, and the product washed with hot ACN to obtain the pure compound as a dark garnet solid in 20% yield. <sup>1</sup>H NMR (400 MHz, DMSO-d<sub>6</sub>) δ: 17.91 (1H, s), 10.99 (2H, s), 8.50 (m), 8.42 (m), 8.32 (m), 8.17 (m), 7.97 (4H, d, <sup>3</sup>J=8.0 Hz), 7.85 (4H, d, <sup>3</sup>J= 8.0 Hz), 7.74 (2H, d, <sup>3</sup>J= 15.2 Hz), 7.29 (2H, d <sup>3</sup>J= 15.24 Hz) 6.03 (broad), 5.11 (broad).

### Synthesis of pyApzCCMoid, 13

26 mg of pyACCMoid (0.03 mmol) and 20 µL of N<sub>2</sub>H<sub>4</sub>·H<sub>2</sub>O (0.41 mmol) were dispersed in 1 mL AcOH in a MW vial. The vial was placed into the reactor at 150 °C for 35 minutes. Afterwards, the precipitate was filtered off and dried with Et<sub>2</sub>O to isolate the pure system in 37% yield. <sup>1</sup>H NMR (400 MHz, DMSO-d<sub>6</sub>) δ: 13.02 (1H, s), 10.84 (2H, s), 8.52 (3H, m), 8.44 (7H, m), 8.34 (8H, m), 8.18 (3H, t, <sup>3</sup>J= 7.3 Hz), 7.95 (4H, d, <sup>3</sup>J= 8.3 Hz), 7.64 (4H, d, <sup>3</sup>J= 8.5 Hz), 7.20 (4H, m, <sup>3</sup>J= 16.8 Hz), 6.79 (1H, s).

## Annex (VI)

Figure A6.1.  $^1\text{H}$  NMR spectrum of ACACL2b in  $\text{CDCl}_3$ .Figure A6.2.  $^1\text{H}$  NMR spectrum of hemi- $\text{NH}_2\text{L}_2\text{bCCMoid}$  in  $\text{CDCl}_3$ .



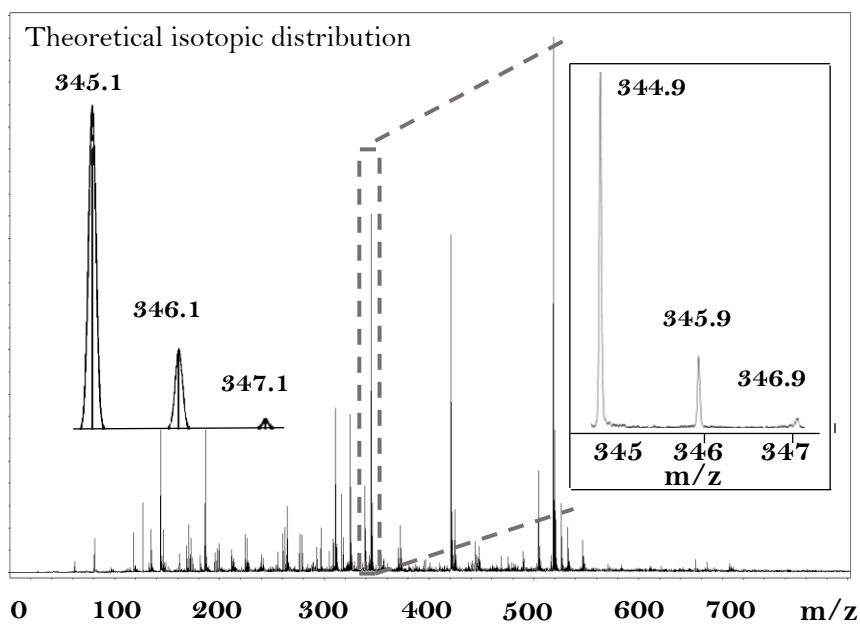


Figure A6.3. MALDI-TOF mass spectrum of compound **10** in negative mode.

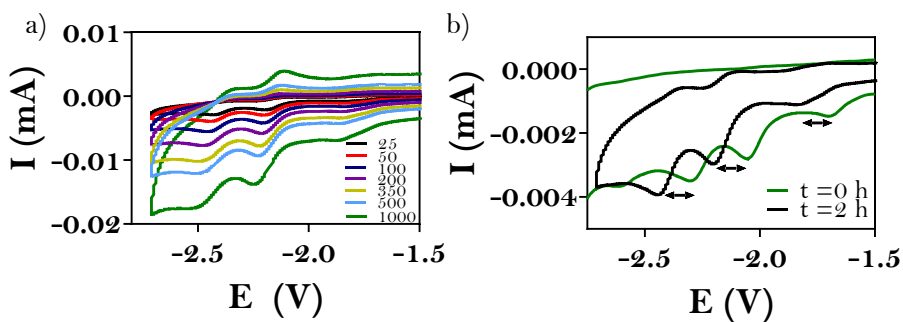


Figure A6.4. a) Reduction CV reversibility studies of **10** at different scan rates. b) Shift in the reduction CV voltammogram of **10** in THF with time due to solvent degradation.

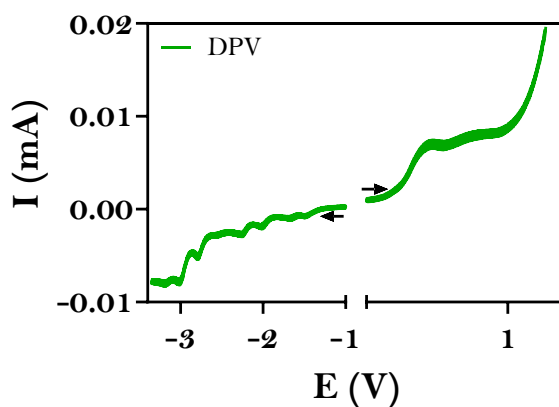


Figure A6.5. Oxidation and reduction DPVs voltammogram of compound **10** in THF.

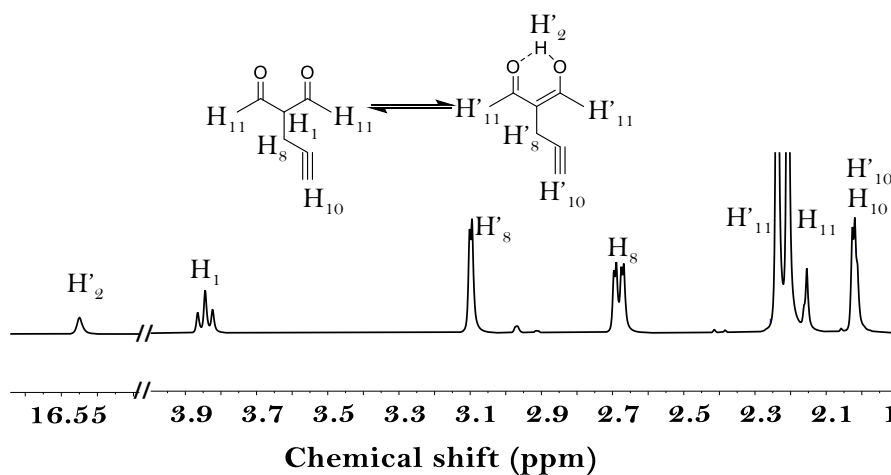
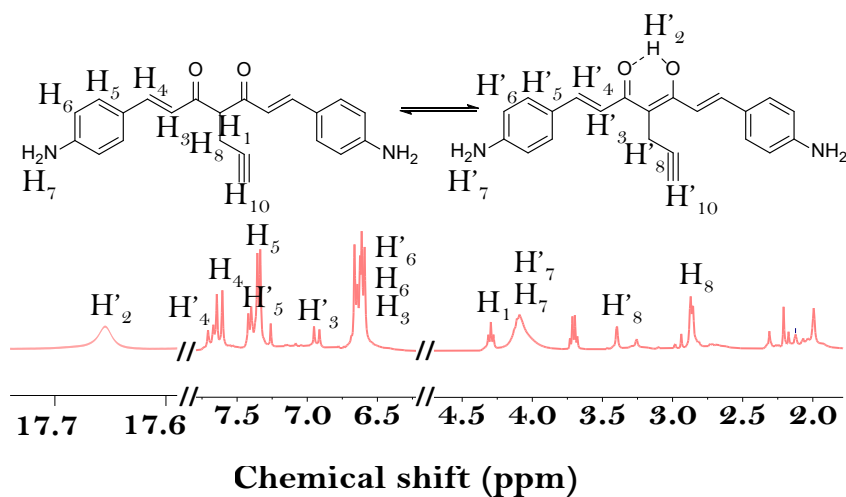
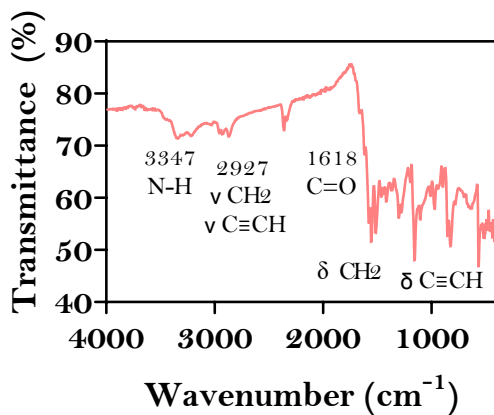


Figure A6.6.  $^1\text{H}$  NMR spectrum of ACACL3b in  $\text{CDCl}_3$ .

Figure A6.7.  $^1\text{H}$  NMR spectrum of compound **11** in  $\text{CDCl}_3$ .Figure A6.8. ATR-FTIR spectrum of compound **11**.

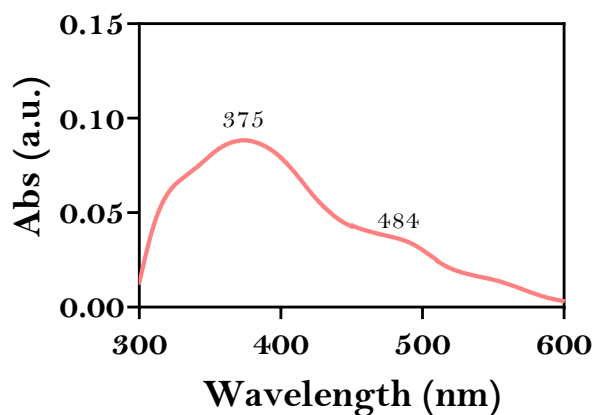


Figure A6.9. UV-Vis absorption spectrum of **11** in THF.

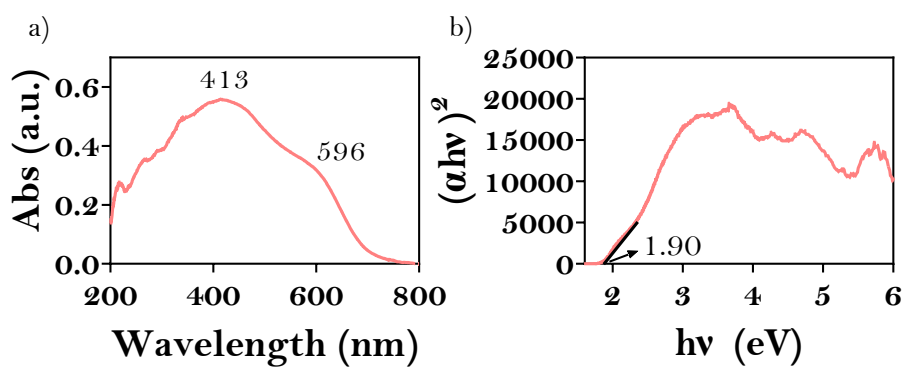


Figure A6.10. a) UV-Vis spectrum of **11** in solid state. b) Tauc's representation of the solid state UV-Vis data of compound **11**.

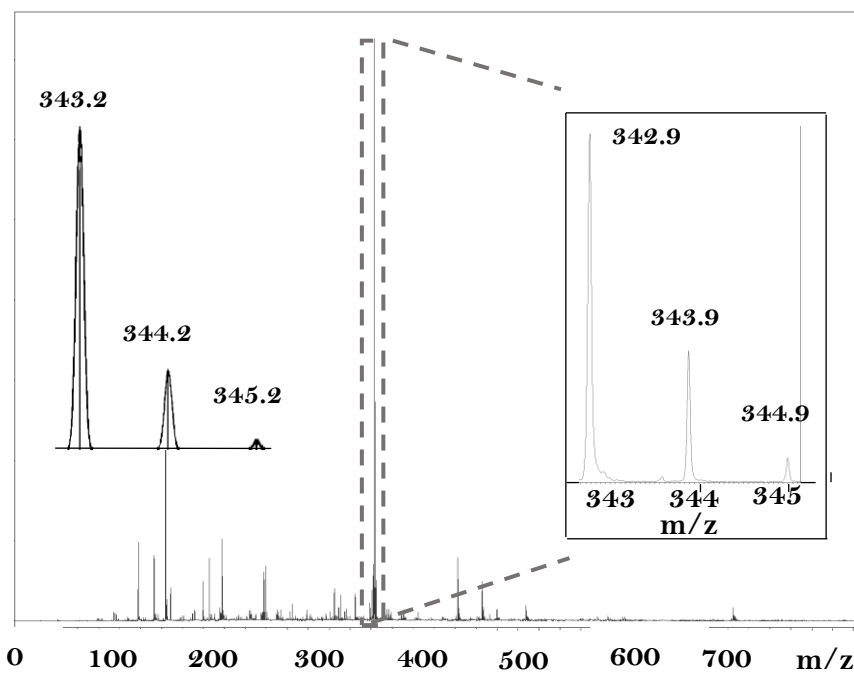


Figure A6.11. MALDI-TOF mass spectrum in negative mode of compound **11**.

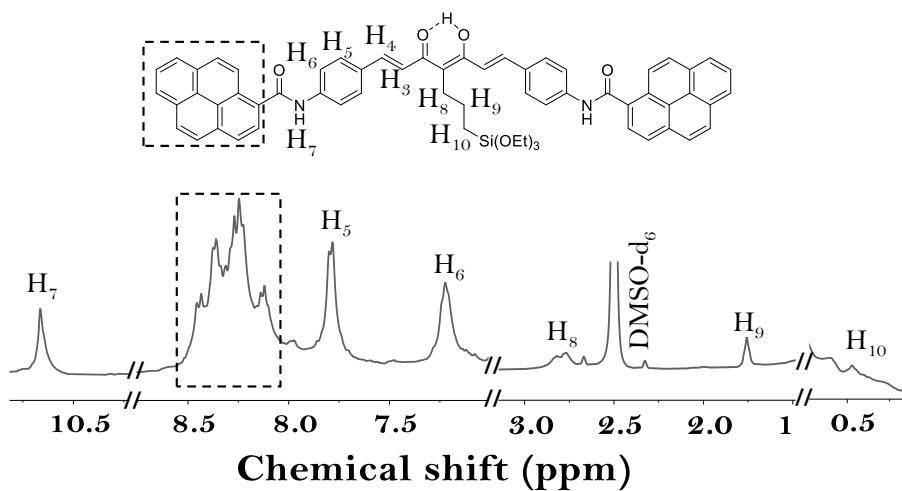


Figure A6.12.  $^1\text{H}$  NMR spectrum of the product from the hydrosilylation reaction of compound **12** in  $\text{DMSO-d}_6$  after 24 h reaction.

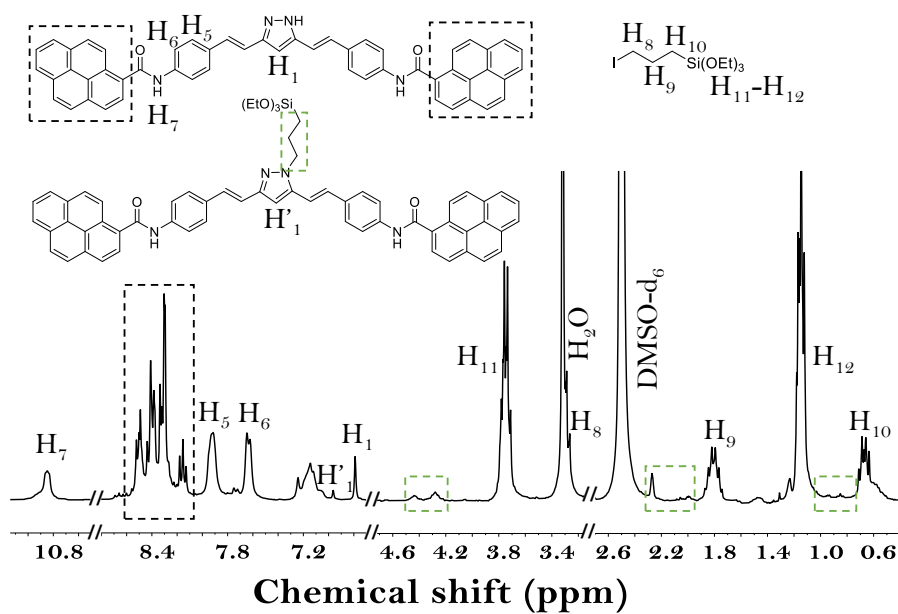


Figure A6.13.  $^1\text{H}$  NMR spectrum of the product from the alkylation reaction of compound **13** in  $\text{DMSO-d}_6$  after 1 h reaction.

## References

- (1) Xiang, D.; Wang, X.; Jia, C.; Lee, T.; Guo, X. Molecular-Scale Electronics: From Concept to Function. *Chem. Rev.* **2016**, *116* (7), 4318–4440.
- (2) Prins, F.; Barreiro, A.; Ruitenberg, J. W.; Seldenthuis, J. S.; Aliaga-Alcalde, N.; Vandersypen, L. M. K.; Van Der Zant, H. S. J. Room-Temperature Gating of Molecular Junctions Using Few-Layer Graphene Nanogap Electrodes. *Nano Lett* **2011**, *11* (11), 4607–4611.
- (3) Xu, Q.; Scuri, G.; Mathewson, C.; Kim, P.; Nuckolls, C.; Bouilly, D. Single Electron Transistor with Single Aromatic Ring Molecule Covalently Connected to Graphene Nanogaps. *Nano Lett* **2017**, *17* (9), 5335–5341.
- (4) Li, S.; Li, Q.; Carpick, R. W.; Gumbsch, P.; Liu, X. Z.; Ding, X.; Sun, J.; Li, J. The Evolving Quality of Frictional Contact with Graphene. *Nature* **2016**, *539* (7630), 541–545.
- (5) Feng, X.; Kwon, S.; Park, J. Y.; Salmeron, M. Superlubric Sliding of Graphene Nanoflakes on Graphene. *ACS Nano* **2013**, *7* (2), 1718–1724.
- (6) Sadeghi, H.; Sangtarash, S.; Lambert, C. Robust Molecular Anchoring to Graphene Electrodes. *Nano Lett* **2017**, *17* (8), 4611–4618.
- (7) El Abbassi, M.; Sangtarash, S.; Liu, X.; Perrin, M. L.; Braun, O.; Lambert, C.; van der Zant, H. S. J.; Yitzchaik, S.; Decurtins, S.; Liu, S. X.; Sadeghi, H.; Calame, M. Robust Graphene-Based Molecular Devices. *Nature Nanotechnol.* **2019**, *14* (10), 957–961.
- (8) Hsu, S. H.; Reinhoudt, D. N.; Huskens, J.; Velders, A. H. Imidazolid monolayers for reactive microcontact printing. *J. Mater. Chem.* **2008**, *18* (41), 4959–4963.
- (9) Schmidt, H.; Scholze, H.; Kaiser, A. Principles of Hydrolysis and Condensation Reaction of Alkoxysilanes. *J. Non-Cryst.* **1984**, *63* (1-2), 1-11.
- (10) Top, S.; Thibaudeau, C.; Vessières, A.; Brulé, E.; Le Bideau, F.; Joerger, J. M.; Plamont, M. A.; Samreth, S.; Edgar, A.; Marrot, J.; Herson, P.; Jaouen,

- G. Synthesis and Structure Activity Relationship of Organometallic Steroidal Androgen Derivatives. *Organometallics* **2009**, *28* (5), 1414–1424.
- (11) Kalaitzakis, D.; Rozzell, J. D.; Smonou, I.; Kambourakis, S. Synthesis of Valuable Chiral Intermediates by Isolated Ketoreductases: Application in the Synthesis of  $\alpha$ -Alkyl- $\beta$ -Hydroxy Ketones and 1,3-Diols. *Adv. Synth. Catal.* **2006**, *348* (14), 1958–1969.
- (12) McLAcnw, R. D.; Nyquist, R. A. The Vibrational Spectra of the Allyl Halides. *Spectrochim. Acta A Mol. Biomol. Spectrosc.* **1968**, *24* (2), 103–114.
- (13) Rigamonti, L.; Orteca, G.; Asti, M.; Basile, V.; Imbriano, C.; Saladini, M.; Ferrari, E. New Curcumin-Derived Ligands and Their Affinity towards  $\text{Ga}^{3+}$ ,  $\text{Fe}^{3+}$  and  $\text{Cu}^{2+}$ : Spectroscopic Studies on Complex Formation and Stability in Solution. *New J. Chem.* **2018**, *42* (10), 7680–7690.
- (14) Nardo, L.; Andreoni, A.; Masson, M.; Haukvik, T.; Tønnesen, H. H. Studies on Curcumin and Curcuminoids. XXXIX. Photophysical Properties of Bisdemethoxycurcumin. *J Fluoresc.* **2011**, *21* (2), 627–635.
- (15) Lenhart, J. A.; Ling, X.; Gandhi, R.; Guo, T. L.; Gerk, P. M.; Brunzell, D. H.; Zhang, S. “Clicked” Bivalent Ligands Containing Curcumin and Cholesterol as Multifunctional  $\text{A}\beta$  Oligomerization Inhibitors: Design, Synthesis, and Biological Characterization. *J. Med. Chem.* **2010**, *53* (16), 6198–6209.
- (16) de Almeida, L. D.; Wang, H.; Junge, K.; Cui, X.; Beller, M. Recent Advances in Catalytic Hydrosilylations: Developments beyond Traditional Platinum Catalysts. *Angew. Chem. Int. Ed.* **2021**, *60* (2), 550–565.
- (17) Pillot, J.-P.; Birot, M.; Dao, T. M.; Vu, M. D.; Hoang, N. L. T.; Tran, T. S. The Use of Naturally-Occurring Phenols in the Synthesis of Novel Functional Polysiloxanes. *Surf. Coat. Int.* **2001**, *84* (3), 197–204.
- (18) Arkles, B. Curcumin and its derivatives for use as silicon colorants. US 2007/0204412 A1, September 7, **2007**.



- (19) González-Campo, A.; Juárez-Pérez, E. J.; Viñas, C.; Boury, B.; Sillanpää, R.; Kivekäs, R.; Núñez, R. Carboranyl Substituted Siloxanes and Octasilsesquioxanes: Synthesis, Characterization, and Reactivity. *Macromolecules* **2008**, *41* (22), 8458–8466.
- (20) Semenov, V. V.; Cherepennikova, N. F.; Grigor'Ev, I. S.; Klapshina, L. G.; Kuznetsova, O. V.; Lopatin, M. A.; Bushuk, B. A.; Bushuk, S. B.; Kal'vinkovskaya, Y. A.; Douglas, W. E. Europium, Terbium, and Ytterbium 3-(3'-Triethoxysilylpropyl)Pentane-2,4-Dionates. Synthesis and the Formation of Luminescent Sol-Gel Films. *Russ. J. Coord. Chem.* **2007**, *33* (1), 68–78.
- (21) Ahsan, N.; Mishra, S.; Jain, M. K.; Surolia, A.; Gupta, S. Curcumin Pyrazole and Its Derivative (N-(3-Nitrophenylpyrazole) Curcumin Inhibit Aggregation, Disrupt Fibrils and Modulate Toxicity of Wild Type and Mutant  $\alpha$ -Synuclein. *Sci. Rep.* **2015**, *5* (1), 9862.
- (22) Minetto, G.; Raveglia, L. F.; Taddei, M. Microwave-Assisted Paal-Knorr Reaction. A Rapid Approach to Substituted Pyrroles and Furans. *Org. Lett.* **2004**, *6* (3), 389–392.
- (23) Kronstein, M.; Akbarzadeh, J.; Drechsel, C.; Peterlik, H.; Neouze, M. A. Tailoring Photoluminescence Properties in Ionic Nanoparticle Networks. *Chem. Eur. J.* **2014**, *20* (34), 10763–10774.

## General conclusions

In the course of this doctoral thesis, we have developed 13 new CCMoids to be used in the field of Molecular Electronics. Some of them have been designed for single-molecule transport studies and others to analyse their electronic behaviour when assembled in monolayers. Specifically:

The successful preparation of self-assembled monolayers (SAMs) of supramolecular host-guest units formed by a CCMoid which contains ferrocene groups (guest, FcCCMoid, **1**), together with cucurbit[7]uril (host, CB[7]) or thiolated *beta*-cyclodextrin (host, SH- $\beta$ CD) on gold surfaces allowed to explore the electrical performance of the systems through their junction with eutectic gallium indium (EGaIn). Our results suggest that in the tested conditions, the CCMoid does not have any significant effect in the conductivity of the system. Additionally, the complexes do not act as a rectifier in this type of sandwiched two-terminal devices.

The synthesis of an amino substituted CCMoid, (named NH<sub>2</sub>CCMoid, **4**) yielded as a byproduct an additional CCMoid: the hemiCCMoid system called hemiNH<sub>2</sub>CCMoid, **5**. This opens the possibility to design asymmetric CCMoids with diverse attractive functionalities.

Additionally, the reactive amino groups of compound **4**, allowed the extension of the CCMoid *arms* by its reaction with different aldehyde and carboxylic acid functional groups comprised in polycyclic aromatic hydrocarbons (PAHs). In this way, two novel enlarged CCMoids resulted: compound **6**, peICCMoid including perylene moieties, that proved to be unstable in contact with water, and with time, and compound **7**, pyACCMoid which comprises pyrene units and presents great stability. The length and chemical structure of the latest converted compound **7** into a promising candidate to be analysed as active molecule in graphene-based three-terminal devices. The electrical characterization performed in a single

molecule regime, has shown the increase in the current intensity once the system was deposited by dip coating methods onto electroburned nanogapped graphene electrodes. This first attempt seems to agree with previous investigations published in the literature, where the conductance behaviour relates to the presence of the CCMoid over the device, in this case by the  $\pi$ - $\pi$  interaction between the pyrene moieties within the molecule and the graphene electrodes.

T-shaped CCMoids, with an anchoring alkosylsilane group in the middle of the backbone, were proposed for the fabrication of robust graphene-based three terminal devices. The synthetic efforts were focused on two different strategies. On the one hand, the introduction of a *leg* within the molecule, which derived into the achievement of intermediate products containing amino terminal arms and double (NH<sub>2</sub>L2bCCMoid, **10**) or triple bond *legs*, (NH<sub>2</sub>L3bCCMoid, **11**), respectively, together with the consecutive extension of the arms using 1-pyrenecarboxylic acid has led to the achievement of pyAL2bCCMoid, **12**. On the other hand, in the formation of the *hat*, compound **13**, pyApzCCMoid, with pyrene extended arms and a pyrazole central unit, was synthesized. Despite of the efforts applied in the preparation of the terminal alkosylsilane derivatives, inconclusive results were obtained and not confirmation of the introduction of the reactive silane groups was achieved. Therefore, there is still work in progress to find out the optimal conditions for the synthesis of the final T-shaped CCMoids.

Overall, most of the main objectives set in this project, regarding the synthesis of novel CCMoids, have been accomplished and with the present results, new possibilities to the field of CCMoids and Molecular Electronics have been opened.

# Materials and Equipment

## Solvents

Dimethylformamide (DMF), methanol (MeOH) sulphuric acid ( $\text{H}_2\text{SO}_4$ ) and acetic acid (AcOH) were supplied by Carlo Erba. Ethyl acetate (EtOAc), hydrogen peroxide ( $\text{H}_2\text{O}_2$ ), high purity dichloromethane (DCM) and tetrahydrofuran (THF) were provided by Scharlab. Diethyl ether ( $\text{Et}_2\text{O}$ ), absolute ethanol (EtOH), acetone, acetonitrile (ACN), chloroform ( $\text{CHCl}_3$ ) (JT Baker), hexane (Hex), isopropanol, dioxane and hydrochloric acid (HCl) were supplied by Serviqualia from the brand ChemLab.

DMSO HPLC quality from ROMIL was used in the SAMs formation supplied by Teknocrima. Nitric acid ( $\text{HNO}_3$ ) was supplied by Panreac. 1,1,2,2-tetrachloroethane (TCE) was supplied by Merk-Sigma Aldrich.

Important note: dry THF and dry DCM were extracted from a solvent purification system PS-MD-3 provided by Inert Technologies.

## Reagents

Acetylacetonate (ACAC,  $\text{C}_5\text{H}_7\text{O}_2$ ), boron trioxide ( $\text{B}_2\text{O}_3$ ), tributyl borate ( $(\text{BuO})_3\text{B}$ ,  $\text{C}_{12}\text{H}_{27}\text{BO}_3$ ), n-butyl amine (n-BuNH<sub>2</sub>,  $\text{C}_4\text{H}_{11}\text{N}$ ), ferrocenecarboxaldehyde ( $\text{C}_{11}\text{H}_{10}\text{FeO}$ ), mesyl chloride ( $\text{CH}_3\text{ClO}_2\text{S}$ ), thiourea ( $\text{CH}_4\text{N}_2\text{S}$ ), potassium hydrogen sulphate ( $\text{KHSO}_4$ ), 4-nitrobenzaldehyde ( $\text{C}_7\text{H}_5\text{NO}_3$ ), di-tert-butyl di-carbonate ( $\text{C}_{10}\text{H}_{18}\text{O}_5$ ), sodium hydrogen carbonate ( $\text{NaHCO}_3$ ), sodium chloride (NaCl) magnesium sulphate ( $\text{MgSO}_4$ ) 4-aminobenzyl alcohol ( $\text{C}_7\text{H}_9\text{NO}$ ), potassium permanganate ( $\text{KMnO}_4$ ), manganese (II) sulphate monohydrate ( $\text{MnSO}_4 \cdot \text{H}_2\text{O}$ ), sodium hydroxide (NaOH), 1-ethyl-3-(3-dimethylaminopropyl)carbodiimide (EDC,  $\text{C}_8\text{H}_{17}\text{N}_3$ ), N-hydroxysuccinimide (NHS,  $\text{C}_4\text{H}_5\text{NO}_3$ ), 3-perylenecarboxaldehyde

(C<sub>21</sub>H<sub>12</sub>O), 1- pyrenecarboxaldehyde (C<sub>17</sub>H<sub>10</sub>O), thionyl chloride (SOCl<sub>2</sub>), triethylamine (Et<sub>3</sub>N, C<sub>6</sub>H<sub>15</sub>N), methyl-4-formylbenzoate (C<sub>9</sub>H<sub>8</sub>O<sub>3</sub>), lithium hydroxide (LiOH), sodium hydride (NaH), allyl bromide (C<sub>3</sub>H<sub>5</sub>Br), potassium carbonate (K<sub>2</sub>CO<sub>3</sub>), propargyl bromide (C<sub>3</sub>H<sub>3</sub>Br), hydrazine monohydrate (N<sub>2</sub>H<sub>4</sub>·H<sub>2</sub>O) were provided by Sigma Aldrich, ABCR, Fluorochem and TCI Chemicals.

β-cyclodextrin (β-CD, C<sub>42</sub>H<sub>70</sub>O<sub>35</sub>) and cucurbit[7]uril (CB[7], C<sub>42</sub>H<sub>42</sub>N<sub>28</sub>O<sub>14</sub>) were supplied by Strem Chemicals

Single walled carbon nanotubes (SWCNTs) were provided by Sigma Aldrich and its purification was carried out in collaboration with Dr. Stefania Sandoval and Dr. Gerard Tobias (ICMAB).

### **Microwave (MW) reactor**

Microwave synthesis was carried out using borosilicate vials of 10 or 30 mL with a polyether ether ketone cup in a Monowave-400 MW from Anton Paar.

### **Nuclear Magnetic Resonance (NMR)**

<sup>1</sup>H and <sup>13</sup>C NMR measurements were performed in a Bruker Avance DPX of 360 MHz (8.4T) and in a Bruker Avance-III of 400 MHz (9.4T) at Servei de Ressonancia Magnètica Nuclear (SeRMN) in Universitat Autònoma de Barcelona (UAB) to elucidate the chemical structure of the synthesized compounds. The data analysis was carried out using MestReNova software, referenced to the central peak of the deuterated solvent.

## **Fourier Transform Infrared Spectroscopy (FT-IR)**

The synthesized CCMoids were analysed by Attenuated Total Reflectance (ATR) -FTIR in a FT-IR JASCO 4700LE from 400 to 4000  $\text{cm}^{-1}$  to detect vibrations assigned to specific chemical bonds.

## **Ultraviolet-Visible Absorption Spectroscopy (UV-Vis)**

UV-Vis absorption were measured in solution as well as in solid state in a JASCO V-780 UV-Vis/NIR spectrometer with the liquid or the integrating sphere accessories in a 200-800 nm range.

## **Cyclic Voltammetry (CV) and Differential Pulse Voltammetry (DPV)**

CV and DPV experiments were conducted to gain insight into the HOMO, LUMO and electrochemical bandgap of the compounds in a three electrodes cell connected to a SP-50 potentiostat from Biologics.

## **Mass Spectrometry (MS)**

Mass spectra of the compounds were obtained with a Bruker ULTRAFLEXEXTREME mass spectrometer at Servei de Proteòmica I Biologia Estructural from UAB and Servei de Proteòmica i imatge from Institut de Química Avançada de Catalunya (IQAC) to identify the mass to charge ratio of the ions of the sample in a matrix-assisted laser desorption/ionization time of fly (MALDI-TOF) measurement. The software used for the data analysis were mMass and FlexAnalysis.

## **Elemental Analysis (EA)**

Elemental Analysis was performed with a Thermo Scientific Flash 2000 and Flash Smart elemental analyser in IQAC to know the exact elemental composition in the sample evaluating C, H and N.

## **Contact angle (CA)**

Contact angle measurements were recorded in a Attension Theta Lite instrument from Biolin Scientific analysed using One Attention software in order to study the wettability of the functionalised surfaces.

## **Ellipsometry**

Ellipsometry was employed to determine the thickness of the SAMs. We measured  $\psi$  ( $\Psi$ ), which is the ratio of the amplitudes of the p- and s-polarized light, and  $\Delta$ , which is the phase difference between them, of the reflected light for incident angles of  $65^\circ$ ,  $70^\circ$  and  $75^\circ$  in an alpha-SE Ellipsometer from J.A. Woollam Ellipsometry Solutions at UAB with help of Dr. Alejandro Martin and Prof. Eliseo Ruiz. To obtain an experimental value of the thickness, the provided data was fitted to the Cauchy model by varying the refractive index and thickness set of parameters in CompleteEASE software.

## **X-Ray Photoelectron Spectroscopy (XPS)**

XPS studies were conducted in a SPECS PHOIBOS 150 from SPECS GmbH at Institut Català de Nanociència i Nanotecnologia (ICN2) to identify C, N, O, S, Fe elements present in the samples.

## **Infrared Reflection Absorption Spectroscopy (IRRAS)**

IRRAS spectra, which provide information about the functional groups and their orientation in organic SAMs on a reflective surface were obtained in a Vertex 70 spectrometer from Bruker placed inside the Clean Room facilities of Institut de Ciència de Materials de Barcelona (ICMAB).

## **Eutectic Gallium Indium (EGaIn)**

The EGaIn measurements (current density vs voltage) were conducted in collaboration with Maria Elisabetta Giglio, Dr. J. Alejandro de Sousa, Dr. Núria Crivillers and Dr. Marta Mas (ICMAB) in a home-made set-up using a Keithley 2004B controlled by an in-house software developed with LabVIEW.

## **Transmission Electron Microscopy (TEM)**

TEM images of CNTs were recorded in a 120 KV JEOL 1210 microscope to visualize the morphology of the materials.

## **Scanning Electron Microscopy (SEM)**

SEM images were obtained by Dr. Rossella Zaffino provided by an Auriga-40 microscope from Carl Zeiss located at Instituto de Microelectrónica de Barcelona (IMB-CNM).



## **Atomic Force Microscopy (AFM)**

The topographic images of the samples were recorded by Dr. Rossella Zaffino (ICMAB) in an ICON/NAnoscope V from Bruker located at IMB-CNM.

## **Raman spectroscopy**

Raman spectroscopy was performed using a Xplora TM Plus spectrometer from Horiba Jobin- Yvon at Centres Científics I Tecnològics de la Universitat de Barcelona (CCiT-UB).

## **Probe station**

Electrical measurements of the three terminal devices were conducted by Dr. Rossella Zaffino (ICMAB) in a Lakeshore Cryostation connected to 2 Keithley 2540 source.

# Annex VII. Update of the electrical results of compound 7 described in Chapter 5.

## Polycyclic Aromatic Hydrocarbon-based curcuminoids in graphene nano-junctions

Teresa Cardona-Lamarca,<sup>a,‡</sup> Thomas Y. Baum,<sup>b,‡</sup> Rossella Zaffino,<sup>\*a</sup> Daniel Herrera,<sup>a</sup> Raphael Pfattner,<sup>a</sup> Silvia Gómez-Coca,<sup>c,d</sup> Eliseo Ruiz,<sup>c,d</sup> Arántzazu González-Campo,<sup>\*a</sup> Herre S. J. van der Zant<sup>\*b</sup> and Núria Aliaga-Alcalde<sup>\*a,e</sup>

<sup>a</sup> ICMA-B-CSIC (Institut de Ciència dels Materials de Barcelona), Campus de la Universitat Autònoma de Barcelona, 08193 Bellaterra, Spain

<sup>b</sup> Kavli Institute of Nanoscience, Delft University of Technology, Lorentzweg 1, 2628 CJ Delft, The Netherlands

<sup>c</sup> Departament de Química Inorgànica i Orgànica, Universitat de Barcelona, C/Martí i Franqués 1-11, 08028 Barcelona, Spain

<sup>d</sup> Institut de recerca de Química Teòrica i computacional, Universitat de Barcelona, Diagonal 645, 08028 Barcelona, Spain

<sup>e</sup> ICREA (Institució catalana de Recerca i Estudis Avançats), Passeig Lluís Companys 23, 08018 Barcelona, Spain

<sup>‡</sup>All the authors contributed equally.

**KEYWORDS** molecular design; curcumin derivatives; curcuminoid; polycyclic aromatic hydrocarbons (PAHs); single-electron transport; ultrasmall electronic three-terminal devices; graphene nano-junctions, graphene nano-gap electrodes; DFT calculations.

**ABSTRACT:** Exploiting the potential of curcuminoids (CCMoids) as molecular platforms, we have synthesized an extended system (3 nm) compromising a CCMoid with amino-terminal groups (NH<sub>2</sub>-CCMoid, **1**) that in a second step can adequate polycyclic aromatic hydrocarbon (PAH) groups at both endings of the molecule (pyACCMoid, **2**). In addition, we show the results from an experimental study of charge transport through molecule **2** trapped in graphene nano-junctions formed using feedback-controlled electroburning. The measured I-V characteristics show gate-dependent behavior at room temperature and at 10 K, with increased conductance values compared to shorter CCMoids previously reported, and in agreement with DFT calculations. Our results show that by optimizing molecular design the charge transport can be enhanced, as system **2** separates the conductive backbone from the anchoring groups, which tend to planarize upon contact with the graphene electrodes.

Molecular platforms are fundamental in the development of many topics in nanoscience and nanotechnology<sup>1,2</sup>. Regarding molecular electronics (MEs) the structural variations of these key units assist in the creation of hybrid materials (molecule-substrate)<sup>3,4</sup>, allowing the investigation of their interface, and providing an understanding of charge transport phenomena (monolayers and/or single molecules)<sup>5</sup> to generate extrapolated patterns. Porphyrinoids<sup>6</sup>, fullerenes<sup>6</sup>, and Schiff bases<sup>7</sup>, among others, are examples of such families of molecular systems applied in this field.

Curcuminoids (CCMoids)<sup>8</sup> have entered this group recently; apart from their extensive contribution to the biomedical field<sup>9,10</sup>, these building blocks and coordination derivatives are explored on surfaces using the UHV-STM tech-

nique<sup>11</sup> and studied, for example, as efficient near-IR emitters<sup>12-13</sup>, owing to the impact of their conjugated configuration. Indeed, CCMoids conjugated skeletons accompanied by aromatic side groups are suitable for single-molecule electronic<sup>14-16</sup>. This type of backbone provides a high density of  $\pi$ -electrons able to mediate charge transport that can be coordinated to a variety of side groups enabling both covalent bonding<sup>17</sup>, and  $\pi$ - $\pi$  stacking to graphene electrodes, respectively<sup>14-16</sup>. Regarding the first, some of us have performed single-electron transport studies in a set of CCMoids with different anchoring groups coupled to gold electrodes using the mechanically controlled breaking junction technique<sup>18,19</sup>. We have established a correspondence between the affinity of the terminal moieties and the Au electrodes with the conductance values, and the possible configurations of the molecules embedded between the electrodes. The effect of coordination in some of these sys-

tems has also been explored, finding the conditions under which certain CCMoids exhibit electronic switch behaviour<sup>20</sup>. Exploring molecular  $\pi$ - $\pi$  stacking with graphene electrodes, we have synthesized a family of CCMoids containing small polycyclic aromatic hydrocarbons (PAHs) arms (Figure 1) and studied their inclusion on graphene-based electrodes in a three-terminal device configuration (graphene/SiO<sub>2</sub>/Si)<sup>14–16</sup>.

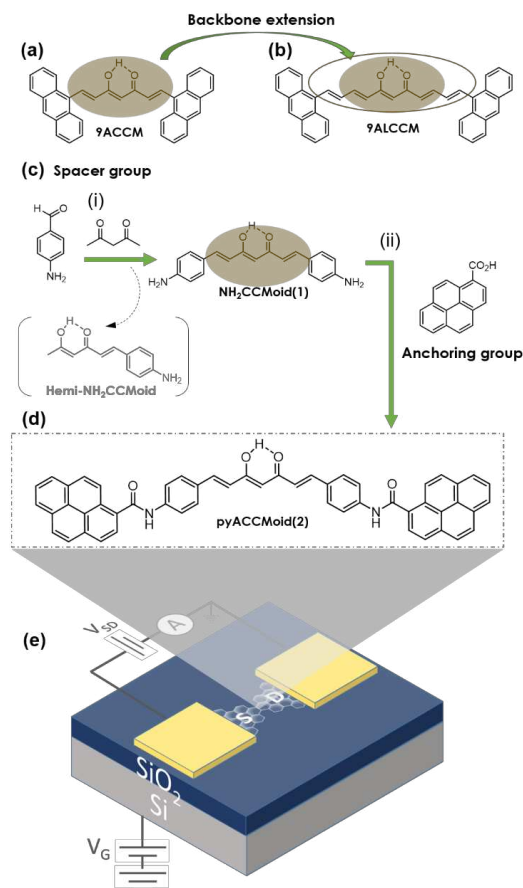


**Figure 1.** Chemical structures of (a) 9ACCM and (b) 9ALCCMoid with an increased backbone length, previously studied in graphene-hybrid molecular junctions<sup>14,15</sup>. (c) Synthetic pathway of (d) pyACCMod (2): (i) inclusion of the spacer group through the Pabon reaction and (ii) addition of the anchoring group by the formation of the amide bond to obtain the extended system. The pyACCMod system is integrated in a three-terminal single-layer graphene (SLG) device where a doped silicon substrate is covered with 300 nm of thermal SiO<sub>2</sub> and used as back-gate (e), to modulate charge transport of the molecule trapped in graphene nano-gaps opened by feed-back controlled electroburning. The pyrene groups stabilize the molecule in the junctions through  $\pi$ - $\pi$  stacking to the electrodes.

These studies were motivated by the low atomic mobility of graphene at room temperature, its convenient work function suitable for harmonizing with the discrete energy levels of molecules, and the reduced shielding of the gate electrode<sup>17,21–23</sup>. Feedback-controlled electroburning is a widely used approach to obtain graphene nano-gaps between 1–2 nm<sup>14</sup>. In the past, the CCMoids depicted in Figure 1 were embedded between few layers' graphene FLG electrodes<sup>14,15</sup>. At that time, our goal was to find CCMoids that act as nanowires, by studying and varying the intrinsic chain of the CCMoid. The two CCMoids (Figure 1a, 1b) share the same anthracene anchor groups, but had different backbone lengths: the first has a 7 C extension, called 9ACCM (Figure 1a) and the second, called 9ALCCMoid (Figure 1b) has 11 C, instead. In addition, with the 9ALCCMoid we found the co-existence of vibrational excitations with Coulomb blockade physics at low temperature<sup>15</sup>. These works conclude that the extension of the CCMoid skeleton (Figure 1b) improves the coupling between the FLG electrodes and the anthracene groups, compensating the longer length and yielding room-temperature conductance values of the same order (approximately  $10^{-6}G_0$ ).

Here, we show CCMoids that react with PAHs leading to a molecule with extended arms, and improved  $\pi$ - $\pi$  stacking with graphene. One of the advantages of this methodology over chain extension (as in 9ALCCMoid, Figure 1b) is that standard CCMoids are synthesized in a one-step reaction<sup>22</sup>. Hence, by carefully choosing the ending moieties, we can engineer commonly used post-reactions that simplify the addition of groups of interest.

This work describes the synthesis of CCMoid 1 (Figure 1c–(i), NH<sub>2</sub>CCMoid 1) and its reactivity with 1-pyrene carboxylic acid units, leading to CCMoid 2 (pyACCMod 2, Figure 1d) containing amide bonds and featuring extended dimensions while adding flexibility, and enhancing its  $\pi$ - $\pi$  interactions capability towards a better accommodation between graphene electrodes (Figure 1e). The resulting PAH-CCMoid system has been tested using graphene nano-gap electrodes in a three-terminal device configuration as depicted in Figure 1e. We provide detailed studies of its single-electron transport features corroborating that electronic behavior profits from improved molecular design, in agreement with the theoretical calculations.

## Results and discussion

### Molecular synthesis and characterization

The synthesis of CCMoids is a one-step process<sup>24</sup> based on the use of acetylacetone, its coordination with boron derivatives and its subsequent bilateral growth, through the process of condensation with an aldehyde. This approach can present variations mainly depending on the solubility and reactivity of the latest. In our case, the optimal synthesis of NH<sub>2</sub>CCMoid (1, Figure 1c) was achieved by performing the reaction in DMF and using an excess of freshly made 4-aminobenzaldehyde<sup>24</sup> (30% yield). Interestingly, in the same process, the asymmetric system, the Hemi-NH<sub>2</sub>CCMoid (8% yield), was identified and isolated by fil-

tration (Figure 1c-(i)). Both CCMoids have been characterized by standard methods (Figure S1-S13, SI) and, their HOMO-LUMO energy gaps estimated by cyclic voltammetry in solution, and in the solid-state by UV-Vis absorption spectroscopy (Figure S4-S5, S10-S11, SI), with  $E_{g\text{elec}}$  and  $E_{g\text{op}}$  values slightly above 2.0 eV for both.

As discussed above,  $\text{NH}_2\text{CCMoid}$  (**1**) has been reacted with PAH-based units having a terminal acidic group, giving rise to a PAH-CCMoid using amide bonds: PyACCMoid (**2**) (Figure 1d). Optimal conditions for the synthesis of **2** include the use of a MW reactor<sup>25-27</sup>. Like **1**, the new system has been characterized in a similar manner (Figures S13-S20), finding  $E_{g\text{elec}}$  and  $E_{g\text{op}}$  values of 2.4 and 2.5 eV, correspondingly. The comparison of the estimated HOMO-LUMO gaps for systems **1** and **2** shows the effect of the donor character of the amino group ( $\text{NH}_2\text{CCMoid}$ ) in the energy gap compared to the more acceptor amide-containing system (PyACCMoid), being smaller for the first (Figure S21). The data is in full agreement with Density Functional Theory (DFT) calculations performed for the two systems (SI), summarized in Table S1, and with additional theoretical studies on CCMoids<sup>28</sup>. Regarding the molecular size, the optimized theoretical structure (Figure S22) shows dimensions between the most distant C atoms of 3.06 nm for **2**, which is a substantially longer compared to previously published systems (9Accm and 9ALCCM, Figure 1a, 1b and S22) with distances of 1.68 and 2.07 nm, respectively. In addition, it is interesting to emphasize the flexible and rotational character of the amide bond<sup>29</sup>, which provides degrees of freedom to the CCMoid when accommodating on the graphene, in the deposition process (see DFT section and SI).

### Graphene nano-junctions in three-terminal devices: processing and measurements.

For device fabrication, we used commercial substrates with single-layer chemical vapor deposited (CVD) graphene on  $\text{SiO}_2/\text{Si}$  (300 nm  $\text{SiO}_2$ ) to increase device reproducibility and fabrication throughput. A scheme of the process is provided in the SI (Figure S26). As a brief description, graphene is patterned in a bow-tie shape with a constriction of about 400 nm combining e-beam lithography and  $\text{O}_2$  plasma etching. Then, the gold contacts are deposited by laser lithography, metal evaporation and lift-off. Graphene nano-junctions (GNJs) are then obtained by using feed-back controlled electroburning. This process relies on Joule heating which in the presence of atmospheric oxygen promotes the removal of carbon atoms progressively narrowing down the constriction<sup>30</sup>. It is performed in air and at room temperature by ramping a voltage up to 10 V across the graphene constriction. In the electroburning process, the output current from the voltage ramp is monitored by feed-back software that sets the bias voltage rapidly to zero once the target resistance value across the junction is reached. The maximum voltage flowing through the junction is slowly increased until resistance values above 500 M $\Omega$  are achieved, preventing the formation of large gaps with the subsequent creation of split widths larger than a molecule at their closest points.

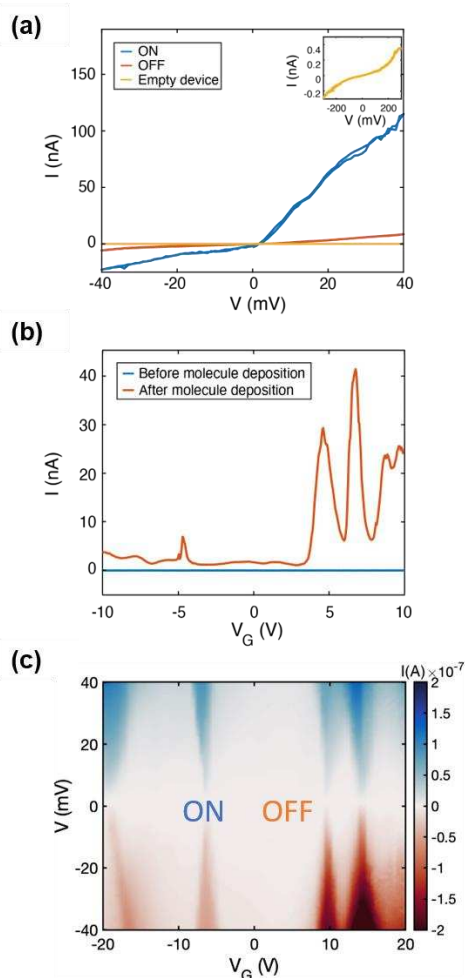


**Figure 2.** (a) Current vs. bias voltage (I-V) characteristic of devices through the different steps of the experiment: right after the electroburning procedure (empty device, yellow curve) and after molecular deposition: in high current (ON) and blocked regions (OFF) measured at 10 K. Empty devices display order of magnitude lower current and non-linear increase at high voltage bias values, as depicted in the inset. (b) Current between source and drain for a fixed bias voltage of 10 mV as a function of gate voltage (gate-sweep) before (blue, room temperature) and after (orange, 10 K) deposition of molecules. The low-temperature gate-sweep displays a clear current increase attributed to molecular resonances; the room-temperature gate-sweeps also exhibit features in the current shown in Figure S31. (c) Current as a function of source-drain bias and gate voltage (stability diagram) measured at 10 K. Alternating regions of high (ON) and low (OFF) current are visible giving rise to diamond-shaped areas (corresponding line cuts are shown in (a)).

Opened constrictions are measured in vacuum and at room temperature by applying a bias voltage ( $V$ ) and measuring the output current ( $I$ ), and display the typical tunnel I-V characteristics (see inset of Figure 2a and Figure S28-S29), indicate that the GNJs are in the order of a few nanometers. Their sizes can be estimated by using the Simmons model<sup>31</sup> with the tunnelling barrier height (determined by the work function of the electrodes), the width, and the area in the bias-voltage response, as fit parameters (see SI). The overview of experiment statistics, based on the measurement of the zero-bias resistance after each step of the procedure, i.e., electro-burning, molecule deposition, and cooling down, is detailed and discussed in the SI (Figure S25).

Before molecule deposition, the measurement of the current at fixed bias, as a function of the gate voltage applied through the Si bottom substrate, represented in Figure 2b (referred to as a “gate-sweep” in the following) and reported in Figure 2c, does not show any current modulation. The same is observed for the I-V characteristics measured as a function of gate voltage and shown in Figure S29. These observations with the nanometric size of the junctions imply that they can be used in the subsequent measurements. Molecules are deposited by dip coating the electroburnt devices, in a 0.1 mM solution of pyACCMoid in THF for 1 hour followed by rinsing with pure THF (an AFM picture of the surface functionalization is shown in SI Figure S30). The solvent is chosen to dissolve the molecular compound without altering the graphene surface. Before starting the measurements, the samples are left in air for 30 min, and dried under vacuum for another 30 min more, to ensure complete solvent evaporation. We started the electrical characterization of the molecular devices at room temperature in vacuum ( $10^{-5}$  mbar) observing a resistance decrease of an order of magnitude, or higher, in about 12% of the devices incubated, suggesting the presence of molecules inside the GNJ (see Figure S27 for the overview of the experiment statistics). We observed current variations in the order of a few picoamperes distinct from noise in the gate-sweep measurements shown in Figure S31. We note a resistance variation of about an order of magnitude in the I-V characteristics, measured as a function of bias and gate voltage compiled in the stability diagram, shown in Figure S32.

At low temperatures ( $\sim 10$  K), the conductance modulations in the gate sweeps become more defined, as seen in Figure 2b (orange trace). Note, that the cooling may cause some open GNJs to close, and the opposite, some closed GNJs to open, highlighting the presence of tensile stress building up in the graphene monolayer as the temperature changes. From over 39 junctions measured at low temperatures, 12 did not show gate leakage and displayed resistances in the range expected for a molecule bridging electrodes (hundreds of  $M\Omega$  up to  $G\Omega$ ), among which two showed clear signs of molecular signatures in the gate voltage range accessible (Figure 2b and Figure S33). The yield is close to values reported in the literature for devices fabricated with a similar procedure<sup>32</sup>. We observed variations of the current intensity measured in the gate-sweep between different devices (as highlighted for the two molecular junctions measured at low-

temperature in Figure S34) as well as on repeated measurements on the same device. These variations can be attributed to the different molecular conformations.

In GNJs, molecular species typically present weak/intermediate coupling<sup>14-16</sup> to the source and drain graphene electrodes, resulting in charge transport dominated by single-electron transistor (SET) behavior. In our case, the pyrene units are the main anchor to the graphene electrodes, leading to current suppression (Coulomb Blockade) when the molecular energy level falls outside the bias voltage range. This group is commonly used to provide reliable molecule-graphene  $\pi$ - $\pi$  bonding without compromising the solubility in organic solvents of the molecular systems<sup>33</sup>. By applying a gate voltage, the molecular orbital levels align with the chemical potential of the electrodes causing resonant charge transport, as evidenced by current resonance in gate-sweeps (Figure 2b orange trace) and Coulomb Diamonds (CD) in the stability diagram (see Figure 2c) characterized by current-blockaded regions (whitish areas) alternating with resonant transport regions (blue and red areas). Resonant peaks correspond to a change in the ground state of the molecule, indicating a transition of its electronic state at zero bias voltage. This point is referred to as the charge degeneracy point (CDP). A comparison of the stability diagrams of the 9ACCM and 9ALCCM systems<sup>14,15</sup> (Figure 1a) with that of compound 2 shows that the signal intensity has now increased, confirming the contact enhancement of our new system vs. the earliest.

The gate coupling,  $\alpha$ , can be extracted from the slopes of the Coulomb diamonds,  $\beta$  and  $\gamma$  (as explained in the SI and illustrated in Figure S35). We find  $\alpha=0.005$  (0.5%) for the diamond around  $V_G=-25$  V and  $\alpha=0.011$  (1.1%) for that around  $V_G=-8$  V. These values are in the lower range expected for graphene-based molecular junctions in three-terminal devices with 300 nm of  $SiO_2$  as gate dielectric<sup>34</sup>. We have also calculated the gate couplings for both diamonds of the second device (shown in Figure S36), reporting a large difference between the two accompanied by opposite source-drain coupling asymmetry. Both observations point to a different origin of the corresponding CDPs, as discussed in the SI. For both molecular junctions we find similar, and large, addition energy spacing (more than 400 meV). Large addition energies are typically observed in molecular junctions as opposed to a graphene island associated with lower, and more variable, addition energy<sup>33</sup>.

It should be stressed that in graphene-based molecular junctions, the gate field can affect the chemical potential of the electrodes giving rise to spectroscopic features associated with quantum interferences from the electrodes that are not intrinsic to the molecule<sup>35-37</sup>, and limiting the possibility of measuring accurately the molecular resonances. This has been already observed<sup>35-37</sup> and here it is supported by the presence of lines not running parallel to the diamond edges (as displayed in the conductance map shown in Figure S36(left)).

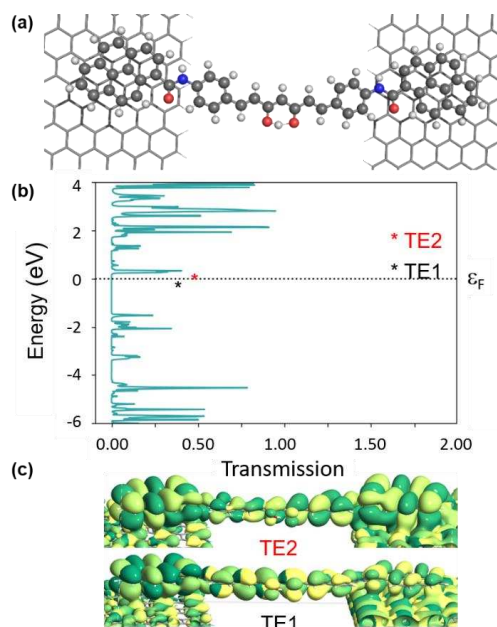


**Figure 3.** (a) DFT optimized structure of pyACCMoid2 on a given graphene-based nano-gap. (b) Transmission spectrum for the system shown above. (c) Transmission eigenfunctions corresponding to the first two empty peaks in the transmission spectrum are highlighted with an asterisk. Transmission eigenfunctions are plotted for some frontier orbitals. The transmission eigenfunctions are obtained by diagonalizing the transmission matrix, and the corresponding transmission eigenvalues indicate the importance of each eigenfunction in transport. As it is a complex wave function, the color map represents the phase of the function from 0 to  $2\pi$  by dark green to yellow colors. The threshold value employed for the isosurfaces is 0.1.

In addition to the experimental part, the transport properties of molecule **2** deposited on a graphene nano-gap have been also analyzed by using Non-Equilibrium Green Function (NEGF)-DFT methods (SI Computational details section). The calculated transmission curve shows that the levels closest to the Fermi level (see Figure 3), are unoccupied transmission eigenfunctions (described as TE1 and TE2, respectively). The comparison of the shape of these transmission eigenfunctions with the frontier orbitals of the isolated molecule **2** (see Figure S23) indicates that TE1 is essentially related to the LUMO orbital while TE2 corresponds to LUMO+1 slightly mixed with the LUMO indicating that the charge transport is electron mediated. This fact is also evidenced by the projected local density of states (Figure S24). Furthermore, there is an enhancement of the semiconducting character in the regions of molecule/graphene contact (Figure 3a), especially for the occupied band near the Fermi level. The calculation of the conductance for this configuration gives a value of  $8.9 \cdot 10^{-4} G_0$

that fits the range obtainable from the experimental data. In addition, transmission pathways represented in Figure S23 show that the transport is exclusively through the molecule.

## Conclusions

We have synthesized, in an optimized number of steps, a new CCMoid, the pyACCMoid (**2**) containing pyrene side groups connected through amide bond to the  $\pi$ -conjugate CCMoid backbone and resulting in a total effective length for the molecule of 3.06 nm. Because of the amide bond, the extended arms confer flexibility to the system favoring its accommodation between the heterogeneous edges of GNJs obtained by electroburning. This allowed demonstration of gate-dependent charge transport of the pyACCMoid coupled through  $\pi$ - $\pi$  stacking to SLG electrodes. In agreement with DFT calculations, we report improved conductance values compared to previously explored graphene-CCMoids molecular devices, despite length enhancement. The large ON/OFF current ratio linked to the molecule CDP can be distinguished from quantum interference in the electrodes by a different capacitive coupling and asymmetry. This result validates the chemical strategy explored here based on the introduction of a spacer group between the conductive backbone and the anchoring groups. Our methodology can be extrapolated to other PAH derivatives, where anticipation of potential solubility difficulties (by adding groups such as alkyl chains) can lead to more extensive systems. Part of our aim is to study the creation of nanoribbon-based nanowires with the CCMoid backbone providing coordination sites.

## AUTHOR INFORMATION

### Corresponding Authors

**Rossella Zaffino** – ICMAB-CSIC (Institut de Ciència de Materials de Barcelona), Campus de la Universitat Autònoma de Barcelona, 08193, Bellaterra, Spain, <https://orcid.org/0000-0001-7574-5793>

**Arántzazu González-Campo** – ICMAB-CSIC (Institut de Ciència de Materials de Barcelona), Campus de la Universitat Autònoma de Barcelona, 08193, Bellaterra, Spain, <https://orcid.org/0000-0001-5725-2135>

**Herre S. J. van der Zant** - Kavli Institute of Nanoscience, Delft University of Technology, Lorentzweg 1, Delft 2628 CJ, The Netherlands, <https://orcid.org/0000-0002-5385-0282>

**Núria Aliaga-Alcalde** – ICREA (Institució Catalana de Recerca i Estudis Avançats), Passeig Lluís Companys. 23, 08018, Barcelona, Spain; ICMAB-CSIC (Institut de Ciència de Materials de Barcelona), Campus de la Universitat Autònoma de Barcelona, 08193, Bellaterra, Spain, <https://orcid.org/0000-0003-1080-3862>

## Author Contributions

T.C.L. and D.H. investigation, molecular data collection, and data analysis-molecular synthesis and characterization; T.B. and R.Z. conceptualization, investigation, device fabrication and characterization, electrical transport measurements and data analysis; R.P. assistance in device preparation and analysis of physical data; R.Z., A.G.C., H.Z. and N.A.A. conceptualization, investigation, data analysis, validation, supervision; all authors contributed to the writing and editing of the article. ‡T.C.L. and T.B. contributed equally.

## Notes

The authors declare no competing financial interest.

## ACKNOWLEDGMENT

This work has received funding from the European Research Council (ERC) under the European Union's Horizon 2020 R&D program under grant agreement No. 724981 (Tmol4TRANS) and from the European Union Horizon 2020 research and innovation program under grant agreement No. 863098 (SPRING). This work was also supported by the projects PID2019-108794GB-I00 and PID2021-122464NB-I00 funded by MCIN/AEI/10.13039/501100011033 from the Ministerio de Ciencia e Innovación. R.P. acknowledges support from the Ramón y Cajal Fellowship (Ref. RyC2019-028474-I). E.R. thanks Generalitat de Catalunya for an ICREA Academia award, Spanish Ministry Science for a Maria de Maeztu excellence grant (CEX2021-001202-M), and BSC for computational resources. The CSIC authors acknowledge the financial support from the Spanish Ministry Science, through the "Severo Ochoa" Programme for Centres of Excellence (FUNFUTURE, 2020-2023).

## ABBREVIATIONS

CCMoid, curcuminoid; PAH-CCMoid, polycyclic aromatic hydrocarbon-based curcuminoid; DMF, dimethylformamide; THF, tetrahydrofuran; GNJ, graphene nano-junction; SLG, single layer graphene; FLG, few layer graphene; SET, single electron transistor; DFT, density functional theory; CD, coulomb diamond; CDP, charge degeneracy point; TE, transmission eigenfunction.

## REFERENCED

- (1) Tejedor, D.; López-Tosco, S.; Méndez-Abt, G.; Cotos, L.; García-Tellado, F. Propargyl Vinyl Ethers and Tertiary Skipped Diynes: Two Pluripotent Molecular Platforms for Diversity-Oriented Synthesis. *Acc. Chem. Res.* **2016**, *49* (4), 703–713. <https://doi.org/10.1021/acs.accounts.5b00545>.
- (2) Valášek, M.; Mayor, M. Spatial and Lateral Control of Functionality by Rigid Molecular Platforms. *Chem. - A Eur. J.* **2017**, *23* (55), 13538–13548. <https://doi.org/10.1002/chem.201703349>.
- (3) Kong, G. D.; Byeon, S. E.; Park, S.; Song, H.; Kim, S. Y.; Yoon, H. J. Mixed Molecular Electronics: Tunneling Behaviors and Applications of Mixed Self-Assembled Monolayers. *Adv. Electron. Mater.* **2020**, *6* (2), 1–19. <https://doi.org/10.1002/aelm.201901157>.
- (4) Liu, J.; Huang, X.; Wang, F.; Hong, W. Quantum Interference Effects in Charge Transport through Single-Molecule Junctions: Detection, Manipulation, and Application. *Acc. Chem. Res.* **2019**, *52* (1), 151–160. <https://doi.org/10.1021/acs.accounts.8b00429>.
- (5) Gupta, R.; Fereiro, J. A.; Bayat, A.; Pritam, A.; Zharnikov, M.; Mondal, P. C. Nanoscale Molecular Rectifiers. *Nat. Rev. Chem.* **2023**, *7* (2), 106–122. <https://doi.org/10.1038/s41570-022-00457-8>.
- (6) Longevial, J. F.; Clément, S.; Wytko, J. A.; Ruppert, R.; Weiss, J.; Richeter, S. Peripherally Metalated Porphyrins with Applications in Catalysis, Molecular Electronics and Biomedicine. *Chem. - A Eur. J.* **2018**, *24* (58), 15442–15460. <https://doi.org/10.1002/chem.201801211>.
- (7) Kagatkar, S.; Sunil, D. Schiff Bases and Their Complexes in Organic Light Emitting Diode Application. *J. Electron. Mater.* **2021**, *50* (12), 6708–6723. <https://doi.org/10.1007/s11664-021-09197-9>.
- (8) Riba-López, D.; Zaffino, R.; Herrera, D.; Matheu, R.; Silvestri, F.; Ferreira da Silva, J.; Sañudo, E. C.; Mas-Torrent, M.; Barrera, E.; Pfattner, R.; Ruiz, E.; González-Campo, A.; Aliaga-Alcalde, N. Dielectric Behavior of Curcuminoid Polymorphs on Different Substrates by Direct Soft Vacuum Deposition. *iScience* **2022**, *25* (12). <https://doi.org/10.1016/j.isci.2022.105686>.
- (9) Esatbeyoglu, T.; Huebbe, P.; Ernst, I. M. A.; Chin, D.; Wagner, A. E.; Rimbach, G. Curcumin-from Molecule to Biological Function. *Angew. Chemie - Int. Ed.* **2012**, *51* (22), 5308–5332. <https://doi.org/10.1002/anie.201107724>.
- (10) Shah, M.; Murad, W.; Mubin, S.; Ullah, O.; Rehman, N. U.; Rahman, M. H. Multiple Health Benefits of Curcumin and Its Therapeutic Potential. *Environ. Sci. Pollut. Res.* **2022**, *29* (29), 43732–43744. <https://doi.org/10.1007/s11356-022-20137-w>.
- (11) Leoni, T.; Nony, L.; Zaborova, E.; Clair, S.; Fagès, F.; Para, F.; Ranguis, A.; Becker, C.; Loppacher, C. Stereoisomeric Selection upon Adsorption: A Structural and Optical Study of Curcuminoid Derivatives on Ultrathin Films of KCl on Au(111) and on Bulk KCl(001). *Phys. Rev. B* **2021**, *104*

- (20).  
<https://doi.org/10.1103/PhysRevB.104.205415>
- (12) Choi, K. R.; Kim, D. H.; Lee, Y. U.; Placide, V.; Huynh, S.; Yao, D.; Canard, G.; Zaborova, E.; Mathevet, F.; Mager, L.; Heinrich, B.; Ribierre, J. C.; Wu, J. W.; Fages, F.; D'Aléo, A. Effect of the Electron Donating Group on the Excited-State Electronic Nature and Epsilon-near-Zero Properties of Curcuminoid-Borondifluoride Dyes. *RSC Adv.* **2021**, *11* (60), 38247–38257. <https://doi.org/10.1039/d1ra08025c>.
- (13) Polishchuk, V.; Stanko, M.; Kulinich, A.; Shandura, M. D- $\pi$ -A- $\pi$ -D Dyes with a 1,3,2-Dioxaborine Cycle in the Polymethine Chain: Efficient Long-Wavelength Fluorophores. *European J. Org. Chem.* **2018**, *2018* (2), 240–246. <https://doi.org/10.1002/ejoc.201701466>.
- (14) Prins, F.; Barreiro, A.; Ruitenberg, J. W.; Seldenthuis, J. S.; Aliaga-Alcalde, N.; Vandersypen, L. M. K.; Van Der Zant, H. S. J. Room-Temperature Gating of Molecular Junctions Using Few-Layer Graphene Nanogap Electrodes. *Nano Lett.* **2011**, *11* (11), 4607–4611. <https://doi.org/10.1021/nl202065x>.
- (15) Burzurí, E.; Island, J. O.; Díaz-Torres, R.; Fursina, A.; González-Campo, A.; Roubeau, O.; Teat, S. J.; Aliaga-Alcalde, N.; Ruiz, E.; Van Der Zant, H. S. J. Sequential Electron Transport and Vibrational Excitations in an Organic Molecule Coupled to Few-Layer Graphene Electrodes. *ACS Nano* **2016**, *10* (2), 2521–2527. <https://doi.org/10.1021/acsnano.5b07382>.
- (16) Island, J. O.; Holovchenko, A.; Koole, M.; Alkemade, P. F. A.; Menelaou, M.; Aliaga-Alcalde, N.; Burzurí, E.; Van Der Zant, H. S. J. Fabrication of Hybrid Molecular Devices Using Multi-Layer Graphene Break Junctions. *J. Phys. Condens. Matter* **2014**, *26* (47). <https://doi.org/10.1088/0953-8984/26/47/474205>.
- (17) Guo, X.; Small, J. P.; Klare, J. E.; Wang, Y.; Purewal, M. S.; Tam, I. W.; Hong, B. H.; Caldwell, R.; Huang, L.; O'Brien, S.; Yan, J.; Breslow, R.; Wind, S. J.; Hone, J.; Kim, P.; Nuckolls, C. Covalently Bridging-Gaps in Single-Walled Carbon Nanotubes with Conducting Molecules. *Science (80-. )* **2006**, *311* (5759), 356–359. <https://doi.org/10.1126/science.1120986>.
- (18) Van Veen, F. H.; Ornago, L.; Van Der Zant, H. S. J.; El Abbassi, M. Benchmark Study of Alkane Molecular Chains. *J. Phys. Chem. C* **2022**, *126* (20), 8801–8806. <https://doi.org/10.1021/acs.jpcc.1c09684>.
- (19) Arroyo, C. R.; Tarkuc, S.; Frisenda, R.; Seldenthuis, J. S.; Woerde, C. H. M.; Eelkema, R.; Grozema, F. C.; Van Der Zant, H. S. J. Signatures of Quantum Interference Effects on Charge Transport through a Single Benzene Ring. *Angew. Chemie - Int. Ed.* **2013**, *52* (11), 3152–3155. <https://doi.org/10.1002/anie.201207667>.
- (20) Olavarria-Contreras, I. J.; Etcheverry-Berrios, A.; Qian, W.; Gutiérrez-Cerón, C.; Campos-Olguín, A.; Sañudo, E. C.; Dulić, D.; Ruiz, E.; Aliaga-Alcalde, N.; Soler, M.; Van Der Zant, H. S. J. Electric-Field Induced Bistability in Single-Molecule Conductance Measurements for Boron Coordinated Curcuminoid Compounds. *Chem. Sci.* **2018**, *9* (34), 6988–6996. <https://doi.org/10.1039/c8sc02337a>.
- (21) Feldman, A. K.; Steigerwald, M. L.; Guo, X.; Nuckolls, C. Molecular Electronic Devices Based on Single-Walled Carbon Nanotube Electrodes. *Acc. Chem. Res.* **2008**, *41* (12), 1731–1741. <https://doi.org/10.1021/ar8000266>.
- (22) Caneva, S.; Gehring, P.; García-Suárez, V. M.; García-Fuente, A.; Stefani, D.; Olavarria-Contreras, I. J.; Ferrer, J.; Dekker, C.; van der Zant, H. S. J. Mechanically Controlled Quantum Interference in Graphene Break Junctions. *Nat. Nanotechnol.* **2018**, *13* (12), 1126–1131. <https://doi.org/10.1038/s41565-018-0258-0>.
- (23) Sarwat, S. G.; Gehring, P.; Rodriguez Hernandez, G.; Warner, J. H.; Briggs, G. A. D.; Mol, J. A.; Bhaskaran, H. Scaling Limits of Graphene Nanoelectrodes. *Nano Lett.* **2017**, *17* (6), 3688–3693. <https://doi.org/10.1021/acs.nanolett.7b00909>.
- (24) Pabon, H. J. A Synthesis of Curcumin and Related Compounds. *Recl. des Trav. Chim. des Pays-Bas* **1964**, *83* (4), 379–386. <https://doi.org/10.1002/recl.19640830407>.
- (25) Nüchter, M.; Ondruschka, B.; Bonrath, W.; Gum, A. Microwave Assisted Synthesis – a Critical Technology Overview. *Green Chem.* **2004**, *6* (3), 128–141. <https://doi.org/10.1039/b310502d>.
- (26) Dallinger, D.; Kappe, C. O. Microwave-Assisted Synthesis in Water as Solvent. *Chem. Rev.* **2007**, *107* (6), 2563–2591. <https://doi.org/10.1021/cr0509410>.
- (27) Tehfe, M. A.; Dumur, F.; Contal, E.; Graff, B.; Morlet-Savary, F.; Gimes, D.; Fouassier, J. P.; Lalevée, J. New Insights into Radical and Cationic Polymerizations upon Visible Light Exposure: Role of Novel Photoinitiator Systems Based on



- the Pyrene Chromophore. *Polym. Chem.* **2013**, *4* (5), 1625–1634. <https://doi.org/10.1039/c2py20950k>.
- (28) Vera-de la Garza, C. G.; Martinez, R. J.; Belmont-Bernal, F. Electronic Structure of Curcuminoids with Potential Medicinal Applications: A Theoretical Insight. *Struct. Chem.* **2023**, *34* (4), 1427–1438. <https://doi.org/10.1007/s11224-022-02080-1>.
- (29) Kubatkin, S.; Danilov, A.; Hjort, M.; Cornil, J.; Brédas, J. L.; Stuhr-Hansen, N.; Hedegård, P.; Bjørnholm, T. Single-Electron Transistor of a Single Organic Molecule with Access to Several Redox States. *Nature* **2003**, *425* (6959), 698–701. <https://doi.org/10.1038/nature02010>.
- (30) El Abbassi, M.; Pósa, L.; Makk, P.; Nef, C.; Thodkar, K.; Halbritter, A.; Calame, M. From Electroburning to Sublimation: Substrate and Environmental Effects in the Electrical Breakdown Process of Monolayer Graphene. *Nanoscale* **2017**, *9* (44), 17312–17317. <https://doi.org/10.1039/c7nr05348g>.
- (31) Simmons, J. G. Generalized Formula for the Electric Tunnel Effect between Similar Electrodes Separated by a Thin Insulating Film. *J. Appl. Phys.* **1963**, *34* (6), 1793–1803. <https://doi.org/10.1063/1.1702682>.
- (32) Limburg, B.; Thomas, J. O.; Holloway, G.; Sadeghi, H.; Sangtarash, S.; Hou, I. C. Y.; Cremers, J.; Narita, A.; Müllen, K.; Lambert, C. J.; Briggs, G. A. D.; Mol, J. A.; Anderson, H. L. Anchor Groups for Graphene-Porphyrin Single-Molecule Transistors. *Adv. Funct. Mater.* **2018**, *28* (45). <https://doi.org/10.1002/adfm.201803629>.
- (33) Mol, J. A.; Lau, C. S.; Lewis, W. J. M.; Sadeghi, H.; Roche, C.; Cnossen, A.; Warner, J. H.; Lambert, C. J.; Anderson, H. L.; Briggs, G. A. D. Graphene-Porphyrin Single-Molecule Transistors. *Nanoscale* **2015**, *7* (31), 13181–13185. <https://doi.org/10.1039/c5nr03294f>.
- (34) Thijssen, J. M.; Van Der Zant, H. S. J. Charge Transport and Single-Electron Effects in Nanoscale Systems. *Phys. Status Solidi Basic Res.* **2008**, *245* (8), 1455–1470. <https://doi.org/10.1002/pssb.200743470>.
- (35) Gehring, P.; Sowa, J. K.; Cremers, J.; Wu, Q.; Sadeghi, H.; Sheng, Y.; Warner, J. H.; Lambert, C. J.; Briggs, G. A. D.; Mol, J. A. Distinguishing Lead and Molecule States in Graphene-Based Single-Electron Transistors. *ACS Nano* **2017**, *11* (6), 5325–5331. <https://doi.org/10.1021/acsnano.7b00570>.
- (36) Gehring, P.; Sadeghi, H.; Sangtarash, S.; Lau, C. S.; Liu, J.; Ardavan, A.; Warner, J. H.; Lambert, C. J.; Briggs, G. A. D.; Mol, J. A. Quantum Interference in Graphene Nanoconstrictions. *Nano Lett.* **2016**, *16* (7), 4210–4216. <https://doi.org/10.1021/acs.nanolett.6b01104>.
- (37) Gehring, P.; Thijssen, J. M.; van der Zant, H. S. J. *Single-Molecule Quantum-Transport Phenomena in Break Junctions*; 2019; Vol. 1. <https://doi.org/10.1038/s42254-019-0055->

# Polycyclic Aromatic Hydrocarbon-based curcuminoids in graphene nano-junctions

Teresa Cardona-Lamarca,<sup>a,‡</sup> Thomas Y. Baum,<sup>b,‡</sup> Rossella Zaffino,<sup>\*a</sup> Daniel Herrera,<sup>a</sup> Raphael Pfattner,<sup>a</sup> Silvia Gómez-Coca,<sup>c,d</sup> Eliseo Ruiz,<sup>c,d</sup> Arántazu González-Campo,<sup>\*a</sup> Herre S. J. van der Zant<sup>\*b</sup> and Núria Aliaga-Alcalde<sup>\*a,e</sup>

<sup>a</sup> *ICMAB-CSIC (Institut de Ciència de Materials de Barcelona), Campus de la Universitat Autònoma de Barcelona, 08193, Bellaterra, Spain*

<sup>b</sup> *Kavli Institute of Nanoscience, Delft University of Technology, Lorentzweg 1, Delft 2628 CJ, The Netherlands.*

<sup>c</sup> *Departament de Química Inorgànica i Orgànica and Institut de Nanociència i Nanotecnologia, Universitat de Barcelona, Diagonal 645, 08028, Barcelona, Spain.*

<sup>d</sup> *Departament de Química Inorgànica i Orgànica and Institute de Recerca de Química Teòrica i Computacional, Universitat de Barcelona, Diagonal 645, E-08028, Barcelona, Spain.*

<sup>e</sup> *ICREA (Institució Catalana de Recerca i Estudis Avançats), Passeig Lluís Companys 23, 08018, Barcelona, Spain.*

<sup>‡</sup> These authors contributed equally.

## Contents:

1. Materials	2
2. Measurements	3
3. Synthetic procedures	4
4. Molecular characterization	6
5. Computational details	19
6. Device: fabrication and electrical measurements	22

## 1. Materials

*Acetylacetonate* ( $C_5H_7O_2$ , *acac*), *boron trioxide* ( $B_2O_3$ ), *tributyl borate* ( $(BuO)_3B$ ,  $C_{12}H_{27}BO_3$ ), *n-butyl amine* ( $n-BuNH_2$ ,  $C_4H_{11}N$ ), *4-aminobenzyl alcohol* ( $H_2NC_6H_4CH_2OH$ ), *potassium permanganate* ( $KMnO_4$ ), *manganese (II) sulfate monohydrate* ( $MnSO_4 \cdot H_2O$ ), *sodium hydroxide* ( $NaOH$ ), *1- pyrenecarboxaldehyde*, *thionyl chloride* ( $SOCl_2$ ) and *triethylamine* ( $Et_3N$ ) were provided by Sigma Aldrich, ABCR, Fluorochem and TCI Chemicals. *Dimethylformamide* (*DMF*), *Diethyl ether* ( $Et_2O$ ), *dichloromethane* (*DCM*), *acetone*, *tetrahydrofurane* (*THF*), *acetonitrile* (*ACN*), *1,1,2,2-tetrachloroethane* (*TCE*) and *chloroform* ( $CHCl_3$ ) were supplied by Carlo Erba and Scharlab.

## 2. Measurements

*<sup>1</sup>H-NMR and <sup>13</sup>C-NMR spectra were recorded on a Bruker Avance III spectrometer at 298 K at Servei RMN from UAB. Fourier transform infrared (FTIR) spectra were measured on a JASCO 4700LE FT-IR between 400 and 4000 cm<sup>-1</sup>. UV/Vis absorption spectra were obtained with a JASCO V-780 UV/Vis/NIR spectrophotometer using quartz cells in a 200–800 nm range in transmittance mode. Elemental analyses were performed with a Thermo Scientific Flash 2000 and Flash Smart elemental analyser. MALDI-TOF mass spectra were obtained with a Bruker ULTRAFLEXTRME mass spectrometer at Servei de Proteòmica I Biologia Estructural from UAB and Servei de Proteòmica i imatge from IQAC. Electrochemical measurements were conducted in a three electrodes cell using reference and auxiliary platinum electrodes and glassy carbon working electrode with a 0.1 M solution of tetrabutylammonium hexafluorophosphate (TBAPF<sub>6</sub>) in THF as electrolyte. The experiments were registered at 50 mV/s in a Biologic SP-50 potentiostat and referenced versus ferrocene/ferrocenium couple, used as an internal reference. Luminescent experiments were performed using a Fluorimetre Nanolog<sup>TM</sup> Horib Jobin Yvon IHR320 (detects fluorescence in the near-IR from 800 to 1700 nm. An integrating sphere was used to measure the quantum yields of **1** and **2**.*

### 3. Synthetic procedures

#### Synthesis of MnO<sub>2</sub><sup>1</sup>

An aqueous solution of MnSO<sub>4</sub> (11.5 g, 68.0 mmol in 20 mL Milli-Q water) and NaOH (14 g, 350 mmol in 16.5 mL Milli-Q water) was added dropwise to a solution of KMnO<sub>4</sub> (13.0 g, 85.2 mmol in 80 mL Milli-Q water) heated at 40 °C. After 1 h, the reaction was cooled to room temperature, filtered through a filter plate and thoroughly washed with Milli-Q water. Finally, the product was dried in an oven at 100 °C for 3 nights. Yield 60 %

#### Synthesis of 4-aminobenzaldehyde<sup>2</sup>

9 g of freshly synthesized MnO<sub>2</sub> (103.5 mmol) was added into a solution of 4-aminobenzyl alcohol (2.00 g, 16.2 mmol) in 48 mL of dry DCM. After 2 days, the mixture was filtered through celite and the solvent was evaporated under vacuum to provide 4-aminobenzaldehyde in 94 % yield. <sup>1</sup>H-NMR (360 MHz, CDCl<sub>3</sub>) δ: 9.73 (1H, s) 7.69 (2H, d, J=8.5 Hz), 6.69 (2H, d, J=8.5 Hz) 4.35 (2H, s). <sup>13</sup>C NMR (90 MHz, CDCl<sub>3</sub>) δ: 190.6, 152.7, 132.4, 127.5, 114.2. MS MALDI-TOF (m/z) calcd for 4-aminobenzaldehyde: 121.0 [M]; found: 122.0 [M+1].

#### Synthesis of 1-pyrenecarboxylic acid (pyCOOH)<sup>3</sup>

A solution of KMnO<sub>4</sub> (664 mg, 4.2 mmol) in 50 mL of Milli-Q water was refluxed with a solution of 1- pyrenecarboxaldehyde (250 mg, 0.108 mmol) in 50 mL acetone for 24 h. Subsequently, the mixture was filtered and extracted with DCM. Afterwards, the aqueous phase was acidified until reaching pH=2 and centrifuged to isolate the product in 59% Yield. <sup>1</sup>H-NMR (400 MHz, DMSO-d<sub>6</sub>) δ: 13.30 (b, 1H) 9.24 (1H, d, J=9.4 Hz), 8.62 (1H, d, J=8.1 Hz) 8.43 (5H, m), 8.27 (1H, d, J= 8.7 Hz), 8.18 (1H, t, J=7.8 Hz). MS MALDI - TOF (m/z): calcd for PyCOOH: 246.07 [M]; found: 245.10 [M-1].

#### NH<sub>2</sub>CCMoid (1)

78 μL of acetylacetone (0.77 mmol) and 53.7 mg of B<sub>2</sub>O<sub>3</sub> (0.77 mmol) in 0.5 mL of DMF were heated at 80 °C for 30 min. Then sequentially, at an interval of 30 min, 0.83 mL of tributylborate (3.07 mmol) and a solution of 425 mg of 4-aminobenzaldehyde (3.50 mmol) in 1 mL of DMF were added. The mixture was allowed to evolve at 80 °C for half an hour before the dropwise addition of a solution of 30 μL of butylamine (0.30 mmol) in 0.4 mL DMF. The reaction was kept at 80 °C for a total of 4 h and subsequently 6 mL of Milli-Q water was added allowing the mixture to cool to RT and stirring for 1 extra hour. Finally, the reaction was filtered, washed with Milli-Q water and dried with Et<sub>2</sub>O. Yield 30 %. <sup>1</sup>H NMR (360 MHz, CDCl<sub>3</sub>) δ: 16.20 (1H, s) 7.59 (2H, d, J=15.9 Hz), 7.40 (4H, d, J=8.2 Hz) 6.67 (4H, d, J= 8.2 Hz), 6.45 (2H, d, J= 15.9 Hz), 5.73 (1H, s), 3.94 (4 H, s). <sup>13</sup>C NMR (90 MHz, CDCl<sub>3</sub>) δ:183.6, 148.7, 140.7, 130.1, 125.7, 120.3, 115.1. Elemental analysis calculated for C<sub>19</sub>H<sub>18</sub>N<sub>2</sub>O<sub>2</sub>·0.5 H<sub>2</sub>O: C: 72.36 %; H: 6.07 %; N: 8.88 %; O: 12.68 %, found: C 72.20 %; H 5.66 %; N: 9.00 %; O: 13.14 %; MS MALDI - TOF (m/z) calculated for NH<sub>2</sub>CCMoid: 306.1 [M]; found: 304.9 [M-1].

### **Hemi-NH<sub>2</sub>CCMoid**

HemiNH<sub>2</sub>CCMoid was obtained as a byproduct in the previous reaction in an 8 % yield. The mother liquid from the final filtration described for **2** contained HemiNH<sub>2</sub>CCMoid as a thin precipitate that was isolated by centrifugation, washed with Milli-Q water and dried with Et<sub>2</sub>O. <sup>1</sup>H NMR (360 MHz, CDCl<sub>3</sub>) δ: 15.58 (1H, s) 7.55 (1H, d, J=15.9 Hz), 7.37 (2H, d, J=8.4 Hz) 6.67 (2H, d, J= 8.4 Hz), 6.30 (1H, d, J= 15.9 Hz), 5.59 (1H, s), 3.94 (2H, s), 2.14 (3H, s). <sup>13</sup>C NMR (100 MHz, CDCl<sub>3</sub>) δ: 196.3, 140.6, 130.0, 118.7, 115.1, 110.13, 100.5, 26.8. Elemental analysis calculated for C<sub>12</sub>H<sub>13</sub>NO<sub>2</sub>·0.5 H<sub>2</sub>O: C 67.94 %; H: 6.65 %; N: 6.60 %; O: 18.31 %, found: C 67.98 %; H: 6.33%; N: 7.23 %; O: 18.46 %; MS MALDI- TOF (m/z) calculated for HemiNH<sub>2</sub>CCMoid: 203.1 [M]; found: 202.1 [M-1].

### **pyACCMoid (2)**

30 mg pyCOOH (0.12 mmol) were dissolved in 0.8 mL of SOCl<sub>2</sub> (11.2 mmol) and refluxed for 3 h. Subsequently, the excess of SOCl<sub>2</sub> was removed under vacuum. A solution of the product in 5 mL of dry THF was transferred into a MW vial, together with 16 μL of Et<sub>3</sub>N (0.11 mmol), and a dispersion of NH<sub>2</sub>CCMoid (18.4 mg, 0.06 mmol) in 12 mL of dry THF. The mixture was placed into the microwave reactor at 60 °C for 90 minutes. After that time, the mixture was filtered, the solvent evaporated, and the product washed with hot ACN to obtain the pure product as a solid in 25 % yield. <sup>1</sup>H NMR (400 MHz, DMSO-d<sub>6</sub>) δ: 16.28 (1H, s), 10.98 (2H, s), 8.51 (2H, d, J=9.1 Hz), 8.43 (16H, m) 8.33 (9H, m), 8.17 (2H, t, J= 7.4 Hz), 7.99 (4H, d, J= 8.8 Hz), 7.82 (2H, d, J= 8.8 Hz), 7.70 (2H, d, J= 16.1 Hz), 6.95 (2H, d, J= 16.1 Hz), 6.20 (1H, s); Elemental analysis calculated for C<sub>53</sub>H<sub>42</sub>N<sub>2</sub>O<sub>4</sub>·4 H<sub>2</sub>O: C 76.24 %; H: 5.07 %; N: 3.36 % found: C 76.86 %; H: 4.25 %; N: 3.35 %; MS MALDI - TOF (m/z): calcd for PyACCMoid: 762.2 [M]; found: 761.3 [M-1].

## 4. Molecular characterization

### NH<sub>2</sub>CCMoid (1)

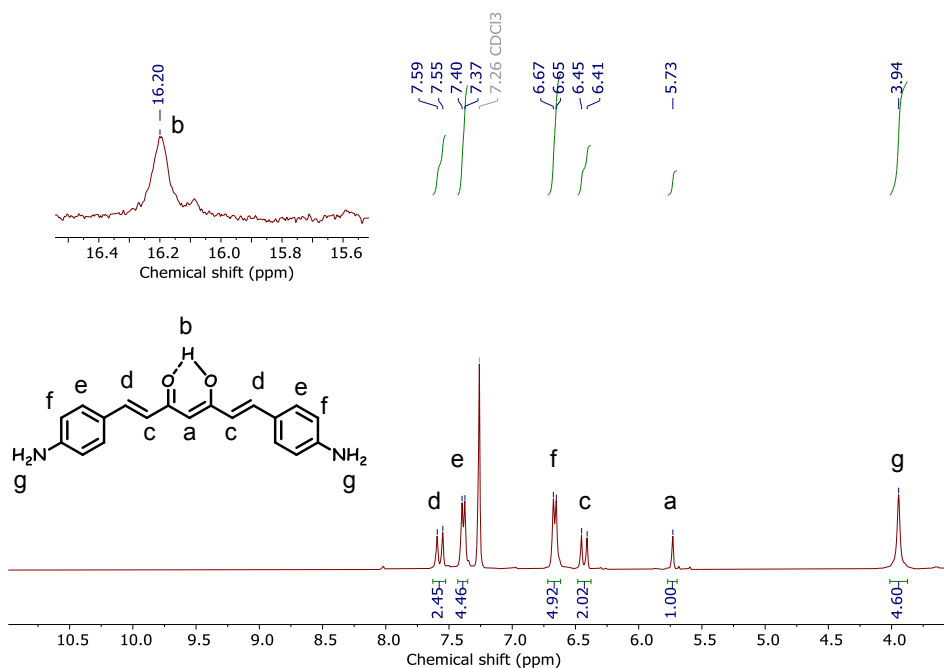


**Figure S1.** <sup>1</sup>H-NMR spectrum of **1** in CDCl<sub>3</sub>.

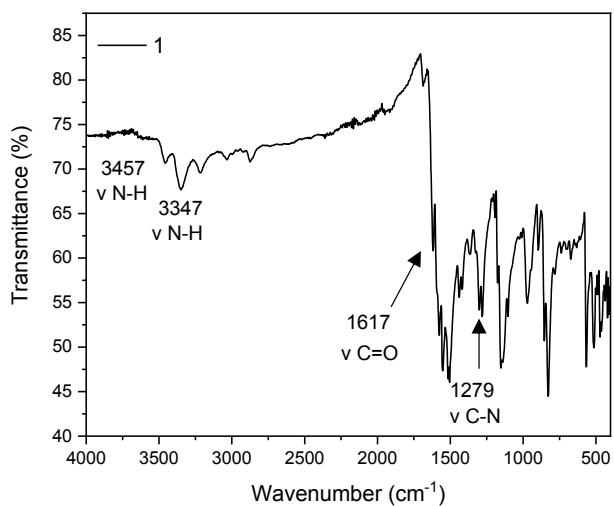


**Figure S2.** ATR-FTIR spectrum of **1**.

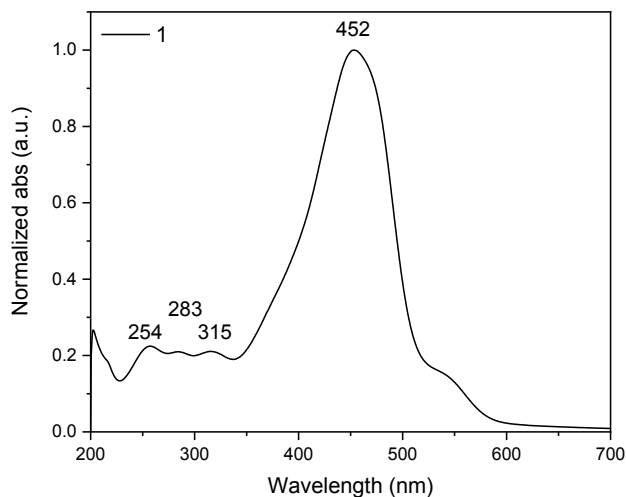


**Figure S3.** UV-vis absorption spectrum of **1** in THF.

The solvatochromic behavior of CCMoids <sup>1</sup> hinders the estimation of the energy band gap from the solution spectra. That's why we performed the estimation of the band gap using absorption spectroscopy in the solid-state, and the Tauc's equation<sup>2</sup> as it is described in Eq S1.

$$(\alpha h\nu)^{1/n} = A (h\nu - E_g) \quad (\text{Eq S1})$$

Where:

$$\alpha(\text{absorption coefficient}) = \frac{2.303 * \text{absorbance}}{l}$$

$l$  = sample thickness (cm)

$h$  =Plank's constant (J/s)

$$\nu = \text{photon frequency} = \frac{c}{\text{wavelength (m)}}$$

$c$  = speed of light (m/s)

$n=1/2$  (for direct allowed transitions)

$A$ = proportionality constant



Plotting the  $(\alpha h\nu)^{1/n}$  versus  $(h\nu)$ , the optical bandgap,  $E_{g_{op}}$ , corresponds to the intersection between the  $x$  axis with the tangent of the curve.

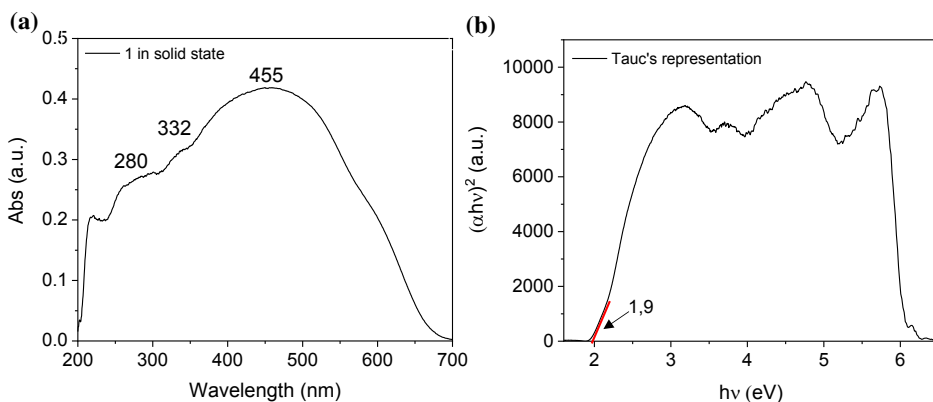


**Figure S4.** (a) Solid-state UV-vis absorption spectrum of **1** (b) Tauc's representation of the solid-state spectrum of **1**.

The differential pulse voltammetry (DPV) plot was also employed to estimate the HOMO-LUMO values, which can be related to the energy required to extract or to introduce an electron. Therefore, they can be correlated to the first electrochemical oxidation and reduction processes, as Eqs. S2 and S3 indicate.

$$E_{HOMO} = -(E_{onset\ oxidation}) + 4.8 \quad (\text{Eq. S2})$$

$$E_{LUMO} = -(E_{onset\ reduction}) + 4.8 \quad (\text{Eq. S3})$$

Where 4.8 eV is the energy level value of the Fc/Fc<sup>+</sup> pair in vacuum.

Finally, the bandgap can be calculated following Eq S4.

$$E_g = (E_{HOMO}) - (E_{LUMO}) \quad (\text{Eq. S4})$$

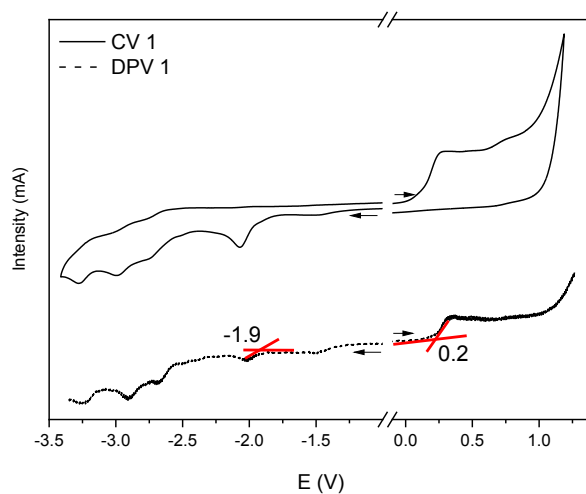


**Figure S5.** Cyclic voltammetry (CV) and differential pulse voltammetry (DPV) of **1**.

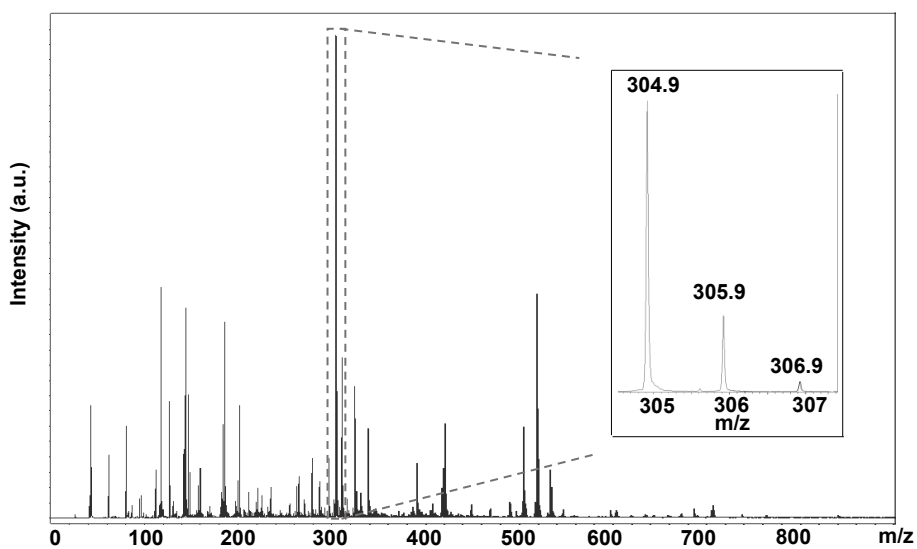


**Figure S6.** MALDI-TOF spectrum of **1** in negative mode

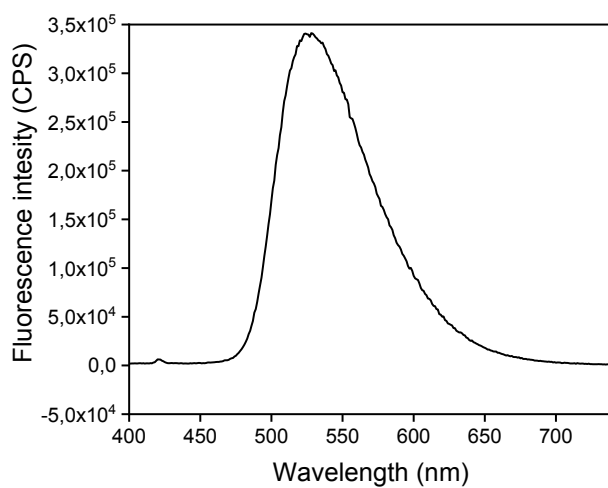


**Figure S7.** Fluorescent spectrum of **1** in THF at RT. The excitation wavelength ( $\lambda_{exc}$ ) is 375 nm. QY= 1.48%

### Hemi-NH<sub>2</sub>CCMoid

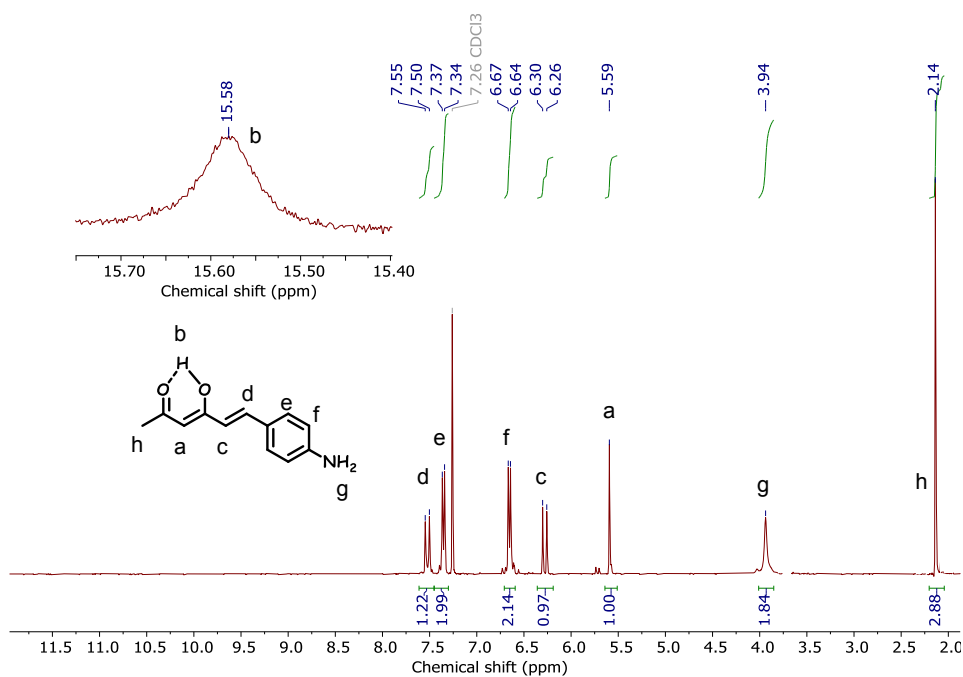


**Figure S8.** <sup>1</sup>H-NMR spectrum of Hemi-NH<sub>2</sub>CCMoid in CDCl<sub>3</sub>.

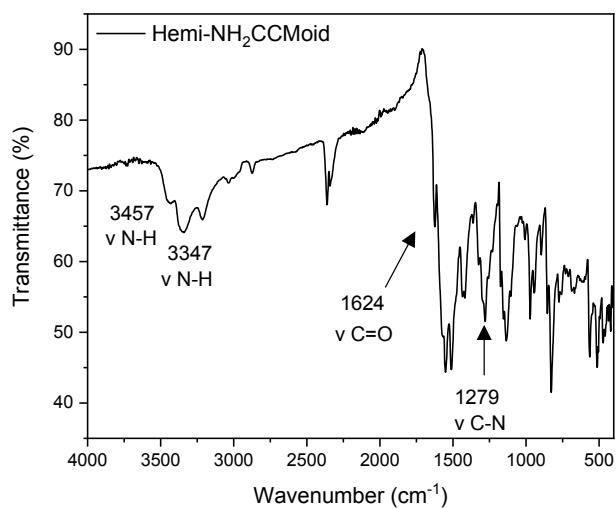


**Figure S9.** ATR-FTIR spectrum of emi-NH<sub>2</sub>CCMoid.

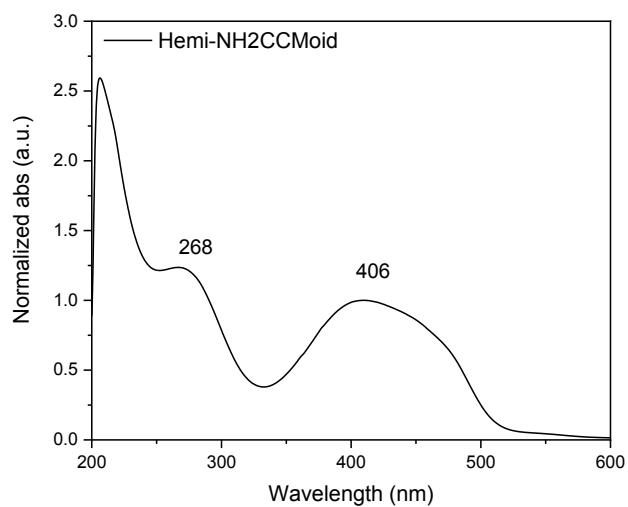


**Figure S10.** UV-Vis absorption spectrum of hemi-NH<sub>2</sub>CCMoid in THF.

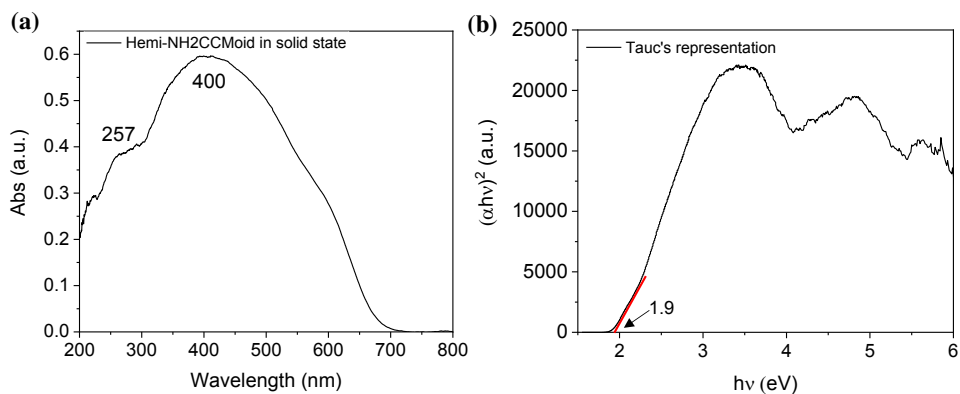


**Figure S11.** (a) Solid- state UV-vis absorption spectrum of hemi-NH<sub>2</sub>CCMoid (b) Tauc's representation of the solid-state spectrum of hemi-NH<sub>2</sub>CCMoid.

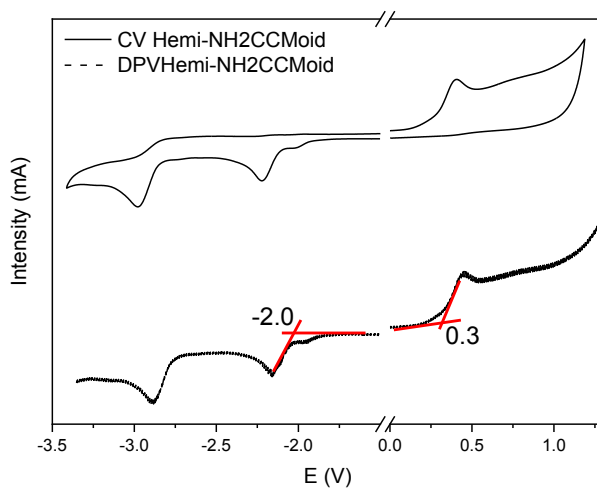


**Figure S12.** CV and DPV of compound hemi-NH<sub>2</sub>CCMoid.

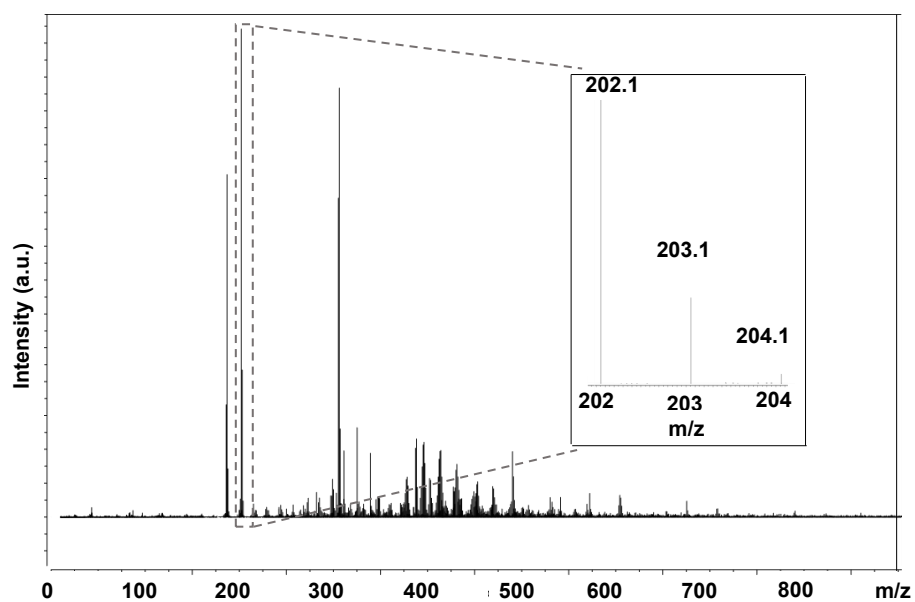


**Figure S13.** MALDI-TOF spectrum of hemi-NH<sub>2</sub>CCMoid in negative mode.

pyACCMoid (2)

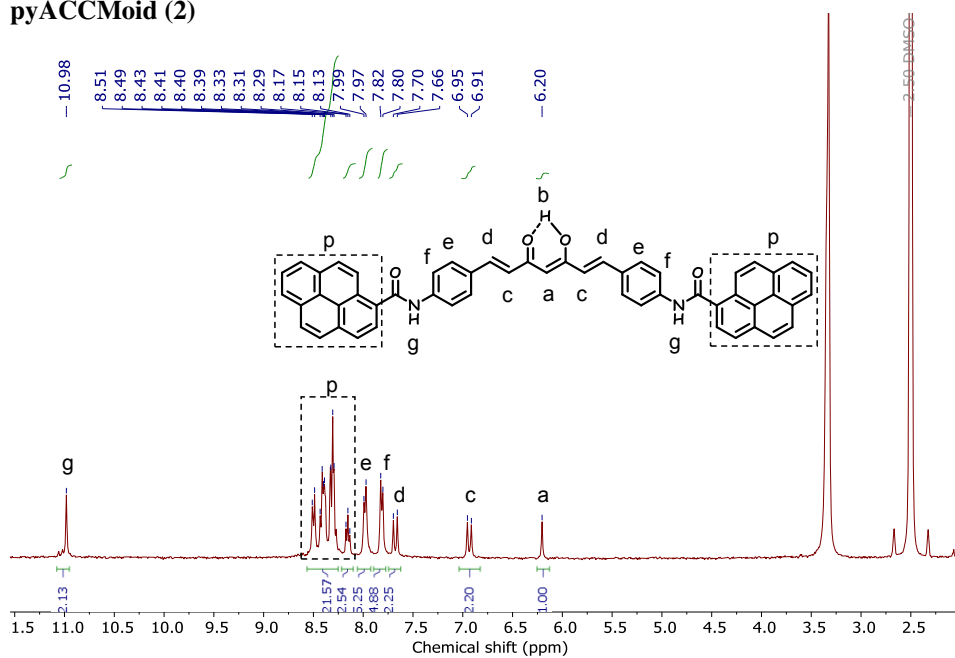


**Figure S14.** <sup>1</sup>H-NMR spectrum of **2** in DMSO-d<sub>6</sub>.

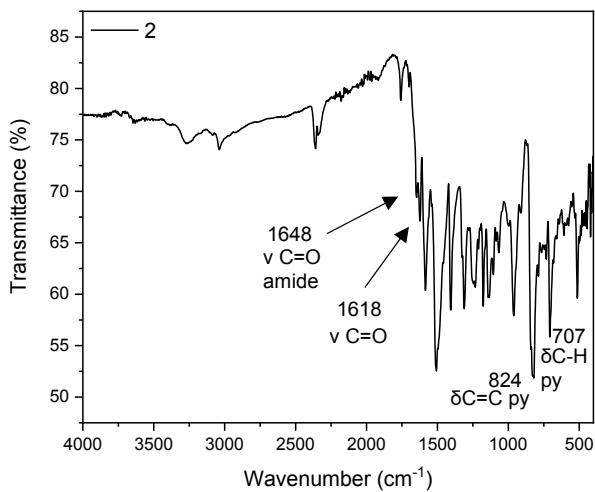


**Figure S15.** ATR-FTIR spectrum of **2**.

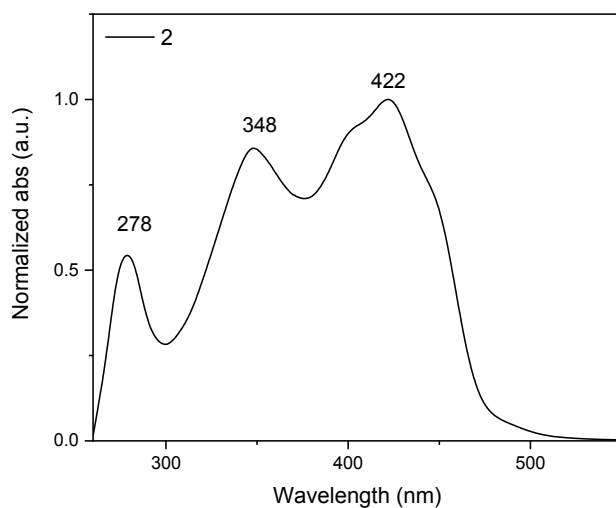


**Figure S16.** UV-vis absorption spectrum of **2** in THF.

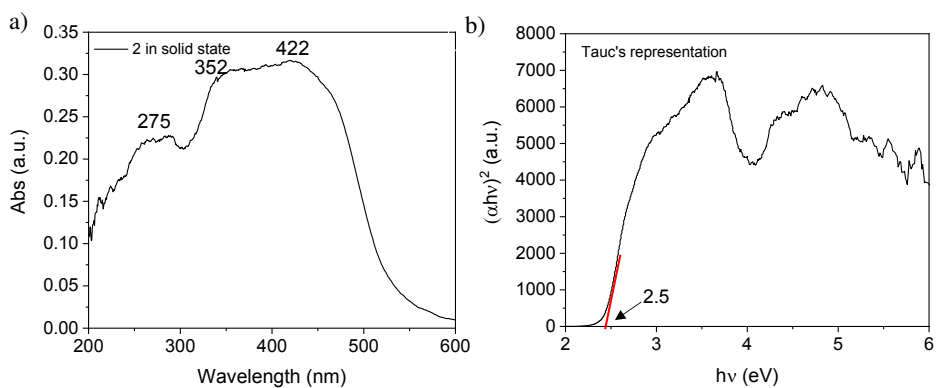


**Figure S17.** (a) Solid-state UV-vis absorption spectrum of **2** (b) Tauc's representation of the solid-state spectrum of **2**.



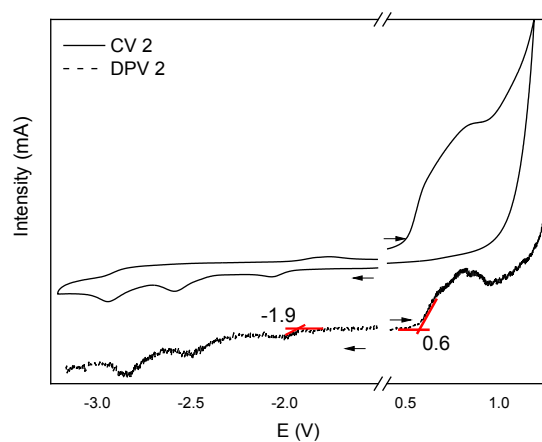


**Figure S18.** CV and DPV of **2**.

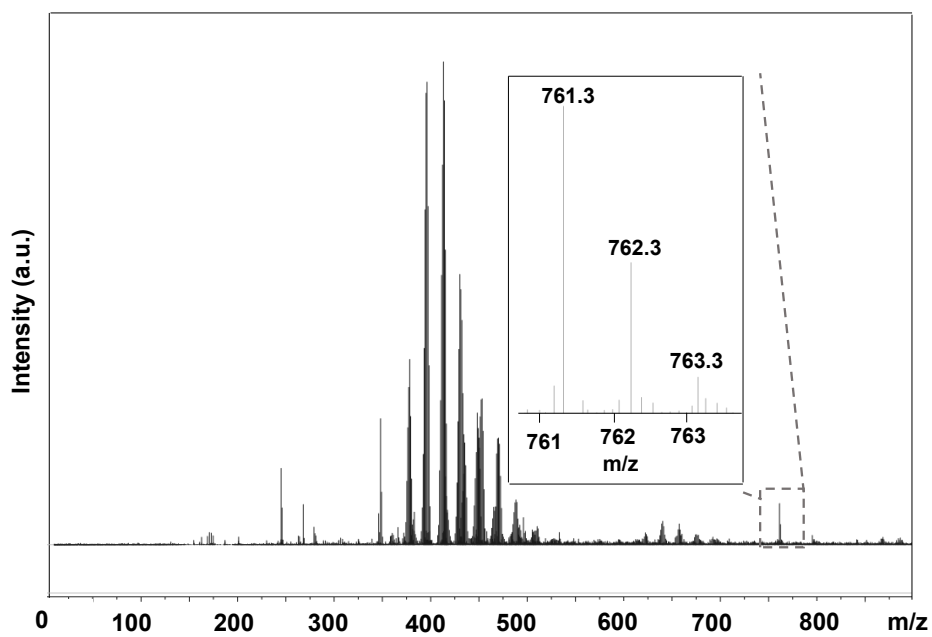


**Figure S19.** MALDI-TOF spectrum of **2** in negative mode.

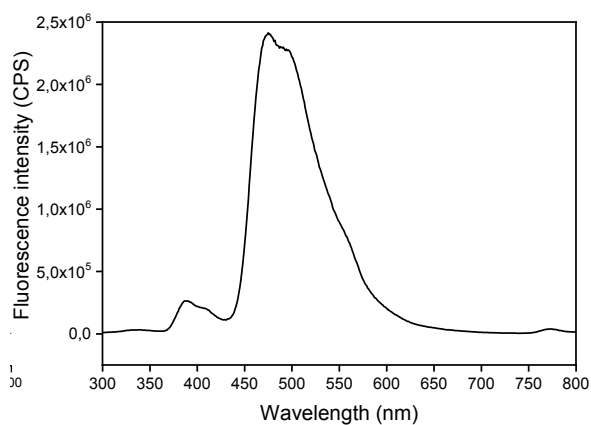


**Figure S20.** Fluorescent spectrum of compound **2** in THF at RT. The excitation wavelength ( $\lambda_{\text{exc}}$ ) is 280 nm. QY= 0.84%

#### Energetic diagram of CCMoids estimated by electrochemistry

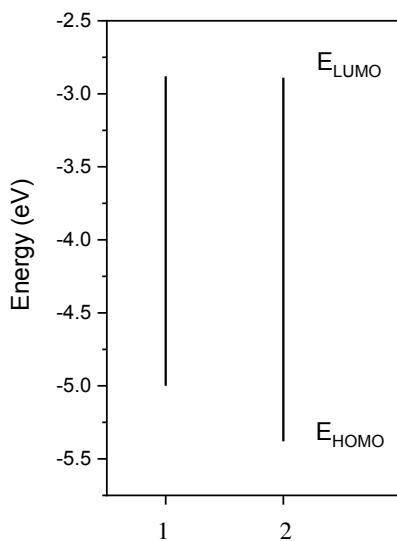
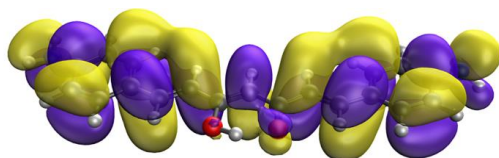


**Figure S21.** HOMO and LUMO energetic diagram of compounds **1** and **2**.

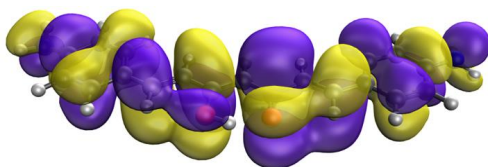
<b>CCMoids</b>	$Eg_{op(exp)}$	$Eg_{elec(exp)}$	HOMO exp	LUMO exp	B3LYP <sub>T</sub> DDFT	B3LYP	HOMO <sub>B3LYP</sub>	LUMO <sub>B3LYP</sub>
<b>1</b>	2.0	2.1	-5.0	-2.9	2.7	3.2	-5.3	-2.1
<b>2</b>	2.5	2.5	-5.4	-2.9	2.6 (2.5)	3.0 (2.9)	-5.8(-5.8)	-2.8(-2.9)

**Tab S1.** List of experimental and theoretical energetic data (in eV) and comparison between systems 1-2.

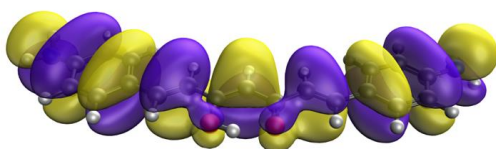
## 5. Computational details.



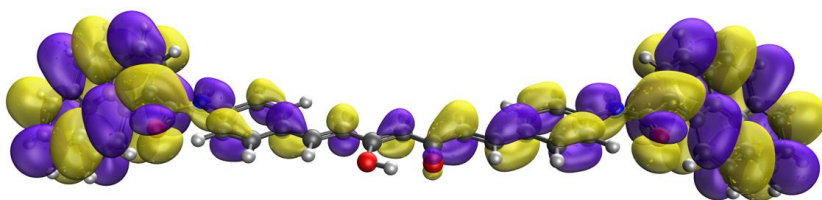
1 LUMO+1



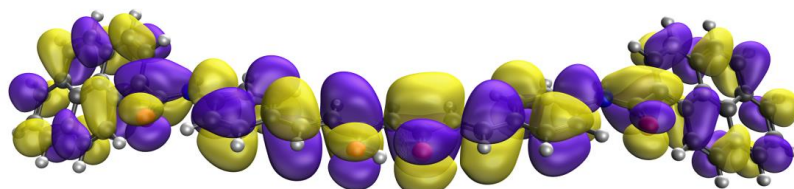
1 LUMO



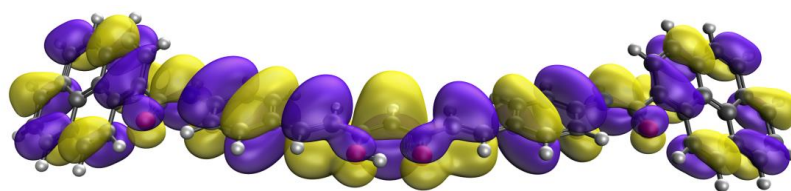
1 HOMO



2 LUMO+1



2 LUMO



2 HOMO

**Figure S22.** Frontier orbitals for the optimized structures of **1** and **2** using B3LYP calculations.

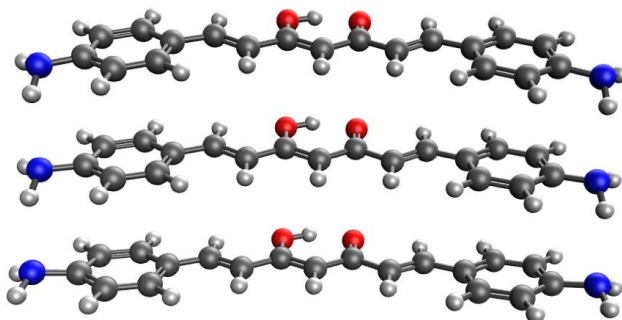
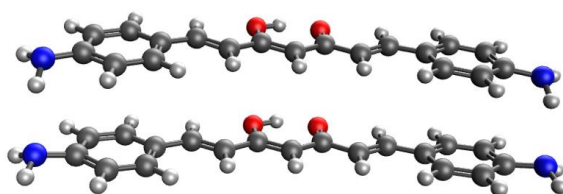


**Figure S23.** DFT optimized structure for the dimer (above) and trimer (below) of **1**.

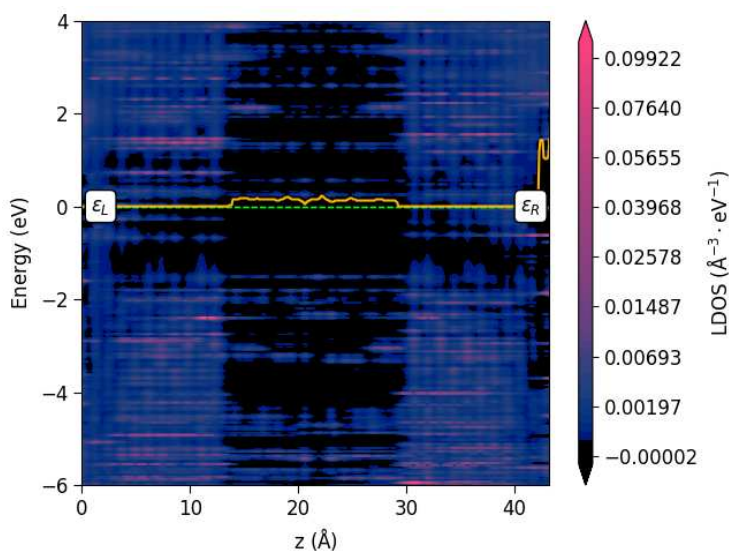


**Figure S24.** Projected local density of states for **2** on a graphene nano-gap. The x axis corresponds the distance of the to the left electrode in the device. Fermi level is highlighted in a dashed green line while the orange line indicated the energy of the conduction band edge.

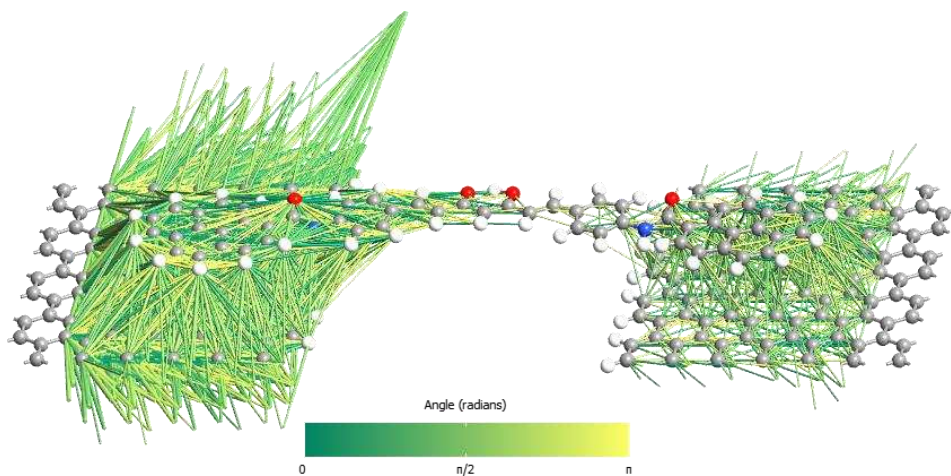


**Figure S25.** Transmission pathways for **2** on a graphene nano-gap. The color of the arrows (in CCM) indicates the angle of the direction of the transport, green ( $0^\circ$ , forward) and yellow ( $180^\circ$ , backward), respectively, and intermediate colors ( $0-180^\circ$ ). The width of the arrow is proportional to the magnitude of the transport. A threshold value of  $1 \cdot 10^{-7}$  was employed. Transmission pathways are calculated by the projection of the total transmission in pair contributions between atoms employing localized orbitals. This decomposition can be represented in real space by arrows indicating forward and backward current flow.

## 6. Device: fabrication and electrical measurements

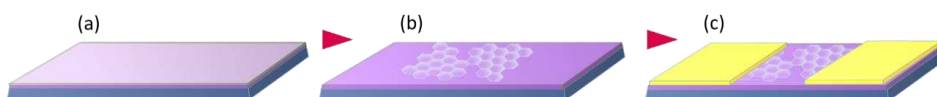


**Figure S26. Devices fabrication steps.** (a) 1 cm x 1 cm monolayer CVD graphene on 300 nm SiO<sub>2</sub> on doped silicon (used as back-gate) was purchased from Graphenea. (b) First, graphene is patterned into bow-tie shapes with a 400 nm wide constriction using e-beam lithography and oxygen plasma etching. (c) Contact pads are patterned by using laser lithography followed by thermal evaporation of 5 nm chromium, as adhesion layer, and 40 nm gold.

### Electrical characterization of nano-gaps.

We have performed electroburning of 279 devices with initial resistance values between  $(2 \div 20)$  K $\Omega$ . Of these, a total of 154 (>55%) devices could be burnt while the remaining could not be opened after reaching a threshold resistance value, as already observed<sup>5</sup>. Most successfully burnt devices showed finite resistance values between  $(0.5 \div 10)$  G $\Omega$ . In the other cases, the feedback control was not fast enough to prevent uncontrolled electroburning resulting in nano-gaps with infinite resistance values ( $>10$  G $\Omega$ ). The global statistics of device resistance evolution throughout the different stage of the experiment is depicted below.

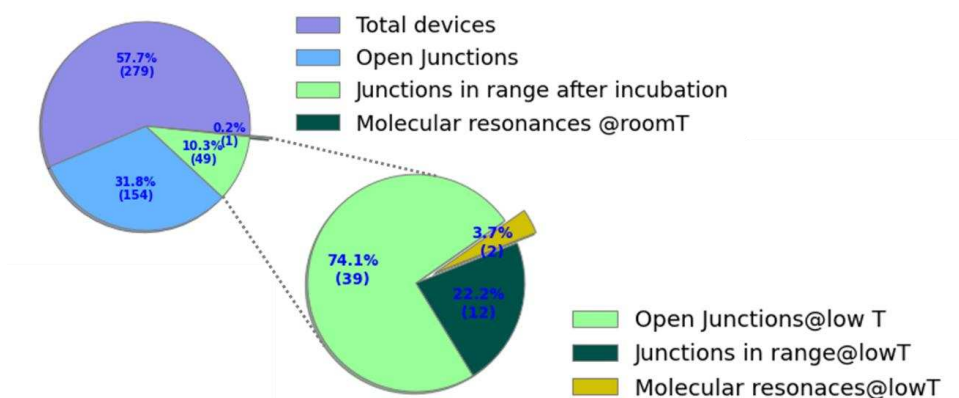


**Figure S27. Overview of experiment statistics.** Devices distribution according to the values of zero bias resistances measured after each step of the experiment: electroburning (open junctions), deposition of molecules (Junction in range after incubation), molecular devices showing molecule signature at room temperature (Molecular resonance @ room T); and after cooling down (Open Junction@lowT), junctions with resistances in range and no leakage after cooling (Junctions in range@lowT) and finally molecular devices with Coulomb diamond(s) at low temperature (Molecular resonances@lowT).

Here, “Open junctions” are junctions with resistance values in the range of (0.5-10) G $\Omega$ ; “Junctions in range after incubation” are the ones showing a resistance decrease after incubation with values in the range (0.2-10) G $\Omega$ . After the cooling down, we report a redistribution of the device resistances towards values falling either in the very low or very high range, meaning closing of the gap or opening to an infinite resistance (>10 G $\Omega$ ). We attributed this occurrence to the building up of tensile stress in the graphene layer during the system’s cooling down. Beyond this, the total number of measurable devices left after each experiment step decreases due to gate leakage.

Current-voltage characteristics of burnt devices with finite resistances were measured at room temperature and ambient pressure in the low bias voltage range ( $\pm 200$  mV). The set-up used to perform the electrical characterization is custom-built at Delft University, and it consists of a low-noise IVVI-DAC rack together with a matrix module.

Devices showing tunneling-like  $I$ -Vs like that represented in Figure S28 allow the estimation of the gap size by fitting the data through the Simmons model<sup>6</sup> assuming a rectangular potential barrier:

$$I = \frac{Ae}{h^2} \left[ \left( \varphi - \frac{eV_{bias}}{2} \right) - e \left( -\frac{4\pi d}{h} \sqrt{2m \sqrt{\left( \varphi - \frac{eV_{bias}}{2} \right)}} \right) + \left( \varphi + \frac{eV_{bias}}{2} \right) - e \left( -\frac{4\pi d}{h} \sqrt{2m \sqrt{\left( \varphi + \frac{eV_{bias}}{2} \right)}} \right) \right] \quad (\text{Eq. S5})$$

where  $e$  and  $m$  are the elementary electron charge and mass,  $h$  is the Planck constant,  $\varphi$  the electrode’s work function, which in the case of graphene is 4.3 eV. Finally,  $A$  is the area and  $d$  the size of the nano-gap.

It is well known that when applying the Simmons model different parameter sets could lead to very similar curve families. For this reason, a carefully selection of the initial parameters is important especially when the uncertainty is higher, as it is in the case of the junction area. We can assume that  $A$  is greater than a single carbon atom and smaller than the initial bow-tie cross-section (400 nm) while for the height we can assume it to be equal to a single carbon atom. Considering this, we performed the Simmons fit by using the two limiting area values corresponding to the above cases, i.e., 0.01 nm<sup>2</sup> and 100 nm<sup>2</sup>. However, the difference between the resulting fitting parameters only affects higher decimals, and independently from the junction area, we obtain average values for the size of  $d = (2.4 \pm 0.3)$  nm and  $\varphi = (1.7 \pm 0.4)$  eV for the barrier height.



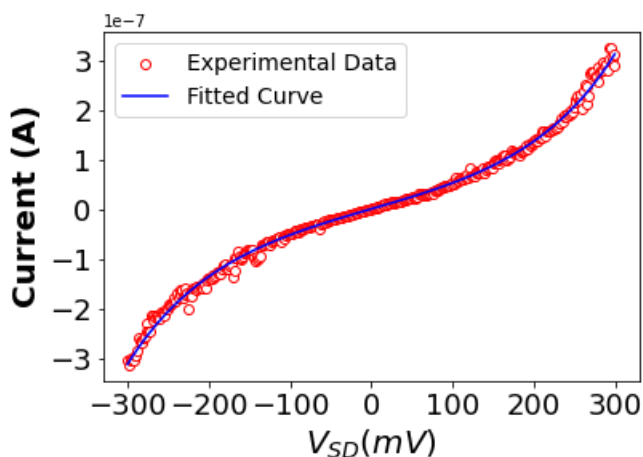


**Figure S28. I-V bias characteristics of an open constriction.** Current as a function of the voltage measured in an open constriction, showing an exponential dependence at bias voltages above hundreds of mV associated with single barrier tunneling. The corresponding fit of the experimental data to the Simmons model is shown as the drawn blue line.

The  $I$ - $V$  characteristics measured at different gate voltages is shown in Figure S29 (left) with the corresponding differential conductance  $\frac{dI}{dV}$  represented as a function of the bias and gate voltage (right), showing absence of gate-voltage dependence. These observations are a strong indication that the nano-junctions are empty and applicable for the analysis of electron transport through single molecules.

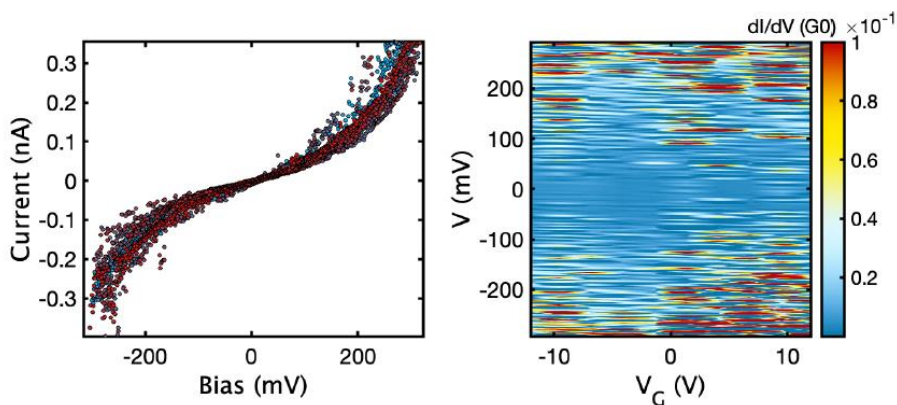


**Figure S29. Open junction characterization at room temperature.** (Left) Current as a function of bias for different gate voltages of an open junction, and (Right) corresponding differential conductance as a function of bias and gate voltage, compiled in a stability diagram highlighting the absence of gate dependence of  $I$ - $V$  characteristics associated with current tunneling.

### Molecule deposition characterization.

We have deposited pyACCM (2) molecules on the graphene nano-junctions by dip coating of the devices during 1 h in a 0.1 mM solution of the compound in THF. The pyrene groups are extended  $\pi$  systems that provide more robust stacking on graphene electrodes compared to anthracene groups alternatively used to functionalize graphene by  $\pi$  -  $\pi$  stacking interactions. The deposition method was selected after comparing the results of molecular functionalization of pristine graphene surfaces by drop casting and dip coating, as shown in the figure below.

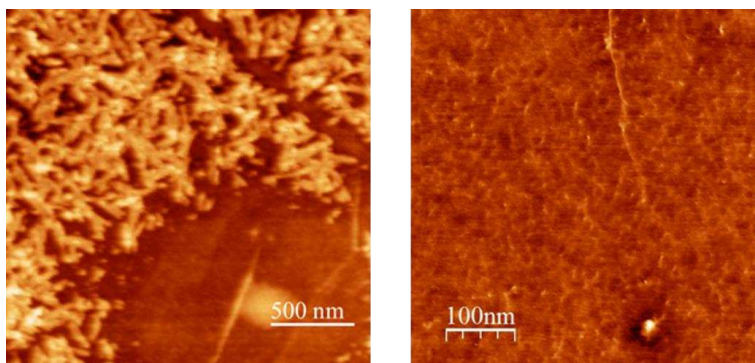


**Figure S30. Molecular deposition. (Left)** Atomic Force Microscope (AFM) picture of the single-layer graphene substrate after drop cast of the pyACCMoid molecular solution in THF. Large polymerization on the surface is observed as a result after drop cast of the compound. **(Right)** When the molecules are deposited by dip coating the resulting repartition on the surface looks more uniform indicating less compound polymerization.

### Room-temperature electrical characterization of nano-junctions after molecule deposition.

After the deposition of pyACCMoid molecules, we checked the zero-bias resistances of the junctions to select the ones with values between  $(0.2 \div 10) \text{ G}\Omega$ . Molecular resonances tend to occur far from the zero-gate window, and measurement of zero-bias conductance is, in general, not sufficient to detect changes after molecular functionalization. However, taking advantage of using a probe-station based setup, it is possible to move easily from device to device and perform a detailed check of the junction resistances. We measured resistances at zero gate voltage with values in the range  $(0.2 \div 10) \text{ G}\Omega$  for a total of 49 junctions. In the case of one junction, we detected changes in the gate dependence after molecular deposition at room temperature, Figure S31.

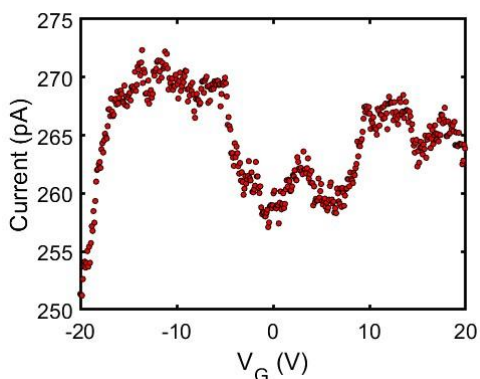


**Figure S31. Gate sweep at room temperature.** Current as a function of the gate voltage for fixed 10 mV bias (gate-sweep) measured at room temperature on a hybrid graphene-pyACCMoid nano-junction showing conductance variation of about 10 pA.

We characterized the device of Figure S31 in more detail by measuring the current as a function of the bias and gate voltage compiled into a stability diagram that is shown in Figure S32 (right) that displays a strong gate dependence of the output current revealing a non-empty gap.

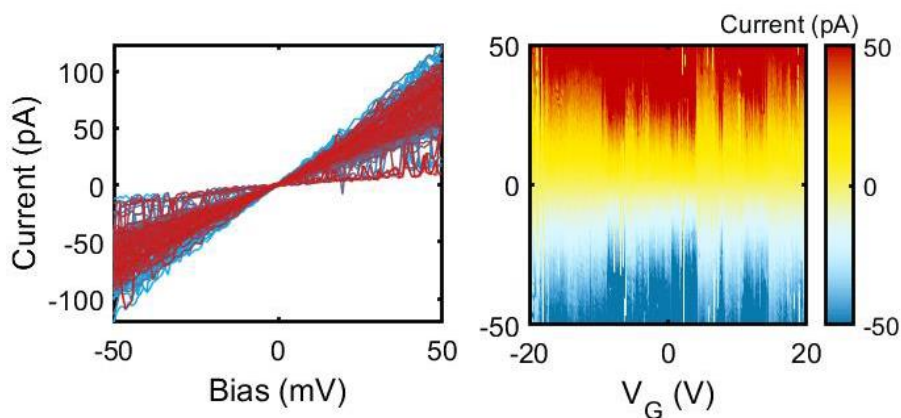


**Figure S32. Stability diagram at room temperature. (Left)** Current as a function of bias voltage for different gate voltages measured after molecule deposition. **(Right)** Stability diagram measured for the same device at room temperature showing gate modulation of the current (and thus conductance).

Low-temperature electrical characterization of molecular junctions.

Low-temperature measurements were carried out by using a cryogenic probe station (LakeShore) allowing to reach a temperature of about 10 K. After cooling down the system, we repeated the check of the zero-gate resistances across the junctions finding a total of 12 devices in the range of interest. Of these, we detected molecular resonances in

2 devices. Here, we report the results obtained from the measurement of the current as a function of the gate voltage for the other junction (*junction 2*) not described in the manuscript.

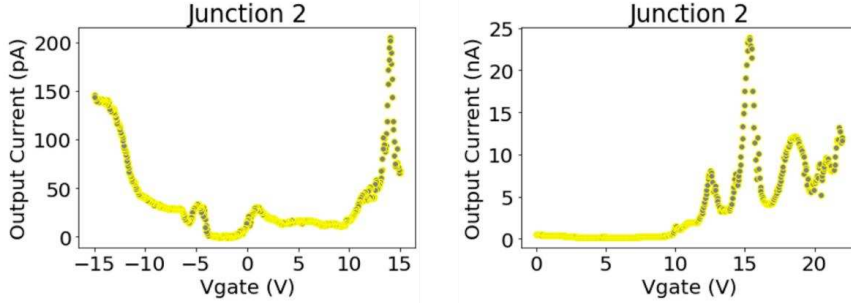


**Figure S33. Gate-sweeps of junction 2 at low temperature.** Gate-sweep measured after molecules deposition and cool down to 10 K of a hybrid graphene molecular junction. **(Left)** and **(Right)** are obtained in two subsequent measurements over a different voltage range. Similar features are found in both gate sweep with different intensity, however, they shift with respect to the gate in the time interval between the two measurements repetition.

Figure S33 shows peak-like structures at  $V_G = 12.55$  V; 15.20 V and 18.85 V, and at  $V_G = -15$  V and -5 V. In both junctions, we observed a shift of the resonance peaks with respect to the applied voltage during measurement repetitions, as illustrated in Figure S34.

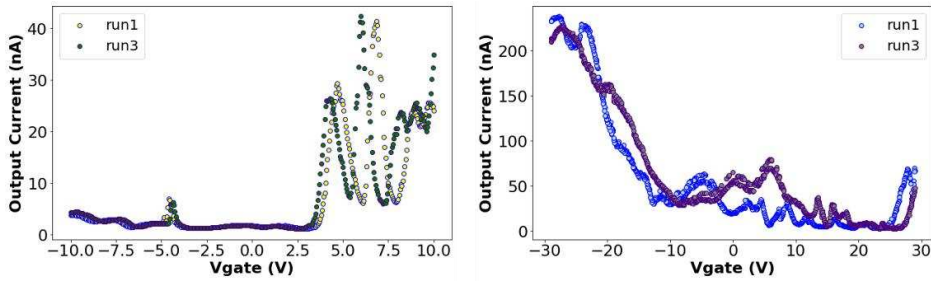


**Figure S34. Gate-sweep of a graphene hybrid molecular junctions** **(Left)** corresponds to the junction discussed in the main text; and **(Right)** is the other pyACCMoid graphene nano-junction with gate dependent features at low temperature.

### Electrostatic characterization.

Under the assumption of weak/intermediate molecular coupling to the electrodes, the transport process can be analyzed by using the constant interaction model<sup>7</sup>. Accordingly, the gate coupling,  $\alpha$ , is defined as<sup>8</sup>:

$$\alpha = \frac{1}{\frac{1}{\beta} + \frac{1}{\gamma}} \quad (\text{Eq. S6})$$

with  $\beta$  and  $\gamma$  being the positive, and negative, slopes of the Coulomb diamond edges, as represented in Fig. S35. In doing so, we find  $\alpha = 0.011$  (1.1%) for the CD around  $V_G = -8$  V (Figure S35) and  $\alpha = 0.005$  (0.5%) for the diamond around  $V_G = -25$  V (see Figure 2(c) for the complete stability diagram).

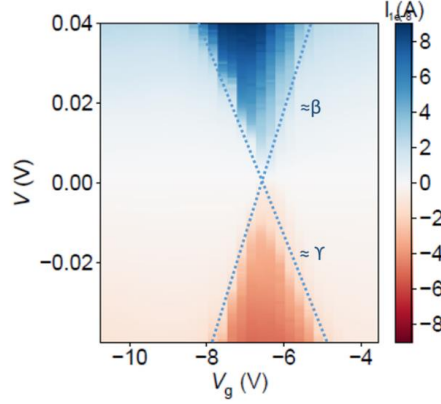


**Figure S35.** Stability diagram around a charge degeneracy point (CDP) for *junction 1* at low temperature. The slopes separating the low- and high-current regions correspond to the relative source ( $C_S$ ) and drain ( $C_D$ ) capacitive couplings to the gate ( $C_G$ ), labelled as  $\gamma = C_G/C_S$  and  $\beta = \frac{C_G}{C_S} + C_D$ .

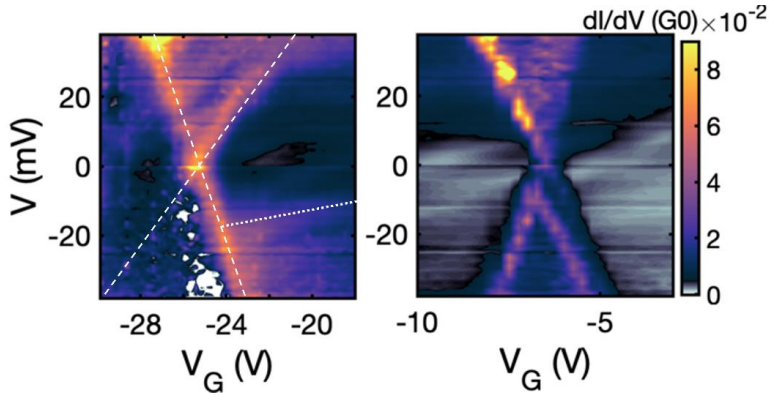


**Figure S36 (Left).** Differential conductance,  $\frac{dI}{dV}$ , of high current regions in the negative gate voltage range around  $V_G = -25$  V and  $V_G = -6$  V **(Right)**. Alternating high and low conduction resonances can be observed in the  $\frac{dI}{dV}$  spectrum of (Left) for the positive bias voltage range, as well as NDC for the negative bias voltages (white area). Here, it is also noted a missing edge of the diamond structure (bottom left area of the plot) and shifting of excitations with respect to the gate voltage (bottom right area of the plot) with conduction lines running not parallel to the edge of the CD, as highlighted by the dotted line.

Figure S36 shows two CDP's for junction 1 in greater detail. Note, that the CDP shifted in gate voltage by about -5 V between measurements displayed in Figure 2(c) and the subsequent one depicted in Figure S36 (Left). The shift with respect to the gate voltage is smaller for the CDP around -6 V as seen by the stability diagram shown in Figure S36 (Right). Both panels in Figure S36 present low-current regions with currents more than one order of magnitude smaller than on resonance (region between the dashed lines in the left panel). White areas indicate the presence of negative differential conduction (NDC). The large difference in gate coupling parameters ( $\alpha(\text{left}) \approx 2\alpha(\text{right})$  with  $\alpha(\text{left})$  and  $\alpha(\text{right})$  being the gate coupling calculated for the CDP's in Figure 36 (Left) and (Right)) is accompanied by opposite source-drain coupling asymmetry:  $C_{D/S} = \frac{C_D}{C_S} = \frac{\beta}{\gamma} - \gamma$  giving  $C_{D/S}(\text{left}) = 1.24$  and  $C_{D/S}(\text{right}) = 0.69$ . This suggests a different origin of the two CDPs, i.e., the presence of two molecules in parallel. As discussed by Gehring *et al.*<sup>9</sup>, the observation of conduction lines running not parallel to the edges of the diamond as highlighted by the dotted line in Figure S36 (Left) can be explained by quantum interference effects involving the graphene electrodes.

- (1) Torres, R. D. PhD Thesis, University of Barcelona (UB), 2018.
- (2) Takahashi, T.; Hijikuro, I.; Sugimoto, H.; Kihara, T.; Shimmyo, Y.; Niidome, T. Preparation of Novel Curcumin Derivatives as Bsecretase Inhibitors. WO 2008066151 A1, 2008.
- (3) Liu, J.; Huang, X.; Wang, F.; Hong, W. Quantum Interference Effects in Charge Transport through Single-Molecule Junctions: Detection, Manipulation, and Application. *Acc. Chem. Res.* **2019**, 52 (1), 151–160. <https://doi.org/10.1021/acs.accounts.8b00429>.
- (4) Liu, T.; Huang, Z.; Feng, R.; Ou, Z.; Wang, S.; Yang, L.; Ma, L. J. An Intermolecular Pyrene Excimer-Based Ratiometric Fluorescent Probes for Extremely Acidic PH and Its Applications. *Dye. Pigment.* **2020**, 174 (November 2019), 108102. <https://doi.org/10.1016/j.dyepig.2019.108102>.
- (5) El Abbassi, M.; Pósa, L.; Makk, P.; Nef, C.; Thodkar, K.; Halbritter, A.; Calame, M. From Electroburning to Sublimation: Substrate and Environmental Effects in the Electrical Breakdown Process of Monolayer Graphene. *Nanoscale* **2017**, 9 (44), 17312–17317. <https://doi.org/10.1039/c7nr05348g>.
- (6) Simmons, J. G. Generalized Formula for the Electric Tunnel Effect between Similar Electrodes Separated by a Thin Insulating Film. *J. Appl. Phys.* **1963**, 34 (6), 1793–1803. <https://doi.org/10.1063/1.1702682>.
- (7) Limburg, B.; Thomas, J. O.; Sowa, J. K.; Willick, K.; Baugh, J.; Gauger, E. M.; Briggs, G. A. D.; Mol, J. A.; Anderson, H. L. Charge-State Assignment of Nanoscale Single-Electron Transistors from Their Current-Voltage Characteristics. *Nanoscale* **2019**, 11 (31), 14820–14827.

<https://doi.org/10.1039/c9nr03754c>.

- (8) Thijssen, J. M.; Van Der Zant, H. S. J. Charge Transport and Single-Electron Effects in Nanoscale Systems. *Phys. Status Solidi Basic Res.* **2008**, *245* (8), 1455–1470. <https://doi.org/10.1002/pssb.200743470>.
- (9) Gehring, P.; Sowa, J. K.; Cremers, J.; Wu, Q.; Sadeghi, H.; Sheng, Y.; Warner, J. H.; Lambert, C. J.; Briggs, G. A. D.; Mol, J. A. Distinguishing Lead and Molecule States in Graphene-Based Single-Electron Transistors. *ACS Nano* **2017**, *11* (6), 5325–5331. <https://doi.org/10.1021/acsnano.7b00570>.







